Conducting polymer-based flexible thermoelectric materials and devices: from mechanisms to applications

Shengduo Xu, Xiao-Lei Shi, Matthew Dargusch, Chongan Di, Jin Zou, Zhi-Gang Chen

PII: S0079-6425(21)00064-5
DOI: https://doi.org/10.1016/j.pmatsci.2021.100840
Reference: JPMS 100840

To appear in: *Progress in Materials Science*

Received Date: 14 December 2020
Revised Date: 12 June 2021
Accepted Date: 25 June 2021

Please cite this article as: Xu, S., Shi, X-L., Dargusch, M., Di, C., Zou, J., Chen, Z-G., Conducting polymer-based flexible thermoelectric materials and devices: from mechanisms to applications, *Progress in Materials Science* (2021), doi: https://doi.org/10.1016/j.pmatsci.2021.100840

Conducting polymer-based flexible thermoelectric materials and devices: from mechanisms to applications

Shengduo Xu,[a,1] Xiao-Lei Shi,[b,1] Matthew Dargusch,[a] Chongan Di,[*,d] Jin Zou,[*,a,c] and Zhi-Gang Chen[*,b,a]

[a]School of Mechanical and Mining Engineering, The University of Queensland, Brisbane, Queensland 4072, Australia.

[b]Centre for Future Materials, University of Southern Queensland, Springfield central, Queensland 4300, Australia.

[c]Centre for Microscopy and Microanalysis, The University of Queensland, Brisbane, Queensland 4072, Australia

[d]Beijing National Laboratory for Molecular Sciences, CAS Key Laboratory of Organic Solids, Institute of Chemistry, Chinese Academy of Sciences, Beijing 100190, China.

[1]These authors contribute equally to this work.

Email: zhigang.chen@usq.edu.au (ZGC); j.zou@uq.edu.au (JZ); dicha@iccas.ac.cn (CAD)

KEYWORDS: thermoelectric; conducting polymer; mechanism; strategy; device.

Abstract

Conducting polymers have drawn considerable attention in the field of wearable and implantable thermoelectric devices due to their unique advantages, including availability, flexibility, lightweight, and non-toxicity. To date, researchers have made dramatic breakthroughs in achieving high-performance thermoelectrics; however, the figure of merit *ZT* of conducting polymers is still far below that of the high-performance thermoelectric Bi_2Te_3-based alloys at room temperature. This challenge lies in the complex interrelation between electrical conductivity, Seebeck coefficient, and thermal conductivity. In this review, we overview the state-of-the-art on conducting polymers and their thermoelectric devices, starting with the summary of the fundamentals as well as several well-accepted theoretical models. Furthermore, this review examines the key factors determining the charge transport mechanisms in this family of materials and previously reported optimization strategies are discussed and classified. Finally, this review further introduces several favourable device fabrication techniques including illustrating and demonstrating the performance of several typical thermoelectric prototypes, which highlights the bright future of polymer-based flexible thermoelectric devices in wearable and implantable electronics.

Table of Contents

1. Introduction

Exploiting abundant waste energy, to generate green electricity power is a viable solution to solve both energy shortage and environmental pollution directly caused by the massive consumption of fossil resources [1-6]. Thermoelectric (TE) technology converts heat directly to electricity and thereby has attracted considerable attention [7-10]. This technology applies materials that are known as TE materials for their ability to produce electrical potential with temperature gradient at two ends based on the Seebeck effect [11]. **Figure 1a** shows the progress of TE materials since the discovery of the Seebeck coefficient, *S*. Other than thermal couples, a device used for TE power generation is named as TE generator (TEG). However, one single thermoelement can only produce rather small TE voltage and output power. Therefore, a TEG normally consists of a large number of n-type and p-type thermoelements alternatively connected electrically in series and thermally in parallel so that sufficiently high TE voltage and output power can be obtained to power electronics [12].

TEGs possess many merits. For examples, TEGs operate in a silent and green mode since no harmful by-products are produced during their operation. TEGs are also able to obtain electrical power from low-grade heat at low temperature, and generally have a long working life [13]. These merits enable TEGs being considered for broad applications where traditional engines are not suitable, and this attracts both scientists and engineers to develop and synthesize better TE materials over the past two centuries. So far, many state-of-the-art inorganic materials, such as bismuth telluride (Bi_2Te_3)-based alloys [14-16] and SnSe [17], have been developed. Apart from these TE materials, the emerging conductive polymers (CPs) and related materials attract significant attention from when they were synthesized in a laboratory in 1973 [18]. These materials are composed of abundant elements, mainly carbon, oxygen, sulfur, and nitrogen, making them non-toxic, easily available, and flexible, as shown in **Figure 1b**. Additional merits are their environmental stability, low weight, and typically low thermal conductivities [19]. These merits make CPs promising materials for applications in TEGs.

A TEG made of CPs is termed as flexible TEG (FTEG) due to its excellent flexibility. The FTEGs can be applied to power micro-watt electronics such as sensors or watches. Implantable devices based on the nontoxic FTEGs may also be suitable to supply power for heart pumps [20]. Such applications of FTEGs are favoured in applications where the FTEGs exploit human body heat instead of chemical energy [21]. With the higher figure of merit *ZT* of CPs, the energy efficiency of an FTEG increases, as shown in **Figure 1c**. Notably, when *ZT* of the TE material reaches 1, the efficiency is 1 % with a hot end temperature of 36.5 ℃. With such a small temperature gradient, even the Carnot engine shows an efficiency of not higher than 6 %. Therefore, the suitable applications for FTEGs should be at the micro-watt level to serve as a power source by exploiting the body heat. Here, *ZT* is used to quantitatively evaluate the performance of TE materials. Its definition is given below [22-26]:

$$ZT = \frac{S^2 \sigma T}{\kappa} \tag{1}$$

where σ represents the electrical conductivity, κ denotes the thermal conductivity, and T is the absolute temperature. Particularly, $S^2\sigma$ is defined as the power factor used to evaluate the output power of TE materials. The energy conversion efficiency is given by the following formula [20]:

$$\eta = \frac{T_\mathrm{h} - T_\mathrm{c}}{T_\mathrm{h}} \left(\frac{\sqrt{ZT_\mathrm{avg} + 1} - 1}{\sqrt{ZT_\mathrm{avg} + 1} + T_\mathrm{c}/T_\mathrm{h}} \right) \tag{2}$$

where T_h and T_c are respectively the hot end temperature and cold end temperature. ZT_avg is estimated by the average *ZT* at a particular temperature ranging from T_h and T_c.

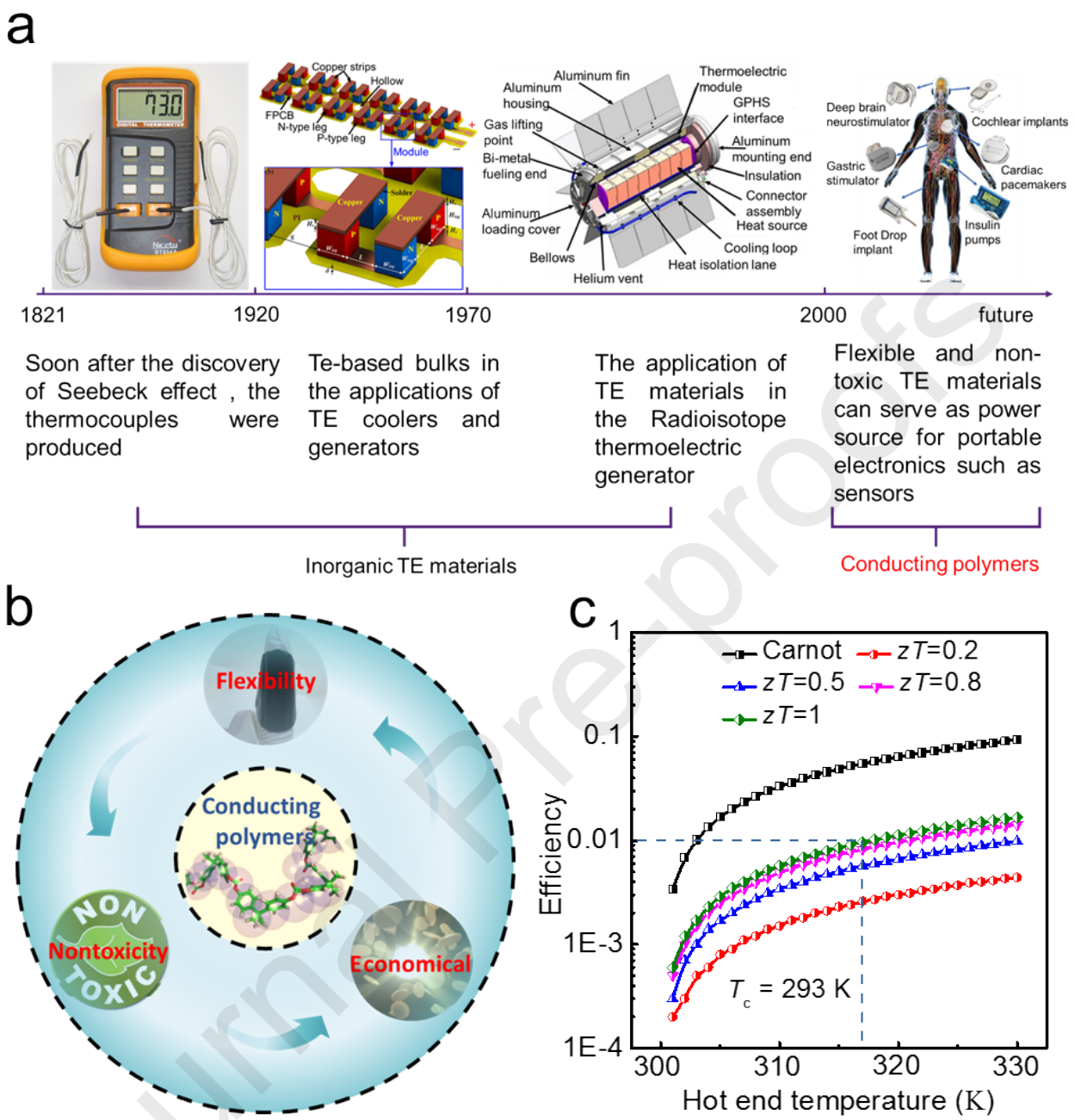

Figure 1. a) Progress in the development and application of thermoelectric (TE) materials since the discovery of the Seebeck effect; b) Merits of conducting polymers (CPs); c) Theoretical conversion efficiency of CPs-based flexible TE generators (FTEGs) for commercial applications.

CPs are not composed of rigid crystal structures which generally exist in crystalline inorganic materials. Such dissimilarity disables the common strategies used for the performance improvement of inorganic TE materials, e.g., band or nanostructure engineering [27-34], to be applied to enhance

the TE properties of CPs. In fact, their unique molecular structure requires different approaches including doping [35-38], secondary doping [39-41], polymerization [42,43], post-treatment [44-47], and hybridization [48,49]. To date, the highest *ZT* of CPs-based TE materials had been improved to 0.42 [50] and 0.58 [48] for pure poly(3,4-ethylenedioxythiophene):poly(styrene sulfonate) (PEDOT:PSS) and PEDOT/Bi_2Te_3 at room temperature, respectively. The former work presented a decent TE performance of pure CPs by ethylene glycol (EG) post-treatment, while the latter work adopted physical vapor deposition (PVD) and vapor phase polymerization (VPP) techniques to hybridize the PEDOT matrix and Bi_2Te_3 filler to exploit both high $S^2\sigma$ of Bi_2Te_3 and low κ of PEDOT, resulting in the highest *ZT* of CPs-based TE material so far. These two pieces of work as well as other studies [49,51,52] suggest that further *ZT* improvements in CPs-based TE materials are achievable by suitable optimization methods [53,54]. Although researchers have achieved considerable progress on CPs-based thermoelectrics, it should be noted that compared to most conventional inorganic TE materials (*ZT*s > 1.0), CPs-based TE materials still show relatively low *ZT*s, and their application temperatures are always lower than that of inorganic materials due to the fact that CPs can be damaged by high temperatures. Generally, although CPs have received extensive attention in thermoelectric research fields, there is still a huge gap in their applications. Therefore, more emphasis should be placed on basic research issues. For example, the challenges lie in the decoupling of σ and S to realize synergetic enhancement in these two electrical properties, and this will require a deeper understanding of the charge transport within the polymers due to their morphological complexity [55]. Similarly, there are other considerable challenges including the development of theoretical models, the in-depth understanding of the organic-inorganic interaction mechanisms in hybrid-based materials, the topological design of FTEGs, the standardization of CPs-based TE materials and devices, the commercialization of FTE devices, and the interdisciplinary applications of CPs-based TE materials and devices.

Over the decades, there have been some reviews covering two aspects of CPs: strategies used to enhance the TE performance of CPs and the potential applications of CPs-based FTEGs in low power portable electronics [56-59] and the physical basics of charge carrier transport in CPs [60,61]. Therefore, a comprehensive review covering recent theoretical studies and summarizing those proposed models is highly essential. To achieve this goal, this review starts with recent theoretical work on CPs and several well-known models. Meanwhile, the underlying physics of charge carrier transport are also discussed in detail. With regard to the performance optimization of CPs, several significant factors affecting the TE properties of CPs including oxidation level, morphological crystallinity and filtering effect, and their correspondent strategies are elucidated. Moreover, we have also reviewed several typical prototypes and their correspondent device fabrication techniques reported recently. By performance analysis, some of these prototypes presented power output high enough to sufficiently power portable electronics, which appreciates the significance of proper structure design for FTE devices. Lastly, we figure out the controversies, challenges, and outlooks toward future developments of FTE materials and devices.

2. Fundamentals for Conducting Polymers

This chapter firstly builds up a connection between the unique structures and electrical properties of CPs. Generally, the special molecular structures of CPs (sp^2 hybridization and backbones) enable the excitation of π bond electrons and the viable transportation for those excited electrons [13]; however, that is not sufficient for high electrical performance. The intrinsically low quinoid (favoured for uncoiled structures) percentage hinders the effectiveness of electronic charge transport [62]. Therefore, strategies, such as increasing the doping level or controlling the polymerization rate [63,64], should be applied to depress the benzoid structure. These strategies also lead to a narrower bandgap between the valence band (Highest Occupied Molecular Orbital, HOMO) and conduction band (Lowest Unoccupied Molecular Orbital, LUMO), making CPs more like metals in terms of the band structure [65]. The quinoid and benzoid structures further form crystalline domains and disordered

regions in CPs where charge carriers behave very differently. Excited charges directionally move in the crystalline domains like in metals, while excited charges transfer in the disordered regions with thermally-assisted hopping or fluctuation-induced tunnelling. The efficiency of electronic charge transport in a crystalline domain is much higher than that in a disordered region since both hopping and tunnelling are transport pathways with low carrier mobility μ. As a result, promoting the formation of crystalline domains strongly improves the electrical performance of CPs.

In the second part, several typical theoretical transport models for CPs are summarized. Due to the non-crystalline structure of CPs, the band theory suitable for crystalline materials cannot be applied to describe the transport mechanism in CPs. Therefore, exploiting other ways to understand how the charge carrier transport occurs in CPs is essential. However, there is no universal theory for CPs due to their complicated microstructures. Notably, the variable range hopping (VRH) model and mobility edge (ME) model proposed by Mott initially in the realm of disordered systems are two well-known theoretical models applied to predict the electrical properties of CPs [13]. The VRH model describes the hopping behaviour of charge carriers in the disordered region, while in the crystalline domains, the transport of charges can be described by the ME model. These two models indeed grasp the essence of some important transport parameters, but the preliminary assumptions cannot cover the complexity of CPs and match the simulation results with the experimental data very well. As a result, in the past decades, many researchers have endeavoured to elaborate on Mott's models and adapt them to different CPs. The recently emerging models are discussed in detail later.

A summary of some basic insight of thermal conduction in CPs is discussed in the end. Dissimilar with traditional semiconductors, electronic charges barely contribute to overall thermal conductivity κ due to the amorphous morphology of CPs. Therefore, the lattice thermal conductivity κ_l is dominant with regard to thermal conduction within CPs. In the assessment of κ, several factors are highlighted, including the chain length, chain structure, crystallinity, and chain orientation. Generally, highly amorphous CPs composed of poorly oriented short backbones with multiple side chains has lower κ.

2.1 Molecular and Nanostructures

The discovery of CPs in 1977 not only awarded the discoverers the 2000 Nobel Prize [66], but also developed a pathway for the development of flexible devices. Since then, new types of CPs have been gradually developed, and summarized in **Figure 2,** which shows several conventional CPs and their molecular formulae.

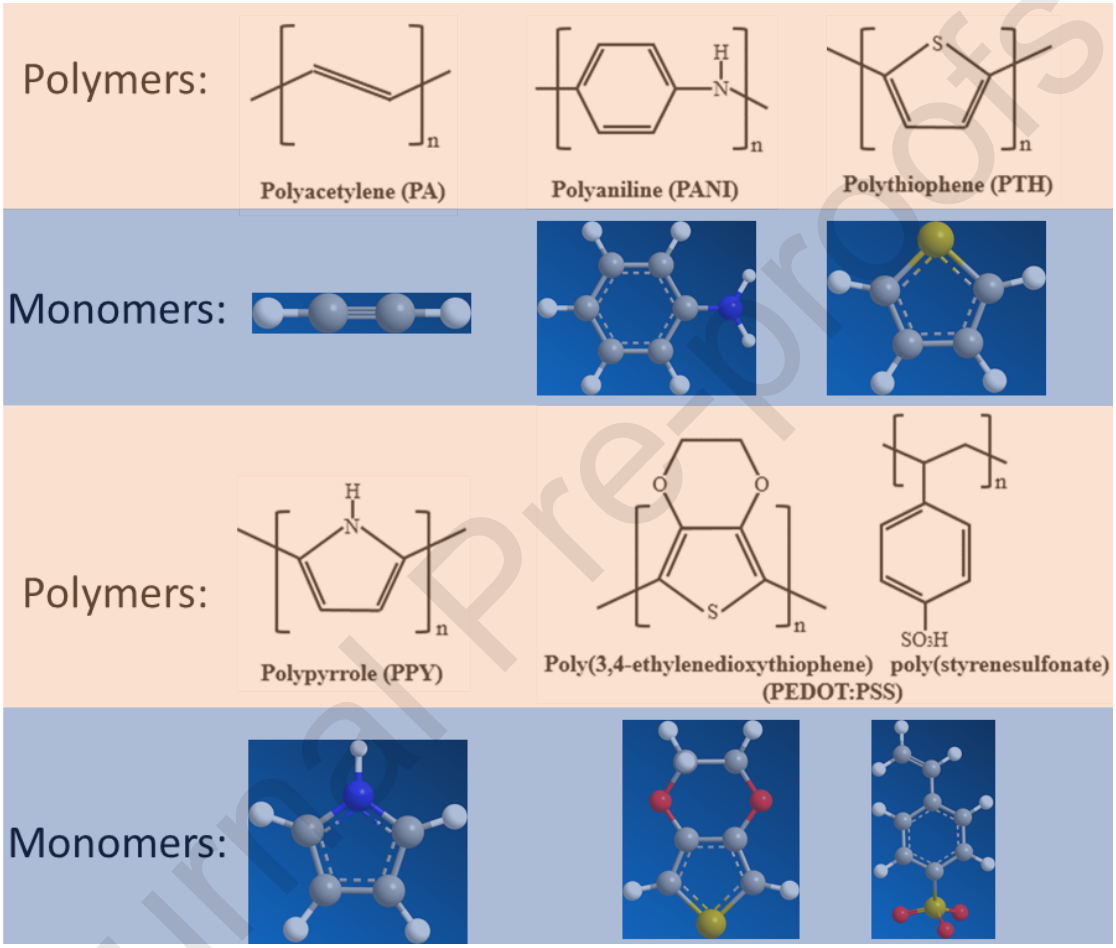

Figure 2. Several common CPs, including Polyacetylene (PA), Polyaniline (PANI), Polythiophene (PTH), Polypyrrole (PPY) and Poly(3,4-ethylenedioxythiophene): Poly(styrenesulfonate) (PEDOT:PSS), and the ball-stick model of their monomers.

2.1.1 Sp^2 Hybridization and Backbones

CPs are conjugated polymers consisted of consistent unsaturated conjugated π-π bonds, enabling electrons in the outer layer of carbon atoms to be easily activated and transported along the backbones

due to the relatively unstable shared electron orbitals [13]. As shown in **Figure 3a**, carbon atoms of conjugated polymers are sp^2 hybridized with three electrons from their outer shells filling out three low energy hybridized orbitals; while the last electron is consequently delocalized in the high energy orbital with electron density dominant in the *z* direction pointing perpendicular to the skeleton. These p_z orbitals of the successive carbon atoms, due to overlapping, form a consistently interactive carbon chain, i.e., backbones as shown in **Figure 3b**. The orbitals interaction between different conjugated monomers leads to the evolution of the divided π orbitals and π* orbitals with a bandgap between them, as illustrated by **Figure 3c** [67]. The π orbitals form valence bands with HOMO as the top border, while π* orbitals emerge from the conduction band, bordered by LUMO. The longer the length of the backbone, the narrower the bandgap that can form between HOMO and LUMO [19]. Notably, unexcited electrons tend to fill the traps within HOMO instead of the delocalized status beyond LUMO where they behave in a similar way to electron behave in metals. Therefore, the conjugated system is necessary but not sufficient for high electrical performance.

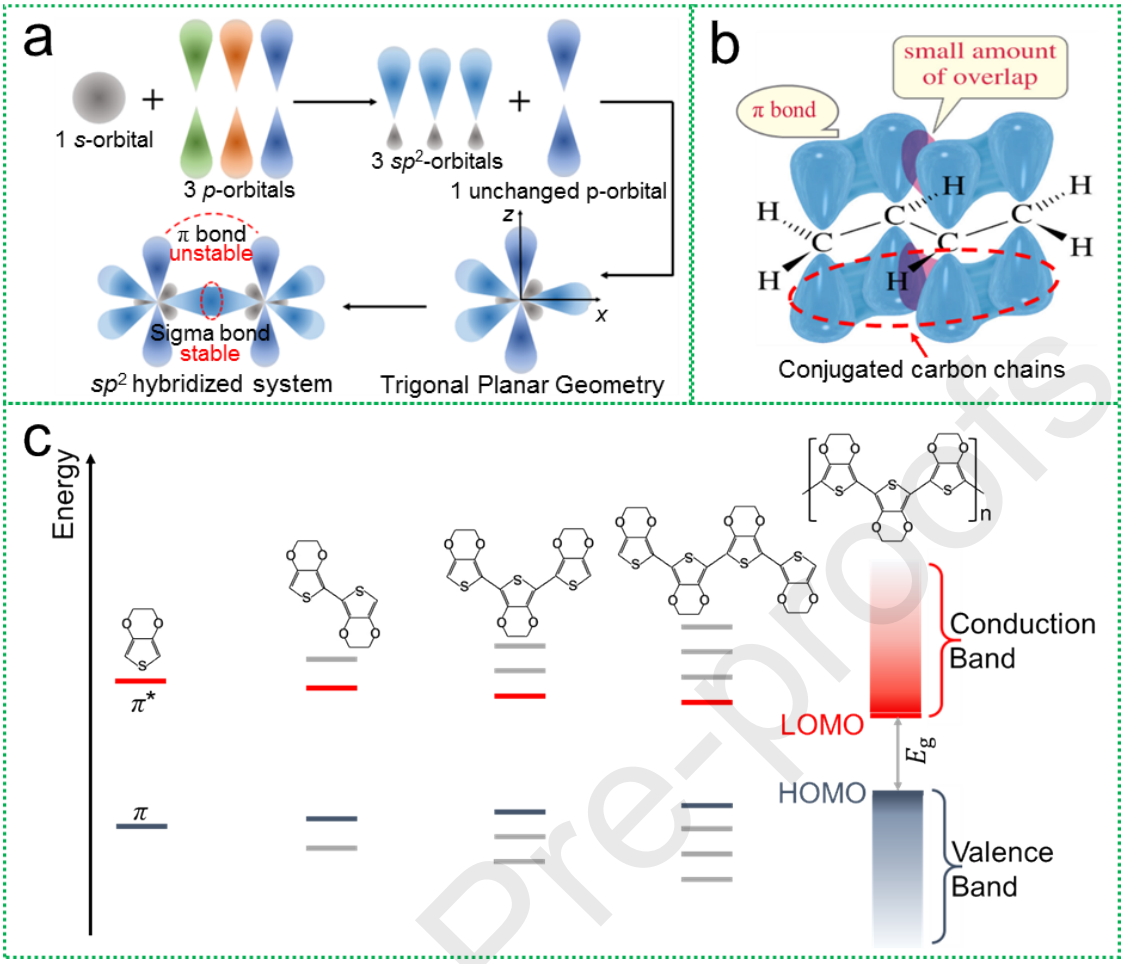

Figure 3. Schematic diagrams of a) sp^2 hybridization, b) backbones in CPs, and c) evolution of band structure with increasing the number of EDOT repeated units.

2.1.2 Benzoid and Quinoid Structures

Benzoid and quinoid structures are two resonant structures based on sp^2 hybridized carbon atoms, and segments of conjugated chains in thiophene-based conjugated polymers. Both generally exist simultaneously. The benzoid structure favours a coiled conformation where the C_α-C_β bond between two thiophene rings is strong and similar to the bond with a low density of π electrons [68]. In contrast, the quinoid structure favours an uncoiled conformation where the bond length alternation of the conjugated chain occurs (single bonds become double bonds and *vice versa*), and the thiophene rings can be nearly oriented in the same plane, leading to stronger electron cloud overlapping between every

two thiophene rings [69]. Obviously, the charge carriers tend to be localized in the benzoid structure, while the uncoiled structure in the quinoid structure facilitates their movements in orientation due to the weak binding between the thiophene rings throughout the entire conjugated chain.

The benzoid/quinoid ratio in a conjugated polymer is tuneable. Two main factors are generally found to impact the quinoid percentage in a conjugated polymer, i.e., doping level and polymerization rate [63]. Specifically, increasing the doping level induces a larger quinoid percentage due to the electronic charge states that transition from neutral to polaron or even bipolaron. Polaron and bipolaron are quasi-particles composed of positive charges, which are associated with the local lattice distortion [70]. Without positive charge, the quasi-particles are called neutral. These three electronic charge states can be found in polymers [71,72]. In undoped conjugated polymers, neutral is the dominant state, but can be transformed into polarons and bipolarons when the polymers are oxidized chemically or electrochemically [73,74]. As the number of counter-ions increases, more neutrals can be transformed into polarons and bipolarons where bond length alternation occurs [65]. In this case, some polymers, e.g. PEDOT, can even present stretched conjugated chains, as schematically shown in **Figure 4a**. Therefore, the quinoid percentage increases. As for the polymerization rate, rapidly polymerized conjugated polymers have a relatively lower percentage of quinoid structure than those synthesized with inhibitors [63]. **Figure 4b** shows that lowering the polymerization rate, leads to the longer backbone and shorter conjugated length of the bipolaron [63]. As a result, more polarons and bipolarons and a higher percentage of quinoid structure can be obtained. Another uncommon factor that was found to be effective in the conformation change from the benzoid structure to the quinoid structure of PEDOT:PSS is ultraviolet (UV) irradiation [68]. Such a change stems from the interaction between the dipole moment within the conjugated PEDOT chains and the electric field of the UV irradiation.

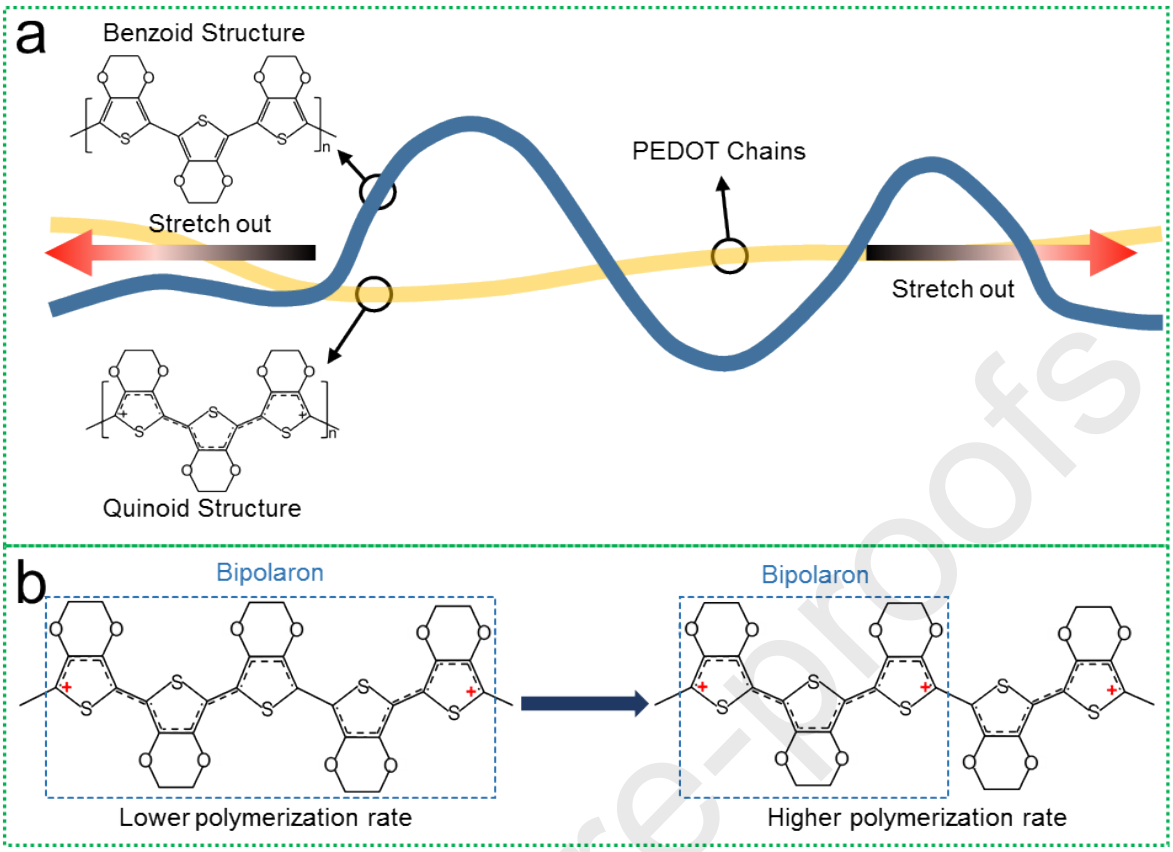

Figure 4. Schematic diagrams of a) stretched PEDOT chains after the benzoid-to-quinoid character transformation and b) longer polymer chains by lowering the polymerization rate.

2.1.3 Crystalline Domains

With increasing the structural order and molecular organization of CPs, such as increasing the chain alignment, S and σ of CPs can be simultaneously enhanced [75], which are mainly derived from the significantly improved μ [76,77], contributing to a high $S^2\sigma$ [78]. In order to compare the ordered and disordered structures in CPs, we first introduce the definition of crystalline domain. Crystalline domains mainly consist of orderly oriented quinoid segments, where charge carriers behave like in metals, showing metallic temperature-dependent σ at ~0 K [65]. Two parameters, namely the crystallinity and the structural coherence length L_{struct} are used to describe the crystalline domains. The former parameter is defined as the volume fraction of the crystalline phase, and the latter one stands for the dimension of the crystalline domain, as illustrated in **Figure 5a** [19,65]. Obviously, the

crystallinity and L_{struct} together determine the effectiveness of electronic charge transport within the crystalline domains of conjugated polymers. With high crystallinity, the conjugated polymers present high electrical performance, while without large L_{struct}, charge carriers suffer exponential decay in the disordered regions which separate the crystalline domains, leading to poor electrical performance.

The crystallinity and L_{struct} are two intrinsic parameters partly determined by the degree of polymerization when CPs are prepared. Generally, a rapid reaction can result in higher concentrations of defects or a lower degree of polymerization, which usually leads to low crystallinity and small L_{struct} for the prepared polymer [63,79]. However, the polymerization rate can also be controlled. By applying inhibitors such as Poly(ethylene glycol)-block-poly(propylene glycol)-blockpoly(ethylene glycol) triblock copolymer (PEPG) in the polymerization process [80], the reaction rate will slow down, inducing large L_{struct} and high crystallinity. Except for inhibitors, the basicity of the dopant also has a considerable influence upon the reaction rate. Generally, dopant with higher basicity would reduce the reaction rate and potentially enable the polymer to possess higher percentage of conjugated structures, while increasing the acidity of the dopant would rather boost the reaction rate and lead to a decreased quinoid/benzoid ratio [63]. **Figure 5b** shows such two opposite effects of dopants with different basicity on the synthesis of PEDOT. Here the dopants OTf, OTs, DBSA, BNSA and CSA refer to triflate, tosylate, dodecylbenzenesulfonate, butylnaphthalenesulfonate and camphorsulfonate respectively. They possess distinctive acidities which are evaluated by the pKa values [63,81]. Taking the PEDOT:OTs and PEDOT:DBSA as instances, the former material possesses higher percentage of conjugated structure than the latter one, since the stabilization effect of positive charges created by the counter-ion is enhanced with increasing basicity of the doping anions (i.e. -2.8 for OTs and -1.8 for DBSA), making it possible to sustain a higher conjugated length in the bipolaron [63]. Notably, although the σ of a polymer is determined by multiple factors, doping with dopant with high basicity would in general yields a higher σ. It was reported that PEDOT:OTf exhibits an ultrahigh σ of nearly

5000 S·cm^{-1} [82], much higher than most other PEDOT family members, including PEDOT:OTs [52] and PEDOT:DBSA [63].

Another significant factor is doping, whose influence upon the crystallinity and L_{struct} varies from different CPs and dopants [37,63,83]. It was reported that the introducing of 2,3,5,6-tetrafluoro-7,7,8,8-tetracyanoquinodimethane (F4TCNQ) into P3HT imposes no impact on the degree of crystallinity and L_{struct} of the matrix, as the dopants reside primarily in the amorphous regions of the film as well as in the P3HT lamellae between the side chains, but do not π-stack within the polymer crystallites. However, in PEDOT:PSS, the long PSS polyanion resides in the matrix and twists with the PEDOT chains, resulting in an amorphous polymer with limited crystallinity and L_{struct} [63]. Small molecule-doped PEDOT (for example, tosylate (OTs) or triflate (OTf)) has higher σ and S because of the closed compact and ordered polycrystalline structure [84].

2.1.4 Disordered Regions

The disordered region is the other component of a conjugated polymer and mainly consists of benzoid structures where charge carriers are localized. Instead of crystalline domains, disordered regions are more like matrices in conjugated polymers due to their soft long conjugated chains which tend to coil and entangle together rather than be orderly arranged in rigid arrays. **Figure 5a** shows schematic nanostructures of the disordered region where the conjugated chains interact with each other in the form of three ways, such as tie chains, entanglements, and disconnected chains [19]. The inter-connected nanostructures (tie chains and entanglements) are responsible for the macro properties such as ductility and flexibility, accounting for the fact that most of the conjugated polymers are flexible. In terms of electronic transportation, given the complex structures in disordered regions, the charge carriers in conjugated polymers transfer through the disordered region between two crystalline domains by both inter-chain hopping/tunnelling between entanglements and intra-chain movement along the same chain [60]. As the intra-chain movement is very different from the inter-chain hopping/tunnelling, these two electronic behaviours will be further discussed separately later.

As revealed in the buckets effect, the strength of a system is determined by its regions of weakness. Similarly, the electrical performance of disordered regions (weakness) usually determines the overall electrical performance of a conjugated polymer film. As a result, improving the effectiveness of electronic charge transport within the disordered regions is of critical significance for high electrical performance. Several post-treatments methods have been proposed to modify the disordered structures in conjugated polymers, including annealing at relatively high temperature (235 ℃) for PBTTT [44], mechanical stretching for P(MeOPV-co-PV) [47], and dedoping treatments for PEDOT:PSS [46,85]. The enhanced μ in the samples after these post-treatments indicates the effectiveness for the modification of the disordered regions in polymers. The typical morphological changes within conjugated polymers after post-treatments are schematically illustrated in **Figure 5c**.

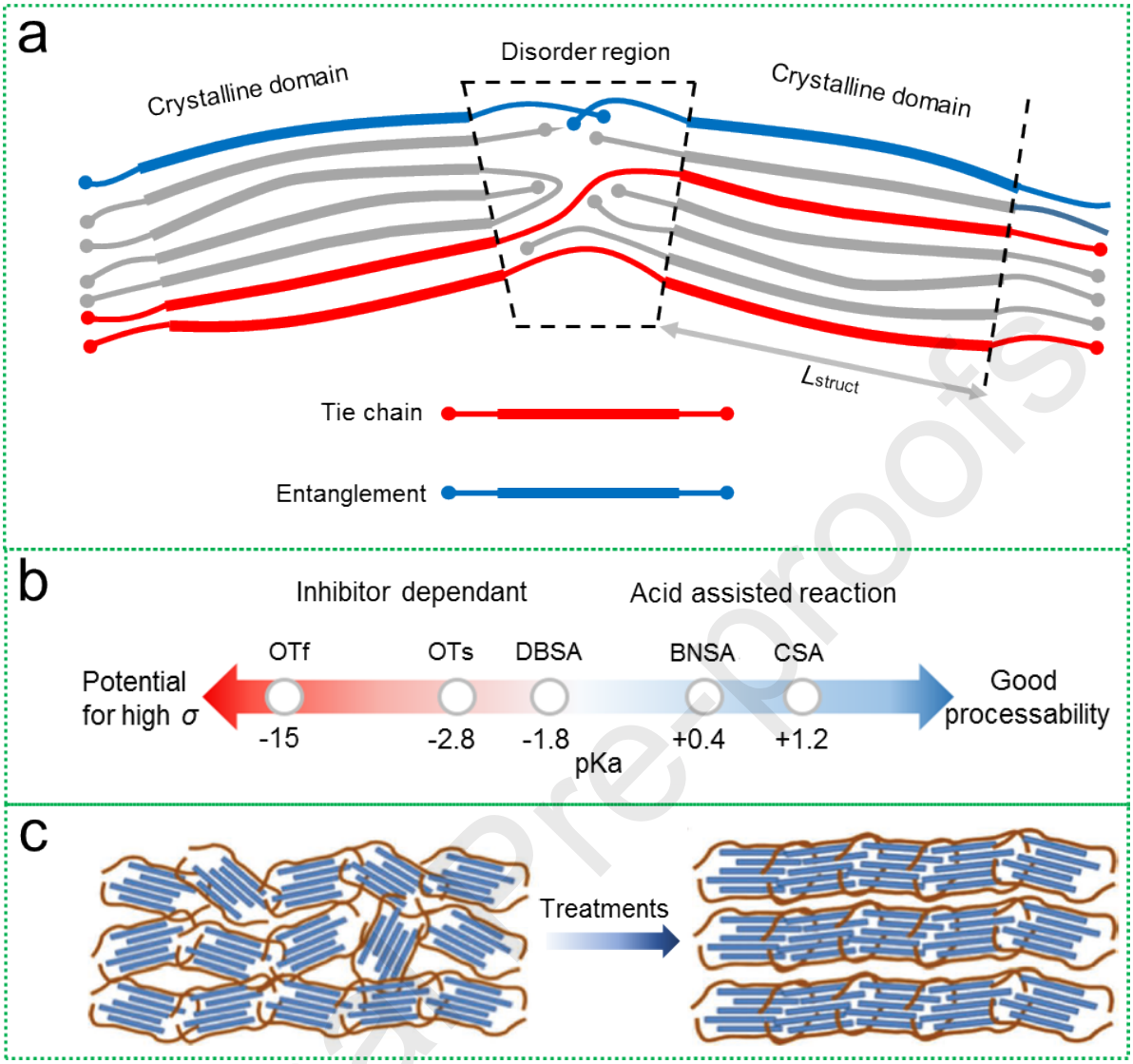

Figure 5. Schematic diagrams of a) nanostructures in conducting polymers; b) schematic diagram showing the two opposite effects of dopants with different basicity on the synthesis of PEDOT. The pKa value can be used to evaluate the acidity (positive value) or basicity (negative value) of a material; Reproduced under a Creative Commons Attribution 4.0 International License [63]; Copyright 2017, Springer Nature. c) morphology change within conjugated polymers after post-treatments. Reproduced with permission [86]; Copyright 2013, Wiley-VCH.

The molecular structures and microstructures play indispensable roles in the electronic charge transport in CPs. These structures are interrelated and eventually determine the electrical performance

of conjugated polymers. The sp^2 hybridization and conjugated backbones build up the cornerstone of electrical conduction, in which the transition from benzoid to quinoid structure further facilitates the charge transport. Such benzoid and quinoid structures form disordered regions and crystalline domains at the sub-micron scale. The ratio and texture (lengths and orientations) of these two microstructures determine the electrical performance of a conjugated polymer. The interdependency of the electrical performance upon these structures will be further discussed in the later part.

2.2 Electronic Charge Transport

For conventional inorganic TE materials [9,87,88], charge carrier concentration (n, where n_e indicates electron carriers and n_p indicates hole carriers) is a key parameter that couples the main thermoelectric parameters by $S = \frac{8\pi^2 k_B^2}{3eh^2} m^* T\left(\frac{\pi}{3n}\right)^{2/3}$ and $\sigma = ne\mu$ [6], where k_B is the Boltzmann constant, e is the electrical charge, h is the Planck constant, and m^* is the carrier effective mass. It can be seen that tuning n can result in optimized $S^2\sigma$. However, these relationships are not suitable for CPs, although there is a similar definition of n. Pristine CPs show poor electrical properties due to their low n and unaligned structures. Generally, n can be modified by effectively doping. Larger numbers of charge carriers can be excited from the base states in HOMO to the energized states in LUMO for charge transport (metallic transport, hopping, and tunnelling). Suitable post-treatments of CPs can facilitate the achievement of high μ in order to induce higher charge transport. However, S is generally reversely proportional to n since S is proportional to the average energy per unit charge, which decreases when the bandgap between LUMO and HOMO becomes narrower due to the increased n. Therefore, tuning n to achieve an optimal compromise between σ and S is essential for high electrical performance of CPs. In order to clarify the meaning of the term "doping" here, we suggest that the process can be best understood as a kind of redox reaction where the original neutral CP loses outer layer electrons to transform into an ionic complex made up of a polymer cation/anion and a counter-ion which is the reduced/oxidized form of the oxidizing/reducing agent.

The conjugated system facilitates the formation of band-like broad regions of electronic states with a relatively broad bandgap (1~4 eV), as illustrated in **Figure 3c**. Similar to the band structures of inorganic crystalline materials, these two band-like regions correspond to the valence band with HOMO (top edge) and conduction band with LUMO [89]. The electronic states in HOMO and LUMO are respectively localized states and delocalized states. Electronic charges occupying delocalized states can be transported like in metals while localized charges are transported either by hopping or tunnelling. The overall effects of these three transport behaviours of electronic charges together define the electrical conduction of a CP. Notably, the effectiveness of metallic conduction is much higher than that of either hopping or tunnelling. This is why most disordered CPs show poor σ. Generally, three factors have been proven to influence the electrical conduction: temperature, morphology, and oxidation level. Charges are more easily delocalized under high temperatures. As for morphology, the energy disorder caused by the structural disorders introduces obstacles in the transport of electronic charges, while highly ordered structures induce relatively uniform potential distribution within the CPs, as shown in **Figures 6a** and **6b**. The oxidation level directly determines the amounts of charge carriers contributing to the electrical conduction of CPs, which, simultaneously, directs the morphology towards that of crystalline materials by the repulsive Coulomb force between counter-ions. A conjugated polymer with highly crystalline structures and high oxidation levels at room temperature has a higher σ than that of some inorganic crystalline semiconductors, e.g., iodine doped polyacetylene (PA) [18,66].

In undoped CPs, electrons are seldom excited above LUMO to transfer like in metals, leading to small n of $<10^{14}$ cm^{-3} for undoped CPs. The electrostatic potential landscape created by the counter-ions (i.e. positive charges) is discontinuous with significant energy barriers that electrons can seldom overcome [90]. The range of the attractive Coulomb potential field, i.e., the localization length l_{Loc}, induced by each counter-ion is 20 nm in radius. These Coulomb potential fields, known as Coulomb traps, suppresses the mobility of electrons. As a result, the transport of charge carriers highly depends

on the assistance of the local lattice, i.e., phonon-assisted hopping between two energy levels in a Gaussian disorder [65]. In this case, the morphology dominates in the determination of electrical conduction. The phonon-assisted hopping of charge carriers on the polymer chains is impacted by two key parameters, namely the residence time τ and the electronic transfer energy [91-93]. The disorder of the molecular structures for CPs decreases the electronic transfer energy to hinder the transport of charge carriers, leading to an increase τ when electrons pass a Coulomb trap [94,95]. If τ is larger than the typical time for a vibrational mode (~10^{-13} s), which usually occurs in highly disordered CPs, the polymer chain has enough time to relax its structure locally by absorbing the kinetic energy of the electron and create new localized electronic states. This is known as the localization of electronic states [90]. which can also be explained by the wave function of the electron as a function of the position. Specifically, two types of wave functions can be summarized with different degrees of localization, as shown in **Figures 6c** and **6d**. The wave function of **Figure 6c** indicates the possibility of distribution of electrons under localized conditions, while the wave function of **Figure 6d** shows a strong localization case. Obviously, for strong localization, the wave function is maximized with a very sharp slope extending to positions far away, indicating that the probability of a charge carrier is near unity. In both localization conditions, the potential barriers between different sites cannot be neglected and these depend on the activation energy that determines if hopping can occur. Usually, charges under strong localization conditions require higher activation energy (e.g., lattice vibration under high temperature) to complete the hopping behaviour. More specifically, for charges with sufficient activation energy to complete the hopping, their hopping destinations are rather determined by two factors, namely the spatial distance and the energy barrier between two sites. If the energy barrier is not able to be neglected, both two factors together determine the site to where the charge jumps and this location is within a variable range rather than in the nearest space, as shown in **Figure 6e**, which is also known as VRH. However, in the case that all electronic states locate in a narrow energy band, the energy barrier between each pair of sites is able to be neglected to make the energy-dependency

less decisive, thus distance-dependency dominates. As a result, electronic charges tend to jump to the sites nearest in space, as shown in **Figure 6f**, and this behaviour is called nearest-neighbouring hopping (NNH). These two hopping behaviours usually occur in disordered domains, resulting in poor charge transfer efficiency.

As the degree of disorder decreases, the crystalline domains gradually play a role in electrical conduction that cannot be neglected. The ordered structures enable the electronic charge to pass a Coulomb trap with small τ. If τ is smaller than the typical time (occurring in highly ordered structures in CPs), a large probability of the charges are delocalized and transport on the conjugated chains like in metals, leading to relatively high μ, as demonstrated in a previous study [96], in which μ as high as ~88.08 $cm^2 \cdot V^{-1} \cdot s^{-1}$ has been observed in single-crystal Poly(3,4-ethylenedioxythiophene) nanowires produced by vapor-phase polymerization. This value is much higher than its pristine counterpart [97,98], owing to the high crystalline structures with a small π-π stacking distance.

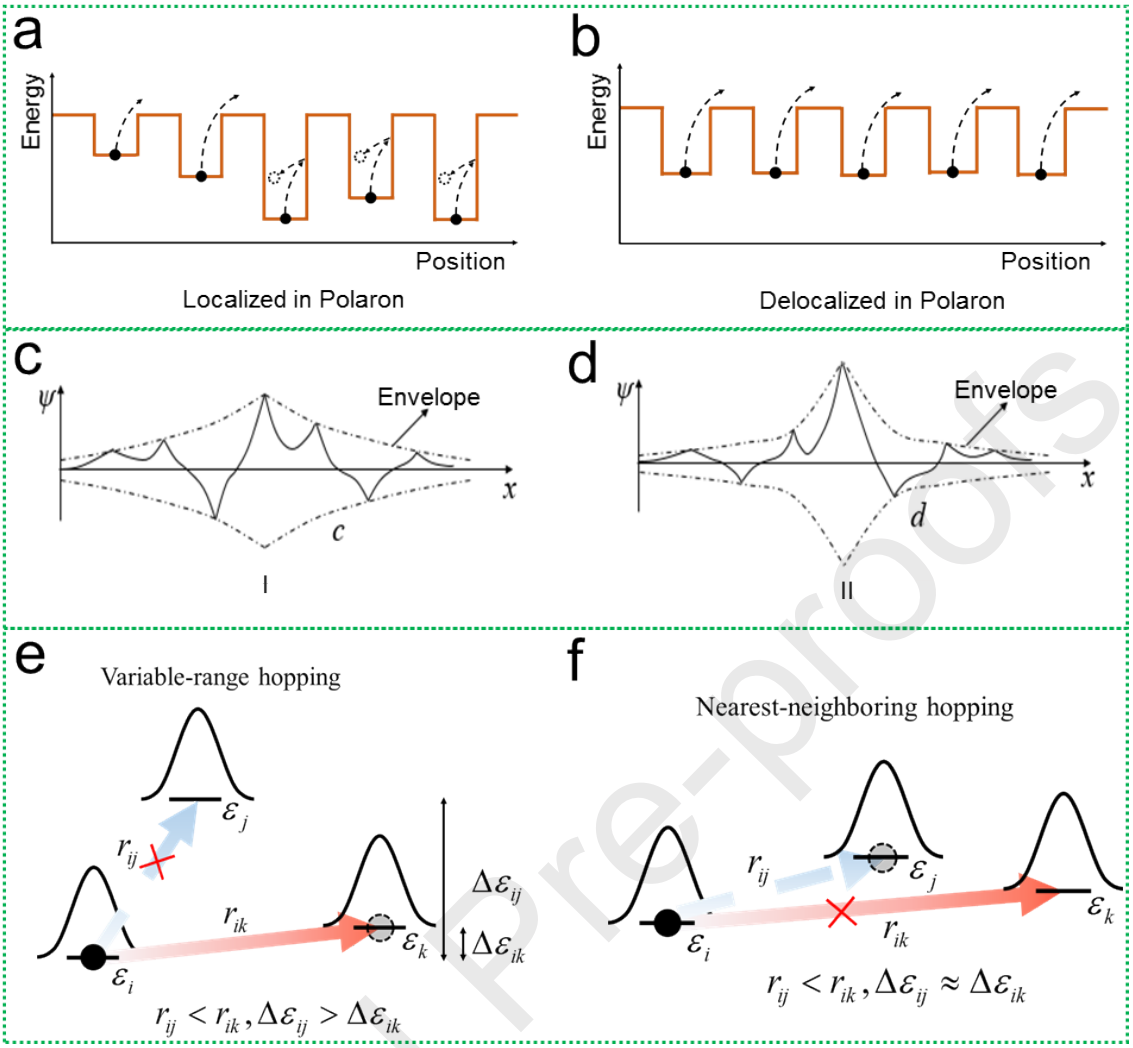

Figure 6. Potential wells landscapes in a) disordered structures and b) ordered structures [99]. Wave functions of c) weak localized state and d) strong localized state [90]. Diagrams of charges in the form of e) variable-range hopping behaviours and f) nearest-neighbouring hopping behaviours [100].

Except for increasing the degree of ordering, increasing the oxidation level is another effective method to enhance σ of conjugated polymers. Plenty of charge carriers are produced due to the redox reaction between matrices and dopants, leading to σ in a broad range from 10^{-9} S·cm^{-1} to 10^{5} S·cm^{-1} [101]. At the atomic level, the introduced dopant molecules capture π electrons to form negative counter-ions, leaving positive polarons (bipolarons) in the conjugated chains. The electrostatic potential needs to be overcome by the dopant molecules, and energy is absorbed by the polaron

(bipolaron), which produces a localized electronic state in the forbidden gap resulting from a local upward shift $\Delta\varepsilon$ of HOMO and downward shift of LUMO [74]. Such new localized energy levels are also known as polaronic (bipolaronic) levels. Electrons occupying the bonding level can be excited up to the antibonding level by consuming less energy, i.e., the ionization energy is lower by an amount $\Delta\varepsilon$. The activation energy can be measured in the ultraviolet-visible-infrared absorption spectrum, as shown in **Figure 7a** [73]. The electronic optical transition at ~600 nm corresponds to neutral (from HOMO to LUMO) due to the large excitation energy required to overcome the bandgap. As the energy gaps between polaronic levels and bipolaronic levels become narrower, polarons and bipolarons require less excitation energy to accomplish the electronic optical transition (from bonding level to antibonding level) by absorbing photons with longer wavelengths of ~900 and ~1000 nm, respectively.

Figure 7b shows the evolution of the band structure of CPs for oxidation levels of higher than 30 %. In this case, the distance between counter-ions can be reduced down to around 1.5 nm [65]. The neighbouring Coulomb traps strongly overlap with each other to facilitate the charge transport within the coupling range. Two types of coupling can be found in CPs, namely inter-chain coupling and intra-chain coupling [65]. The inter-chain coupling is created by the interaction of (bi)polarons in adjacent chains, while the intra-chain coupling occurs in the same carbon chain. The chain or the assembly of chain coupling can produce many continuous (bi)polaronic levels below LUMO and above HOMO, which form the band-like structures. Obviously, the formation of two band-like structures further narrows the energy gap, making it much easier for electronic charges to be delocalized and transport like in metals. **Figure 7b** also plots the evolution of DOS distribution with increasing oxidation level. As the local lattice distortion around two charges is stronger than one charge, the energy shift $\Delta\varepsilon$ (i.e., the reduce of ionization energy) for a bipolaron is larger than that for a polaron. Therefore, the bipolaronic levels are further away from the band edge than the polaronic levels. Moreover, in the case of inter-chain or intra-chain coupling, the coupling effect leads to a Gaussian DOS distribution region consisting of various electronic states with quasi-continuous energy levels. The transport energy level

E_t (corresponds to the mobility edge) assumed to be fixed at the centre of the Gaussian peak is an energy boundary over which the charges are delocalized to transport effectively [100,102].

The increase of the oxidation level has a significant influence on μ of CPs. For undoped CPs, their poor n ($< 10^{14}$ cm^{-3}) induces a discrete distribution of charges and isolated Coulomb traps, as shown in **Figure 7c (I)**. The energy barrier ΔU is large enough to suppress the charge hopping from one trap to another, resulting in poor μ, as shown in **Figure 7d**. When the doping level is at the range from 0.01 % to 1 %, the augmentation of dopants is not sufficient to produce enough charges to achieve the overlapping of their Coulomb traps, and the dopant molecules suppress μ by scattering the charges. In this situation, μ is negatively linked with doping level. When the doping increases to a high level with a high n of ~10^{17} cm^{-3} and the decreased ΔU, the overlapping between Coulomb traps occurs to facilitate the hopping of charges, as shown in **Figure 7c (II)**. When the effect of the overlapping of Coulomb traps begins to overtake the scattering effect of dopant molecules, μ starts to increase. Such a tendency can be maintained until the doping limit. Notably, with a high doping level, the CP with crystalline structures could present an electrical potential landscape as smooth as that in inorganic crystalline materials, as shown in **Figure 7c (III)** and **(IV)**.

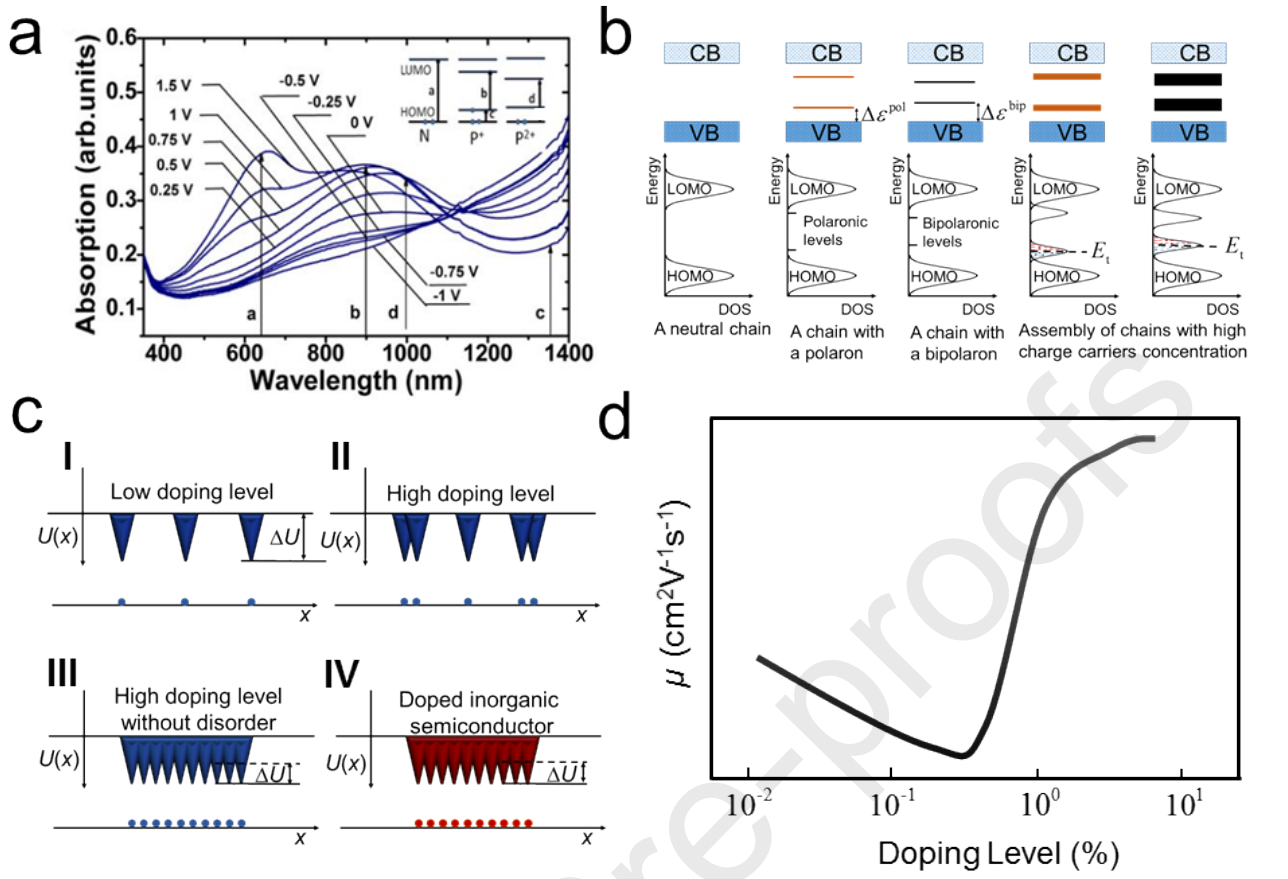

Figure 7. a) Electronic optical transition for neutron, polaron, and bipolaron; a) Reproduced with permission [73]. Copyright 2012, American Chemical Society. b) Schematic diagram of the energy band structures for CPs with different doping levels; c) Schematic diagram of the energy barriers distribution for CPs with different degrees of ordering, $U(x)$ denotes the potential energy; d) Evolution of μ with doping level. Reproduced with permission [65]. Copyright 2012, Royal Society of Chemistry.

2.3 Theoretical Models for S and σ

In CPs, electronic charges with energy higher than a particular value, i.e. mobility edge E_c or transport edge E_t, are delocalized and transport like in metals, whereas charges carrying energy lower than those values transport mainly by hopping between localized states. These distinct behaviours of electronic charges demand different approaches to describe σ and S for CPs when compared to those of crystalline inorganic semiconductors. Particularly, σ in CPs does not follow the Drude model $\sigma = ne\mu$ [103], which is commonly used in crystalline materials; instead, σ of CPs follows either $\sigma =$

$\sigma_0 \exp\left[-\left(\frac{\Delta}{k_B T}\right)^{\gamma}\right]$ (in the non-degenerate limit) [100] or $\sigma = \sigma_0\left(\frac{\Delta}{k_B T}\right)^{s}$ (in the degenerate limit) [60]. Here $\Delta(T)$ is activation energy, the power exponent γ depends on the materials and the transport parameter s equals 3 for most CPs. The Drude model is barely applied in CP system because the existed localized electronic charges transport by hopping rather than free-like transportation. Instead, the electrical properties can be derived from the generalized Boltzmann transport equations and σ can be described as [60]:

$$\sigma = \int \sigma_E \left(-\frac{\partial f}{\partial E}\right) dE \tag{3}$$

where σ_E is transport function and f is the Fermi distribution function. For S, it can be defined as the average energy of charge carriers (relative to the Fermi energy) weighted by their contribution to σ [61]:

$$S = \frac{1}{\sigma}\left(\frac{k}{e}\right)\int \left(\frac{E - E_F}{k_B T}\right)\sigma_E \left(-\frac{\partial f}{\partial E}\right) dE = \left(\frac{k_B}{e}\right)\frac{\langle E - E_F \rangle}{k_B T} \tag{4}$$

where $\langle E\text{-}E_F \rangle$ is the average energy of the electrons relative to the Fermi energy E_F. Similar with the crystalline semiconductors, S of CPs is strongly related with the doping level. In the degenerate limit, E_F shifts into the delocalized states band where plenty of delocalized electronic charges transport with small "excess energy" $\langle E\text{-}E_F \rangle$, hence S is generally poor. Instead, decreasing the doping level by reduction treatment can effectively improve S by even two magnitudes of order [45,52].

In general, the hopping behaviour of electronic charges can be described by either the NNH model [104] or the VRH model [105]. In contrast, the metallic conduction of charges above E_c or E_t is calculated using the mobility edge model or transport edge model.

2.3.1 Nearest-Neighbour Model

Hopping is a continuous behaviour by which electronic charge transfers from site B to site C, leaving site B filled by another charge simultaneously. It can be used under the circumstance that the CPs are heavily doped. It is one of the most fundamental models that explain the carrier transport behaviour of CPs, especially under the thermal excitation. It is simple and easily understand, but the

drawback is that the accuracy needs further improvement. The hopping rate v_{ij} is used to characterize probability of a charge to successfully complete its hopping between two localized states. v_{ij} can be determined by both spatial and energy-dependent factors as below [104]:

$$v_{ij}(r,E_i,E_j) = v_0 \exp\left(-\frac{2r_{ij}}{l_{\mathrm{Loc}}}\right) \times \exp\left(-\frac{E_j - E_i + |E_j - E_i|}{2k_{\mathrm{B}}T}\right) \quad (5)$$

where l_{Loc} is the localization length, r_{ij} denotes the distance between site i and j, E is the energy level of the site, and the pre-exponential factor v_0 is usually assumed to be of the order of the phonon frequency (~10^{13} s^{-1}). When the localized states mainly distribute in a narrow energy band around E_{F} with a width smaller than $k_{\mathrm{B}}T$, the energy-dependent term is neglectable when comparing to the spatial term. As a result, electronic charges tend to hop to the special nearest sites, as shown in **Figure 8a**. Specifically, σ_{NNH} can be expressed as [65]:

$$\sigma_{\mathrm{NNH}} = \sigma_0 \exp\left(-\frac{E_A}{k_{\mathrm{B}}T}\right) \quad (6)$$

where E_{A} is the activation energy, and σ_0 is the pre-exponential coefficient depending on various factors including density of localized sites between which charges hop, characteristic hopping distance, n, hopping rate, and temperature. However, this dependence is often neglectable compared to the much stronger temperature dependence of the exponential term. S_{NNH} is given as [65]:

$$S_{\mathrm{NNH}} = \frac{1E_{\mathrm{A}}}{e\,T} + W \quad (7)$$

where W represents a temperature-dependent kinetic term. **Figure 8a** schematically shows the typical charge transport path described by a nearest neighbour hopping model. **Figure 9a** plots the σ-T^{-1} curve of the spin-coated PEDOT:PSS film, verifying the linear relationship between lnσ and T^{-1} predicted by Equation (6). Such a transport is ascribed to hopping behaviours of charges between more widely spaced molecular sites compared to the in-plane charge transport [106]. Notably, since the contact resistances between the probes and the PEDOT:PSS films during the measurements have not been taken into consideration, further experiments should be required for more accurate conclusion.

2.3.2 Variable-Range Hopping Model

If the localized states distribute in a large energy band, the energy-dependent term is no longer neglectable in the determination of σ. Electronic charges do not necessarily jump to the spatial nearest sites, as shown in **Figure 8b**. Similar to the NNH model, VRH model can be used under the circumstance that the CPs are heavily doped, and it is also a fundamental model that explain the carrier transport behaviour of CPs, especially under the thermal excitation.

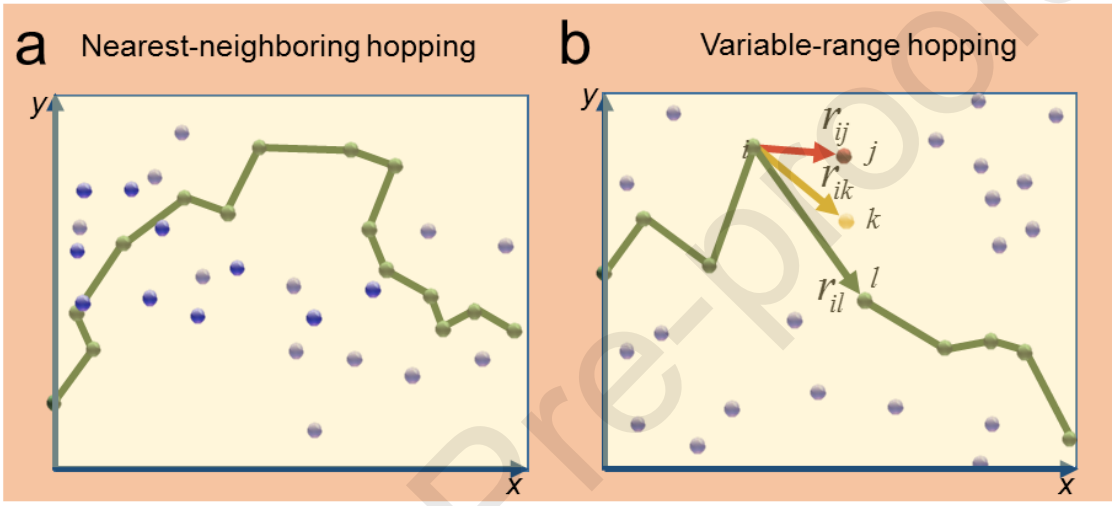

Figure 8. Typical transport paths for a) the nearest neighbouring hopping (NNH) behaviour and b) the variable-range hopping (VRH) behaviour.

The overall effects of both the spatial and energy-dependent terms govern which sites the charges hop to, and the characteristic hopping distance is in a variable range. σ_{VRH} can be expressed as [105]:

$$\sigma_{\mathrm{VRH}} = \sigma_0 \exp\left[-\left(\frac{T_0}{T}\right)^{\gamma}\right] \tag{8}$$

where T_0 is the characteristic temperature, which is a constant for a given sample, γ is a dimensionless parameter that depends on the degree of disorder of the morphology of CPs, usually equals $1/(s+1)$ for s dimension system. Here the pre-exponential coefficient σ_0 is determined by [107]:

$$\sigma_0 = 0.39[N(E_{\mathrm{F}})l_{\mathrm{LOC}}/k_{\mathrm{B}}T]^{1/2}\nu_0 e^2 \tag{9}$$

where v_0 is the hopping attempt frequency and is usually assumed to be the order of optical phonon frequency (10^{13} s^{-1}). Such a description of σ has been demonstrated in the experimental in-plane σ and the results are shown in **Figure 9b**. As can be seen, the ln σ of spin-coated PEDOT:PSS measured in in-plane direction (||) where charge transport follows VRH model is linearly proportional to $T^{-1/4}$. S in VRH regime can be also derived by Mott and track to $T^{1/2}$ as below [105]:

$$S_{\mathrm{VRH}} = \frac{k_{\mathrm{B}}^2 (T_0 T)^{1/2} \partial \ln N(E)}{2e \qquad \partial E}\Big|_{E_F} \tag{10}$$

where N refers to the density of state. This $T^{1/2}$ dependence of S has been proved by many previous experimental studies [106,108,109], and ($\mathrm{d}\ln N/\mathrm{d}E$) at E_{F} was found to be ~2 eV^{-1} [110].

The hopping model gives mathematical descriptions for charge transportation in the disordered CPs, while metallic conduction in crystalline structures requires more suitable models that can accurately quantify the charge behaviour, i.e., mobility edge model [111] and transport edge model [60]. Besides, based on formulars (8)-(10), with increasing the temperature, σ and S tend to show an upward trend. Therefore, by increasing the temperature, the thermoelectric properties (especially $S^2\sigma$) of CPs can be improved within a certain range.

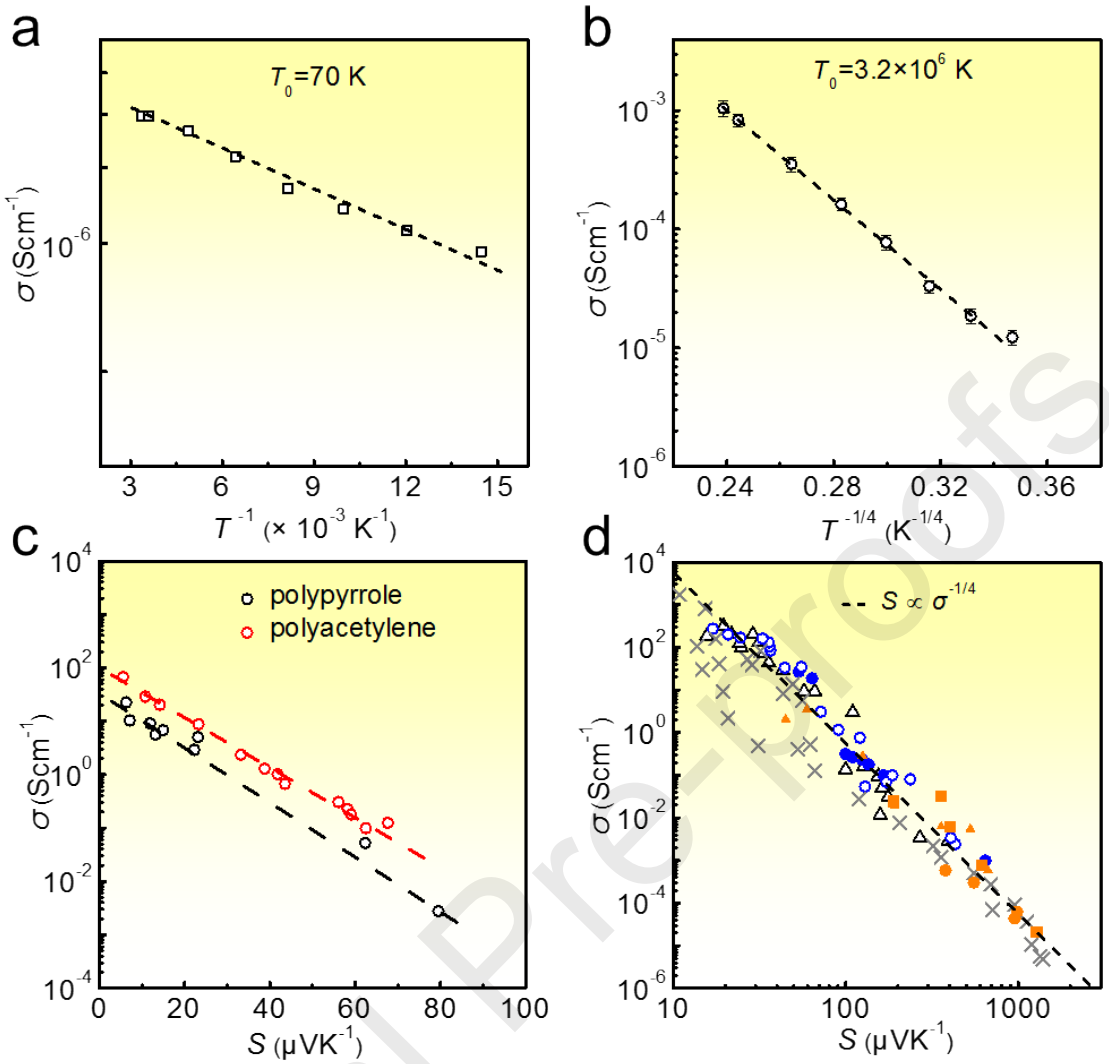

Figure 9. σ versus temperature relations in line with a) nearest neighbouring hopping model and b) variable-range hopping model. The symbols are the measured data [106] while the dashed lines are fits to Equations (4) and (6); c) σ versus S relations in line with the mobility edge model. The symbols are measured data [112] and the dashed line is fit to Equation (11); d) σ versus S relations in line with transport edge model. The dashed lines are fitted to Equation (16). Plotted together are measured data for polyacetylene, PA with various dopants (×) [61], for poly(3-hexylthiophene), P3HT (○) and Poly(2,5-bis(3-tetradecylthiophen-2yl)thieno(3,2-b)thiophene), PBTTT (Δ) [113], for 2,3,5,6-tetrafluoro-7,7,8,8-tetracyanoquinodimethane (F4TCN)-doped P3HT (●), (tridecafluoro-1,1,2,2,-tetrahydrooctyl)-trichlorosilane (FTS)-doped P3HT (●), PBTTT-C14 (▲) and poly(2,5-bis(thiphen-2-yl)-(3,7-diheptadecantyltetrathienoacene)) (P2TDC17-FT4) (■) [108,114].

2.3.3 Mobility Edge Model

For electronic charges excited beyond the mobility edge E_c into the delocalized states, hopping is no longer useful in the quantization of electrical conduction. In the mobility edge model, σ_{ME} can be expressed by Mott [111] as:

$$\sigma_{ME} = \sigma_{min}\exp\left(-\frac{E_C - E_F}{kT}\right) \quad (11)$$

where σ_{min} is σ at the mobility edge in the 0 K limit. A plot of $\ln\sigma_{ME}$ as a function of $1/T$ yields a straight line if the energy gap between E_C and E_F is linearly proportional to T in the measured temperature range [90]. As the electronic charges carry "excess energy" ever the Fermi level, S contributed by charges above the mobility edge is given as [111]:

$$S_{ME} = -\frac{k_B}{e}\left(\frac{E_F - E_V}{k_B T} + A\right) \quad (12)$$

where A is the average energy of the transported charges measured with respect to E_V. The value of A is normally a constant between 2 and 4 [90]. By substituting Equation (11) into Equation (12), S-σ relation can be obtained as [111]:

$$S_{ME} = \frac{k_B}{e}\left[A - \ln\left(\frac{\sigma_{ME}}{\sigma_{min}}\right)\right] \quad (13)$$

The relation between $S_{ME} \propto \ln\sigma_{ME}$ matches well with some CPs [108,115], e.g., polypyrrole and polyacetylene as shown in **Figure 9c** [112], accounting for their much higher σ compared to other CPs whose charge transportations follow the hopping models [60].

2.3.4 Transport Edge Model

The mobility edge model works well with the undegenerated CPs. However, in the degenerate limit, E_F shifts into the delocalized state. In this case, the electrical conduction can no longer be described by the mobility edge model. **Figure 9d** shows some advanced CPs such as PA, P3HT, PBTTT, F4TCN)-doped P3HT, FTS-doped P3HT, PBTTT-C14 and P2TDC17-FT4 have shown high

σ approaching that of metals and well follows $S \propto \sigma^{1/4}$ empirical power law. This phenomenon is explained using the transport edge model which is given below [60]:

$$\sigma_{\mathrm{E}}(E,T) = \sigma_{E_0}(T) \times \left(\frac{E - E_{\mathrm{t}}}{k_{\mathrm{B}}T}\right)^{s} (E > E_{\mathrm{t}}) \tag{14}$$

where $\sigma_{E_0}(T)$ is the temperature-dependent and energy-independent transport coefficient, *s* is transport parameter, and E_{t} denotes the transport edge beyond which charges transport in a similar was to that within metals while below which no charges have any contribution to σ. In the degenerate limit, σ was given as [61,108]:

$$\sigma_{\mathrm{TE}} = \sigma_{E_0}\left(\frac{E_{\mathrm{F}} - E_{\mathrm{t}}}{k_{\mathrm{B}}T}\right)^{s} \tag{15}$$

S can be expressed as:

$$S_{\mathrm{TE}} = \frac{k_{\mathrm{B}}\pi^2}{e\ 3} s\left(\frac{E_{\mathrm{F}} - E_{\mathrm{t}}}{k_{\mathrm{B}}T}\right)^{-1} \tag{16}$$

and the *S*-σ relation derives from Equation (14) and (15):

$$S_{\mathrm{TE}} = \frac{k_{\mathrm{B}}\pi^2}{e\ 3} s\left(\frac{\sigma_{\mathrm{TE}}}{\sigma_{E_0}}\right)^{-1/s} \tag{17}$$

The transport edge model theoretically explains the physical mechanisms behind the empirical relation $S \propto \sigma^{1/4}$. So far, this model is valid for many CPs with high σ.

2.3.5 Heterogeneous Media Model

From the structural point of view, CPs are not entirely disordered or crystalline. Normally, carbon chains of CPs are usually not aligned with each other over their whole length, but only in small crystalline domains whose typical dimensions range from 10 to 50 nm [116]. These crystalline domains are interconnected by disordered regions and connect with each other by several extended polymer chains. Instead of using one model to describe the electrical conduction over the entire sample, Kaiser [61] proposed that a similar heterogeneity plays a significant role in the conduction process for CPs, which is based on the idea that the disordered regions determine the total conduction with poor σ. In

general, the expression for the total σ in the series heterogeneous model with both high and poor σ sections in series was given as [110]:

$$\sigma^{-1} = \sum_i f_i \sigma_i^{-1} \tag{18}$$

where the geometric factors f_i are defined by:

$$f_i = \frac{L_i A}{L A_i} \tag{19}$$

where L and A are the total effective length and cross-sectional area of the sample, L_i and A_i are the length and effective cross-sectional area of the micro-region with intrinsic σ_i. This model was applied to predict σ for PEDOT polymerized with OTf anion (PEDOT:OTf) by combining the quasi-1-D metallic conduction in crystalline domains [117], fluctuation induced tunnelling [118], and the disordered metallic conduction [100] in the disordered regions together [82].

In contrast to the contributions of heterogeneous structures to σ, the overall S is not determined by the electrical resistances, but weighted by the thermal resistance as [61]:

$$S = \sum_i (W_i/W) S_i \tag{20}$$

where W_i is the intrinsic thermal resistances and S_i the intrinsic S of various micro regions. The series heterogeneous model can be used in a system either composed of several CPs whose charges transport mechanisms are distinct or consisted of only one CP with different microstructures.

2.4 Thermal Conductivity

κ is used to evaluate the ability of a material to transfer heat under a temperature gradient. Both carriers and phonons can contribute to κ, namely electronic thermal conductivity κ_e and lattice thermal conductivity κ_l. In crystals, κ_e is usually calculated by the well-known Wiedemann-Franz law:

$$\kappa_e = \left(k_b/e\right) L T \sigma \tag{21}$$

where L is the Lorentz number. So far, the applicability of this law on CPs is still controversial. Zhu et al. claimed this law is invalid in conjugated polymers due to their strong charge-lattice coupling [25], whereas Chen et al. believed that the application of this law is possible by adapting the Lorentz

number to different doping level and σ [119]. Generally speaking, if put aside the Wiedemann-Franz law and only discuss κ of CPs qualitatively, κ_e indeed varies remarkably for CPs with different doping level. For the lightly doped CPs whose σ is smaller than 2.5×10^3 S·cm^{-1}, e.g. doped PANI, only tiny variation of κ can be observed when σ expands several orders of magnitude, indicating a negligible κ_e [120]. For moderately doped CPs, such as PEDOT:PSS whose σ is between 10^2 ~ 10^3 S·cm^{-1}, the contribution of κ_e to κ is still controversial. Kim et al. reported that κ of spin-coated PEDOT:PSS was unrelated with σ [50], while the κ-σ relation was also presented to be linear for the same material in Crispin's work [121]. The intrinsic disagreement between these two opinions is whether the electronic κ_e is overwhelmed by κ_l. Particularly, Crispin's data showed a high κ of 1.8 W·m^{-1}·K^{-1} when σ was ~450 S·cm^{-1} and predicted an even higher κ for PEDOT:PSS films with ultrahigh σ, indicating that this CP might not be as promising as expected. For highly doped CPs, such as I-doped PA whose σ is even over 10^4 S·cm^{-1}, κ might be dominated by κ_e and κ could reach beyond 10 W·m^{-1}·K^{-1} [122,123]. It should be pointed that more experimental data of κ of different CPs with various dopants, doping level, and σ should be provided to make a more comprehensive and reasonable summary of the real contribution of κ_e to κ.

Unlike κ_e, κ_l can be obtained from the Debye equation [124]:

$$\kappa_l = \frac{C_p v l}{3} \tag{22}$$

where C_p is the specific heat, v is the phonon velocity, and l is the phonon mean free path. Compared to most crystalline inorganic semiconductors, l of CPs, is extremely small due to the disordered structures, accounting for the much lower κ_l. For conjugated polymer, κ_l is in the range of 0.1~0.5 W·m^{-1}·K^{-1} [119].

Table 1. κ of several CPs.

CPs	κ ($W \cdot m^{-1} \cdot K^{-1}$)	Ref.
PPy	0.17	[125]
polythiophene (PT)	0.17	[126]
P3HT	0.15~0.2	[127]
PANI	0.09~0.16	[120]
PEDOT	0.19~0.37	[128]
PEDOT:tos	0.37	[52]
Poly[K_x(Ni-ett)]	0.2	[129]
Poly[Cu_x(Cu-ett)]	0.35	[129]
PA	0.69~13	[130]
poly(3-methylthiophene) (P3mT)	0.15~0.17	[126]
PEDOT:PSS	0.17~0.52	[131]

Table 1 summarizes κ of several typical CPs and most of κ is in the range of 0.1~0.5 $W \cdot m^{-1} \cdot K^{-1}$ [120,128-130,132-135]. However, molecular dynamics simulations and experimental studies have shown that a single polymer chain could possess a remarkable ability to transfer heat, i.e., a very high κ even up to 350 $W \cdot m^{-1} \cdot K^{-1}$ when the chain length is longer than 100 nm [136]. Although high κ is not acceptable in TE conversion, we still need to figure out how κ is determined in CPs. As reported by multiple previous studies [124,137-140], κ of polymers follows general trends: 1) Well-aligned crystalline polymers have high κ; 2). Side-chains usually have a negative influence on κ, i.e., κ of polymers depends on three factors, including the chain structure, crystallinity, and the orientation of the polymer chains.

As polymers are composed of many polymer chains, their κ_l depends on the transportation of phonons both on individual polymer chains and between neighbouring connected chains. The chain structure is the first level of structure that determines the thermal conduction in polymers. It usually consists of a rigid backbone and soft side chains (functional groups). As revealed by recent large-scale molecular dynamics simulations [141-143], the rigid backbone consisted of alternating π bonds in a polymer enables a high v, while the conformational disorders stemmed from side chains tend to induce

phonon scattering and thus reduce the phonon mean free path [141,144]. Therefore, polymer chains with multiple functional side chains are weak in thermal conduction.

Another factor impacting κ is the crystallinity of polymers. Efficient phonon transport is challenging in amorphous areas where individual polymers are entangled with themselves or other chains, as the phonon mean free path is greatly shortened by both the strong phonon scattering effect and ineffective phonon transportation, as illustrated in **Figure 10a**. However, in crystallized domains, the stretched conjugated chains depress phonon scattering and support the effective transportation of phonons following the temperature gradient, as shown in **Figure 10b**. Generally, crystallization can decrease the intrinsic disorder, accounting for the phenomenon that κ is higher in the case of crystallized CPs [140]. Besides the overall crystallinity, morphologies of the crystalline polymers also affect κ. A previous study [145] has verified that the polymers with thick lamellar structures present more efficient thermal conduction than the polymers with thin lamellar structures, suggesting that the thick lamellas are responsible for high κ. At the same time, foam-like micro-structures in CPs/carbon nanotube nanocomposites are reported to possess an ultralow κ of only ~0.05 $W \cdot m^{-1} \cdot K^{-1}$, although their σ is low (0.06 $S \cdot cm^{-1}$) due to their foam-like structures [146].

Except for the factors mentioned above, the anisotropy of κ in both in-plane and out-of-plane directions is also a primary consideration. As phonons tend to transfer efficiently along the conjugated backbone through the strong C-C covalent bonding rather than in the transverse direction through the weak van der Waals interaction [147,148], the layer-by-layer stacking polymer chains lead to anisotropic κ, i.e. $\kappa_{\perp}$ and $\kappa_{\parallel}$. Stacking lamellar structures along the perpendicular direction makes the CP film a poor κ in this direction, with a ratio of $\kappa_{\parallel}$ to $\kappa_{\perp}$ ranging from 2~4 times [149-151]. Interestingly, this ratio is not a constant as $\kappa_{\perp}$ is much more stable than $\kappa_{\parallel}$. As a result, the increased crystallinity of the CP film by mechanical stretching or/and other methods can further increase the ratio of >4 [152].

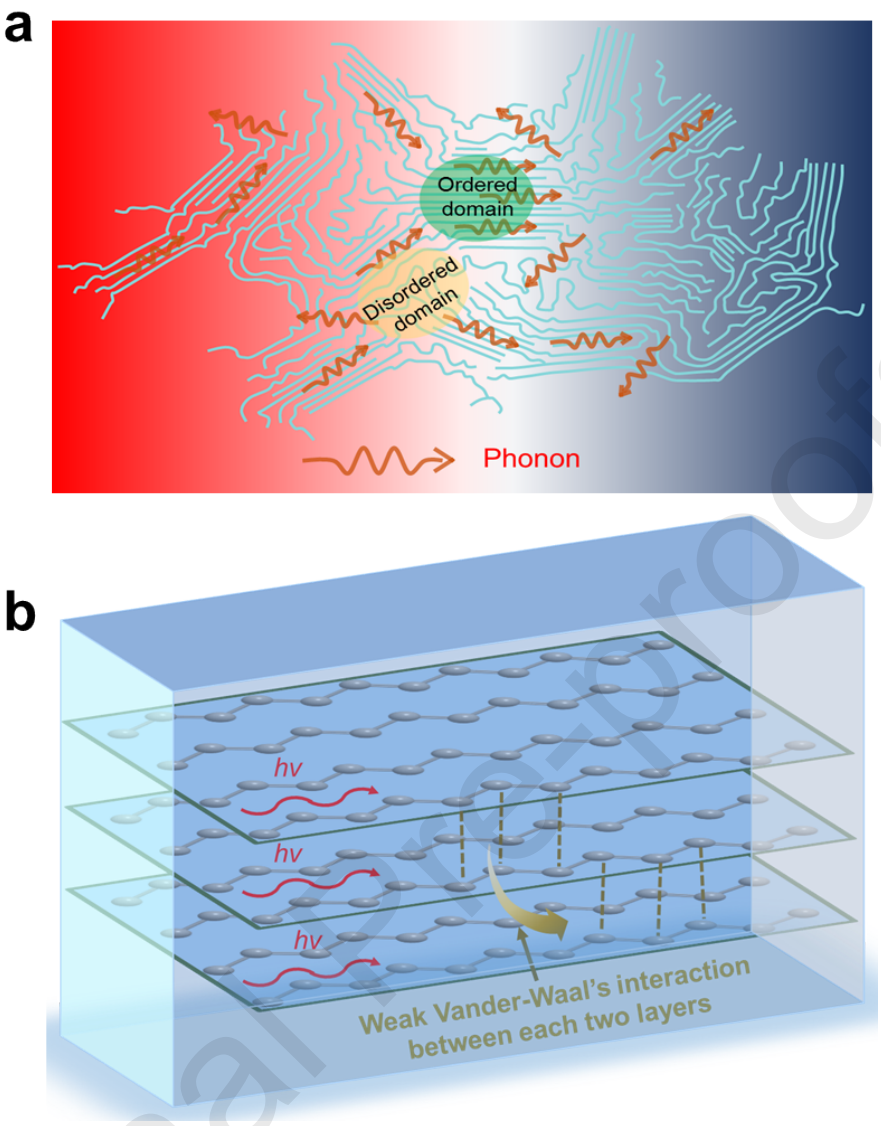

Figure 10. Schematic diagrams of a) in-plane thermal conductivity and of b) anisotropic thermal conductivity within conducting polymers.

To summarize, thermoelectric conversion in CPs is mainly realized by carrying heat during the transport of electrons and phonons. This process involves carrier/phonon scattering and electro-acoustic coupling, which makes the theoretical research and related application exploration of CP-based TE materials face huge challenges. Moreover, compared with inorganic TE materials, there are weak interactions between organic molecules, and the charge transport mechanism is not clear, especially the lack of research on phonon transport and electro-acoustic coupling, which further

increases the difficulty on the understanding of the related mechanisms. Generally, to achieve an "ideal" structure of CPs, comprehensively considering the multiple transport and scattering mechanisms of electrons and phonons, the development of low-dimensional structured CPs and superlattice-like long-range ordered molecular assemblies is an important direction for the structure regulation of organic TE materials. However, the reported conjugated TE molecules are difficult to realize the fine assembly of the above-mentioned structure, which need to be further explored in the near future.

3. Optimization Strategies for Conducting Polymers

TE performance of CPs is measured by its ZT and $S^2\sigma$, both of which are strongly related to the electrical properties (S and σ) of CPs [153]. Generally, the electrical properties depend on both n and μ. Specifically, σ measures the ability of electronic charges to transport in CPs. Therefore, σ is proportional to both n and μ, and S reflects the average energy carried by charges referring to E_F. As a result, shifting E_F away from the delocalized states by decreasing n for a highly doped CP is effective in the enhancement of S. For CPs, n is directly related to oxidation level and μ is mainly determined by the morphological crystallinity. Experimentally, researchers have exploited several strategies to optimize the TE performance by tuning n and μ, including redox-based doping [36,114], secondary doping [50,86], post-treatments [150,154], and polymerization [80,96], as summarized in **Table 2** [36,37,43,47,50-52,114,150,154-205]. As can be seen, the most prominent CPs and their derivatives have achieved dramatically improved ZT of 0.4 ~ 0.8, indicating a further performance enhancement by suitable strategies is highly possible.

Table 2. A summary of the properties for state-of-the-art conducting polymers and their derivatives.

Materials	Strategies	type	σ (S·cm^{-1})	S (μV·K^{-1})	κ (W·m^{-1}·K^{-1})	$S^2\sigma$ (μW·m^{-1}·K^{-2})	ZT_{max}	Ref.
CPs								
PA	Iodine doping	p	11110	28.4	0.7	896	0.38	[114]
PCDTBT	$FeCl_3$ doping	p	160	34		19		[36]
polyselenophene (PSE)		p	0.1~54	20~98	0.02~0.15	13	0.034	[206]
PANI	Doped with various dopants	p	10^{-7}~320	16~225	0.02~0.54		0.011	[120]
PPy	PF_6 doped	p	155	7.14		0.79		[207]
PPy	PF_6 doped	p	0~340	-1~40	0.2		0.03	[208]
PTT	Electrosynthesized	p	1.5	85	0.16	1.08	0.0023	[209]
PTh	Doped with various dopants	p	201	23		10.6		[210]
P3MeT	BF_4	p	73	76	0.15		0.031	[126]
P3HT	small molecule epitaxy	p	320	269	0.15~0.2	62.4	0.1	[211]
PEDOT	BTFMSI doping and hydrazine reduction	p	1134	36	0.19	147	0.22	[37]
PEDOT:PSS	DMSO secondary doping and EG post-treatment	p	886	73	0.34	469	0.42	[50]
PEDOT:PSS	Triple post-treatments with formamide (CH_3NO), concentrated sulphuric acid (H_2SO_4), and	p	1786	28.1	-	141	-	[201]

	sodium borohydride							
PEDOT:PSS	Post-treatments with acid and base	p	2170	39.2	0.2-0.34[a]	334	0.49	[150]
PEDOT:PSS	Screen-printed on paper	p	800	18	-	26	-	[155]
PEDOT:PSS	Treating PEDOT:PSS with ethylene glycol, polyethylene glycol, methanol, and formic acid	p	1900	20.6	-	80.6	0.32	[154]
PEDOT:PSS	Treatment with organic solutions of inorganic salts	p	1473	22.6	0.2	75	0.125	[156]
PEDOT:PSS	Ion accumulation on surface	p	1595	63.3	0.26	640	0.75	[157]
PEDOT:PSS/DMSO/Triton X-100	Self-Healing and Stretchable thermoelectrics	p	137-94	13.4	0.27	2.5-2.1		[212]
PEDOT:S-PHEF	Doping with fluorine-containing polyanion as dopant	p	320	17.8		10.1		[213]
P(MeOPV-co-PV)	Mechanical stretching with 4.4-fold stretching ratio	p	183.5	43.5	-	34.8	-	[47]
PEDOT:Tos	Oxidation level tuning by vapour phase polymerization	p	300	40	0.37	324	0.25	[52]
Co-polymers								
P3BT/PS	Mixing in solution	p	0.002	600	0.25	0.07	-	[158]

PANI/ polyelectrolyte/ phytic acid	Self-healing and stretchable thermoelectrics	p	0.24	7500	0.449	1600	1.04	[214]
P3HT/PEDOT:PSS	Electrochemical polymerization	p	200.5	17	-	5.8	-	[159]
P3MeT/PEDOT:PSS	Electrochemical polymerization	p	137.5	16	-	4.5	-	[159]
PTh/PEDOT:PSS	Electrochemical polymerization	p	125	11.5	-	1.5	-	[159]
PANI/PEDOT:PSS	Layer-by-layer deposition	p	1585	17.5	-	49	-	[159]
PEDOT NWs/PEDOT:Tos	Vapor phase polymerization	p	1270	59.3	0.26	446.6	0.44	[160]
PEDOT:PSS/ water-borne polyurethane (WPU)/ ionic liquids (ILs)	Drop cast and laser patterning	p	140	22		6.77		[215]
Poly(selenophene-co-3, 4-ethylenedioxythiophene)	Electropolymerization	p	0.91	12		0.014		[216]
Organic-inorganic hybrids								
PPy/SWCNTs	Common vacuum filtration	p	400	22	-	20	-	[161]
PANI/graphene	Mixing in solution	p	856	15	-	19	-	[162]
PANI/graphene	*In-situ* polymerization	p	814	26	-	55	-	[163]
PANI/graphene/DWCNTs	Layer-by-layer assembling	p	1900	120	-	2710	-	[164]
PANI/graphene/DWCNTs	Layer-by-layer assembling	p	1080	130	-	1825	-	[165]
PANI/CNTs	*In-situ* polymerization	p	61.47	28.6	0.5	5.04	0.003	[166]
PANI/SWCNTs	Hybridization of PANI and SWCNT to form highly conductive interfaces between two components	p	769	65	0.43	176	0.12	[167]

PANI/SWCNTs	*In-situ* polymerization	p	125	40	1.5	20	0.004	[202]
PANI/SWCNTs	*In-situ* polymerization	p	1440	38.9	0.44	217	-	[168]
PANI/SWCNTs + Te	*In-situ* polymerization	p	345	54	0.3	101	-	[169]
PANI/DWCNTs	Mixing in solution	p	610	61	-	220	-	[170]
PANI/Au-doped CNTs	Directly spun CNT webs	p	1500	150	3.6	2500	0.2	[171]
PANI/$SnSe_{0.8}S_{0.2}$ + CNTs	$SnSe_{0.8}S_{0.2}$ nanosheets are chemically exfoliated from a bulk ingot, and camphorsulfonic acid-doped PANI (CSA-PANI) is coated on the surface of the nanosheets	p	30	316	-	300	-	[203]
PANI/Te	Mixing in solution	p	102	102	0.21	105	-	[172]
PANI/NiO	Sol-gel combination and chemical oxidative polymerization	p	0.139	331		1.25		[217]
PANiPy/SWCNT	nanostructured polyaniline/ carbon nanotube composites	p	425	41		70		[218]
PANI/Bi_2Te_3	*In-situ* polymerization	p	11.6	36	0.1	1.5	-	[173]
P3HT/SWCNTs	Mixing in solution	p	1100	29	-	95	-	[174]
P3HT/SWCNTs	Mixing in solution and bar-coating	p	2760	31.1	-	267	-	[175]
P3HT/Bi_2Te_3	Mixing in solution	p	10	117	0.54~0.86	13.6	-	[176]

PVAc/CNT/PEDOT	Hybridization of three components to form interconnected network between fillers and polymer	p	380	27	0.34	25	0.02	[177]
PEDOT:PSS/graphene	*In-situ* polymerization	p	637	26.8	-	45.7	-	[43]
Sb_2Te_3/PEDOT:PSS-PVP/Sb_2Te_3 (STPPST)	Multi-Step Coating	p	365	124		563		[219]
PEDOT:PSS/graphene	Mixing in solution	p	1160	17	-	32.6	-	[200]
PEDOT:PSS coated Te (PC-Te) nanorod/PEDOT:PSS	Drop cast and H_2SO_4 treatments	p	204.6	83.27		141.9		[220]
PEDOT:PSS/graphene + C_{60}	Mixing in solution	p	720	34	0.25	83.2	-	[178]
PEDOT:PSS/graphene + Te	Mixing in solution	p	35	202	0.21	143	-	[179]
PEDOT:PSS/SWCNTs	Dilution-filtration method	p	900	30	-	85	-	[180]
PEDOT:PSS/SWCNTs	Mixing in solution	p	1000	18~34	-	160	-	[204]
PEDOT/a-SWCNT	Electro-polymerization and mixing in solution	p	3470	32		350		[221]
PEDOT:PSS/DWCNTs	Mixing in solution	p	780	43.7	-	151	-	[181]
PEDOT:PSS/Vertically aligned CNTs forest	Using a razor blade and integration into the composite	p	255	55	-	79	-	[182]
PEDOT:PSS/SnSe	Li-intercalated SnSe nanosheets; physical mixture of PEDOT:PSS and SnSe nanosheets	p	320	110	0.36	387	0.32	[51]
PEDOT:PSS/SnSe	Li-intercalated SnSe	p	320	110	-	390	-	[205]

	nanosheets; physical mixture of PEDOT:PSS and SnSe nanosheets							
PEDOT:PSS/ $Bi_{0.5}Sb_{1.5}Te_3$	Electroless plating and solution mixing	p	2300	37		312		[222]
PEDOT:PSS/ $SnSe_{0.97}Te_{0.03}$	Li-intercalated $SnSe_{0.97}Te_{0.03}$ nanosheets; physical mixture of PEDOT:PSS and SnSe nanosheets	p	18.5	90	-	15	-	[183]
PEDOT:PSS/PEDOT-coated $SnSe_{0.97}Te_{0.03}$	Li-intercalated $SnSe_{0.97}Te_{0.03}$ nanosheets coated with PEDOT; physical mixture of PEDOT:PSS and nanosheets	p	320	80	0.36	200	0.18	[184]
PEDOT:PSS/PEDOT-coated $SnSe_{1-x}Te_x$	Li-intercalated $SnSe_{1-x}Te_x$ nanosheets coated with PEDOT; physical mixture of PEDOT:PSS and nanosheets	p	150	124	-	222	-	[185]
PEDOT:PSS/Si	Spin-coating technique	p	49	73	-	26.2	-	[186]
PEDOT:PSS/Cu_2Se	Wet-chemical process	p	1047	50.8	0.25-0.3	270.3	0.3	[223]
PEDOT:PSS/Te	*In-situ* synthesis to form highly conductive interfacial layer between PEDOT:PSS and Te nanorods	p	19.3	163	0.22	51	0.1	[187]
rGO/PEDOT:PSS/Te NW	Ternary hybrid composite by wet-chemical	p	34.96	202		143		[179]

	and physical mixing methods							
PEDOT:PSS/Te	Simple and efficient vacuum-assisted filtration method	p	700	28	0.15	50	0.1	[188]
SWCNT/PC-Te	vacuum assisted filtration method	p	332	56		104		[220]
PEDOT:PSS/Te	*In-situ* synthesis	p	11	180	0.16	35	-	[189]
PEDOT:PSS/Te	*In-situ* synthesis	p	2	150	-	4.5	-	[190]
PEDOT:PSS/Te	*In-situ* synthesis	p	115	215	-	284	-	[191]
PEDOT:PSS/Te-$Cu_{1.75}Te$	*In-situ* synthesis	p	17.4	220	-	84	-	[192]
PEDOT:PSS/ Sb_2Te_3	Screen-printing	p	341	92.6	0.44	275	0.2	[193]
PEDOT:PSS/ Bi_2Te_3	Screen-printing	n	73	-137.8	0.25	147	0.16	[193]
PEDOT:PSS/MoS_2	Mixing in solution	p	1250	19.5	0.27	45.6	-	[194]
PEDOT/Te	Electrodeposition	p	561.4	65.4		240		[224]
SWCNT	PEI doping	n	3700	-63	-	1500	-	[195]
$(HA)_x(H_2O)_y(DMSO)_z/TiS_2$	Hybrid superlattice of alternating inorganic TiS_2 monolayers and organic cations	n	790	-75.5	0.12	450	0.28	[196]
PVDF/Ta_4SiTe_4	Dimensionality/ morphology matching strategy and a proof-of-principle study	n	95	-250	-	594	-	[197]
PCNTI	Doped by N-DMBI-H Solution	n	0.19	-122.9		250		[225]
PCNDTI	Doped by N-DMBI-H Solution	n	0.28	-72.5		100		[225]

PCNI-BTI	Doped by N-DMBI-H Solution	n	23.3	-83.3		10000		[225]
PCNDTI-BTI	Doped by N-DMBI-H Solution	n	0.56	-94.1		330		[225]
PBTI	Doped by N-DMBI-H Solution	n	0.002	-775.7		110		[225]
P(NDI2OD-T2)	doping with N-DPBI	n	0.002	-3000		184		[226]
PEDOT:PSS	Doping with $CuCl_2$	n	0.053	-18000		1700		[227]
PEDOT:PSS	Rhodamine 101 post-treatment	p	1801	47.2		401.2		[228]
BBL:PEI	PEI doping in BBL	n	8	-65		33.8		[229]
PVDF/Ni NW	Solution mixing casting and compressing molding	n	252.6	-31.01		24.3		[230]
N2200/Co nanowires/SWCNTs	Organic–inorganic nanocomposites	n	1860	-45	1.02	483	0.18	[231]
Polyimide/Bi chalcogenides	Thermal evaporation	n	277	-145	1.315	584	0.13	[21]
Polyimide/Sb Chalcogenides	Thermal evaporation	p	943	169	1.285	2694	0.63	[21]
SnSe/SWCNTs	Solution mixing	p	588	49	14	145	0.003	[54]
Bi_2Te_3/SWCNTs	Solution mixing	p	253.9	48		57.8		[53]
PPBH/SWCNTs/PUBI	Lychee-like polymer core covered by carbon nanotube/polyurethane segregated conducting and flexible networks,	p	110	24	-	6.3	-	[198]

	fabricated using a simple aqueous coating strategy							
PS/SWCNTs	Mixing in solution	p	1250	58	0.3	413	-	[199]

3.1 Doping

Intrinsic CPs are generally non-conductive, and doping can generate carriers to conduct electricity. By doping effective dopants through chemical doping, electrochemical doping, and proton acid doping in CPs, the *n* can be rationally adjusted *via* tuning the doping level (or doping concentration), thereby significantly improving its thermoelectric performance. Generally, both theoretical and experimental results confirmed the influence of the doping level on the σ and S of CPs [20,55], and found that their doping behaviours are very similar to that in inorganic semiconductor materials [6], that is, with increasing the doping concentration, the *n* increased, leading to enhanced electrical transport by $\sigma = ne\mu$ and decreased thermopower by $S = \frac{8\pi^2 k_B^2}{3eh^2} m^* T\left(\frac{\pi}{3n}\right)^{2/3}$. Based on the formula of $ZT = \frac{S^2\sigma T}{\kappa}$, an "effective doping" in CPs should be carefully controlling the doping concentration to rationally tune the *n* value, which can lead to optimized $S^2\sigma$ and ZT. In order to achieve this goal, carefully choosing the dopants, as well as rationally adjust the doping level by controlling the dopant amount and synthesis parameters such as temperature and time, are required. Sometimes multiple dopants are needed to finely tune the *n*, therefore achieving an effective doping is a tricky task, and countless work has focused on this. It should be noted that the improving of doping efficiency should be based on the doping methods and mechanisms of CPs. Compared with inorganic materials, the doping methods and mechanisms of CPs are different, which is mainly determined by the jumping model transport mechanism in the CP system. Generally, doping in CPs mainly involves the processes of charge transfer between molecules/atoms, inducing the generation of carriers, strengthening the charge-to-charge interaction (Coulomb correction), and polaron coupling of transition states, which can lead to changes in the local state of materials and shifts in energy levels, and in turn boost the thermoelectric properties.

Doping can enhance σ of CPs by several order of magnitude. For example, iodine doping can improve σ from 10^{-3} S·cm^{-1} to 10^{4} S·cm^{-1} for polyacetylene (PA), the simplest linear conjugated polymer [101]. Other conjugated polymers like PANI show dramatically enhanced σ by doping with HCl or camphor sulfonic acid (CSA) [232,233]. In the doping process, electrons automatically tend to transfer from donor (matrices) molecules to acceptor (dopants) molecules when there is a positive offset between the electron affinity E_a (defined as the energy released for a neutral atom to form an anion) and the ionization energy E_i (defined as the minimum amount of energy required for a neutral atom to form a cation), creating counter-ions or charge carriers, i.e. polarons or bipolarons in the backbones [234-236]. Notably, the intercalation of dopants inevitably introduces structure disorder in polymer films. However, the degree of structure disorder varies under different doping methods. To summarize, the effects of doping depends on three factors: dopant, doping level, and doping method.

Figure 11a illustrates a typical process of electron transfer from matrix molecules to dopant molecules in P3HT films doped with F4TCNQ [237]. According to the Koopmans theorem [238], the values of E_i and E_a are regarded as the negative of the HOMO energy and the LUMO energy. Electrons in HOMO of P3HT tend to be captured by dopants as forming an anion can release energy more than that absorbed in the ionization process [237]. Notably, for a given matrix, E_i is fixed while different dopants with various E_a can introduce distinct energy offsets between these two values, resulting in totally different capability for matrices or dopants to form cations or counter-ions and distinct σ [239,240]. In general, larger E_a leads to more effective enhancement of σ by doping, and less energy is required for the electrons to transfer from matrices to dopants [237,241,242]. Moreover, a linear relationship between the energy offset and the amount of charge transfer was used to estimate n for the doped CPs [238].

Besides the dopants themselves, the doping level directly determines the amounts of electric charges involved in transportation phenomenon associated with electrical conduction. Another term in chemistry called oxidation level is defined as the number of counter-ions per repeated monomer of

polymer is used to describe σ, because not all the dopants can capture electrons, e.g., commercial PEDOT:PSS solution. Both of them impact the electronic transport process in a similar way, however, the doping level is more intuitive. **Figures 11b and 11c** plot S and σ of poly[N-9'-heptadecanyl-2,7-carbazole-alt-5,5'-(4',7'-di-2-thienyl-2',1',3'-benzothiadiazole)] (PCDTBT) doped by $FeCl_3$ as functions of doping level [36]. Obviously, σ increases with increasing doping level. The same phenomenon was reported in another work about poly(3,4-ethylenedioxythiophene):tosylate (PEDOT:Tos) whose σ increases from 6×10^{-4} S·cm^{-1} at 15 % doping level to 300 S·cm^{-1} at 36 % doping level, as shown in **Figure 11d** [52]. These dramatic enhancements of σ of CPs indicate that doping level can significantly impact the electrical conduction properties.

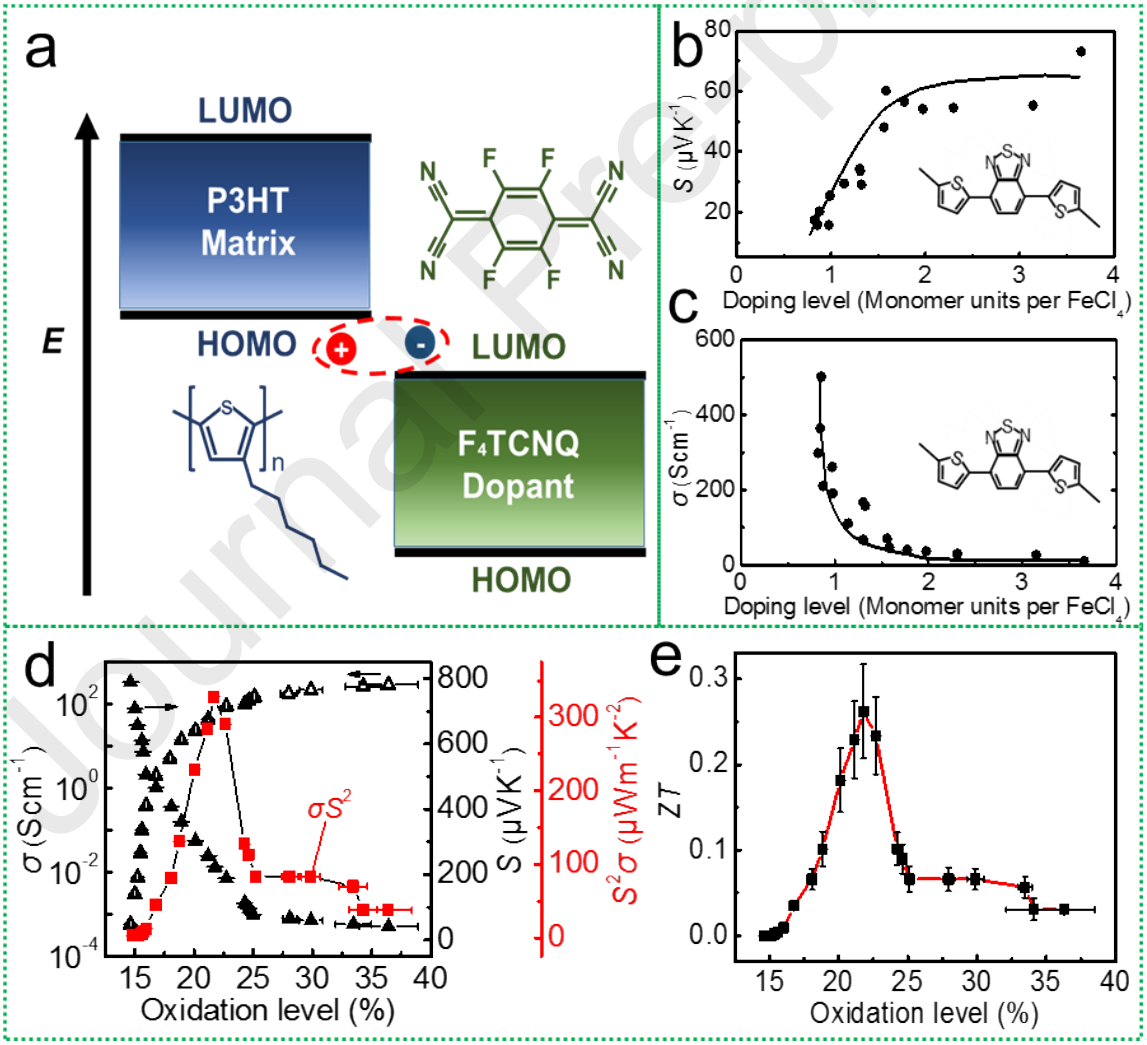

Figure 11. a) Process of electron transfer from matrix molecules to dopant molecules in poly(3-hexylthiophene) (P3HT) films doped with F4TCNQ; a) Reproduced with permission [237]. Copyright 2013, American Physical Society. b) and c) the *S* and σ of poly[N-9'-heptadecanyl-2,7-carbazole-alt-5,5'-(4',7'-di-2-thienyl-2',1',3'-benzothiadiazole)] (PCDTBT) doped by $FeCl_3$; b) and c) Reproduced with permission [36]. Copyright 2009, American Chemical Society. d) and e) the TE properties of poly(3,4-ethylenedioxythiophene):tosylate (PEDOT:Tos) films as a function of oxidation level. d) and e) Reproduced with permission [52]. Copyright 2011, Springer Nature.

Although increasing the doping level leads to higher σ, a high doping level does not always lead to better TE performance of CPs, because *S* usually presents an inversely proportional relationship with the doping level. Therefore, to optimize the TE performance, tuning the doping level is necessary. Quantitatively, the doping level for optimized TE performance is known as the optimal doping level (oxidation level) whose value differs for different CPs, e.g. 14.5 % for PEDOT:PSS [73], 22 % for PEDOT:Tos [52] and 77 % for PCDTBT: $FeCl_3$ [36].

Except for the doping level of dopants, the size of dopants affects σ. ClO_4, PF_6, and bis(trifluoromethylsulfonyl)imide (BTFMSI) were applied in the TE performance enhancement of PEDOT films and this shows a distinct impact upon σ of the films, as shown in **Figure 12a** [37]. In particular, PEDOT film doped by BTFMSI which has the largest size among three dopants shows the highest σ, attributed to the modification of the coil structure of amorphous conjugated polymers. Small anions such as ClO_4 could smoothly neutralize the positive charges of the chain without any significant influence on the backbone of the polymer; while the increase in counter-ion size may produce an extension effect that stretches the compactly coiled polymer chain due to electrostatic repulsion between neighbouring counter-ions. A similar stretching effect caused by the formation of a hydrogen bond between the carbonyl group of CSA and the hydroxyl group of m-resol has also found in PANI doped with m-cresol [167].

The last factor impacting the doping effect is the doping method. Dopant molecules can induce structural disorder in the lamellae composed of backbones, especially at a high doping level. Therefore, using suitable doping methods can reduce such negative effects. A co-deposited doping process in casting solution for blends were developed by simply physically mixing the dopant (F4TCNQ) and the matrix polymer (poly(2,5-bis(3-tetradecylthiophen-2-yl)thieno-[3,2-b]thiophene) (PBTTT-C_{14})) [35], as shown in **Figure 12b** (left side). The favourable energy offset between E_a and E_i facilitates the electrons transfer from PBTTT-C_{14} to F4TCNQ in solutions and films. This doping process completed prior to the casting of uniform films, resulting in the highest σ up to 2 S·cm^{-1} when the molar ratio of dopant to the matrix was 0.25. This σ of doped PBTTT film was improved from 4×10^{-5} S·cm^{-1} of pristine PBTTT film, more than four orders of magnitude. Such dramatic enhancement was attributed to increased *n* stemming from doping. The same materials were also studied in work reported by Henning Sirringhaus et al [38]. However, they believed that the diffusion of a small molecule of dopant into the π-stacked conjugated chains should be responsible for the σ of 2 S·cm^{-1}, though considerable but not high. Hence, they designed an experiment where F4TCNQ was not intercalated into the PBTTT until the matrix conjugated polymer was pre-deposited on the substrate by spin-coating, as shown in **Figure 12b** (right side). This unique solid diffusion doping process resulted in a much larger σ of 248 S·cm^{-1} for the PBTTT:F4TCNQ film with doping level about 20 % ~ 30 % compared to that obtained by the co-deposited doping process. The reason accounting for this difference was that instead of intercalating inside the π-stacked conjugated chains, the dopant molecules were incorporated into the layer of side chains of the matrix, leading to a highly ordered lamellar microstructure.

3.2 Secondary Doping

Phenomenologically, a secondary dopant is an "inert" substance which can further change the physical properties of a primarily doped material, including σ. Although there is no redox reaction between these organic compounds and polymers, such a strategy has been referred to as secondary doping. Secondary dopants such as methyl sulfoxide (DMSO) [86], N, N-dimethylformamide (DMF)

[243], and EG [50] are used to add the PEDOT:PSS aqueous solution to improve σ with ~100 fold increase [243-246]. Sometimes a combination of secondary doping treatment and doping engineering is used to simultaneously increase S and σ, which can be described as a sequential treatment [26].

Table 3 summarizes σ of PEDOT:PSS films treated by several common secondary dopants, such as Ethylene glycol, DMSO, NMP, N,N-dimethylacetomide, and 4-Methoxyphenol. As can be seen, compared to the pristine PEDOT:PSS film (σ of 0.2 $S \cdot cm^{-1}$), the treated films show dramatically enhanced σ, especially for the EG and DMSO treated PEDOT:PSS films. The mechanisms of such enhancements through secondary doping remains unclear. One of the most well-known explanations is that the secondary dopants induce screening effects between the positively charged polymer chains and negatively charged primary dopants to reduce the Coulomb interaction between them, leading to a dramatic enhancement in σ [244]. Therefore, such an enhancement ratio has been related to the dielectric constants of the secondary dopants [244]. It should also be noted that the physical states of the dopants are critical to the enhancement in σ, as the observed σ enhancement only happened after the films were baked at a temperature higher than the melting point of the secondary dopant [247]. Crispin et al. [243] also reported that the secondary dopant EG can reduce the insulated PSS layers surrounding the conductive PEDOT:PSS particles, leading to enhanced σ. The incorporation of secondary dopant EG into the PEDOT:PSS aqueous solution can cause conformational changes and improve the crystallinity of the PEDOT nanocrystals in the solid films, with an increased μ from 0.045 to 1.7 $cm^2 \cdot V^{-1} \cdot s^{-1}$ [86]. Such improved crystallinity can be verified in the 2D grazing-incidence wide-angle X-ray diffraction (GIWAXD) patterns of **Figure 12c** (without EG) and **12d** (with 3 % EG). The comparison between these two patterns indicates the existence of ameliorated morphology with larger average crystal size by adding EG to the solution. Moreover, **Figures 12e** and **12f** plot σ as a function of the volume ratios of DMSO and EG for PEDOT:PSS [39,40]. As can be seen, σ rapidly increases from nearly 0 to over 600 (500) $S \cdot cm^{-1}$ when the volume ratio of DMSO (EG) reaches 5 %, and then decreases

as the volume ratio goes beyond 10 %, meaning that the best volume ratio of this secondary dopant should be within 5 % to 10 %.

Table 3. Electrical conductivity (σ) of PEDOT:PSS films treated by several common secondary dopants with distinct dielectric constant (ε) [69].

Secondary dopants	ε	σ (S·cm^{-1})
Ethylene glycol	37	200
DMSO	49	143
NMP		46
N,N-dimethylacetomide		37
4-Methoxyphenol	11	20
Non		0.2

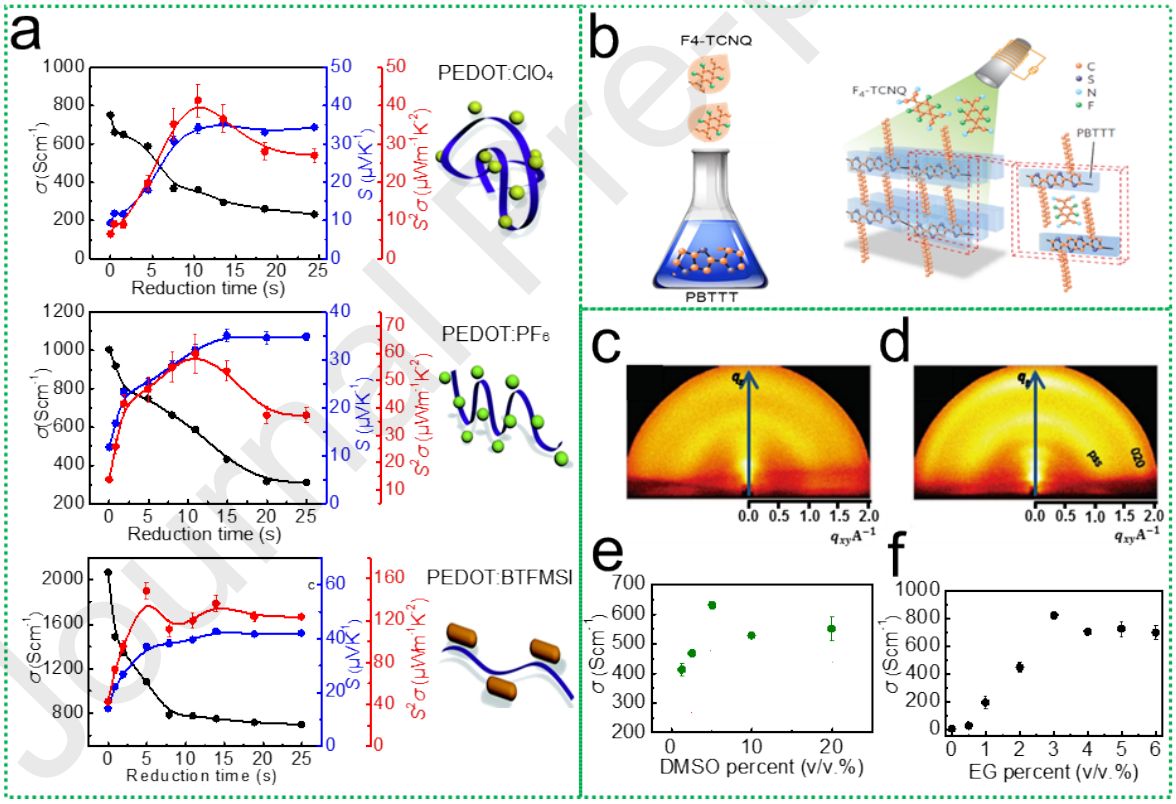

Figure 12. a) TE performances of PEDOT films with ClO_4, PF_6, and bis(trifluoromethylsulfonyl)imide (BTFMSI) as dopants; a) Reproduced with permission [37]. Copyright 2014, Royal Society of Chemistry. b) Two doping methods for CPs. The left side is the co-deposited doping method while the right side is the pre-deposited doping method; b) Reproduced with permission [38]. Copyright 2016,

Springer Nature. The 2D GIWAXD patterns of PEDOT:PSS films: c) without EG, and d) with 3 % EG; c) and d) Reproduced with permission [86]. Copyright 2013, Wiley-VCH; e) The σ of PEDOT:PSS films versus concentration of DMSO relation; e) Reproduced with permission [40]. Copyright 2018, Research India Publications; f) The σ of PEDOT:PSS films versus concentration of EG relation. f) Reproduced under a Creative Commons Attribution (CC BY) license [39]. Copyright 2015, American Institute of Physics.

3.3 Post-Treatments

Increasing σ by ameliorating the morphology or improving S by tuning the over high n has been proven to be an effective method to further enhance TE performance for the CPs films. Specifically, the strategy applied to the CPs films to improve their TE performance is known as post-treatment, including mechanical stretching, annealing treatment, and chemical treatment. Generally, rational post-treatments could enhance the structural ordering in the polymer microstructures, and remove excess insulating phases through phase segregation, and in turn increase σ. These are two fundamental functions of post-treatments. Taking chemical treatment for an example, it involves immersing fabricated CP films into solutions such as EG [50], DMSO [248], methanol [154], DMF [156], formic acid [154], or sulfuric acid [46], and then rinsing. It was reported that for PEDOT:PSS, post-treatments by CH_3NO and H_2SO_4 solutions could selectively remove excess insulating PSS within the films, leading to higher μ and σ; while subsequent $NaBH_4$ treatment optimized the σ and S by modulating the oxidation level, contributing to high $S^2\sigma$ [201]. Other works also indicated that by rational acid-solution treatment, stronger ion interactions between dopants and polymers in acid solutions could be achieved, including dipole–dipole or dipole–charge interactions [156]. These ion interactions lead to higher σ. In this regard, rational post-treatments are of significance to optimize the thermoelectric performance of CPs.

3.3.1 Mechanical Post-treatments

Mechanical stretching is usually used to achieve a high degree of structural order in the crystalline domains in CPs. σ of the Poly(2,5-dimethoxyphenylenevinylene) (PMeOPV) film can be increased by two orders of magnitudes from 2 to 183 $S \cdot cm^{-1}$ without a scarification of S by using mechanical stretching [47]. A similar study shows that PEDOT:PSS has an ultrahigh σ value of 4100 $S \cdot cm^{-1}$ after being stretched under 100 % tensile strain [249]. However, such a high mechanical stretching has a negative impact upon the electrical conduction, resulting in cracks, and in turn damages the highly interconnected conducting network [249]. Other studies have reported that polypyrrole (PPy) doped with hexafluorophosphate shows a high σ value of 1,500 $S \cdot cm^{-1}$ improved from 500 $S \cdot cm^{-1}$ as its polymer chains have been uniaxially oriented after mechanical stretching [250]. Interestingly, no crystalline structure was found when PPy was doped by other dopants, indicating that counterions considerably influence the structural arrangement [251].

3.3.2 Annealing Post-treatments

Annealing post-treatment is an effective method to improve σ of CPs by increasing μ. As most of CPs cannot endure very high temperatures, the annealing treatment is usually carried out below 300 ℃. The annealing treatment can form well-aligned microstructures and highly crystallized domains of the treated polymer films. PBTTT films presented highly ordered microstructures after annealing treatments under different temperatures [44]. Obviously, higher annealing temperature result in highly ordered microstructures, leading to high μ of 10 $cm^2 \cdot V^{-1} \cdot s^{-1}$. A similar phenomenon was also observed in the annealed P3HT/PCBM films [252-254], which shows improved crystallinity and increased μ by even more than three orders of magnitude. Recently, a radical case was reported where the 5,6-dihydroxyindole (DHI) eumelanin films presented a remarkable increase of σ, up to 9 orders of magnitude, from 10^{-7} to 318 $S \cdot cm^{-1}$ after a simply vacuum annealing treatment [255]. Such an obvious improvement in σ was attributed to the structural reorganization within the films [255].

3.3.3 Chemical Post-treatments

Compared with the mechanical stretching and annealing post-treatment, chemical post-treatment is a more common strategy to enhance the TE performance of CPs [256,257]. As one of the most favourable CPs, PEDOT:PSS are processable with high TE performance [258]. However, the overly doped insulating PSS has a negative effect upon the electrical conduction of PEDOT:PSS. Therefore, in order to further improve the TE performance of PEDOT:PSS films, it is necessary to selectively remove these extra insulated PSS. Dipping the deposited PEDOT:PSS films inside some hydrophilic organic solvents was the technique that was used to selectively remove the extra hydrophilic PSS, whereas PEDOT is hydrophobic. **Figures 13a-d** plots the TE properties of PEDOT:PSS films for different EG post-treatments, in which the PEDOT:PSS films secondarily doped with dimethylsulphoxide (DMSO) were simply immersed in EG for a sufficient time period [50]. A record-high peak *ZT* of 0.42 was observed, which was attributed to the simultaneously improved *S* and σ, as shown in **Figures 13a-b**. The selective removal of PSS during the EG treatment can result in enhanced μ, and in turn this leads to a decrease in tunnelling distance, overwhelming the reduction in *n*. Except for EG, treatments with methanol [259,260], DMSO [85], ethanolamine (MEA) [154,261], etc. were also reported to be effective in TE enhancement of PEDOT:PSS films.

In addition to hydrophilic organic solvents, treatments with protonic acids, including sulphuric acid [262], hydroiodic acid [263], phosphoric acid [264], etc., can also effectively improve TE properties of PEDOT:PSS films. Unlike the organic solvents, the mechanism of using protonic acid to selectively remove the extra PSS can be explained by the transfer of protons (i.e. the H^+) from strong acid to strong based cation (i.e. PSS^-), forming the water-soluble weak acid PSSH [265]. For example, H_2SO_4 treatment induces the formation of a dense and interconnected crystalline nanofibril structure (**Figure 13e),** leading to enhanced σ of the PEDOT:PSS film up to 4380 $S \cdot cm^{-1}$ (**Figure 13f)** [46]. Such ultrahigh σ stems from enhanced μ, due to the high crystallization of the PEDOT:PSS films after the H_2SO_4 treatment.

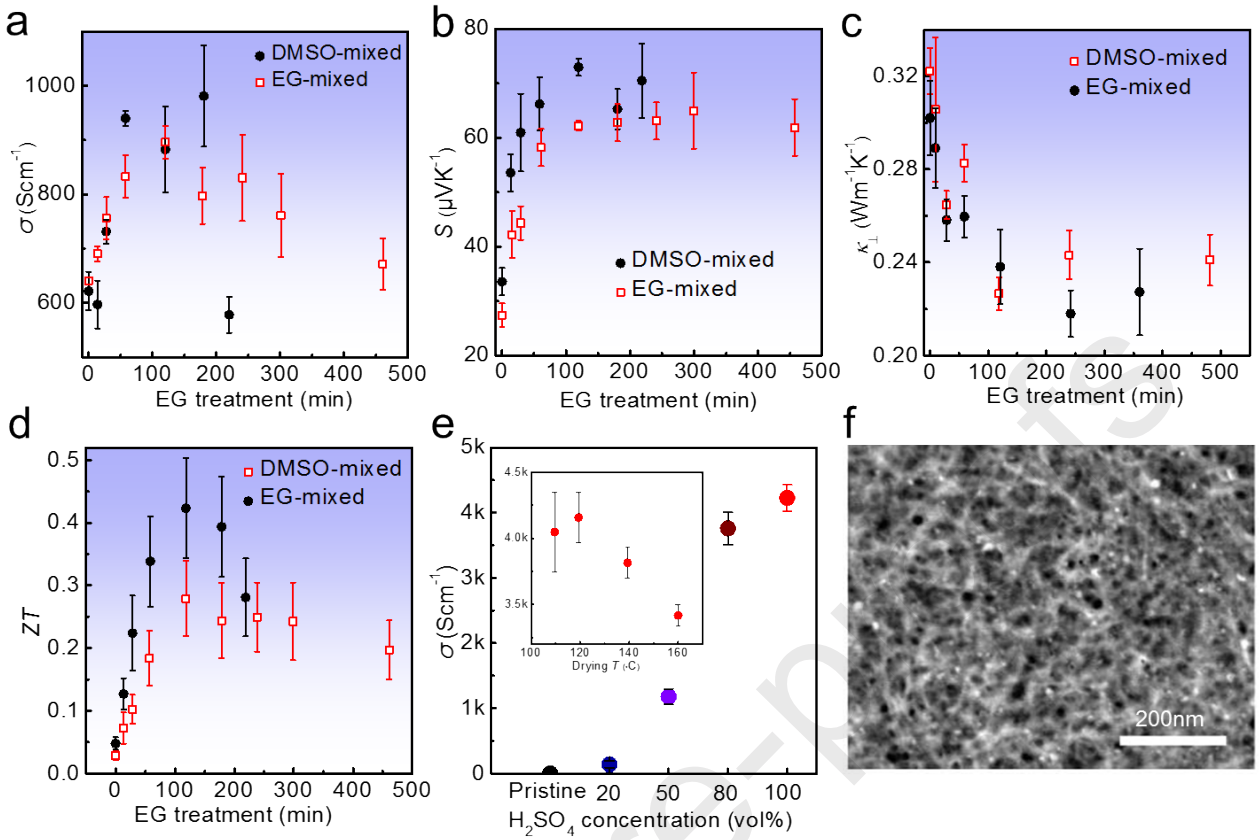

Figure 13. a-d) TE properties of PEDOT:PSS films after EG post-treatment; a)-d) Reproduced with permission [50]. Copyright 2013, Springer Nature; e) σ of PEDOT:PSS films as a function of the concentration of H_2SO_4 solvent; f) HAADF-STEM images of PEDOT:PSS films treated with concentrated H_2SO_4. e) and f) Reproduced with permission [46]. Copyright 2013, Wiley-VCH.

Both the hydrophilic organic solvent treatments and the protonic acid treatments are effective methods for σ enhancement of CPs by selectively removing the excess non-ionized PSS. However, most of S remains unchanged after these treatments, indicating that further enhancement in TE performance exits in increasing S. A few reduction treatments by using hydrazine (N_2H_4), sodium borohydride ($NaBH_4$), sodium thiosulfate ($Na_2S_2O_3$), and tetrakis(dimethylamino)ethylene (TDAE) have been applied to tune n to optimize S of PEDOT:PSS films, and significantly increase S from 18 $\mu V \cdot K^{-1}$ for pristine PEDOT:PSS films to 161 $\mu V \cdot K^{-1}$ for TDAE treated PEDOT:PSS films are observed,

as illustrated in **Table 4**. Such huge enhancement in *S* is ascribed to the transitions of the charge states in the polymer films from di-cations to radical cations or neutral chains.

Table 4. Seebeck coefficient, *S* of PEDOT:PSS films post-treated by various reducing agents with different redox potentials [45].

Reducing agents	Redox potentials (V/SHE)	S ($\mu V \cdot K^{-1}$)
None	N/A	18
$Na_2S_2O_3$	-0.57	37
TDAE	-0.71	161
Na_2SO_3	-0.93	39
Hydrazine	-1.16	153
$NaBH_4$	-1.24	53

Apart from the solo used one single method upon pristine CPs films, the combined reduction treatments, such as acid/hydrophilic organic solvent treatments, are developed to optimize TE performance of CPs. For example, Ouyang et al. reported a method with sequential acid and base treatments to achieve an ultrahigh $S^2\sigma$ of 334 $\mu W \cdot m^{-1} \cdot K^{-2}$ for PEDOT:PSS film [150], in which σ can be dramatically enhanced by more than 100 times with unchanged *S*. It can be concluded that higher σ after the acid (hydrophilic solvents) treatment would potentially lead to a larger $S^2\sigma$ after the reduction treatment [201]. Similar results have also been observed in other studies [266-269]. Besides, combining the advantages of doping, secondary doping, and post-treatments should be effective to comprehensively improve the thermoelectric performance of CPs, but the interactions between different strategies should be carefully concerned.

3.4 Polymerization

Polymerization is a process for reacting monomer molecules together in a chemical reaction to form polymer chains or three-dimensional networks [270]. Compared to the post-treatment method, the polymerization method can effectively tune both the microscopic morphologies and oxidation level of CPs. Specifically, lengths and alignment of the polymerized backbones can be tuned by using suitable surfactants and controlling the reaction rate. The oxidation level can be modulated by applying

reduction treatments to the deposited films or tuning the gate voltage during the polymerization process. Typically, classified by the presence or absence of external gate voltage to facilitate the polymerization process, there are two types of polymerization methods for CPs, namely electrochemical polymerization [271] and oxidative chemical polymerization [52]. However, the electrochemical polymerization method is not suitable for application in the fabrication of patterned CP films as the electrolytes usually cover the entire substrate during the process. Instead, the oxidative chemical polymerization method should be a better alternative. Although the oxidative chemical polymerization method is not as good as the electrochemical polymerization method in tuning the oxidation level, the oxidative chemical polymerization method performs better in fabricating CP films with various patterns, including nanowires or even other specialized patterns.

3.4.1 Electrochemical Polymerization

Classified by conditions, such as the applied voltage and current, the electrochemical polymerization method can be divided into potentiodynamic, galvanostatic, and potentiostatic electrochemical polymerization [271]. Here, we focus on the potentiostatic electrochemical polymerization, which involves the application of constant potential. The value of this electrical potential should be high enough to oxidize and polymerize the monomer, but sufficiently low not to dissolve the metal or induce corrosion. Therefore, both the rate of polymerization and the oxidation level of CP can be controlled according to the applied voltage. Other factors, such as the concentration ratio between the matrix and dopants, the solvents used in the polymerization process, and the supporting electrolytes, can affect the induced morphologies of the polymerized CPs films [210]. It has been reported that electrochemical polymerization solvents (propylene carbonate and acetonitrile) and supporting electrolytes ($TBAClO_4$, $TBABF_4$, $LiClO_4$, and $LiBF_4$) have different effects on the morphologies of PEDOT films [272]. The supporting electrolytes have only a minor effect, while the solvents have a very significant influence on the morphologies of the CPs films. Particularly, films prepared in propylene carbonate have a smoother and flatter surface than that prepared in acetonitrile

[273]. It should be pointed that over-oxidation has a negative effect on the morphology of PEDOT [273,274].

The electrochemical polymerization method was used as an oxidation control approach. **Figure 14c** and **14d** plots σ and S of PEDOT:PSS films by the function of the gate voltage, in which the oxidation level was modulated by the applied gate voltages [73]. Such a process can be realized using a simple electrochemical setup, as illustrated in **Figure 14b**. Similar results were also reported by Kim [80], where a high $S^2\sigma$ of 1270 $\mu W \cdot m^{-1} \cdot K^{-2}$ can be realized in PEDOT:Tos films under a particular gate potential of 0.1 V, as shown in **Figures 14e** and **14f**.

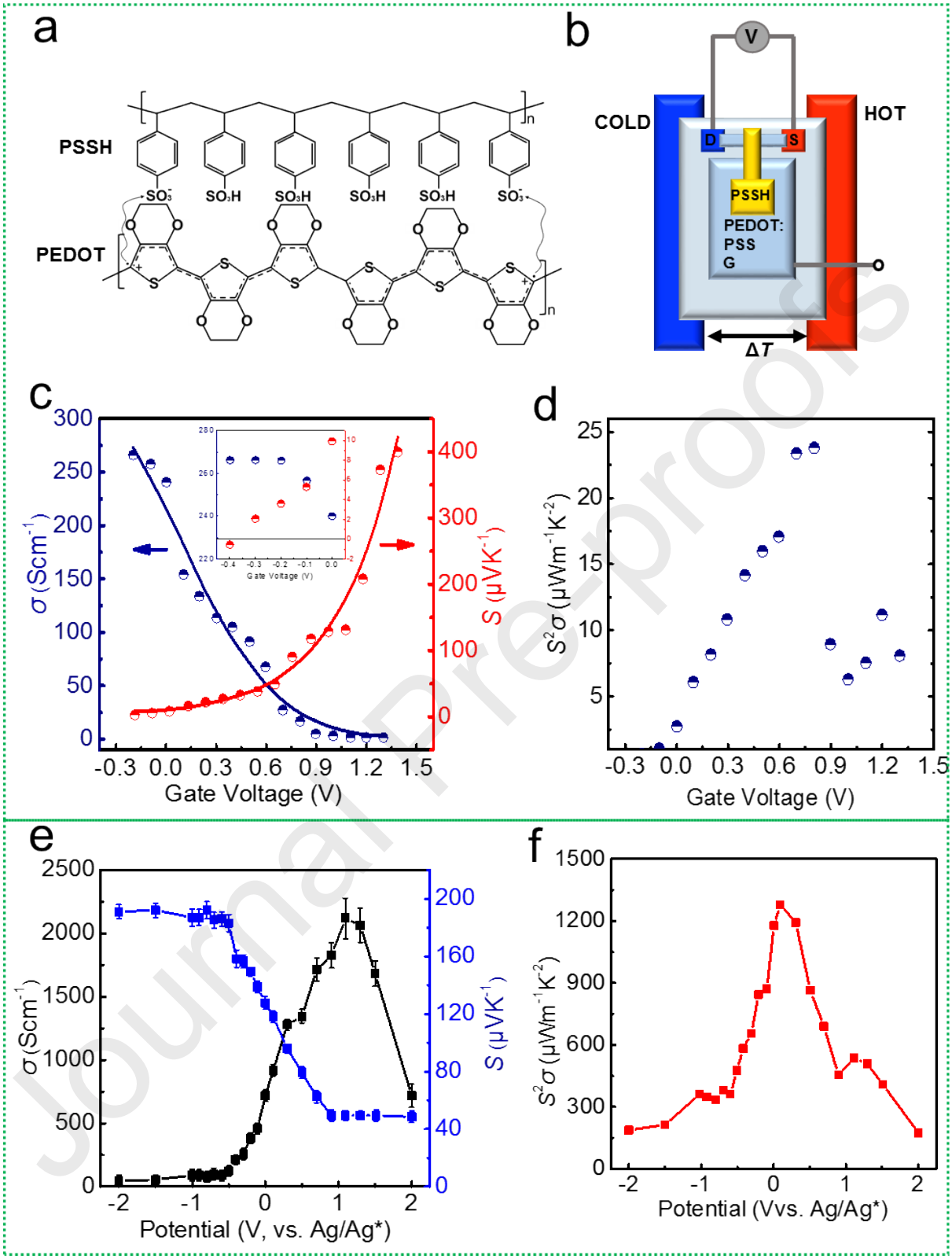

Figure 14. a) Chemical structure of PEDOT–PSS; b) schematic diagram of the electrochemical setup; c) and d) the TE properties of PEDOT:PSS films as functions of gate voltage; a)-d) Reproduced with permission [73]. Copyright 2012, American Chemical Society; e) and f) TE properties of PEDOT:Tos

films as functions of gate potential. e) and f) Reproduced with permission [80]. Copyright 2013, Royal Society of Chemistry.

3.4.2 Oxidative Chemical Polymerization

The oxidative chemical polymerization method involves the application of oxidation agents to polymerize monomers of CPs [275]. Generally, monomers of CPs are deposited upon substrates where oxidation agents have been coated in advance. The polymerization reaction between the monomers and the oxidation agents is spontaneous and controllable. Notably, the morphologies of the polymerized films can be elaborated by using suitable oxidation agents and a rational supply rate of monomers to control the polymerization rate [272]. Typically, a lower polymerization rate is helpful in forming crystalline structures with high σ [63]. Other factors, including temperature [276], surfactants [277], and the thickness of the oxidation agent layer [278], influence the morphologies of the polymerized films. As for the oxidation level, reduction treatments are usually applied to the polymerized films after the polymerization process. The oxidation level can be modulated effectively by controlling the duration of the reduction treatments.

Oxidative chemical polymerization can be applied to fabricate two types of polymerized CPs films, namely the self-assembled films and patterned films. The difference lies in the distribution of oxidation agents upon the substrates. **Figure 15a** shows a typical oxidative chemical polymerization method in which oxidation agents cover the entire top surface of the substrates and react with monomers to form polymer films in a self-assembled manner. **Figures 15b** illustrate the optical images of the evolution of the crystalline growth and **Figures 15c** plots the time-dependent σ of self-assembled PEDOT films fabricated at 30 ℃ [279]. As can be seen, the polymerization process took > 30 minutes to complete and the σ of polymerized films reached 4500 $S \cdot cm^{-1}$. A similar result was also reported for the self-assembled PEDOT films showing high σ of 5400 $S \cdot cm^{-1}$, as shown in **Figure 15d** [82]. Such dramatic

enhancements in σ was attributed to the highly crystallized microstructures, as shown in **Figure 15e**, which is verified by the metallic granular model [65], as aforementioned in **Figure 5a**.

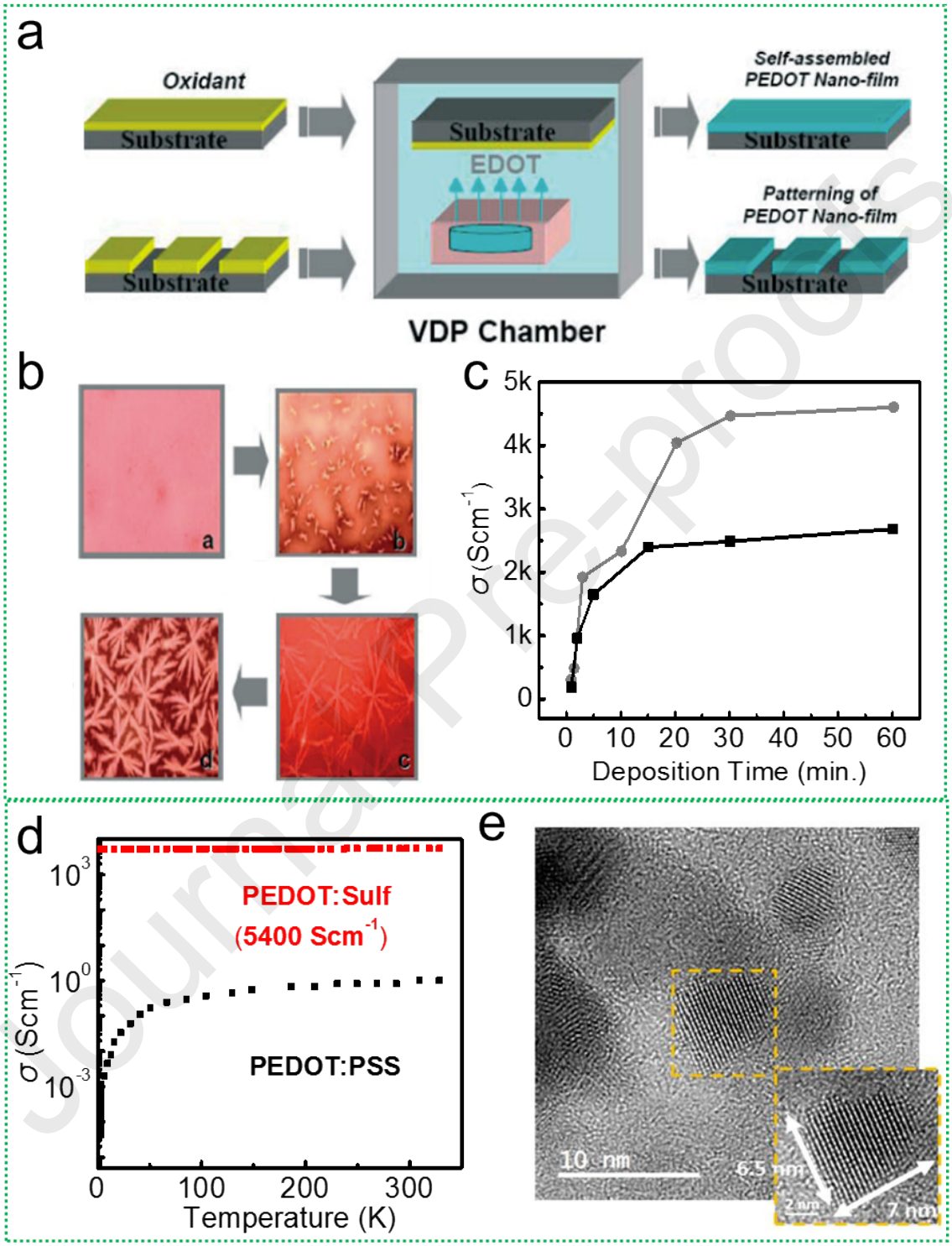

Figure 15. a) schematic diagram of two oxidative chemical polymerization approaches; b) crystalline growth and c) electrical properties of self-assembled PEDOT films fabricated by oxidative chemical

polymerization method at 30 ℃; a)-c) Reproduced with permission [279]. Copyright 2007, Wiley-VCH; d) σ versus temperature relation and e) TEM image of the self-assembled PEDOT films. d) and e) Reproduced with permission [82]. Copyright 2016, American Chemical Society.

As for the patterned films, the oxidation agents should be coated upon the substrates with designed patterns, followed by the deposition of monomers. The reaction between the monomers and the oxidation agents results in the ordering of CPs in a pattern. **Figures 16a** and **16b** show the typical procedure and structural characteristics of single-crystal PEDOT nanowires [96]. σ of >8000 S·cm^{-1} can be observed in PEDOT nanowires (**Figure 16c)**. Such an overwhelming value was attributed to the highly crystalline structures with dramatic enhancement in μ. Notably, σ of polymerized films can span a huge range from 2 to ~10000 S·cm^{-1} [280-283], stemming from the dopant anions used, such as tosylate [52], poly(styrenesulfonate) [73], Cl^- [284], and surfactants [276,278,285]. For example, σ of 3400 S·cm^{-1} can be observed in PEDOT films synthesized with 5800 Da PEG-PPG-PEG, which is much higher than that of PEDOT film synthesized with 2900 Da PEG-PPG-PEG [276]. Such a difference can be attributed to the sheet-like morphology induced by the addition of 5800 Da PEG-PPG-PEG into the oxidant solution [276].

In summary, polymerization is one of the most effective strategies to improve the TE performance of CPs, in which the morphology and oxidation level of polymers can be modulated by controlling the polymerization conditions. Polymerization is not only applied to pure CPs, but is also used as a part of the hybridization methodology for polymer-inorganic composite TE materials [48].

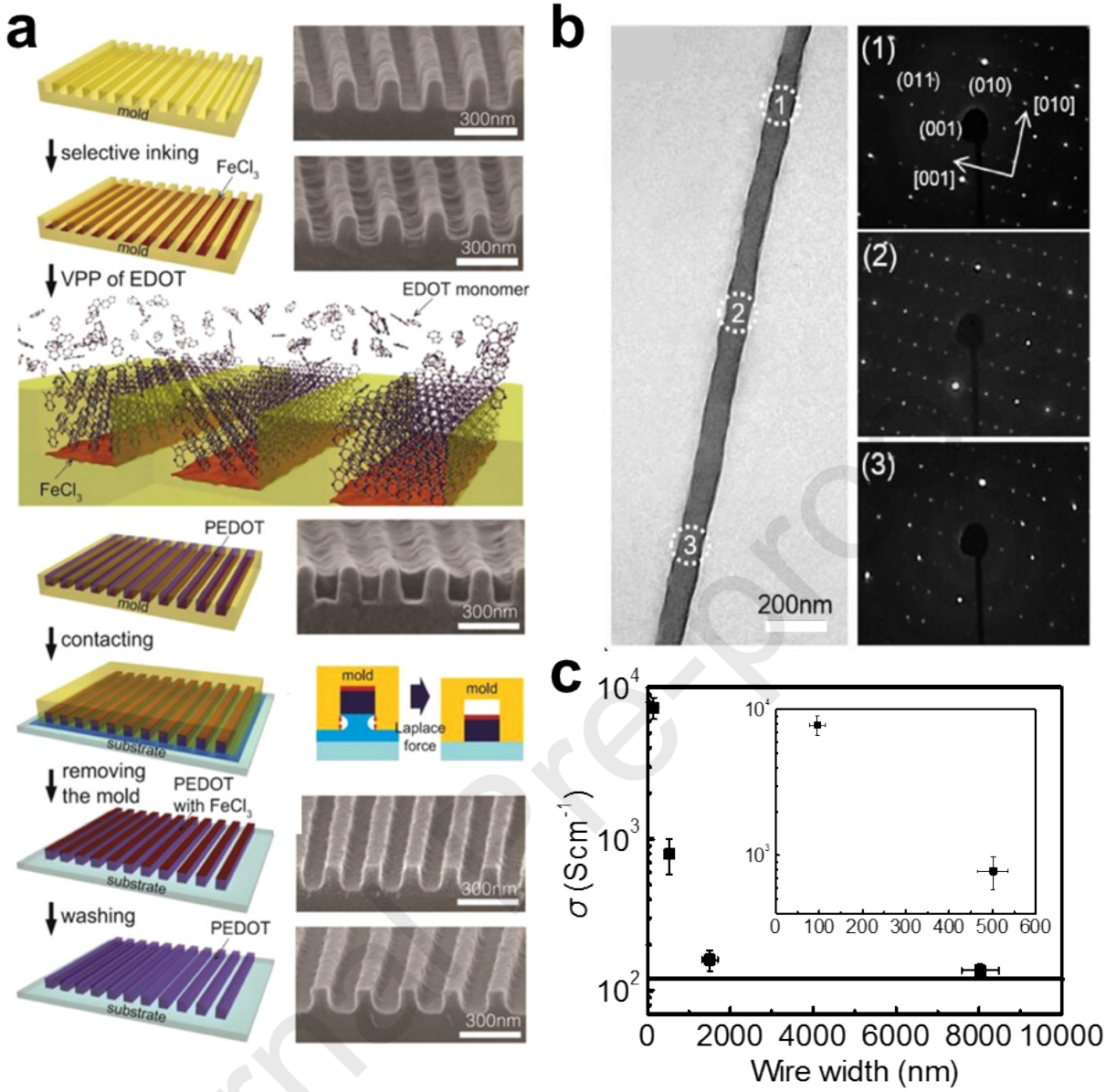

Figure 16. a) Schematic illustration of the procedure used to fabricate a single-crystal PEDOT nanowire; b) A TEM image of a PEDOT nanowire and the corresponding SAED patterns; c) σ versus wire width relation of the PEDOT nanowires. Reproduced with permission [96]. Copyright 2014, American Chemical Society.

3.5 Metal-based coordination polymers

The linear coordination polymers formed by transition metal ions and ethylenetetrathiolate (ett) are ladder-like polymers with a narrow bandgap degenerate semiconducting character. The lack of

rotatable single-bond connections in their molecular structures makes their conjugated backbones more rigid and stretched out, supporting a highly efficient intra-chain charge carrier transport. Therefore, they are expected to possess excellent TE performance as those of typical inorganic TE materials. **Figure 17** shows the temperature dependencies of the TE properties of several typical metal-based coordination polymers. Clearly, all polymers, no matter n-type or p-type, show positive dependency of σ on temperature, as shown in **Figure 17a**, which usually occurs when thermally-assisted hopping behaviour dominates the charge carriers transport [90]. Interestingly, the absolute values S of these polymers also increase with the temperature, similar to doped conducting polymers such as polythiophenes [286] and polypyrrole [208]. Although the S-T relations of the latter two were concluded as linear relation, the metal-based coordination polymers might actually follow the S-$T^{1/2}$ relation as described by equation (10) for VRH model. **Figure 17c** shows the κ of the metal-based coordination polymers. The positive dependencies of all polymers can be ascribed to the enhanced electronic component of κ as the σ increases with temperature. The deduced figure of merits ZT for all polymers were also presented here in **Figure 17d**, showing a pretty high value over 0.32 at 400 K. Notably, these metal-based coordination polymers show not only excellent TE performances but also better photosensitivity than pure polymers, indicating that they can be used as both TEGs [129] and photo detectors [287].

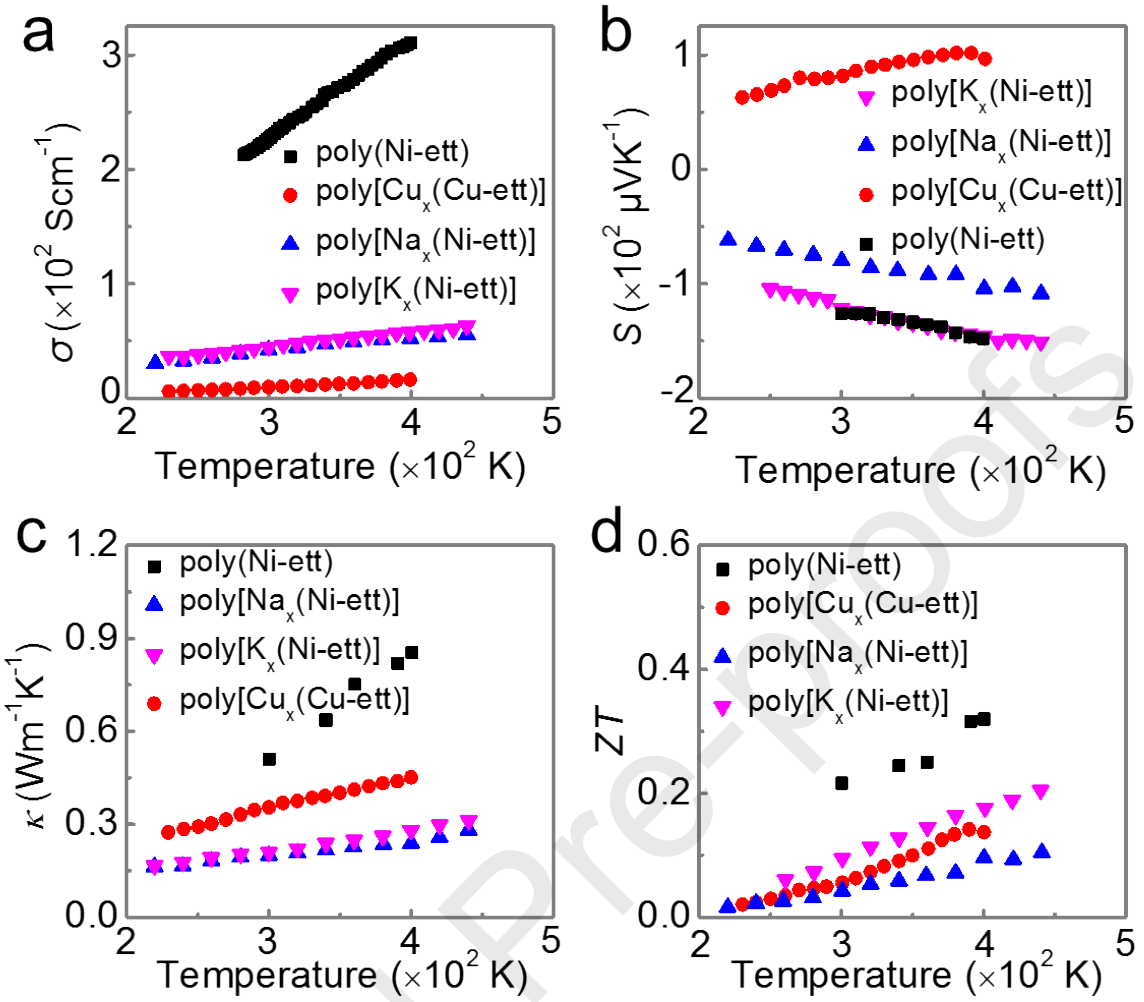

Figure 17. Temperature dependencies of a) σ, b) S, c) κ and d) ZT of four metal-based coordination polymers. Plotted together are measured data for poly(Ni-ett) (■) (reproduce with permission [288], copyright 2016, Wiley-VCH), poly[Cu_x(Cu-ett)] (●), poly[Na_x(Ni-ett)] (▲) and poly[K_x(Ni-ett)] (▼) (reproduce with permission [129], copyright 2012, Wiley-VCH).

3.6 Selenium-substituted polymer

Selenium substitution is an important strategy for fine-tuning the conjugated structure and intermolecular interaction of organic semiconductors, thus serving as an effective approach to realize high mobility [289]. Take diketopyrrolopyrrole (DPP) as example, the selenium-substituted DPP derivatives (PDPPSe-12) show significantly enhanced charge mobility than the sulfur-based DPP derivatives (PDPPS-12). As a result, the power factor of the PDPPSe-12 is more than twice that of

PDPPS-12. Figure 18a shows the chemical structures of PDPPS-12 and PDPPSe-12, where the S atom in the thiophene group is substituted by a larger Se atom. Such Se substitution leads to a superior crystallinity than the PDPPS-12, which can be indicated by the clearer multi-ordered diffractions along the q_z axis and the higher intensity of the p-stacking peak along the q_{xy} axis, as presented in **Figure 18b and c**. This phenomenon was ascribed to the more compact lamellar stacking resulting from the increased π-π stacking distance of 0.07 Å due to the larger size of the Se atoms, as can be seen in **Figure 18d and e** that show the schematic diagrams of the molecular packing of PDPPS-12 and PDPPSe-12. Such compact and highly crystalline molecular structures of PDPPSe-12 lead to significantly enhanced TE performance compared to the PDPPS-12. **Figure 18f, g and h** show the temperature dependencies of the σ, S and power factors of both PDPPS-12 and PDPPSe-12. The remarkably enhanced σ (more than 3 times that of PDPPS-12) of PDPPSe-12 gives an over doubled power factor even though the S is slightly depressed, indicating that such a significant enhancement of power factor mainly comes from the improvement of carrier mobility.

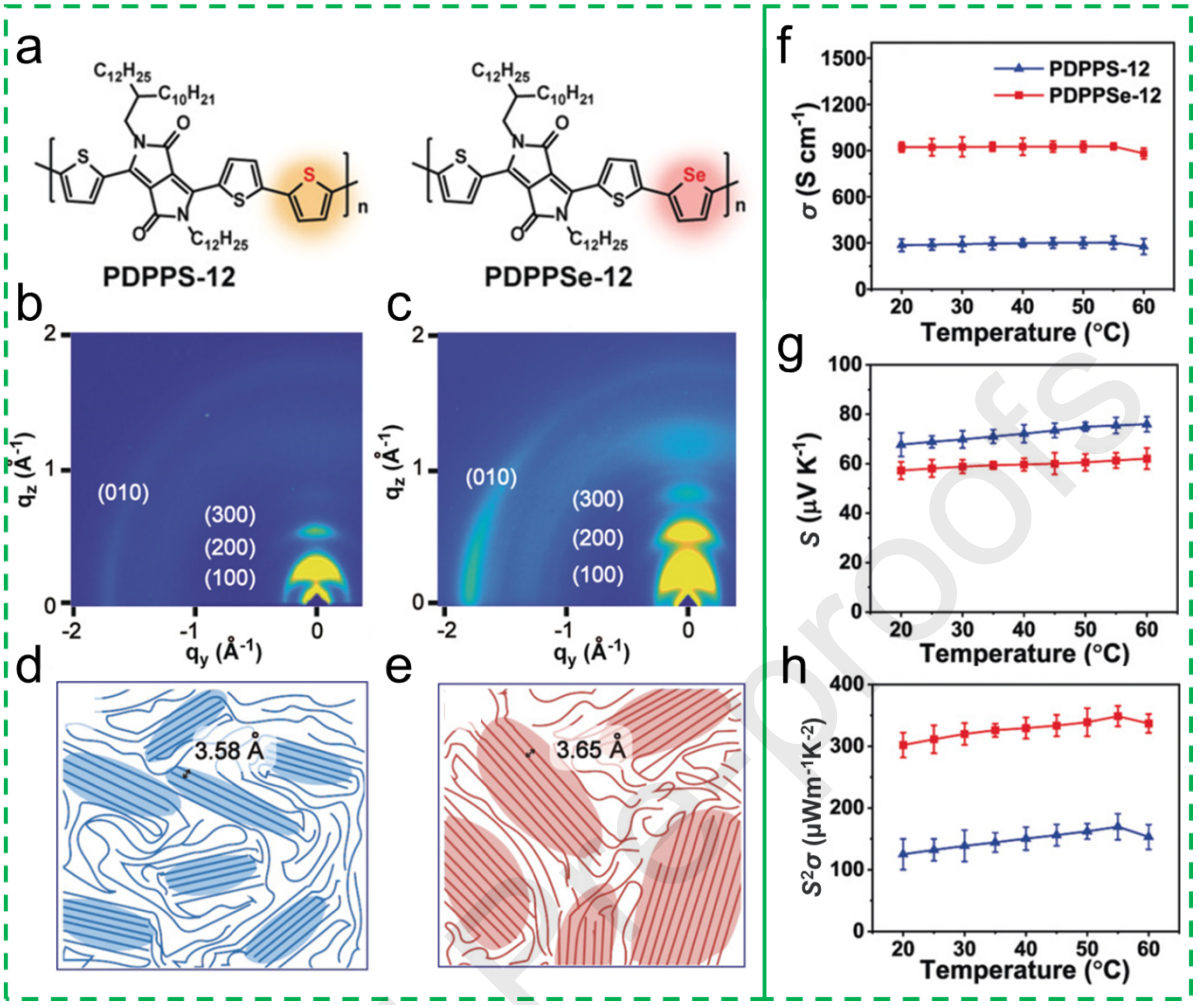

Figure 18. a) Schematic diagrams of PDPPS-12 and PDPPSe-12; GIXRD images of b) PDPPS-12 and c) PDPPSe-12; Schematic diagrams of molecular packing of d) PDPPS-12 and e) PDPPSe-12; Temperature dependencies of f) σ, g) S and h) power factor of both PDPPS-12 and PDPPSe-12. Reproduced with permission [289]. Copyright 2019, Wiley-VCH.

4. Hybrid Composites based on Conducting Polymers

The intrinsically low κ of CPs is naturally uncoupled with the electrical properties as electric charges rarely contribute to κ [65]. However, $S^2\sigma$ of most CPs is inferior to that of some excellent inorganic TE materials which possess highly coupled κ and electrical properties [290-301]. Therefore, a strategy of combining both CPs and inorganic fillers can be expected to inherit both merits and achieve the synergistic optimization of the electrical properties and κ. In addition to significantly improve the

electrical transport, the introduced interfaces tend to block the low energy charge carriers due to the filtering effect, and this in turn effectively improves *S* of the polymer matrix [64,176]. However, at this stage, there is still a lack of systematic and accurate characterization and research methods for the energy filtering effect. Inorganic materials and high-conductivity carbon materials usually have relatively high thermal conductivity, and when combined with conductive polymers, phonon scattering through the interface can effectively reduce the κ of the system. At the same time, the organic components can act as stabilizers and dispersants in the solution to improve the dispersion stability of the inorganic components in the solution.

Generally, the inorganic fillers that have been applied involve carbon-based nanomaterials and inorganic TE semiconductors. The carbon-based nanomaterials usually refer to single-wall carbon nanotube (SWCNT) [167], multi-wall carbon nanotube (MWCN) [166], graphene [275], etc. Their relatively high σ partially accounts for their population as fillers in polymers composites. Besides, these carbon-based molecules can be easily dispersed evenly within the liquid states of polymers such as PEDOT:PSS aqueous solutions. This process is very significant in the preparations of polymer composites films with uniformly distributed fillers. Besides, most inorganic TE semiconductors are potential fillers in the polymer composites. Particularly, several inorganic nanoparticles, including tellurium (Te) [187], bismuth telluride (Bi_2Te_3) [48], and tin selenide (SnSe) [51], were commonly applied in the fabrication of high-performance hybrid composites films. The advantages of being inorganic fillers lies in their outstanding and tunable TE properties so that the TE performance of the polymer composites films can be effectively optimized. However, as these inorganic fillers always tend to aggregate together and sink downward during the solidification process of the polymer composites films, a special technique was required to fabricate high-quality polymer composites films with uniform distribution of inorganic fillers. In addition to inorganic semiconductors and carbons, organic insulating materials can also participate in the construction of composite/hybrid systems, and their role is mostly to improve the solution processability and flexibility of the systems. For example, in the

TTF:TCNQ/PVC [52] and Bi_2Se_3/PVD systems [302], PVC and PVDF improved the processability of the material (can be used for inkjet printing), or helped the composite system to achieve high flexibility.

Except for the fillers mentioned above, polymers were also applied in the preparation of polymer composites films through a layer-by-layer deposition technique to form multi-layer structures with appropriate band alignments [164]. The mechanism behind this structure is known as modulation doping, accounting for the charge carrier diffusion between two materials due to the energy fluctuations between their energy band structures [186]. However, it should be noted that for the organic/inorganic composite material systems, the most significant challenges are making the two components with obvious differences in morphology and density uniformly disperse, and closely contact to achieve the hybrid effect, which are problems that needs to be faced during the preparation process, otherwise the performance of the composite system may not be beyond the upper limit of individual components.

4.1 Carbon-based Nanomaterials as Fillers

For carbon-based nanomaterials such as CNTs and graphene, although they have different morphologies, they both have high μ, which can increase the σ of the hybrid systems. Carbon-based molecules have drawn tremendous attention as fillers for polymer composites due to their high σ of $>10^4$ $S \cdot cm^{-1}$ [303]. Graphene is the most well-known carbon-based molecule as graphene has broken many records in terms of mechanical properties and energy conduction [304-306]. The ultrahigh σ of graphene stems from the two-dimensional sheet-like structure with sp^2 hybridization, where electronic charges can transfer with remarkably high μ of >200,000 $cm^2 \cdot V^{-1} \cdot s^{-1}$ [307]. On the other hand, by rolling the graphene sheets along an axis, the obtained CNTs would retain the excellent properties of graphene. Specifically, the number of rolled graphene sheets determines the form of CNT, such SWCNTs which consists of one single sheet of graphene, and MWCNTs composed of several single tubes nested inside each other with the same rolling axis. CNTs have excellent electrical transport properties, and can form close contact with CPs through interaction to carry out effective charge transport. At the same time, the one-dimensional structure of CNTs can form an effective connection between the conductive regions

and improve the efficiency of carrier transport. These advantages have prompted more attention to the composite and hybridization of CNTs and CPs. Notably, as the ultrahigh σ of these materials mainly originates from their remarkably high μ, using them as fillers in polymer composites usually improves σ without sacrificing S, leading to noticeable enhancement in their $S^2\sigma$. Unfortunately, the enhancements of $S^2\sigma$ are followed by the inevitable increase of κ because of the outstanding intrinsic thermal conductivity of these carbon-based molecules [177], and this explains why most polymer composites with carbon-based molecules as fillers present high $S^2\sigma$ but common ZT.

Carbon-based nanomaterials are effective fillers for polythiophene-based CPs such as P3HT, PEDOT, and PEDOT:PSS. The minor incorporation (2 wt%) of graphene into PEDOT:PSS dramatically improves the overall $S^2\sigma$ to 11.09 $\mu W \cdot m^{-1} \cdot K^{-2}$ due to the large increase in μ by over ten times [307]. This result was attributed to the high μ of graphene and its large surface area bridging the carrier transport by means of the strong π-π interaction with the rings of PEDOT:PSS [307]. In addition to polythiophene-based CPs, PANI is also a suitable organic matrix that can form high-performance organic-inorganic hybrid. Similar to polythiophene, introducing carbon-based nanomaterials such as CNTs and graphene is an effective way to achieve high performance in the hybrids [308]. In terms of the mechanism, in addition to the interaction between PANI and CNTs, group modification of CNTs can also promote the connection and orderly arrangement between the two components [162]. Sometimes, in order to further improve the TE performance of the PANI/carbon composite system, a third material can be introduced to construct a ternary composite system [309]. The introduction of the third component may increase the system interface, enhance the energy filtering effect, increase the S, or improve the contact between the original two components, increase the μ, and optimize the $S^2\sigma$ [309]. It was reported that high values of $S^2\sigma$ were obtained by blending PANI with exfoliated graphene nanoplatelets (GNPs) at 50 wt% loading [310]. The grinding and cold compression moulding of PANI-HCl with graphene grown by the chemical vapor deposition (CVD) method resulted in a $S^2\sigma$ of 14 $\mu W \cdot m^{-1} \cdot K^{-2}$, showing a 1000-fold enhancement with respect to the raw PANI polymer [310]. Such a

dramatic enhancement in $S^2\sigma$ was attributed to the sufficient addition of GNPs, which enables the increase of σ and introduces plenty of interfaces to improve S according to the energy filtering effect, although κ also increases with the GNP contents. Other CPs such as PPy are also suitable organic matrix to form hybrids with carbon nanomaterials. At present, research on the TE properties of composites based on PPy focuses more on the composite system of PPy and carbon-based nanomaterials (CNTs, graphene). In terms of the main reason, firstly, carbon-based nanomaterials usually have relatively high σ. In the composite system, it can improve the σ of PPy to a certain extent; secondly, through the interaction of carbon-based nanomaterials and pyrrole monomer/PPy molecular chains, it can be *in-situ* polymerized. In the mixing process, the two components are brought into close contact, and the molecular arrangement is improved, which is conducive to the transport of carriers. Finally, similar to other polymer/carbon composite systems, the low κ of PPy is beneficial to suppress the κ of the entire composite system, thereby improving the TE performance. As for metal-based coordination polymers, the research on their organic-inorganic hybrids is still at a preliminary stage, such as recently reported poly (Ni-ett)/CNT/PVC [311] and copper-phenylacetylide PhC_2Cu nanobelts/SWCNTs systems [312].

In terms of the selection of carbon-based nanomaterials, although experiments have verified the potential of graphene to be a kind of good filler in polymer composites, the aggregation of fillers as a result of Van der Waals interactions needs to be overcome. Researchers have found that the graphene oxide (GO) presented a good ability to be dispersed in polymer aqueous solutions as GO contains oxygen functionalities (epoxides and alcohols) [313]. However, the TE performance of polymer composites with GO is unacceptable due to the poor σ of GO [313]. It was reported that the PANI/GO composite showed σ of 7.5 $S{\cdot}cm^{-1}$ and ZT of only 4.86×10^{-4} [313]. Therefore, chemical or thermal reduction is necessary for the GO to regain its high σ, where reduced graphene oxide (rGO) was incorporated into PEDOT:PSS to improve σ from 380 $S{\cdot}cm^{-1}$ to 518 $S{\cdot}cm^{-1}$ without decreasing the S [275]. Compared with graphene, polymer composites with CNTs as fillers have garnered more attention as they presented better TE performances [177,202,204,314,315]. Unlike the 2D structures in graphene

where phonons can transfer easily, the 1D structure of CNT enables the scattering of phonons at the interface between two CNTs, which results in a relatively low κ for the composites. The observed energy filtering effect was also helpful in the enhancement of S. It was initially reported that the addition of MWCNTs remarkably enhanced S and $S^2\sigma$ of the PANI/MWCNT composites due to the size-dependent energy filtering effect in the PANI coated CNT bundles [166]. The related typical microscopic structures are shown in **Figures 19a-d** [166]. As can be seen, the conformation expansion of PANI in a solution process using m-cresol solvent prior to the blending of CNTs enables the formation of highly conductive interfaces between two components. This unique effect dramatically improved σ from 300 $S \cdot cm^{-1}$ to nearly 800 $S \cdot cm^{-1}$ (**Figure 19e**), exceeding the values obtained from the series-connected model, and increased S monotonically up to ~65 $\mu V \cdot K^{-1}$ (**Figure 19f**) as predicted by the model, indicating that the conductive interfaces did not suppress the energy filtering effect between two components [167]. On the other hand, κ of the composites remain basically unchanged as the conductive interfaces did not contribute to thermal conduction. As a result, the peak overall $S^2\sigma$ and ZT reached 176 $\mu W \cdot m^{-1} \cdot K^{-2}$ and 0.12 [167].

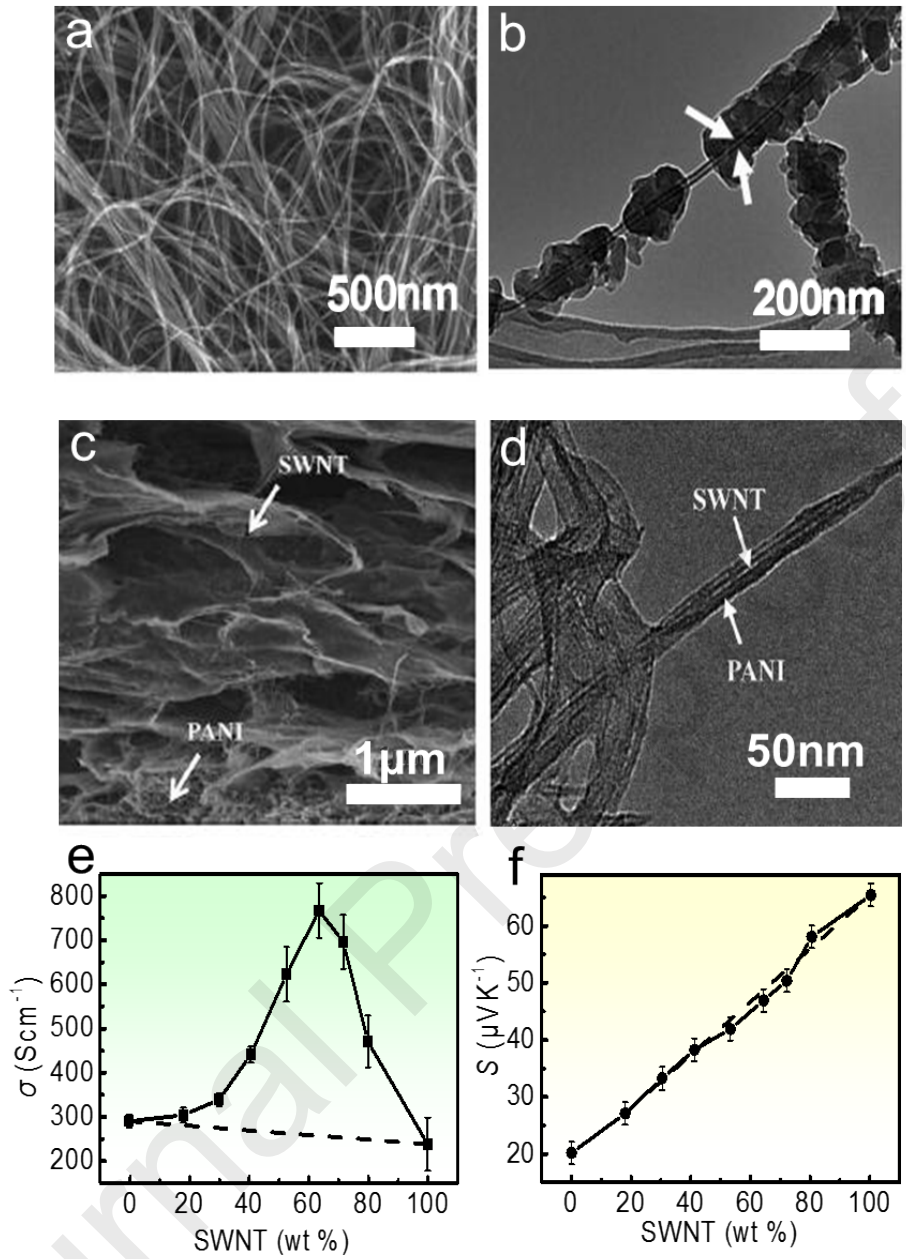

Figure 19. a) SEM image of PANI/MWCNT composites; b) TEM image of individual MWCNT bundles coated with a PANI layer; a) and b) Reproduced with permission [166]. Copyright 2010, Wiley-VCH; c) SEM images of PANI/SWCNT composite; d) TEM image of individual SWNT bundle coated with a PANI layer; e) and f) electrical properties of the PANI/SWCNT composite films. The dash lines represent the values calculated using the series-connected model; c)-f) Reproduced with permission [167]. Copyright 2014, Royal Society of Chemistry.

Distinct effects were also observed in other polymer composites with CNTs. **Figure 20a** shows a schematic diagram of the synthesis process of poly(vinyl acetate) (PVAc)/CNT. As a result, the σ of poly(vinyl acetate) (PVAc)/CNT exponentially increased from nearly 0 to around 50 S·cm^{-1} with the contents of CNT while both S and κ slightly changed, as shown in **Figures 20b** and **20d** [316]. The results were attributed to the segregated-network CNT-polymer composites where thermally disconnected, but electrically connected junctions were believed to be present, as shown in **Figure 20a** and **20c**. Besides, such a segregated network structure also suppressed the energy filtering effect between two components, accounting for the unchanged S.

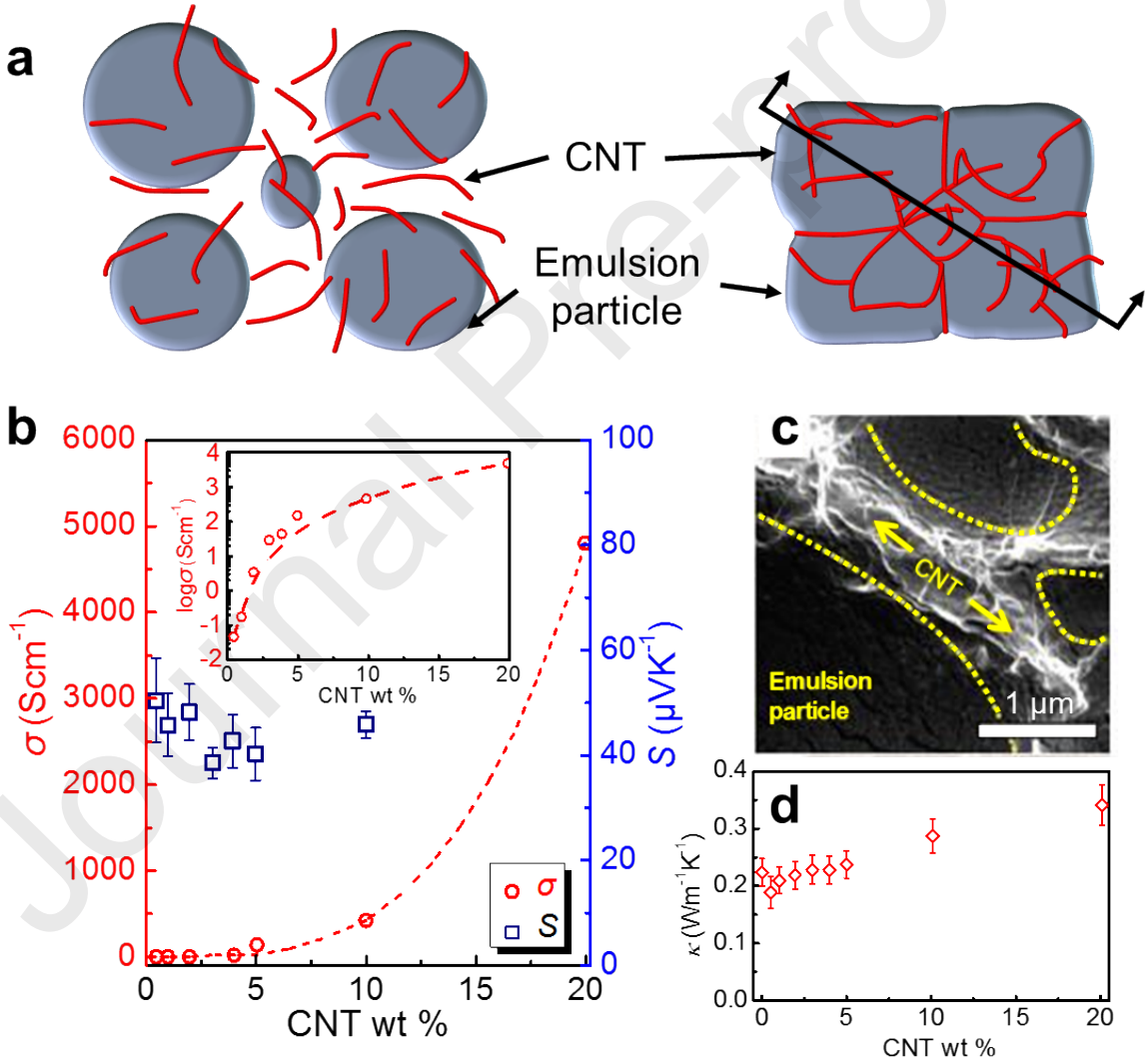

Figure 20. a) Schematic process of CNTs blended with PVAc; b) σ and S of PVAc/CNT composite as functions of CNT contents; c) cross-sectional SEM image of the PVAc/CNT composite at 5 wt%

loading; d) κ of the PVAc/CNT composite as a function of CNT contents. Reproduced with permission [316]. Copyright 2010, American Chemical Society.

The abovementioned work obtained an improved TE performance for PVAc/CNT composites due to the segregated-network between the fillers and the polymer. The improved TE performance is also observed in the PVAc/CNTs composites by incorporating highly conductive PEDOT:PSS to modify the junctions between CNTs and PVAc, as schematically shown in **Figure 21a** [177]. **Figure 21b** and **c** plot the measured σ and S. As can be seen, σ was improved from 50 up to 400 $S \cdot cm^{-1}$ while S remained at the same level [177]. This result can be attributed to the decoration of PEDOT:PSS particles on the surfaces of CNTs, enabling the electronic charges to transfer across the junctions between CNTs. As for κ, it remains comparable to conventional polymeric materials due to the dissimilar bonding and vibrational spectra between CNT and PEDOT:PSS [177].

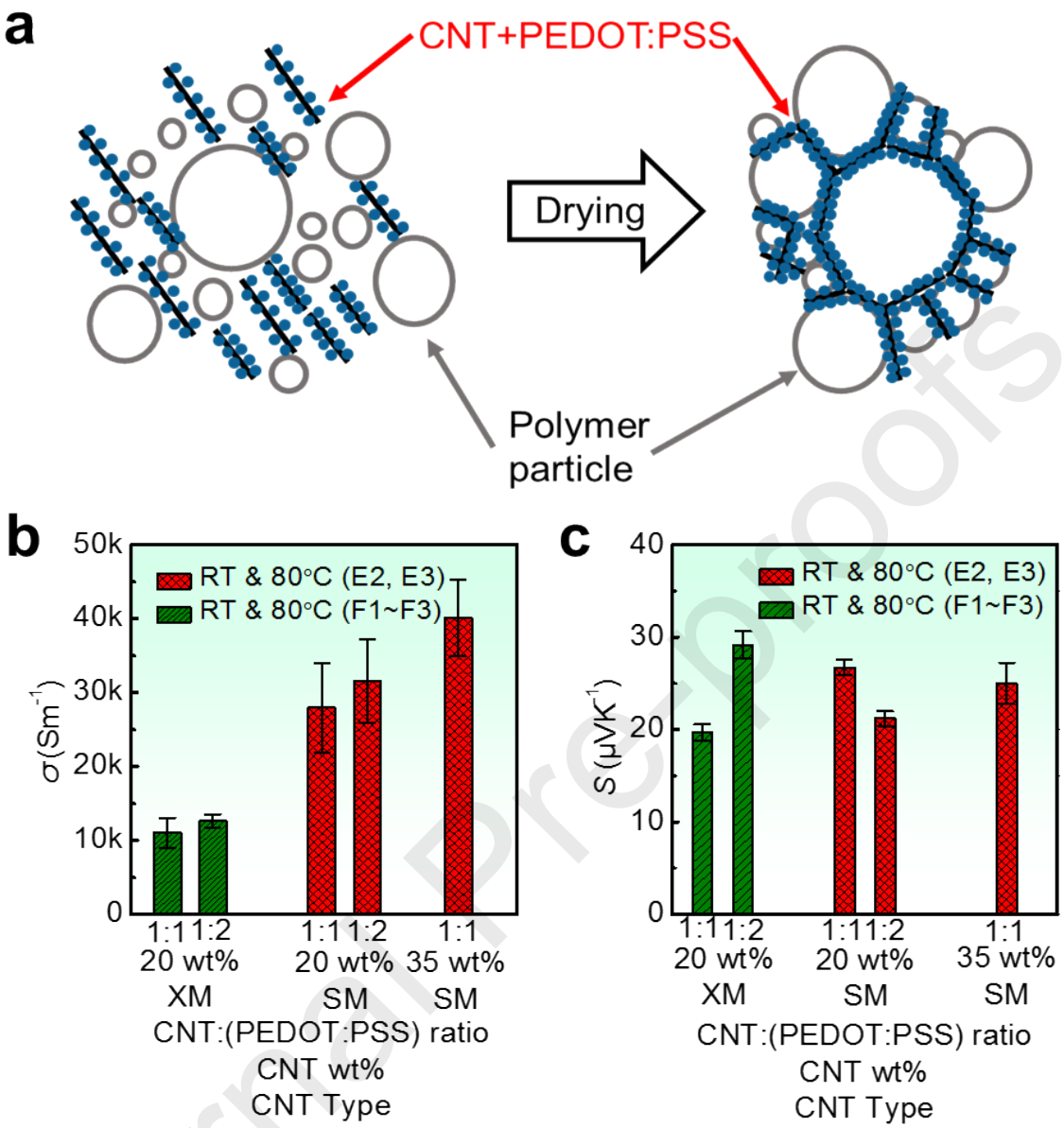

Figure 21. a) CNTs form a three-dimensional network along the surface of spherical emulsion particles; b) σ and c) S of the PVAc/CNT/PEDOT:PSS composite; Reproduced with permission [177]. Copyright 2010, American Chemical Society.

4.2 Inorganic TE Semiconductors as Fillers

To date, the highest ZT of CPs cannot reach half of that of the start-of-the art inorganic TE materials, especially Bi_2Te_3-based alloys. As a result, incorporating inorganic particles into CPs as fillers becomes a promising strategy to combine the advantages of both types of materials and achieve

high-performance TE materials with excellent flexibility. However, depending on incorporation methods, the inorganic filler/polymer composites usually suffer major problems that cause ineffective loadings, such as inhomogeneity, large particle size, and oxidation [64]. Generally, there are four incorporation methods, namely physical mixture [317,318], *in-situ* synthesis [176,187], physical vapor deposition (PVD) loading [48], and electrochemical intercalation [196].

4.2.1 Physical mixing

By simply distributing the inorganic particles into the polymer matrices (usually aqueous solutions) and stirring, the polymers and fillers were physically mixed. The downside is that the polymer-inorganic particle composites may suffer from the previously mentioned problems. Specifically, the incorporated inorganic particles tend to aggregate together and sink downward to be stratified from the polymer layers due to their large densities. Stratification can be observed in the physically mixed products. A typical case is shown in PEDOT: PSS/Bi_2Te_3 composites **(Figure 22a)**, which was drop-cast and dried out upon substrates. In addition, the composite films suffer from inhomogeneity with large particles. Acid treatment (HCl) were used to remove the oxidation layers of the ball-milling inorganic fillers. As a result, the highest $S^2\sigma$ that was reached was 131 $\mu W \cdot m^{-1} \cdot K^{-2}$ at 10 wt% Bi_2Te_3-loaded of PEDOT:PSS (**Figure 22b)** [317]. In another study, Bi_2Te_3-based nanosheets (BST NS) were synthesized by an lithium ion intercalation method and physically mixed with PEDOT:PSS to form BST NS/PESOT:PSS composite films using both drop-casting and spin-coating and the microstructure of BST NS/PESOT:PSS composite films is shown in **Figure 22c** [319]. The Bi_2Te_3-based nanosheets with the thickness of 3-4 nm were claimed to be well dispersed within the PEDOT:PSS aqueous solution and thus in the composite films [320-322]. However, no solid evidence such as a cross-sectional SEM image was provided to prove the uniform distribution of the BST NSs. The peak $S^2\sigma$ of drop-casting BST NS/PESOT:PSS composite films was 32.26 $\mu W \cdot m^{-1} \cdot K^{-2}$ with the BST NSs loading of 4.1 wt% (**Figure 22d)** [319].

Except for Bi_2Te_3-based alloys, SnSe NSs were also used as fillers in the PEDOT:PSS [51,205]. SnSe is a typical layer-structured semiconductor with a bandgap of ~0.9 eV [299,300,323], which exhibit high S of >250 $\mu V \cdot K^{-1}$ at room temperature [323-331], and thus has been treated as a promising filler for incorporation into flexible TE materials. The SnSe NSs with sizes of 200~300 nm were exfoliated from bulk SnSe by a lithium intercalation method [332], and their morphologies are shown in the FE-SEM images of **Figure 22e**. As can be seen, SnSe NSs were well dispersed within the composite films. σ and S of the composite films respectively monotonically decreased and increased with the weight fraction of SnSe in the films, resulting from the reduced n after the incorporation of SnSe NSs. Besides, κ slightly increased with a higher weight fraction of SnSe, which is insensitive to the filler loading compared with the electrical properties. As a result, the peak $S^2\sigma$ and ZT were nearly 400 $\mu W \cdot m^{-1} \cdot K^{-2}$ and 0.32, respectively, as shown in **Figure 22f** [51]. Interestingly, the TE performance of SnSe under low temperature (lower than 373 K) is far worse than that of Bi_2Te_3-based alloys [15-17,333-335], indicating that the TE performance of the composite film cannot be simply determined by the averaged TE performance of each component.

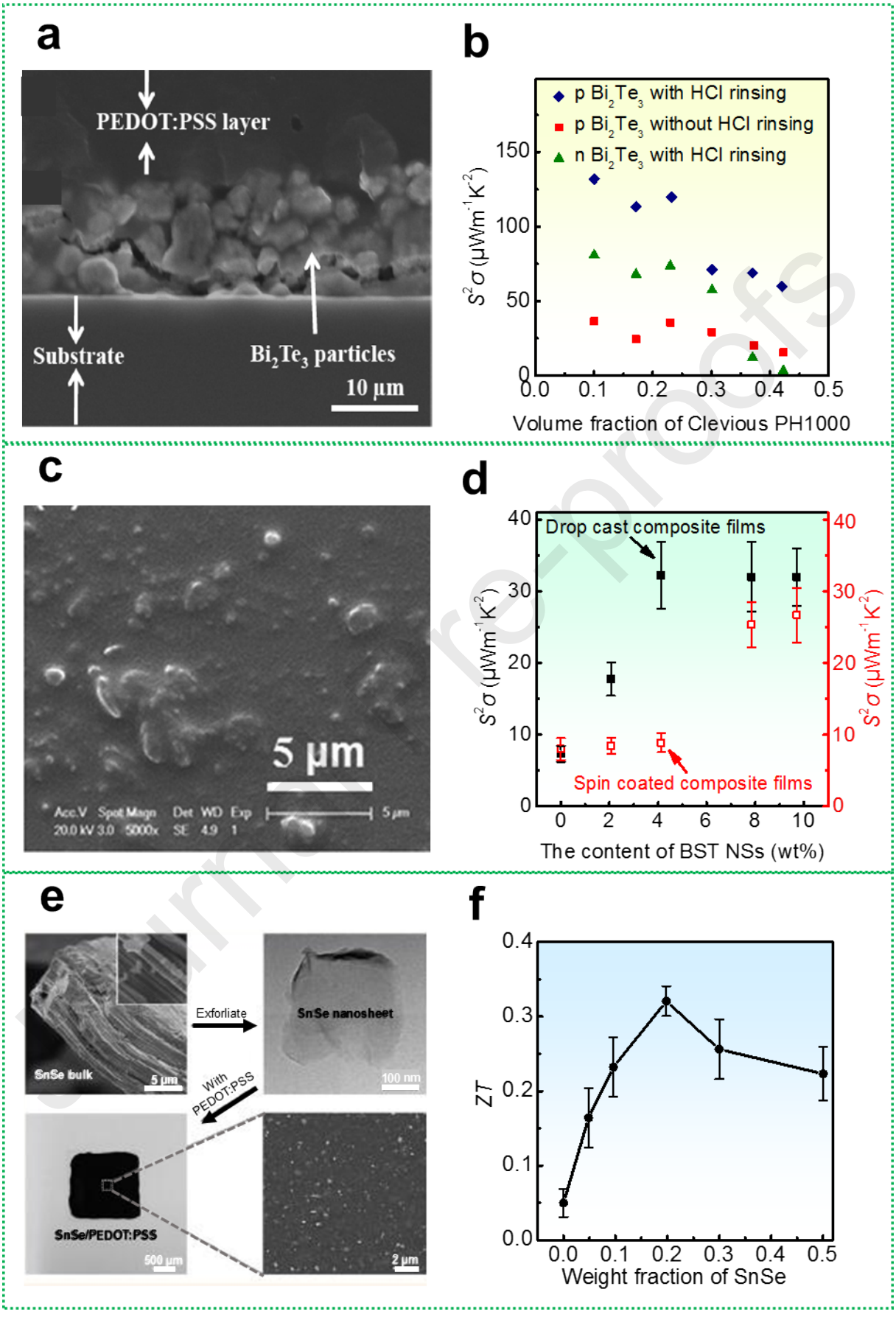
a
PEDOT:PSS layer
Substrate
Bi2Te3 particles
10 μm
b
p Bi2Te3 with HCl rinsing
p Bi2Te3 without HCl rinsing
n Bi2Te3 with HCl rinsing
S2σ (μWm-1K-2)
Volume fraction of Clevious PH1000
c
5 μm
d
Drop cast composite films
Spin coated composite films
S2σ (μWm-1K-2)
The content of BST NSs (wt%)
e
SnSe bulk
5 μm
Exforliate
SnSe nanosheet
100 nm
With PEDOT:PSS
SnSe/PEDOT:PSS
500 μm
2 μm
f
ZT
Weight fraction of SnSe

Figure 22. a) Cross-sectional SEM image of PEDOT:PSS/Bi_2Te_3 composite film; b) $S^2\sigma$ of the PEDOT:PSS/Bi_2Te_3 composite films; a) and b) Reproduced with permission [317]. Copyright 2010, American Chemical Society; c) surface SEM image of PEDOT:PSS/BST nanosheets composite film; d) $S^2\sigma$ of the PEDOT:PSS/BST nanosheets composite films; c) and d) Reproduced with permission [319]. Copyright 2014, American Chemical Society; e) surface SEM images of SnSe nanosheets and their polymer composite; f) *ZT* of the PEDOT:PSS/SnSe nanosheets composite films; e) and f) Reproduced with permission [51]. Copyright 2016, American Chemical Society.

4.2.2 *In-situ* synthesis

Another favourable method used to prepare polymer composites is to synthesize the inorganic fillers in the polymer solution environment, meaning that by the time each particle has been synthesized, the fillers have been well dispersed within the polymer solution. This method is also known as *in-situ* synthesis. The *in-situ* synthesis approach can fabricate nanoscale particles. The oxidation problem of these particles can also be avoided as there is little chance that the particles will be exposed to oxygen. However, the only disadvantage of this method is its weak universality. Mild synthesis conditions for the fillers such as moderate temperature and low pressure are prerequisites, as high temperature and pressure can decompose the polymers.

One successful case which applies the *in-situ* synthesis method is the PEDOT:PSS/Te composite films whose fillers were synthesized in the PEDOT:PSS solution, as shown in **Figure 23a** [187]. The precursors of Te nanoparticles reacted under 90 ℃, providing a mild condition to maintain the TE performance of PEDOT:PSS. SEM images showed that the produced Te nanorods were passivated with PEDOT:PSS, as shown in **Figure 23b**, forming highly conductive interfacial layers between the two materials. Although the intrinsic TE performance of both PEDOT:PSS and Te are poor, $S^2\sigma$ (70.9 $\mu W \cdot m^{-1} \cdot K^{-2}$) and *ZT* (0.1) of the composite films exceeded that of the two components due to the highly enhanced σ, as indicated in **Table 5** [187]. Based on this study, further research work blended

PEDOT:PSS with the PEDOT:PSS functionalized Te nanorods (PF-Te) and investigated the TE performance of the composite films [188]. It turned out that σ monotonically increases with higher functionalized Te content whereas S monotonically decreased, resulting in a peak $S^2\sigma$ of 51.4 $\mu W \cdot m^{-1} \cdot K^{-2}$ at 70 wt% loading of functionalized Te [188].

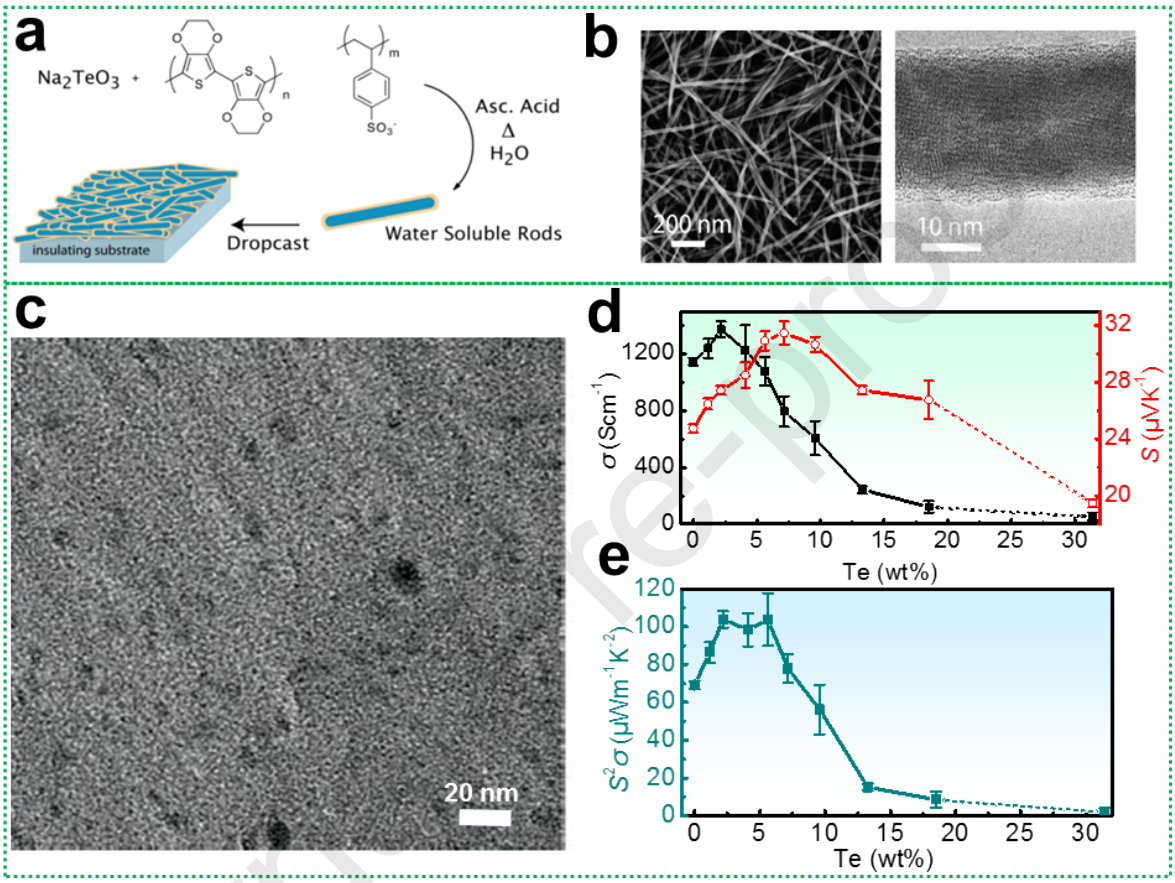

Figure 23. a) Schematic diagram of the *in-situ* synthesis process of the PEDOT:PSS/Te composite films; b) SEM and TEM images of the synthesized Te nanorods; a) and b) Reproduced with permission [187]. Copyright 2010, American Chemical Society; c) HRTEM image of PEDOT:DBSA/Cl-Te nanocomposite films; d) TE properties of the PEDOT:DBSA/Cl-Te nanocomposite films; c) and d) Reproduced with permission [64]. Copyright 2018, Wiley-VCH.

Table 5. Room temperature TE properties of Te/PEDOT:PSS nanocomposite film and its components [187].

System	σ ($S \cdot cm^{-1}$)	S ($\mu V \cdot K^{-1}$)	$S^2\sigma$ ($\mu W \cdot m^{-1} \cdot K^{-2}$)	κ ($W \cdot m^{-1} \cdot K^{-1}$)	ZT_{max}
Te/PEDOT:PSS	19.3±2.3	163±4	70.9	0.22-0.30	0.1
PEDOT:PSS	1.32±0.12	18.9±0.2	0.05	0.24-0.29	6×10^{-5}
Te nanowires	0.08±0.03	408±69	2.7	2	4×10^{-4}

Figure 23c shows an SEM image of PEDOT:DBSA/Cl-Te composites films, in which Te quantum dots were randomly incorporated in PEDOT:DBSA/Cl through *in-situ* synthesis [64]. The obtained composite films successfully avoided the aforementioned three problems, resulting in homogeneous films containing evenly distributed and well-protected Te quantum dots. The well-distributed Te quantum dots yield a great quantity of interfaces where strong energy filtering effect occurs. As a result, S was significantly enhanced. On the other hand, the effective co-doping of $DBSA^-$ supported a high doping level up to 42.9 %, which brought a dramatic σ enhancement for the composite film. As a result, the peak $S^2\sigma$ reached 100 $\mu W \cdot m^{-1} \cdot K^{-2}$ at only 2.1~5.8 wt% Te loadings, as shown in **Figure 23e**. Similarly, energy filtering effect was also observed in the ternary PANI/SWNT/Te nanocomposite film with a high $S^2\sigma$ of 101 $\mu W \cdot m^{-1} \cdot K^{-2}$ [169]. Such a $S^2\sigma$ was ascribed to the enhanced energy filtering effect at the dual interfaces of PANI/SWNTs and PANI/Te. These two instances suggest that introducing interfaces is an effective approach to achieve a high TE performance in polymer-inorganic composites.

4.2.3 Wet chemical method

The wet chemical method is similar to *in-situ* synthesis and can be regarded as an extension of the *in-situ* synthesis method. **Figure 24a** shows a typical process of PEDOT:PSS/Cu_xSe_y (PC-Cu_xSe_y) composite films by using the wet chemical method [223]. Obviously, this process involves several steps and might be more complex when compared to the *in-situ* synthesis method. However, for some polymer-inorganic composites that cannot be synthesized by the *in-situ* synthesis method, the wet chemical method would be a good alternative [179,192]. **Figure 24b** plots the temperature-dependent

σ, S, and $S^2\sigma$ of the PC-Cu_xSe_y films starting from different Cu/Se nominal molar ratios at room temperature [223]. It was pointed out that the PC-Cu_3Se_1 film exhibits the highest $S^2\sigma$ of 270.3 $\mu W \cdot m^{-1} \cdot K^{-2}$, which was ascribed to the intrinsic high S of Cu_2Se since this film consists of $Cu_{2-x}Se$ and Cu_2Se phases, besides a small amount of Cu phase. **Figure 24c** plots the temperature-dependent σ, S, and $S^2\sigma$ of the PC-Cu_3Se_1 composite film. The tendency of S and σ matches with that of the $Cu_{2-x}Se$ pretty well [223], and eventually an even higher $S^2\sigma$ of 389.7 $\mu W \cdot m^{-1} \cdot K^{-2}$ can be observed. This work indicates that some medium-temperature inorganic TE materials could be good alternative for polymer-inorganic composites films applied within 200 ℃.

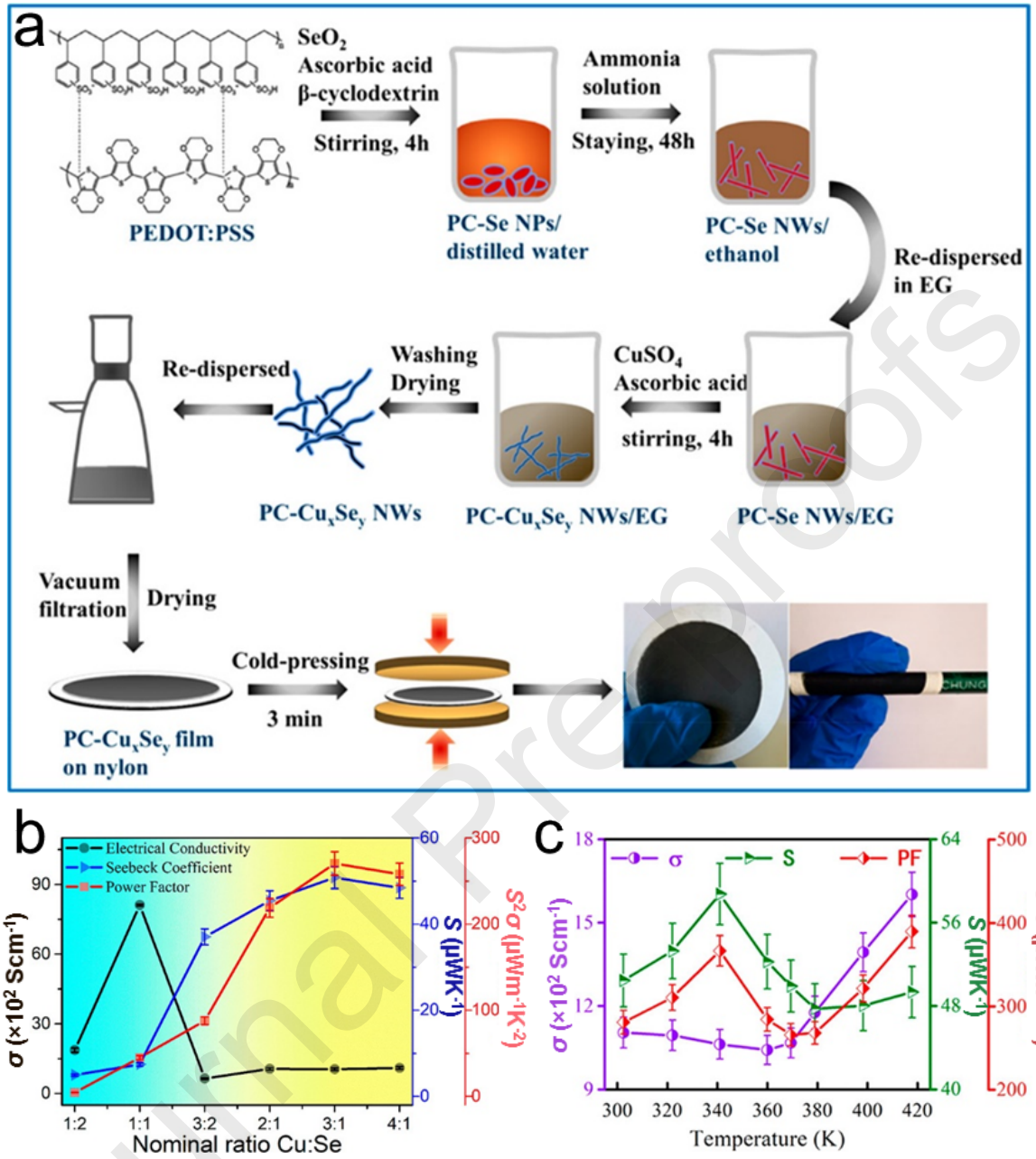

Figure 24. a). Schematic demonstrating the preparation of PEDOT:PSS/Cu_xSe_y (PC-Cu_xSe_y) composite films; b) TE parameters of the PC-Cu_xSe_y films starting from different Cu/Se nominal molar ratios at RT; c) Temperature-dependent σ, S, and $S^2\sigma$ of the PC-Cu_3Se_1 composite film. Reproduced with permission [223]. Copyright 2019, American Chemical Society.

4.2.4 Physical vapor deposition incorporation

Another innovative method to incorporate inorganic fillers into polymer composite films is physical vapor deposition incorporation [336-339]. Inorganic fillers are thermally evaporated and deposited on the substrates. Combining these fillers with some patterning techniques (like lithography and reactive etching), the inorganic fillers can be deposited upon the surface of a substrate in a designed pattern. **Figure 25a** shows the scheme for the controllable design of the PEDOT/Bi_2Te_3 composite films [48]. The prepared films were composed of polymerized PEDOT:Tos and uniformly dispersed Bi_2Te_3 in ordered cylinder arrays, as shown in **Figure 25b**. As the deposition process of the fillers was carried out in an inert atmosphere, the Bi_2Te_3 arrays have not suffered from the oxidation problem. Besides, the size and the distribution of the fillers were highly controlled, yielding the highest $S^2\sigma$ of 1350 $\mu W \cdot m^{-1} \cdot K^{-2}$ in the composite films at a Bi_2Te_3 loading of 30 vol% (**Figure 25c**). Besides, a peak ZT of 0.58 (**Figures 25d-e**) at room temperature was also achieved due to an ultralow in-plane κ of 0.7 $W \cdot m^{-1} \cdot K^{-1}$. Interestingly, the in-plane κ was depressed with higher filler contents, attributed to the strong phonon scattering effect.

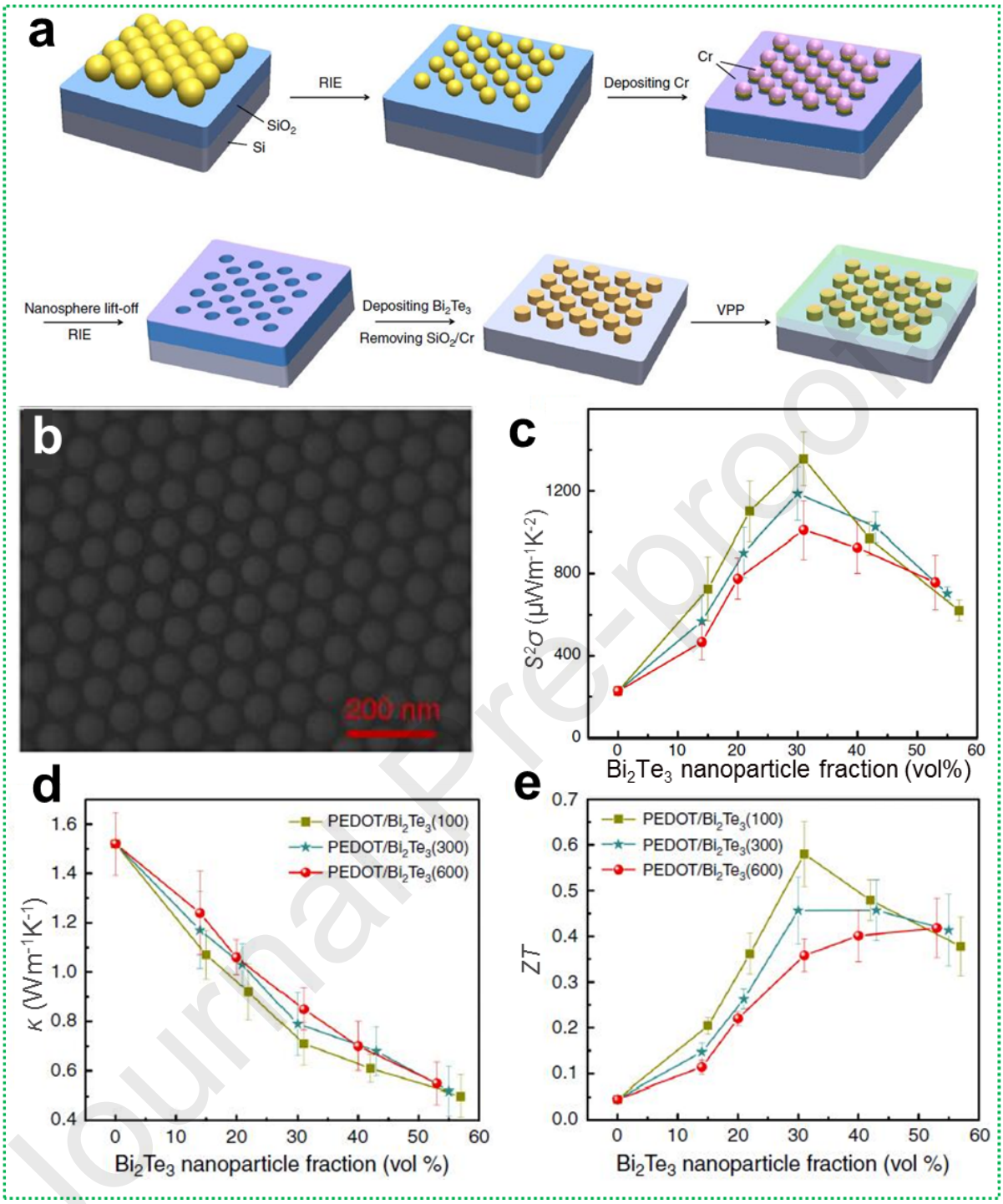

Figure 25. a) the scheme of controllable design for PEDOT/Bi_2Te_3 composite films; b) SEM image of the deposited Bi_2Te_3 arrays on a substrate; c)-e) TE properties of the PEDOT/Bi_2Te_3 composite films as functions of Bi_2Te_3 contents. Reproduced under a Creative Commons Attribution 4.0 International License [48]. Copyright 2018, Springer Nature.

4.3 Polymer-Polymer Composite Films

Unlike the other polymer composites, the polymer-polymer composites usually present layer-by-layer structures where matrices and fillers were deposited alternatively by bilayer or multilayer deposition techniques [340-346]. This method can achieve highly enhanced σ while keeping S at an optimum value by maintaining unequal distributions in the density of states by blending materials with different orbital energy [159]. It was reported that a PEDOT:PSS/PANI–CSA multilayer structure by solution processing through which a synergistic improvement in σ was achieved [159]. The resulted σ and $S^2\sigma$ of 5 PEDOT:PSS/PANI-CSA multilayer films are 1.3 and 2 times higher than those of a single PEDOT:PSS layer while S is without obvious variation [159]. The enhancement of σ occurs via stretching PEDOT and PANI chains and hole diffusion from the PANI-CSA layer to the PEDOT:PSS layer. Such carrier diffusion is governed by the modulation doping mechanism, leading to band alignment in the multilayer structure, which not only enhances σ but also maintains the S at an optimum value [159].

4.3.1 Multi-layer polymer-polymer composites

Although PEDOT:PSS/PANI-CSA composites have presented enhanced TE performance at room temperature, its $S^2\sigma$ is still far below that of the excellent inorganic semiconductors (e.g., Bi_2Te_3 based alloys) [164]. As show in **Figure 26a**, an 80 quad-layers thin film comprised of a PANI/graphene-PEDOT:PSS/PANI/DWNTPEDOT:PSS repeating sequence, exhibits unprecedented σ of 1.9×10^3 $S \cdot cm^{-1}$ and S of 120 $\mu V \cdot K^{-1}$, yielding an unrecorded $S^2\sigma$ of 2710 $\mu W \cdot m^{-1} \cdot K^{-2}$ for a completely organic material, as show in **Figure 26b** [164]. Such high TE performance was ascribed to the highly ordered structure in the multilayer assembly prepared using the layer-by-layer technique. The interconnected architecture of intrinsically CP-covered DWNTs, bridging between graphene sheets (seen in **Figure 26c)**, enables the fluent transfer of charge carriers, leading to the improved σ and S [164].

Modulation doping can be applied to account for the TE performance enhancements of the aforementioned lay-by-layer polymer/polymer composite films [347]. This mechanism describes the

transportation behaviour of charge carriers from a more doped material to adjacent less doped material with high mobility, as shown in **Figure 26d**. Specifically, n, as well as the energy drop of E_F (higher in the highly doped materials), would drive the charge carriers to complete the modulation doping process (filtering low energy charges), leading to enhanced S of the doped materials [153,347,348]. A highly doped PEDOT:PSS/intrinsic Si (001) bilayer composite films presented improved TE performance through the modulation doping process, in which S and $S^2\sigma$ can be increased up to 7.3 fold and 17.5 fold compared to those of pristine PEDOT:PSS films [186], respectively. To extend, the modulation doping process would be an effective approach to modulate the electrical properties of one semiconductor by coating a layer of another semiconductor with different doping level.

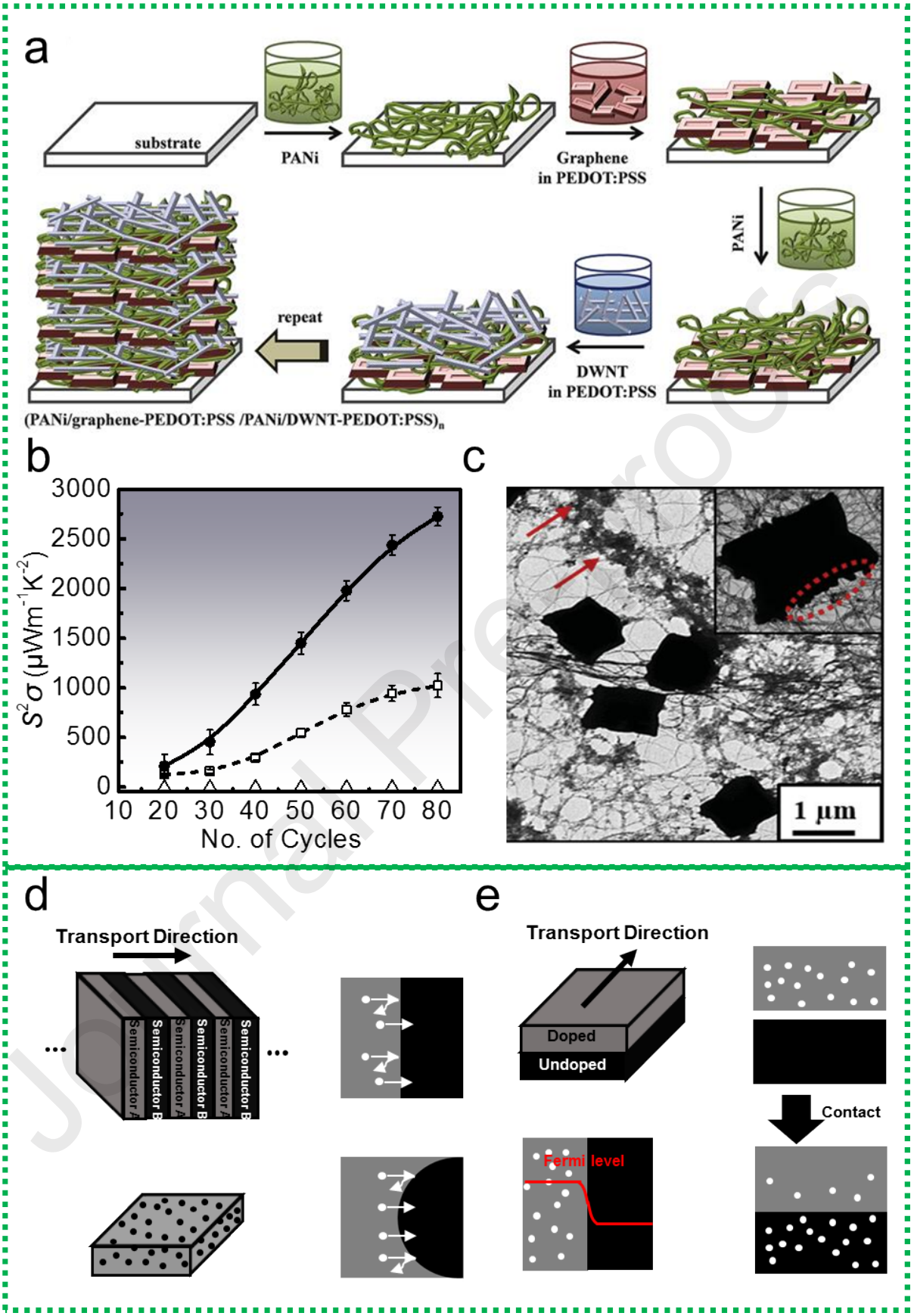
a
substrate
PANi
Graphene
in PEDOT:PSS
PANi
repeat
DWNT
in PEDOT:PSS
(PANi/graphene-PEDOT:PSS /PANi/DWNT-PEDOT:PSS)n
b
$S^2\sigma$ (μWm^{-1}K^{-2})
3000
2500
2000
1500
1000
500
0
10 20 30 40 50 60 70 80
No. of Cycles
c
1 μm
d
Transport Direction
Semiconductor A
Semiconductor B
e
Transport Direction
Doped
Undoped
Fermi level
Contact

Figure 26. a) Schematic of the layer-by-layer deposition process; b) $S^2\sigma$ of the PANI/graphene-PEDOT:PSS/PANI/DWNTPEDOT:PSS composite films as a function of number of cycles; c) SEM image of the PANI/graphene-PEDOT:PSS/PANI/DWNTPEDOT:PSS composite; a)-c) Reproduced with permission [164]. Copyright 2016, Wiley-VCH; d) Schematic comparison of the energy filtering mechanism and modulation doping mechanism; d) Reproduced with permission [186]. Copyright 2016, Royal Society of Chemistry.

4.3.2 Ionic thermoelectric copolymers

So far, most of the proposed energy-harvesting solutions are lack of the necessary mechanical properties, which makes them susceptible to damage by repetitive and continuous mechanical stresses, leading to serious degradation in device performance. Thereby, developing new energy materials that possess high deformability and self-healability is essential to realize self-powered devices [212]. Recently, an intrinsically self-healable and stretchable ionic TE hybrid material, composed of a conjugated polymer (polyaniline), a non-conjugated anionic polyelectrolyte (poly(2-acrylamido-2-methyl -1- propanesulfonic acid)), and phytic acid, was reported to exhibit an excellent *ZT* as well as remarkable stretchability (up to 750 %) and autonomous self-healability without any external stimuli [214]. **Figure 27a** shows the schematic illustration of the proton diffusion in a PANI:PAAMPSA:PA ternary hybrid film under a temperature difference. As an ionic TE copolymer, the ternary TE hybrid film has a built-in concentration gradient of ions upon a temperature gradient and can generate thermopower based on the Socret effect [349-351]. Unlike normal CPs, the primary mobile ionic species (the protons) diffuse from the hot end to the cold end through the sulfonic acid groups in the immobile polymer hybrid instead of the conjugated carbon chains. **Figure 27b-d** plot the thermovoltage and TE properties of the ternary TE hybrid films. As can be seen, *ZT* reaches 1.04 at a humidity of 90 %, which is an ultrahigh value for CP-based TE materials. Such a high *ZT* was attributed to the simultaneously increase of both *S* and σ with higher humidity. Also, the maximum stress of the ternary

hybrid film also showed similar humidity dependency, increasing from 100 % to 750 % when the humidity increases from 30 % to 80 %, as shown in **Figure 27g**. Such a humidity dependency of both electrical and mechanical properties is ascribed to the more dynamic electrostatic interaction between PANI and PAAMPSA and hydrogen bonding interaction in PANI/PA and PAAMPSA/PA with moisture adsorption. This ternary TE hybrid film shows remarkable durability in its self-healing process, as the original *S* and σ can be retained even after 30 cycles of self-healing. This emerge of the self-healable hybrid film paves the way for non-toxic, flexible, and wearable TE device with both excellent TE performance and mechanical stability and durability.

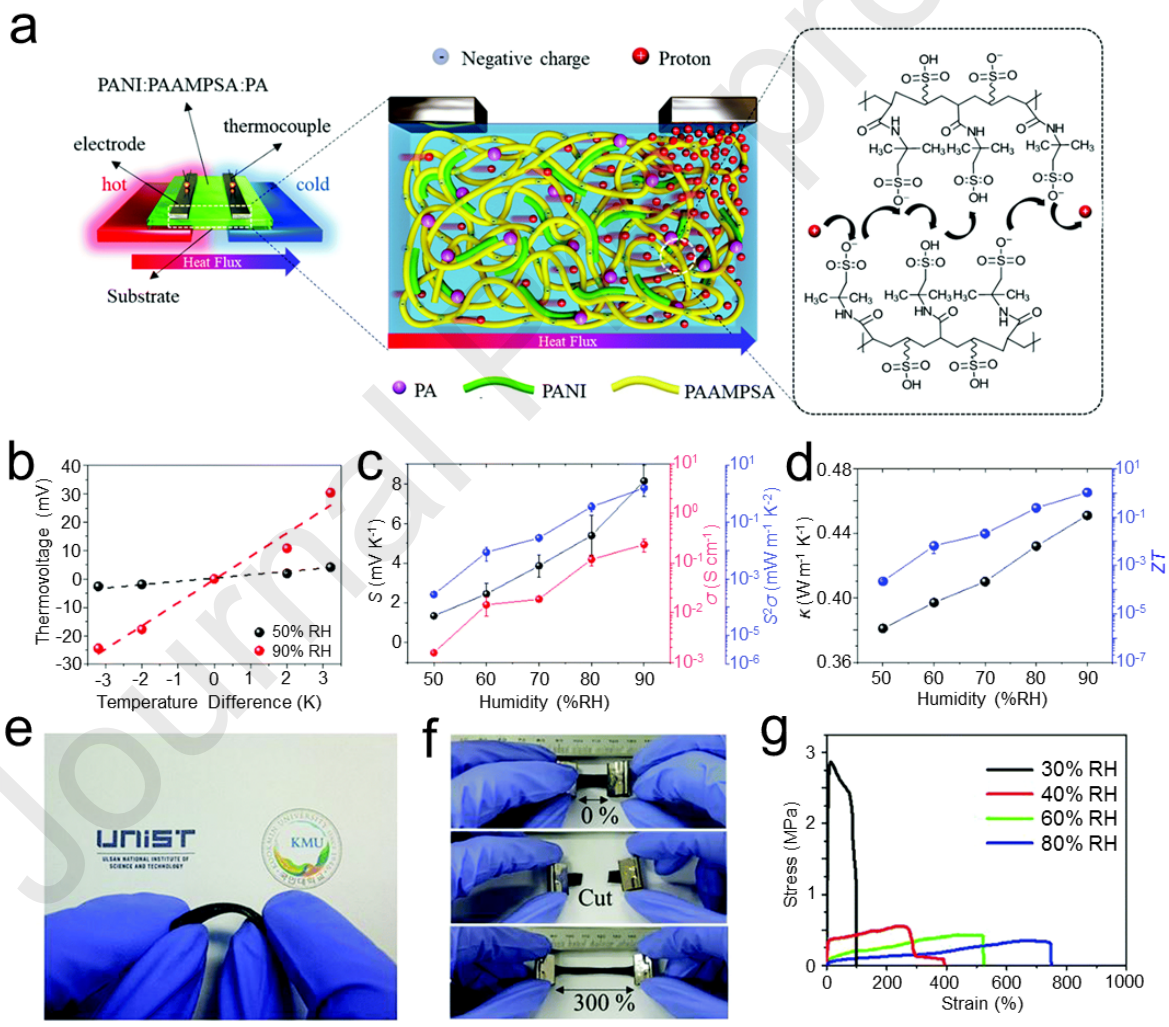

Figure 27. a) Schematic illustration of the proton diffusion in a PANI:PAAMPSA:PA ternary hybrid film under a temperature difference; b) Thermovoltage of the ternary TE hybrid films as a function of

ΔT, at RH 50 % and 90 %; c) S, σ and $S^2\sigma$ of the TE hybrid at different humidity levels; d) κ and ZT of the TE hybrid film at different humidity levels; e) Photograph of a free-standing ternary TE hybrid film; f) Photograph of a TE hybrid film during the self-healing and stretching test; g) Stress–strain curves of the TE hybrid films at various RH levels. Reproduce with permission [214]. Copyright 2020, Royal Society of Chemistry.

5. Flexible Thermoelectric Devices based on Conducting Polymers and their Derivatives

Compared with inorganic TE materials, CPs are not suitable in supplying large amounts of output power with high conversion efficiency due to their relatively low ZT and poor durability at high temperature. However, the flexibility and non-toxicity enable the CPs to be applied as wearable and implantable devices where traditional inorganic materials are constrained [352]. Therefore, the potential applications of CPs-based TE devices should be focused on energy supply for micro-watt portable electronics by harvesting low-grade energy, including human body heat and solar energy [353-356]. Unlike inorganic materials, most CPs can exist in the forms of aqueous solution or organic solvent solution, which can be applied to large-scale device fabrication by suitable techniques. Such easy-availability enables CPs to take the first step in industrialization and commercialization [20,357].

Typically, TEGs usually consist of certain pairs of p-type and n-type TE elements which are alternatively connected electrically in series and thermally in parallel [358]. A typical case is shown in **Figure 28a**. However, a p-p legs configuration composed of one type of TE material is also proposed due to the rareness and poor environmental stability of n-type polymer-based TE materials (**Figure 28b)** [13]. Many previous works have reported home-made FTE modules based on this configuration [155,201,359,360]. However, this configuration could incur heat loss because heat transfers from heat source to heat sink by thermal conduction from the metal wires, which causes degradation of the device performance.

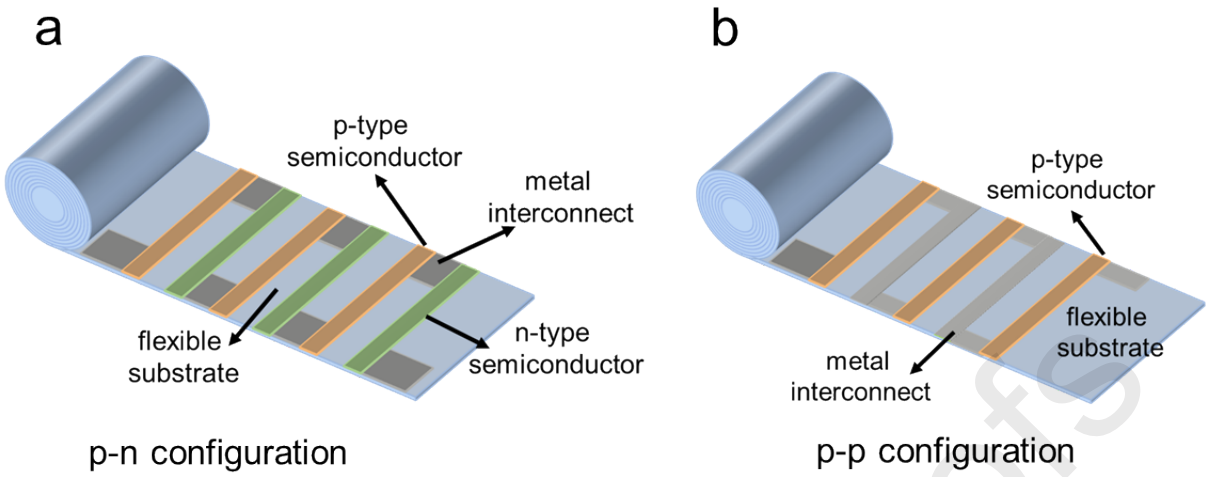

Figure 28. Schematic diagrams of two types of flexible TE device consisting of a) p-n legs and b) p-p legs. Reproduce with permission [361]. Copyright 2011, IOP Publishing.

Table 6 summarizes the design routes and performance of conductive-polymer-based FTE devices, including the p-type and n-type TE elements used, substrates, sizes, units (couples), output voltages, output powers, output power densities, and applied temperature defference ΔT [151,155,171,180,188,193,197,201,362-365]. It should be noticed that compared the conventional TE devices, the performance of FTEGs still need further improvement [366]. However, considering their wide application range due to their much lower dimensions or high-flexibility features, FTE devices are still essential members in the TE family with a fantastic speed of development [25,26,367-372].

Table 6. A summary of the design and performance of conductive-polymer-based flexible devices.

p-type Material	**n-type Material**	**Substrate**	**Size (cm/cm^2)**	**Unit**	**ΔT (K)**	**Output Voltage (mV)**	**Output Power (μW)**	**Output Power Density (μW cm^{-2})**	**Ref.**
PP-PEDOT (roll)	Bi_2Te_3	Polyimide	-	36	10	9~13	0.16	-	[362]
PEDOT:PSS	N-doped graphene	Plastic	8×10	-	10	3	~1.92	~0.024	[360]
PEDOT:PSS	-	Polyimide	-	14	12	2.9	-	~1	[201]

PEDOT:PSS	Te	Polyimide	-	8	13	2.5	-	-	[188]
Sb_2Te_3 + PEDOT:PSS	Bi_2Te_3 + PEDOT:PSS	Polyimide	-	7	50	85.2	-	1220	[193]
-	Bi_2Te_3-epoxy	Polyimide	-	62	20	109	25	-	[363]
PEDOT:PSS/ SWCNTs	PEI-doped SWCNTs	Polyimide	-	6	50	28	0.22	-	[180]
PEDOT:PSS	Ni	Kapton	-	144	65	260	46	-	[364]
PEDOT:PSS	-	Paper	-	14	50	12	16.8	-	[155]
PEDOT:PSS	-	PES	-	5	25	2	-	-	[151]
CNT-coated activated carbon textile	-	PET + Fabric + Wire	2×2	2	31	0.000 472	0.184	0.046	[365]
Au-doped CNT/PANI webs	PEI-doped CNT webs	PANI + CNT Web	-	7	20	~11	1.74	~0.4	[171]
PEDOT:PSS	constantan	silicone rubber	10×4	10	30	12	0.38	~0.1	[373]
$Sb_{37}Bi_2Te_{61}$	$Bi_{19}Te_{75}Se_6$	Polyimide	12×12	112	~13	1.41	26.3	18.63	[21]
PEDOT:PSS	-	wadmal	53×53		65	7.28	1.2	0.04	[374]
SWCNT/WPU/PVA	-	VHB tape		10	55	11	0.23		[375]
P3HT doped by $AuCl_3$	-	3 M flip film	7×130	10	10	4	1.9	0.0185	[376]
Polyurethane/ EMIM:DCA		PTFE			0.4	10		0.0002 4	[377]
PEDOT:PSS	PEDOT:PSS/$CuCl_2$	PET	2×6	10	4.5	1550	0.09	0.038	[227]
Bi_2Te_3/PDMS			60×40		8	24	233	9.7	[378]
Ag_2Se/PVP		Polyimide	20×5	6	36. 2	39.9	8.2	1.37	[379]
-	PVDF/Ta_4SiTe_4	Polyimide	0.5×1	4	35. 5	34	1.7	-	[197]

5.1 Criteria for Performance Optimization

Equation (2) is used to evaluate the maximum energy efficiency of a TE device under ideal conditions. In reality, the actual efficiency of a TE device is impacted by various factors including heat loss, electrical and thermal contact resistances, yielding a lower temperature difference between the hot end and the cold end than expected. As reported previously [380], the real efficiency could be 30 % ~

60 % lower than the calculated maximum efficiency using Equation (2). Therefore, one corrected equation is reported to evaluate the experimental efficiency of a TE system as [380]:

$$\eta = \frac{P}{P + Q_c} \tag{23}$$

where P is the output power of the system, and Q_c denotes the heat dissipated from the cold end of the system. Equation (23) excludes the energy loss from the lateral surfaces, giving an overestimated efficiency. Practically, for flexible/wearable TE devices, the efficiency is quite low as the quality of the exhausted heat we utilize is very poor. Instead, we tend to focus on their output power so as to meet the demands of the portable electronics. The output power density p_m is given as [381]:

$$p_m = \frac{P_m}{WL} = \frac{PFt\Delta T^2}{2\Delta x^2} \tag{24}$$

where P_m is the identical peak output power, t denotes the internal resistance of TE system, ΔT is the temperature difference of the TE system and Δx denotes the length of a TE element. This equation is valid when the external load equals the internal resistance of the TE device. Notably, for a flexible/wearable TE film, ΔT is directly determined by Δx and t of each TE element with a given κ. Quantitatively, according to Fourier's heat transfer equations [382], the temperature transition can be completed within a very small region; on the other hand, a longer element would also suffer from larger internal resistance, leading to a lower output power density. Therefore, to maximize the output power density, the film length should be as short as possible on the premise of guaranteeing the temperature gradient. **Figure 29a** and **29b** plot the one-dimensional simulated temperature distributions along the length for different t and several κ [381]. Clearly, with smaller t and κ, the temperature transition would complete in a narrower region, as the thermal conduction is proportional to the t and κ. By applying suitable Δx for PEDOT:PSS films with given t and κ, a high output power density of 3 μW·cm^{-2} was obtained. This work provides a way for insightful device design method to realize high-performance FTE devices.

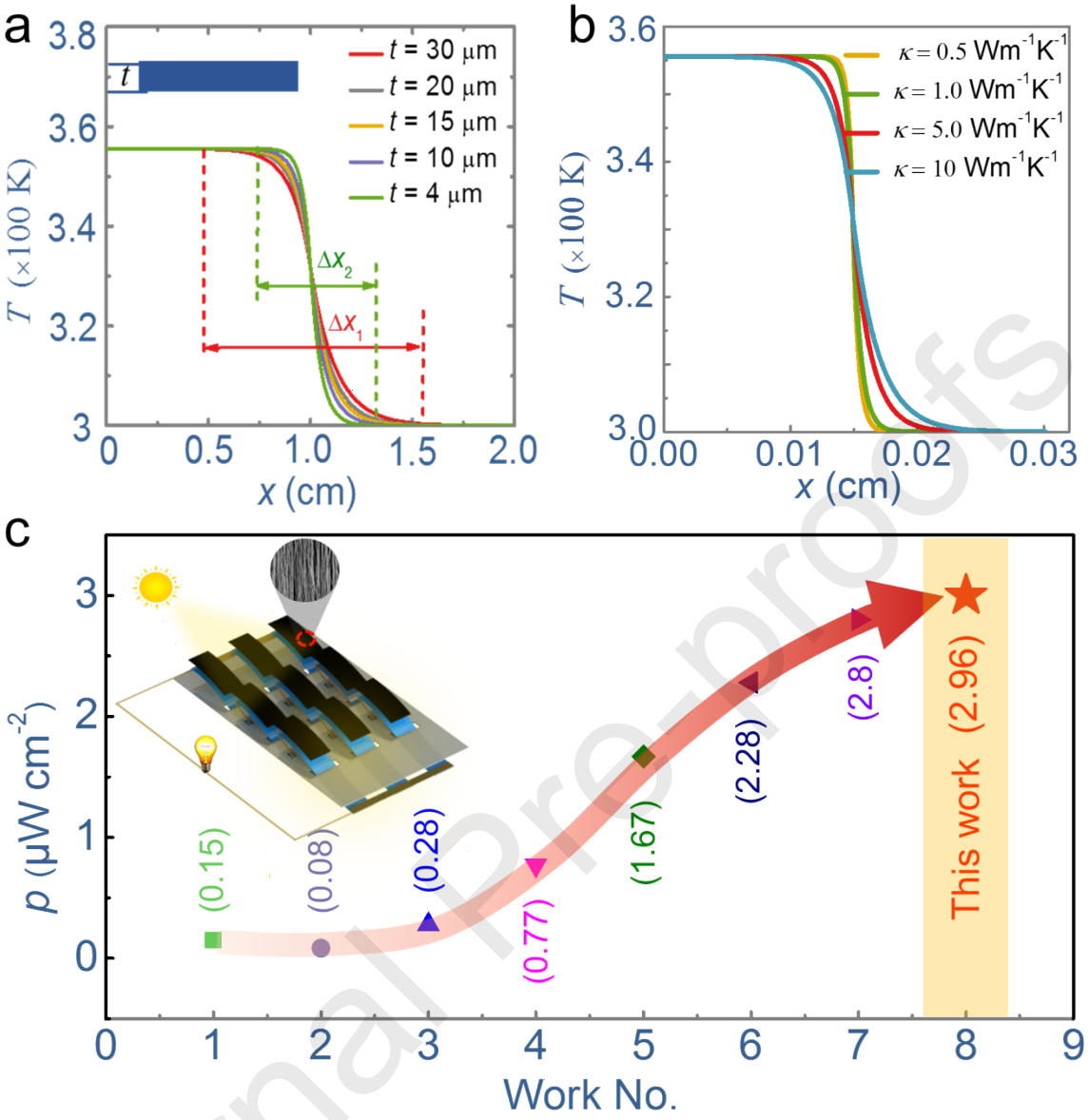

Figure 29. The one-dimensional simulated temperature distributions along the length for different a) film thickness (t) and b) film thermal conductivity (κ). c) The Output power densities of flexible TE devices in recent reported [52,129,195,381,383-386]. The inset shows the designed model of the actual module. Reproduce with permission [381]. Copyright 2020, Royal Society of Chemistry.

5.2 Fabrication Techniques

Generally, there are three effective fabrication techniques for FTE devices, such as the drop-casting technique [201], printing technique [387], and vacuum filtration technique [188]. The drop-cast

technique can fabricate free-standing films and requires further assembly processes to make a device, while the printing technique and vacuum filtration technique can directly fabricate devices.

5.2.1 Drop-casting

The drop-casting technique is successfully used to deposit highly uniform and good adhesion CPs-based FTE films and devices. Taking the fabrication of PEDOT:PSS-based flexible thin films as an example [201], drop-casting refers to "dropping" the PEDOT:PSS filtrate onto the substrates (such as silicon dioxide) that was precleaned with various techniques such as detergent, deionized water, acetone, isopropanol, and plasma cleaner. After being dried in an oven at 60 °C under vacuum or low-oxygen atmosphere, the solutions are "cast" into thin films. Due to the simplicity of the process and high cost-effectiveness, the drop-casting technique has been widely used to fabricate CPs-based FTE thin films.

Figure 30a shows a schematic diagram of the drop-casting technique for fabricating PEDOT:PSS-based FTE thin films and devices, by which free-standing polymer films can be obtained as the films can be automatically lifted up from the substrate during the H_2SO_4 post-treatment [201]. Further reduction treatment can optimize the TE performance of these films. The viability of applying post-treatments upon the free-standing CP films to improve their TE performances is one of the merits of the drop-casting technique. Instead of quartz substrates, filter papers can also be applied to the drop-casting technique [265]. After the drying process, the filter paper was coated with CPs which were dissolved in acetone to obtain free-standing CP films [265]. However, it should be noted that drop-casting is relatively time-consuming, which makes it be less efficient in device fabrication.

5.2.2 Screen-printing

The screen-printing (or stencil printing) technique [387] refers to using emulsion screens, mesh-mount, or frameless metal stencils to deposit inks and pastes, which contain CPs onto various substrates [388]. Owing to their extensive advantages, such as low capital cost, versatile pattern designs, simple operation, and little waste, a screen-printing technique is one of the most widely used methods in fabricating FTE electronics or devices [387]. Currently, the printed FTE thin films can achieve a

thickness of up to ~50 μm, which can satisfy the requirements for the application of FTE devices. Generally, the TE properties of screen-printed CPs-based FTE thin films are largely related to the conductive pastes/inks, which depend on solid loading, particle dispersion, viscosity and rheological behaviour, particle specific surface area, and density [389]. In this regard, an appropriate design for the inks or pastes is significant in order to achieve a high TE performance in a screen-printed TE device [389].

Figures 30b shows a schematic diagram of the screen-printing technique [155], from which the organic TE modules are screen-printed onto paper by using PEDOT:PSS and silver paste. Clearly, efficient device fabrication is the most prominent advantage of these printing techniques. For the screen-printing technique, the patterns of CPs can be well controlled by the metal mask. After the polymer arrays have been fabricated on each panel, a series of connections between every two panels are applied in order to achieve higher open-circuit voltage, which can illuminate light-emitting diodes [155]. The proof-of-concept module has shown high stability, which was tested at 100 ℃ for over 100 h without any encapsulation [155]. However, one issue is that device performance may be decreased due to the degradation of the interface between the CPs and silver paste. In this regard, the stability of the interface must be improved during the screen-printing process.

5.2.3 Roll-to-roll technique

Similar to the screen-printing technique, the roll-to-roll (R2R) technique has been applied to fabricate a super-compact TE device composed of serially connected PEDOT:PSS elements (such as 18000 units [387]). Since a large number of units may compromise the overall size of the device, violating the miniaturization, and providing potential obstacles for the integration of wearable TE electronics [20], the tape-like (or roll-up structured) FTE generators have been designed to overcome this challenge. These devices mainly employ highly-flexible polyimide or fibre substrates to minimize the occupied space and strengthen the flexibility.

Figures 30c shows the schematic diagram of the R2R printing technique [387]. Different from the traditional TE device design which employs complementary p- and n-type materials in order to avoid charge build up in the series connected system, the roll-to-roll printing technique employs only one-type CPs-based TE material for the series connection. When printing the top electrode of a junction, the bottom electrode is simultaneously connected with the adjacent bottom electrode, thus allowing for directional charge transport [387]. The startling TE efficiency of devices produced by this fabrication technique provides an insight into the potential bright future for the commercialization of CPs, although the power output of this R2R printing device was poor and this low performance was attributed to the limited development of PEDOT:PSS and the poor temperature gradient over the device. The latter factor is a consequence of the layer-by-layer assembly technique, which induces electrical potential in the perpendicular direction instead of the in-plane direction.

5.2.4 Ink-jet printing

The ink-jet printing technique involves a non-impact dot-matrix printing technology, in which the droplets of ink are directly jetted from a small aperture to a specified position on a substrate to create thin films [390]. Similar to the screen-printing technique, the key technologies of ink-jet printing are ink design, the printer systems, and substrate treatments. Among these, the design of ink-jet inks formulated for CPs-based materials is very important in the fabrication of filters for FTE materials and devices.

Figure 30d shows the schematic diagram of the ink-jet printing technique [52] for fabricating the thermocouple leg of PEDOT:Tos by spontaneous polymerization when the monomer PEDOT:Tos deposited with the oxidant ($Fe(Tos)_3$) since the PEDOT:Tos is not soluble. Compared with the other two printing techniques, the ink-jet printing technique is not so efficient. However, the ink-jet printing technique can enable further optimization of TE performance of the PEDOT:Tos by tuning the oxidation level [52].

5.2.5 Vacuum filtration

Vacuum filtration (or suction filtration) is an indispensable technique for distillation, extraction, and purification. This method requires a Büchner funnel, filter paper of smaller diameter than the funnel, Büchner flask, and rubber tubing to connect to the vacuum source. Vacuum filtration is commonly used to remove solid impurities from an organic solution or to isolate an organic solid, such as CPs-based solution into thin films. Compared with traditional, gravity-assisted filtration, adding a vacuum to the system can greatly increase both the speed and efficiency of filtration. Currently, the vacuum Filtration technique is one of the most preferred routes employed for quickly drying out a small batch of solutions.

Figure 30e shows a schematic diagram of the vacuum filtration technique [188]. Driven by the pressure difference, CPs can be firmly attached to the filter membrane. Notably, in the case of PEDOT:PSS, the vacuum filtration technique is helpful in the removal of small non-ionized particles such as PSS, leaving the long conjugated chains coated upon the membrane and showing enhanced TE performance [319]. The fabricated films can be subsequently cut into slices to assemble into FTE devices after being dried out. Compared with physical mixing, the vacuum filtration technique should be a better alternative to fabricate hybrid inorganic-organic TE devices, because the fillers are able to be evenly dispersed within the polymers.

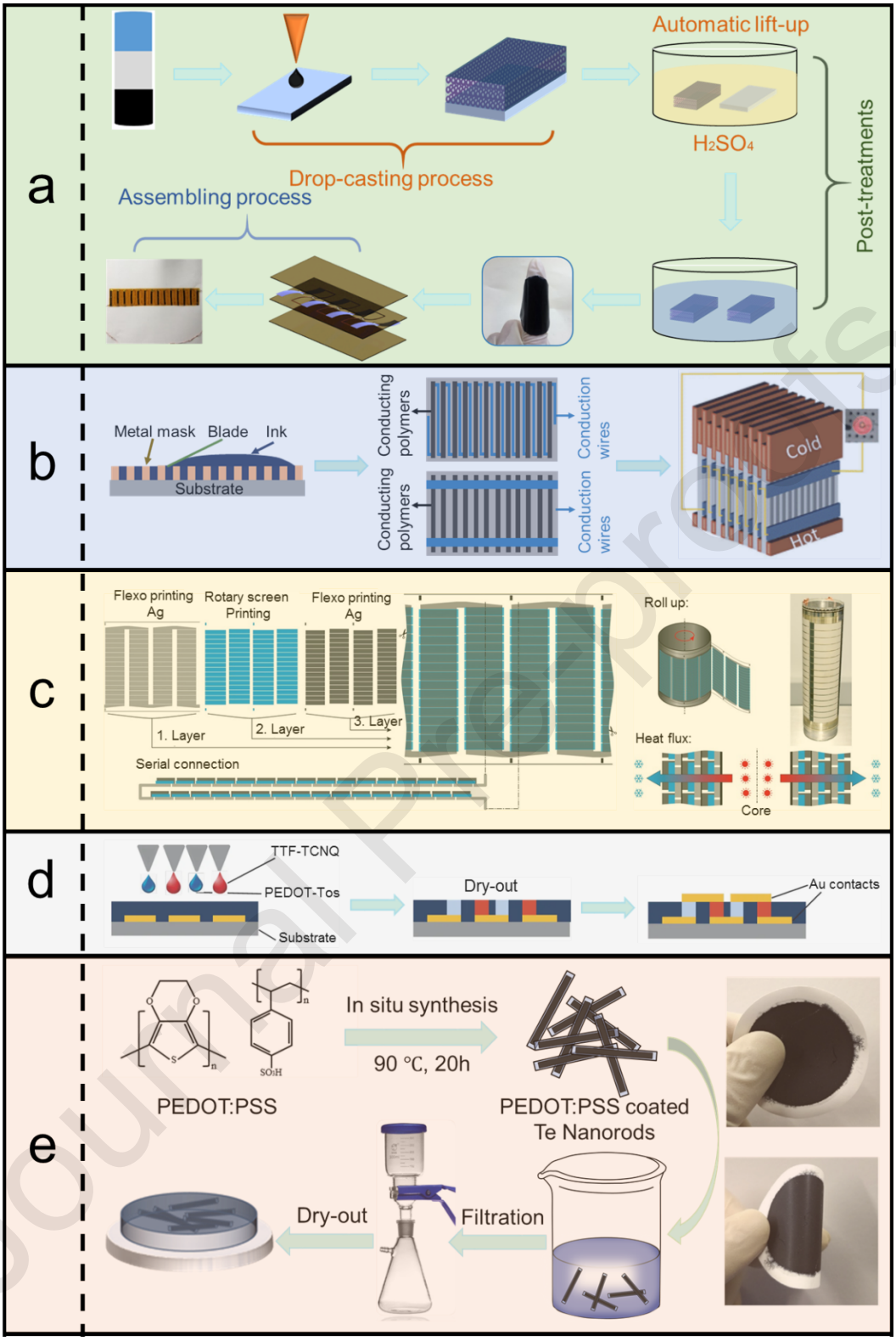

Figure 30. Schematic diagrams for a) drop-cast technique; b) screen-printing technique; Reproduced with permission [155]. Copyright 2014, Royal Society of Chemistry; c) roll-to-roll printing technique; Reproduced under the terms of the Creative Commons CC BY license [387]. Copyright 2013, Wiley-

VCH; d) ink-jet printing technique. Reproduced with permission [52]. Copyright 2011, Springer Nature; e) vacuum filtration technique. Reproduced with permission [188]. Copyright 2017, Elsevier.

5.2.6 3D printing

As one of the advanced manufacturing techniques, three-dimensional (3D) printing offers capabilities to fabricate microscale structures for CPs in a programmable, facile, and flexible manner with a freedom of design in 3D space [391,392]. More importantly, this technique supports very fast and streamlined fabrications of various CP devices, which provides a promising strategy for cost-effective, large scale manufacturing of CPs.

Figure 31a shows the schematic diagram of 3D printing process for PEDOT:PSS multi-layered structures [393]. Clearly, the process is very simple and automatic, in which PEDOT:PSS ink with favoured rheological properties can be converted into 3D printable CP ink by lyophilisation in cryogenic condition and re-dispersion with a solvent and enable the fabrication of multi-layered micro-structures as well as overhanging features. The key point in such a process is that the formation of entanglements among highly concentrated PEDOT:PSS nanofibrils can support hydrogel forms without loss of the original microscale structures and with long-term stability in physiological wet environments.

5.2.7 Moulding and Lithography

Despite the 3D printing technique exhibits great potential in large-scale manufacturing, the resolutions of the printed devices (dozens of microns) cannot meet the demand of some ultrafine electronics consisting of nanoscale patterns. Instead, moulding and lithography would be a better alternative in fabricating nanoscale structures [96,394-397]. **Figure 31b** shows the schematic fabrication process of PEDOT nano arrays by liquid-bridge-mediated transfer moulding [96]. This technique takes the advantages of the interfacial free energy between the mould and the oxidation agent ($FeCl_3$) solution when filling the recessed areas of the patterned mould with the solution, and between the substrate and the solidified PEDOT when loading the product onto the substrate. On the one hand,

the surface free energy oxidative solution is much higher than that of the mould, guaranteeing no residues will be left on the raised surfaces of the mould; on the other hand, the surface free energy of the substrate is quite closed to the that of the solidified PEDOT, resulting in a strong attractive capillary force to provide good conformal contact between them. After drying, the separation of the mould would load the PEDOT arrays onto the substrate.

Beside moulding, lithographical technique is also a sort of mature technique for high-resolution fabrication of CPs. The ultraviolet lithography (UVL) and electron beam lithography (EBL) will be introduced here. **Figure 31c** shows the schematic fabrication process of CP by UVL [396]. Generally, the blended solution of monomer, oxidant and photoresist is spin-coated on a substrate, followed by development by immersion in aqueous developer after UV exposure and the post-exposure bake processes. Upon UV exposure, the cross-linking reaction would happen and make the photoresist insoluble whereas the unexposed areas are dissolved away, leaving a designed pattern on the substrate. Further annealing (post bake) process would boost the polymerization of the monomers and produce the targeting CP patterns. Unlike the UVL, the EBL technique gets rid of the pre-prepared mask and fabricates designed patterns on the photoresist directly. **Figure 31d** shows the schematic fabrication process of EBL [397]. Following the development of designed patterns, CPs would fill in the patterns via chemical polymerization, which results in designed CP patterns after a lift off process. Compared with other manufacturing techniques, EBL supports the fabrications of very complicated patterns; however, the economy and time costs inhibit its extensive applications.

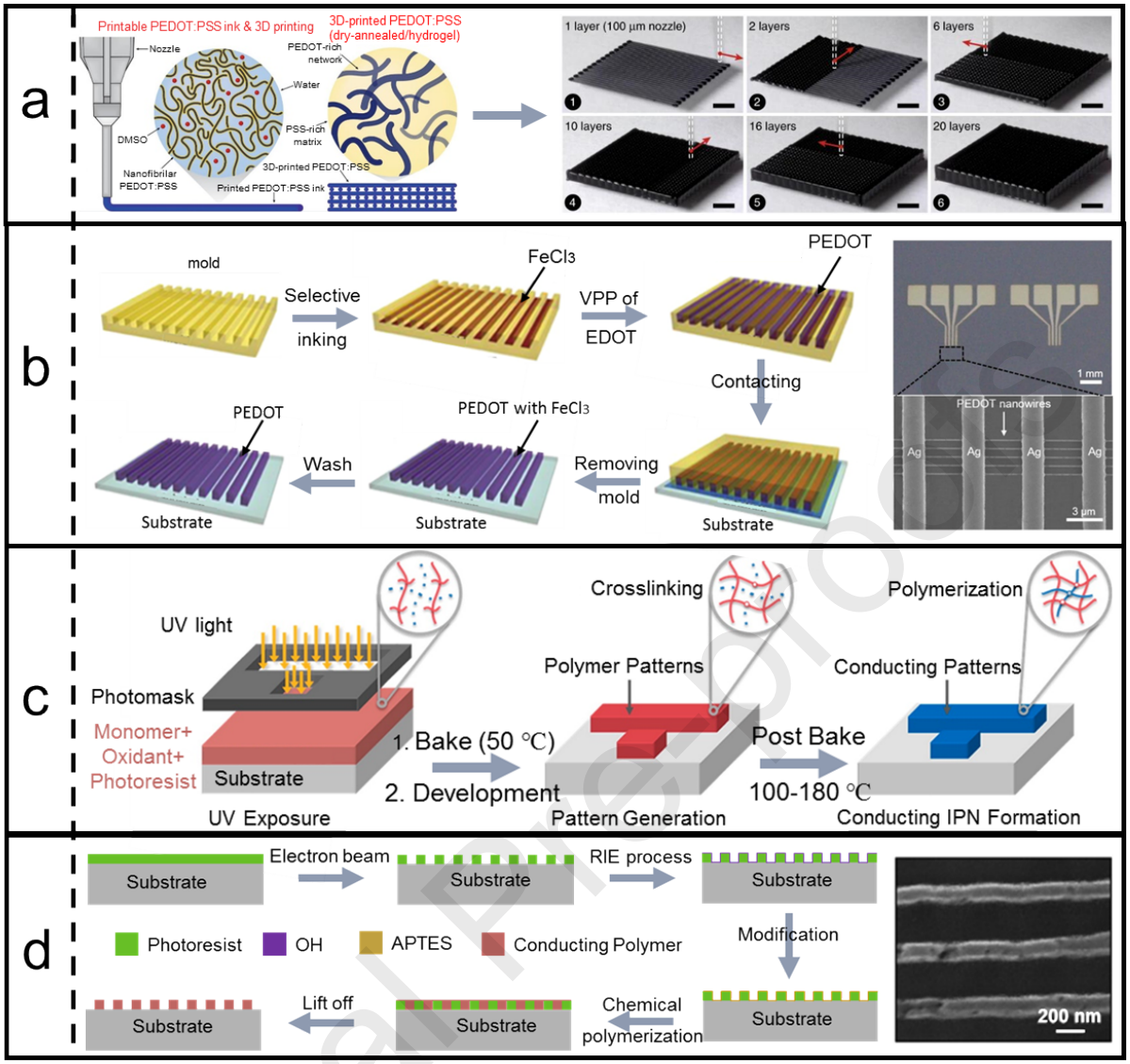

Figure 31. Schematic diagrams for a) 3-dimensional printing. Reproduced under a Creative Commons Attribution 4.0 International License [393]. Copyright 2020, Springer Nature; b) liquid-bridge-mediated transfer moulding; Reproduced with permission [394]. Copyright 2010, Springer Nature; c) UV lithography. Reproduced with permission [396]. Copyright 2013, American Chemical Society; d) Electron Beam lithography. Reproduced with permission [397]. Copyright 2019, Elsevier.

5.3 Significant Progresses

FTE devices usually possess certain flexibility in their shape without damaging their structure, making them good candidates for applications in wearable electronics for power generation and

refrigeration. In this regard, excepting the high performance and high stability, high flexibility should be considered in the design of FTE device. Noticeably, due to the huge potential for commercial and personal uses of FTE device, many advanced design routes have been developed in recent years. The well-developed fabrication techniques enable convenient study and optimization for the CP-based FTE devices, and significant progresses have been made.

5.3.1 Organic elements

The terms organic-based FTE devices refers to devices in which both the TE elements (legs) and substrates are made from organic materials with high flexibility. Because there is no inorganic material added into the device except the electrodes and wires, organic devices are usually continuous and can be bent many times without internal cracking; thus, they have attracted significant attention.

Generally, organic molecules such as PEDOT:PSS [201,398], polypyrrole [399], polythiophene [51,400,401], and PANI [112,120] usually have good flexibility and competitive TE performance, although this performance still needs further improvement due to their low pristine *S*. To achieve this goal, many designs based on novel treatments on these organic TE materials have been performed. To illustrate this, **Figure 32a** shows atomic force microscopy (AFM) images of PEDOT:PSS thin films after different post-treatments [201], namely formamide (CH_3NO), concentrated sulphuric acid (H_2SO_4), and sodium borohydride in sequence, respectively, from which the morphology of the films have been significantly changed after different treatments. **Figure 32b** shows X-ray photoelectron spectroscopy (XPS) results for PEDOT:PSS films with different post-treatments [201], the inset shows the cross-sectional SEM image of the as-designed PEDOT:PSS thin film [201]. The binding energies of sulphur atoms of PEDOT and PSS are respectively below and above ~165.5 eV. It can be seen that CH_3NO treatment leads to a decrease in the mass ratio between PSS and PEDOT, and post-treatment with H_2SO_4 further reducing the mass ratio of PSS and PEDOT. After the $NaBH_4$ treatment, the mass ratio is generally kept stable while a little shift in the Sp^2 binding energy of PEDOT has been detected. These

results indicate that rational treatments can tune the ratios and structures of organic components, leading to potential high TE performance.

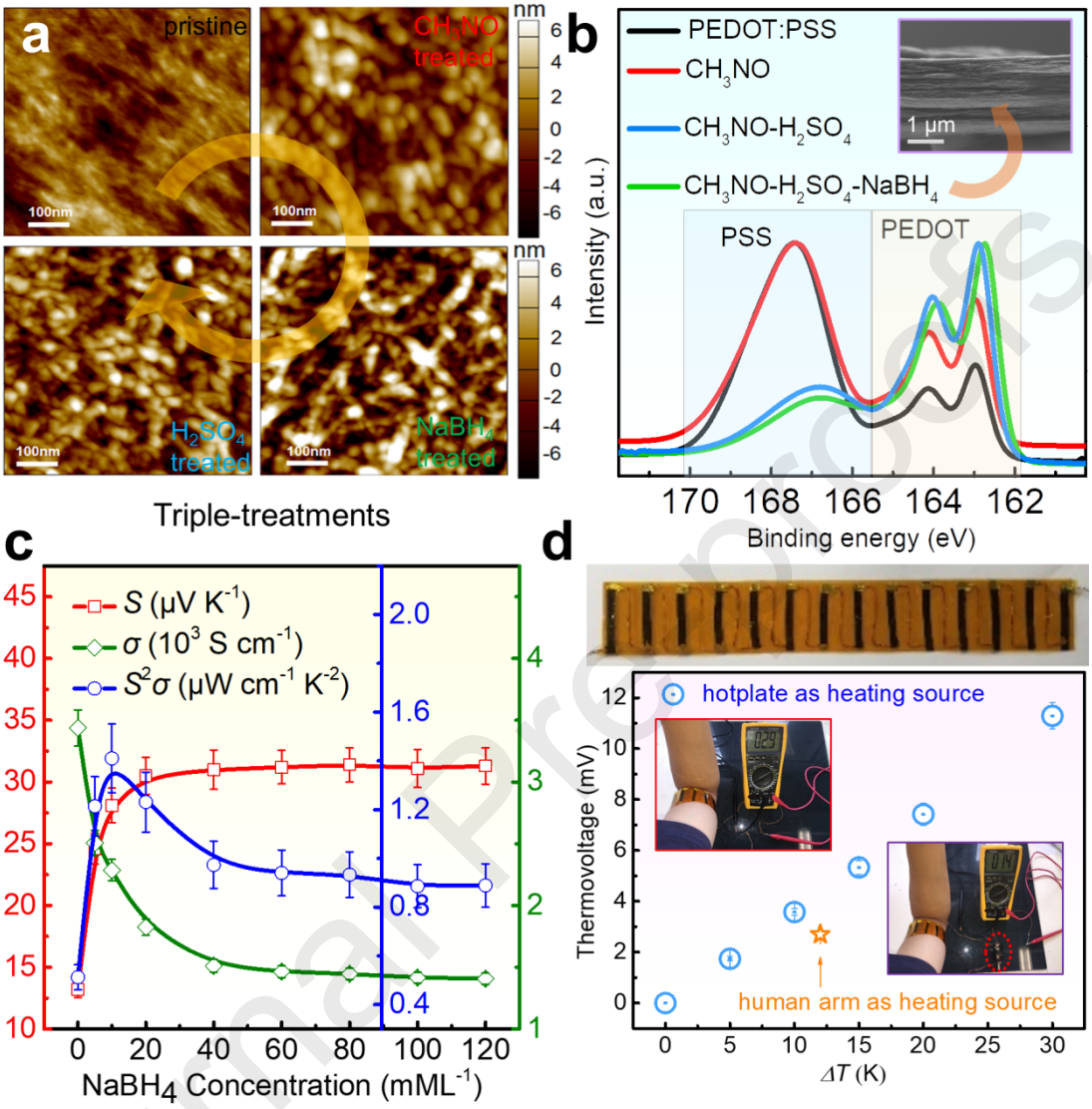

Figure 32. a) AFM images and b) XPS results for PEDOT:PSS films with different treating conditions, the inset in b) shows the cross-sectional SEM image of the as-designed PEDOT:PSS thin film; c) measured σ, S, and $S^2\sigma$ of the thin film as a function of $NaBH_4$ concentration; d) optical image of the as-designed flexible TE device (top) and the output voltage (bottom) under different ΔT by both hotplate and human arm as heating sources shown as inset. Reproduced with permission [201]. Copyright 2019, American Chemical Society.

Figure 32c shows measured σ, S, and $S^2\sigma$ of the as-designed PEDOT:PSS-based thin film as a function of $NaBH_4$ concentration [201], from which a high $S^2\sigma$ of ~1.41 $\mu W \cdot cm^{-1} \cdot K^{-2}$ can be achieved at 300 K with 10 m ML^{-1} $NaBH_4$ treatment, derived from a couple of S (~28.1 $\mu V \cdot K^{-1}$) and σ (1786 $S \cdot cm^{-1}$). Such high $S^2\sigma$ is very competitive for some inorganic TE materials, indicating that the structural changes by the triple post-treatments can effectively improve the TE performance of organic materials. **Figure 32d** shows a FTE device based on PEDOT:PSS after post-treatments as TE legs and flexible polyimide substrate. The legs were connected by Cu wires. The measured thermo-voltages using both the human arm and the heating plate as heating sources were provided in **Figure 32d**, from which a promising thermo-voltage of ~11.5 mV can be achieved at ΔT = 30 K, indicating great potentials for applying to wearable electronic devices for power generation.

5.3.2 Organic/inorganic composite elements

Although organic TE materials and devices possess high flexibility and promising properties, the improvement of their TE performance is historically tricky due to the difficulties of tuning the electrical and thermal transport performance derived from the limited means, and there are much fewer computational works such as band structure and phonon dispersion calculations to guide the design of organic TE materials. To tackle these issues, organic-inorganic composite (or hybrid) materials are developed. The flexible TE devices based on such composite materials can achieve a much higher TE performance, despite the fact that the flexibility of these devices may be limited. In this regard, to design a hybrid-based TE device with both high performance and desirable flexibility is of significance and has gained considerable attention in recent years.

To date, many state-of-the-art organic/inorganic composite elements are designed with high TE performance, high flexibility, and high stability. Carbon-based inorganic fillers and high-performance CPs are commonly used to compose organic/inorganic composite elements with both high performance and high flexibility, such as CNTs/CPs-based composite elements (including CNTs/PANI [164-171,202,402,403], CNTs/PEDOT [404], CNTs/PEDOT:PSS [177,180-182,204,405,406],

CNTs/PDMS [407], CNTs/P3HT [174,175,408], CNTs/PPy [161,406], and CNTs/PS [199]), graphene/PANI [43,162-165], rGO/PEDOT:PSS [178,179,200], and C_{60}/PEDOT:PSS [178]. In addition to carbon/CPs, simple-element/CPs are also attempted, such as Te/PEDOT:PSS [179,187-192,409-411], Te/PEDOT:DBSA [64], Te/PANI [172], Si/PEDOT:PSS [186], and B/PEDOT:PSS [412]. In terms of the compound/CPs-based composite elements which are the most commonly used in FTEGs, many unique composites with both high performance and high flexibility have exhibited significant potentials, such as VA-VIA/CPs (including Bi_2Te_3/PEDOT:PSS [48,193,222,413-415], Bi_2Te_3/PANI [173], Bi_2Te_3/P3HT [176], Sb_2Te_3/PEDOT:PSS [193], and $Bi_{0.5}Sb_{1.5}Te_3$/PEDOT:PSS [416]), tin chalcogenide/CPs (including SnS/PEDOT:PSS [417], SnSe/PEDOT:PSS [51,205,301], $SnS_{1-x}Se_x$/PANI [203], and $SnSe_{1-x}Te_x$/PEDOT:PSS [183-185,418]), copper chalcogenide/CPs (including Cu_2Se/PEDOT:PSS [223] and Cu_2Se/PVDF [419]), MoS_2/CPs [194,420], and complex compound/CPs including Ta_4SiTe_4 whiskers/PVDF [197] and MXene/PEDOT:PSS [421].

To illustrate the designs of novel organic/inorganic composite TE elements employed to the flexible TE devices, **Figure 33a** shows structural model of TiS_2 single crystal and the $TiS_2[(HA)_{0.08}(H_2O)_{0.22}(DMSO)_{0.03}]$ hybrid superlattice [196], from which the $CH_3(CH_2)_5NH_3^+$ were filled into the TiS_2 layers. **Figure 33b** shows high and low magnification (inset) STEM-HAADF images of $TiS_2[(HA)_{0.08}(H_2O)_{0.22}(DMSO)_{0.03}]$ [196], indicating a waved structure and information on the orientation of the hexylammonium ions with long alkyl chains. **Figure 33c** shows *T*-dependent *ZT* of TiS_2 single crystal and the $TiS_2[(HA)_{0.08}(H_2O)_{0.22}(DMSO)_{0.03}]$ hybrid superlattice [196], from which a competitive *ZT* of ~0.28 at ~375 K can be achieved, derived from the low κ of ~0.55 $W \cdot m^{-1} \cdot K^{-1}$ at this temperature. The *ZT* of $TiS_2[(HA)_{0.08}(H_2O)_{0.22}(DMSO)_{0.03}]$ hybrid superlattice was much larger than that of TiS_2 single crystals (~0.075). **Figure 33d** shows SEM images of Cu intercalated Bi_2Se_3 nanoplates/ PVDF TE film, the insets show top view and side view of the film [302], respectively. **Figure 33e** shows TE properties σ, *S*, and $S^2\sigma$ as a function of the Cu content for the film [302], from which a high $S^2\sigma$ of ~1 $\mu W \cdot cm^{-1} \cdot K^{-2}$ can be achieved *via* coupling σ and *S* by tuning Cu content. **Figure**

33f shows fingertip touch response of the as-fabricated film [302], indicating that the TE films can continuously convert the body heat into electricity. **Figure 33g** shows TEM images of MoS_2 nanosheets exfoliated in N,N-dimethylformamide (DMF) solution [194], the HRTEM and AFM images with section line are provided as insets, indicating typical nanostructures. **Figure 33h** shows cross-section SEM with inset of optical image of PEDOT:PSS/MoS_2 thin film [194], indicating an average thickness of <1 μm for the film. **Figure 33i** shows TE properties σ, S, and $S^2\sigma$ as a function of the MoS_2 content for the film [194], from which a competitive $S^2\sigma$ of ~0.45 $\mu W \cdot cm^{-1} \cdot K^{-2}$ can be achieved *via* coupling σ and S by tuning MoS_2 content. These results indicate that there is great potential for employing these flexible organic/inorganic composite thin films to flexible TE applications such as wearable devices for the human body [422].

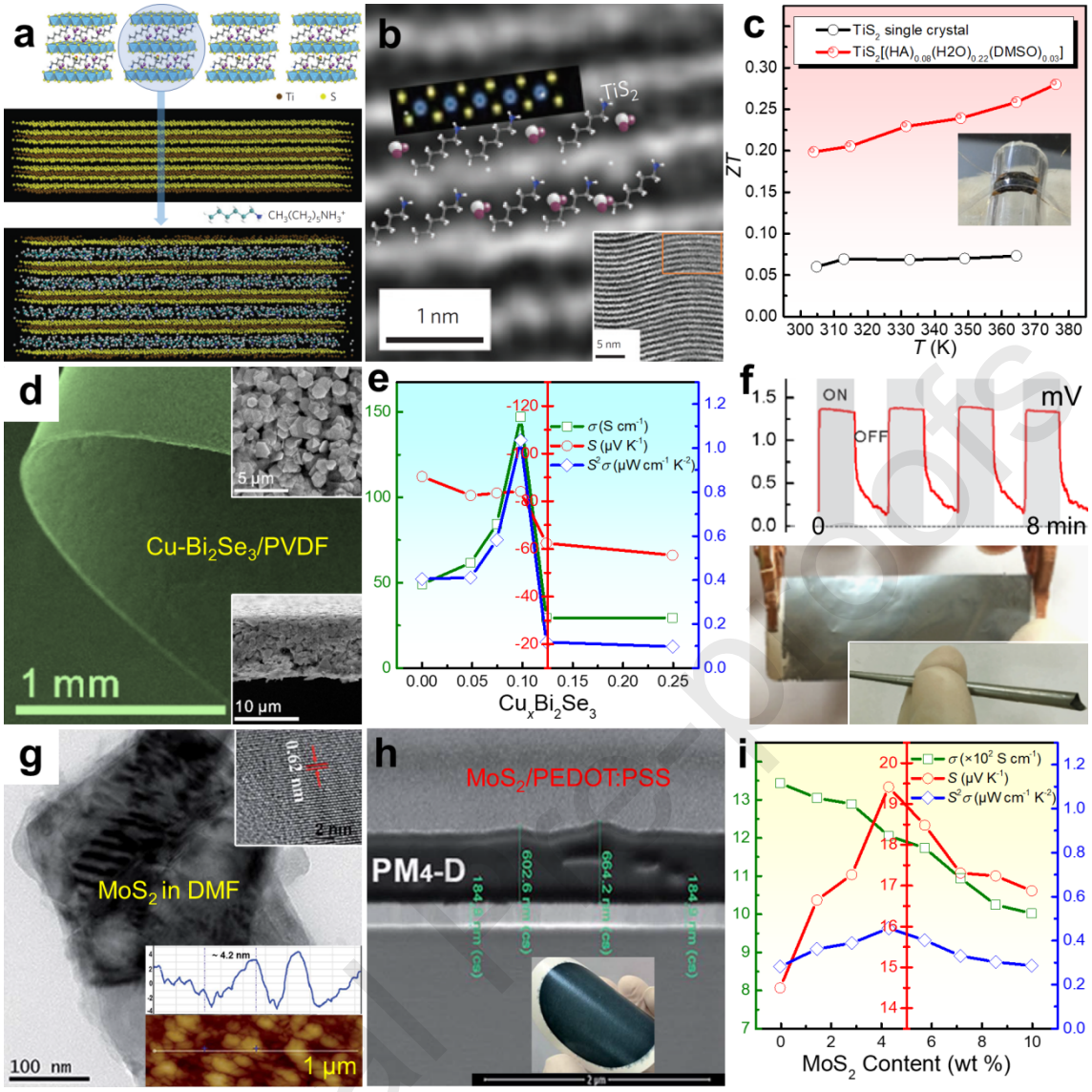

Figure 33. Characterizations of flexible TE composite films. a) Structural model of TiS_2 single crystal and the $TiS_2[(HA)_{0.08}(H_2O)_{0.22}(DMSO)_{0.03}]$ hybrid superlattice; b) high and low magnification (inset) STEM-HAADF images of $TiS_2[(HA)_{0.08}(H_2O)_{0.22}(DMSO)_{0.03}]$; c) *T*-dependent *ZT* of TiS_2 single crystal and the $TiS_2[(HA)_{0.08}(H_2O)_{0.22}(DMSO)_{0.03}]$ hybrid superlattice. Reproduced with permission [196]. Copyright 2015, Springer Nature. d) SEM image of Cu intercalated Bi_2Se_3 nanoplates/PVDF TE film, the insets show top view and side view of the film; e) TE properties σ, *S*, and $S^2\sigma$ as a function of the Cu content for the film; f) fingertip touch response of the film. Reproduced with permission [302]. Copyright 2015, Elsevier. g) TEM images of MoS_2 nanosheets exfoliated in DMF, the HRTEM and AFM images with section line are provided as insets; h) cross-section SEM with inset of optical image

of PEDOT:PSS/MoS_2 thin film; and i) TE properties σ, S, and $S^2\sigma$ as a function of the MoS_2 content for the film. Reproduced with permission [194]. Copyright 2016, Royal Society of Chemistry.

5.3.3 Wearable devices

The design of novel TE elements is of significance because they are key components in flexible TE devices, and these devices possess considerable potential for application to human life, acting as wearable devices or electronics [21,378,379,423-430]. To meet the wearable requirements, the as-designed TE devices should possess both high flexibility and high TE performance, as well as a certain degree of conformability [21,374,428,431-436]. Currently, the design and fabrication of wearable TE devices is in its infancy, and many efforts are necessary to further improve the performance of these wearable TE devices [437-442].

There are two types of wearable TE devices, namely film-base and fabric-base TE devices [75,443-445]. The former one usually consists of two dimensional polymer films [193,201], while the latter one is more of fabric materials knitted by polymer threads or coated by polymers [353,437,446-448]. To illustrate the fabrication process of film-base wearable TE devices, **Figure 34a** illustrates the PEDOT:PSS infiltration into the screen-printed TE thick film [193]. A 40 mm-thick TE film was firstly screen-printed on a highly flexible polyimide (PI) film substrate and annealed at 450 ℃ in a N_2 ambient. The sample was then coated by PEDOT:PSS solution with 5 vol% DMSO additive and held for 10 min. After that, excess PEDOT:PSS solution was removed by a spinning process at 1500 rpm for 30 s. Finally, the sample was dried at 200 ℃ for 1 h. **Figure 34b** shows both top and side views using SEM images for n-type Bi_2Te_3/PEDOT:PSS hybrid TE films [193]. The fine Bi_2Te_3 powders acted as "fillers" in the films, fabricated by a ball-milling route, and the PEDOT:PSS acted as "substrates" to carry these fillers with good distribution in the as-synthesized hybrid films. The deposition of such a hybrid film was based on a screen-printing technique, followed by drying and annealing on a flexible polyimide substrate. The as-fabricated Bi_2Te_3/PEDOT:PSS hybrid films acted as n-type legs in the following

device design. At the same time, p-type Sb_2Te_3/PEDOT:PSS hybrid TE films were fabricated with similar routes, acted as p-type legs.

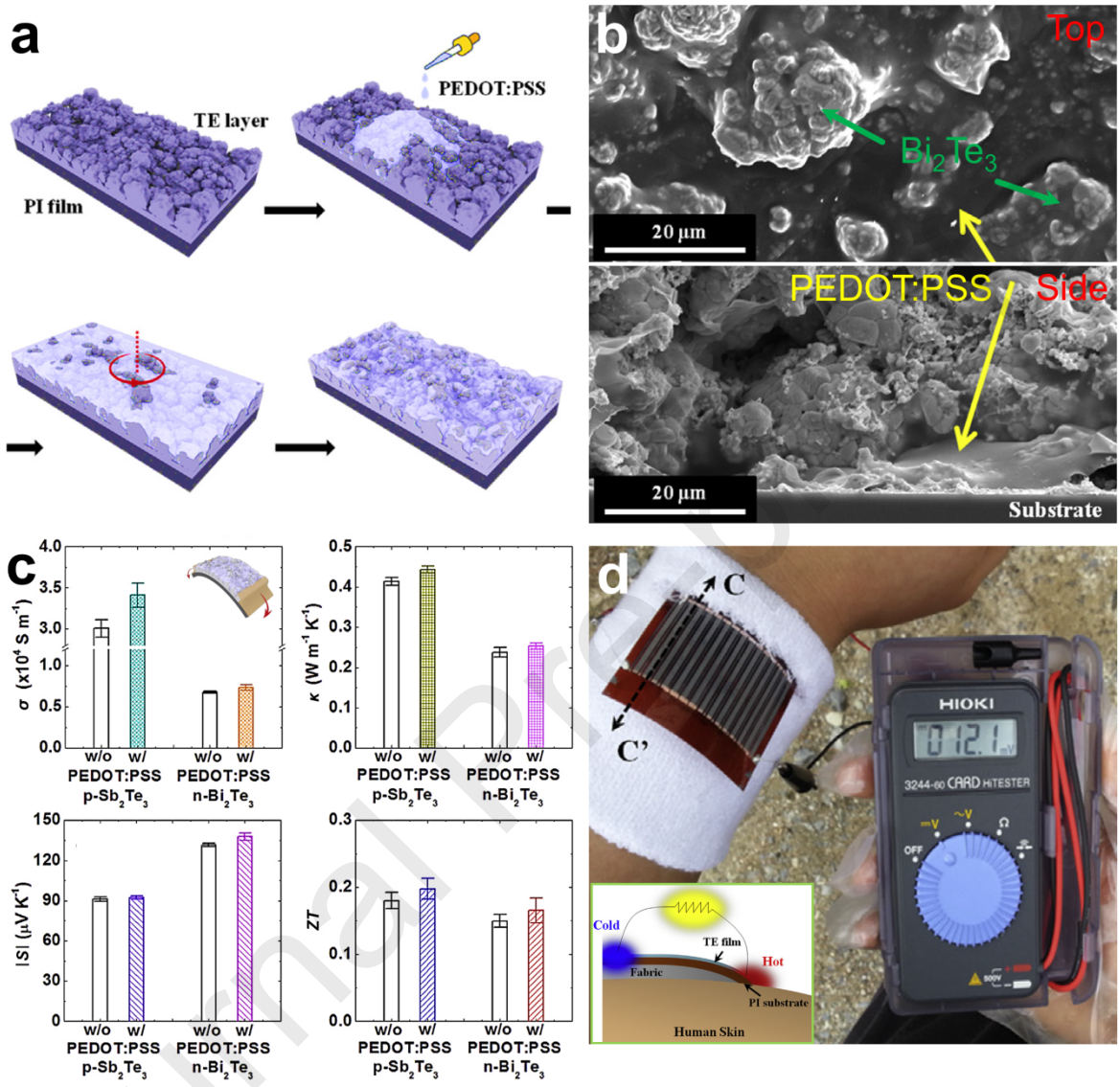

Figure 34. Flexible TE generator design. a) Process flow of PEDOT:PSS infiltration into the screen-printed TE thick film; b) top and side views of SEM images for Bi_2Te_3/PEDOT:PSS hybrid films; c) measured σ, S, κ, and ZT of the films before and after PEDOT:PSS infiltration process; and d) performance of a flexible module with 15 *p-n* couples using the temperature difference between the body temperature and the ambient air temperature as illustrated inset. Reproduced with permission [193]. Copyright 2014, Elsevier.

Figure 34c compares measured σ, S, κ, and ZT of the films before and after the PEDOT:PSS infiltration process [193], from which higher σ and ZT can be achieved after inducing PEDOT:PSS in the films for both n-type Bi_2Te_3 and p-type Sb_2Te_3 despite the κ were also slightly increased, indicating that PEDOT:PSS can be beneficial for achieving high TE performance in the hybrid films. **Figure 34d** shows the performance of a flexible module with 15 *p-n* couples using the temperature difference between the body temperature and the ambient air temperature as illustrated inset [193]. A high thermo-voltage of ~85 mV and a high output power density of 1.2 $mW \cdot cm^{-2}$ can be achieved at ΔT = 50 K, indicating a high device performance. Meanwhile, an excellent bending fatigue strength was confirmed, mainly derived from the flexible polyimide substrate and the flexible organic-inorganic legs, from which the organic elements provided the flexibility, indicating that organic-inorganic hybrid TE materials and devices are promising approaches for fabrication of wearable electronic devices.

Unlike the film-based wearable TE devices, the fabric-based wearable TE devices are either knitted by polymer fibres or made of silk yarns coated by polymers and their derivatives. The polymer fibres can be produced by a wet-spinning process [437]. **Figure 35a** illustrates the wet-spinning process of PEDOT:PSS fibre [437]. The aqueous polymer solution is extruded into H_2SO_4 coagulation bath through a blunt needle with specific nozzle diameter to quantitatively control the size of the fibre. The following washing process in ethanol/water mixture aims to remove H_2SO_4 from the obtained fibre, which would be collected after drying. **Figure 35b** and **35c** shows the schematic diagram and digital image of the fabric-based TE device made of polymer fibre [447]. Although it is p-p configuration, the heat loss via the silver yarn from hot end to the cold end can be neglected due to the small temperature difference. **Figure 35d** plots the TE properties of the fabricated PEDOT:PSS fibre. Clearly, $S^2\sigma$ increases from 2 $\mu W \cdot m^{-1} \cdot K^{-2}$ with higher H_2SO_4 concentration, achieving 30 $\mu W \cdot m^{-1} \cdot K^{-2}$ at 98 % H_2SO_4 concentration [447]. Such an enhancement mainly results from the dramatic improvement of σ from 100 to over 800 $S \cdot cm^{-1}$, while S is basically unchanged. Moreover, $S^2\sigma$ of the PEDOT:PSS fibre might be further improved by adding a reducing process to the obtained PEDOT:PSS fibre. With respect to

the device performance, an output power of ~2.8 nW can be obtained at a temperature gradient of 40 ℃. Such a small output power stems from the insufficient number of connected elements. Thereby, effectively achieving electrical connection in series and thermal connection in parallel for the conducting fibre in a large scale would be of significance for the future development.

Compared with the PEDOT:PSS fibre, it seems that coating CPs onto silk yarns is better as it shows higher output power. **Figure 35g** plots the device performance of the conducting silk yarns. Clearly, a relatively high output power of around 25 nW was achieved a temperature gradient of 46 K [446]. Interestingly, this conducting silk yarns can also serve as satisfactory heating fabric when applying suitable voltage, as presented in **Figure 35h**, indicating that the fabric-based TE devices would be a good wearable personalized thermal regulator [446].

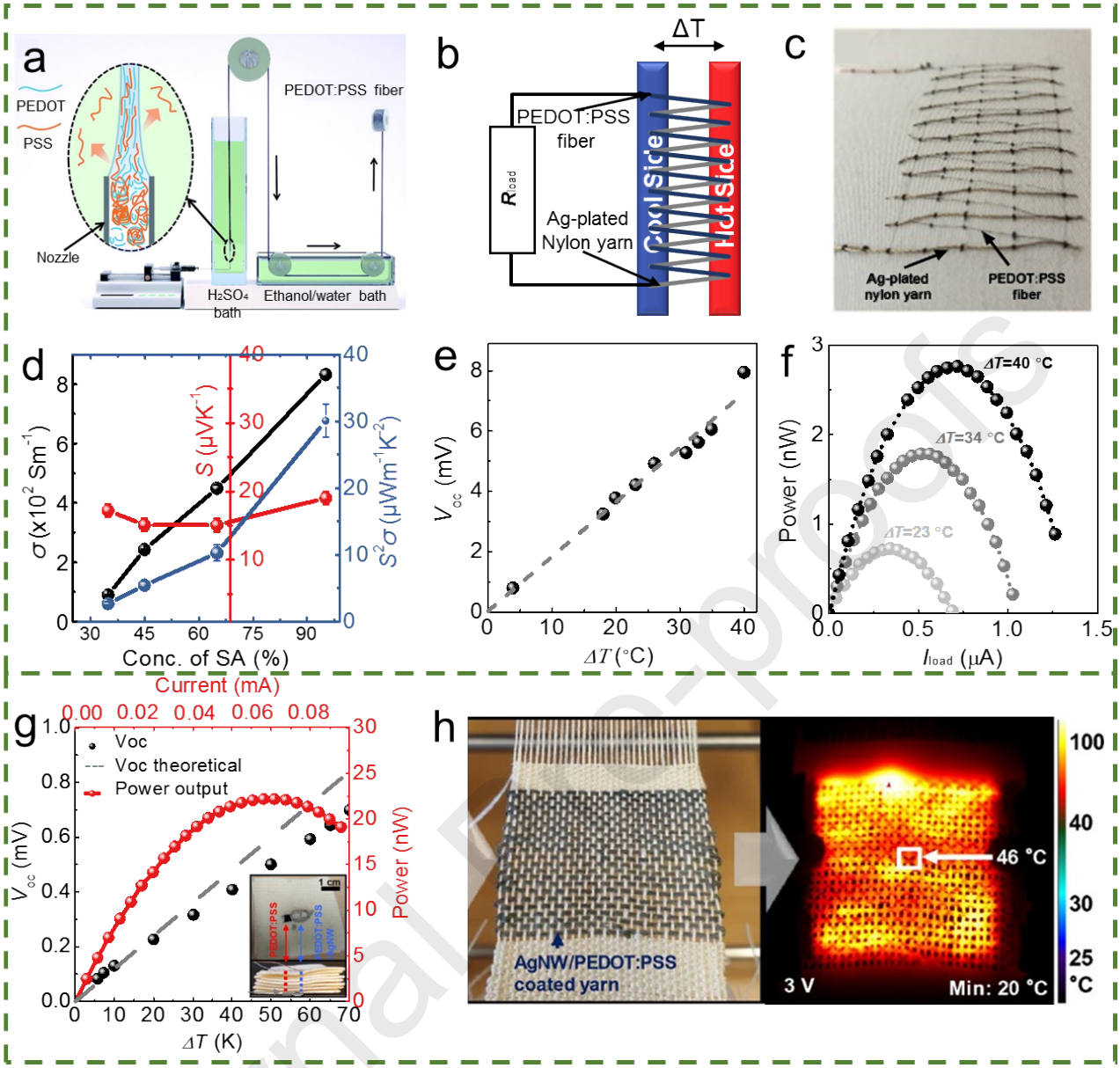

Figure 35. a) Schematic diagram of wet-spinning process. Reproduced with permission [437]. Copyright 2019, Royal Society of Chemistry; b) Schematic and c) photograph of PEDOT:PSS fibre embroidered TE module consisting of ten elements (each comprising one p-type PEDOT:PSS fibre and one silver plated nylon yarn); d) TE properties of the PEDOT:PSS fibre; e) Open circuit voltage (V_{oc}) as a function of temperature difference (ΔT) with respect to the cold end (24 °C); f) Output power P as a function of load current (I_{load}) with three temperature differences (23, 34, and 40 °C). Reproduced under the terms of the Creative Commons CC BY license [447]. Copyright 2017, Wiley-VCH; g) Electrical measurement of the TE device made of Ag NW/PEDOT:PSS coated yarns; h) photograph

(left) and IR image (right) of the heating fabric. Reproduced under a Creative Commons Attribution Non-Commercial No Derivative Works (CC-BY-NC-ND) 4.0 license [446].Copyright 2020, American Chemical Society.

5.3.4 Self-powered temperature-pressure sensor

CPs not only are promising candidates for TE devices, but also can be applied in other flexible electronics, such as sensors. Particularly, the self-powered sensors that consist of CPs to achieve instantaneous and simultaneous sensing of temperature and pressure by exploiting their excellent TE performance and high-pressure-sensing sensitivity now are becoming an attractive topic for the scientific communities. **Figure 36a-j** show the schematic illustration of temperature-pressure (*T*-*P*) sensing mechanism of a microstructure-frame-supported organic TE (MFSOTE) device which is constructed by the deposition of organic TE materials on deformable microstructure frames to enable their temperature and pressure-sensing properties [449]. When the device is exposed to an object with coupled temperature and pressure stimuli, the temperature detection would be achieved via the basic Seebeck effect, i.e. $V_{therm}=S_T\times\Delta T$ (**Figure 36a-d**), while the biased pressure can be detected by analysing the change of resistance of the device caused by frame deformation (**Figure 36e-h**). **Figure 36i and j** show the validity of the MFSOTE device under different temperature difference and pressure stimuli. Clearly, the *I*-*V* curve shifted when there was constant temperature difference, and it shifted more with larger temperature difference applied. By comparison, the *I*-*V* curve deflected when there was constant pressure stimuli and it deflected more profound with larger pressure stimuli. The precise temperature and pressure sensing sensitivity enables the application of the MFSOTE device in e-skin and health-monitoring elements. **Figure 36k and l** show the graphs display the temperature and pressure mapping profiles of pixel signals on the back of the prosthetic hand and on the tip of a prosthetic finger. Clearly, the contact information conducted by the human hand was collected by monitoring the temperature and pressure on a reconstructed map. The changes in the temperature and biased pressure corresponded well to the colours of the pixels in the separated distribution map. This

experiment result proved the effectiveness of the MFSOTE device as an e-skin. On the other hand, the highly integrated MFSOTE array constructed fingertip also showed excellent ability to reconstruct the temperature-pressure signals mapping when touching an ice cube, indicating the precise spatial resolution and dual-parameter-sensing capability of the as-fabricated sensing arrays.

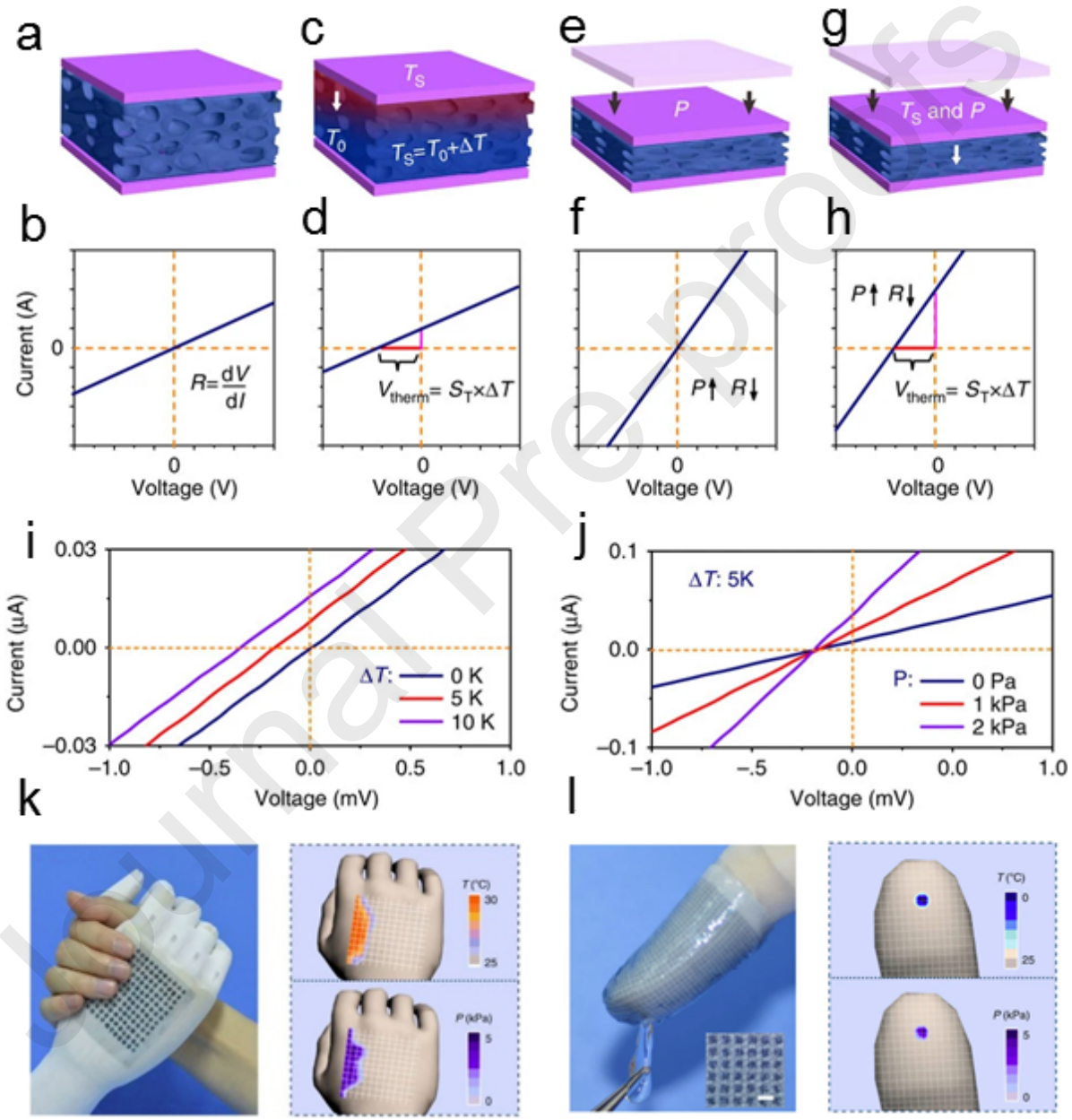

Figure 36. a-h) Schematic illustration of temperature-pressure (*T*-*P*) sensing mechanism: (a,b) pristine. (c,d) a temperature gradient (Δ*T*) is applied across a MFSOTE device. (e,f) a pressure is loaded. (g,h) loading of a coupled temperature and pressure stimuli. Graphs (i and j) show the measured *I*-*V* curves

of a MFSOTE device taken at various ΔT (i) and different loading pressure (j). Graphs (k and l) display the temperature and pressure mapping profiles of pixel signals on the back of the prosthetic hand (k) and on the prosthetic fingertip consists of highly integrated MFSOTE array (l). Reproduce under a Creative Commons Attribution 4.0 International License [449]. Copyright 2015, Springer Nature.

5.3.5 Vertically-aligned devices

Recently, a new topological structure is proposed to maximize the output power density of the flexible TE device, which is vertically aligning TE films upon a flexible substrate. There are mainly two advantages of this exotic structure, including a large temperature gradient between the hot side and the cold side of the TE film caused by their hanging gestures into the flowing air, and a large quantity of TE films upon unit area due to the vertical alignment. As a result, the output power density can even reach dozens of $\mu W \cdot cm^{-2}$ [21]. **Figure 37a** shows the optical images of a 100-leaf-TEG for energy harvesting from the human body heat at room temperature. The flexible device can be attached to the human arm or other curved surfaces [373]. The vertical alignments of TE elements have high sensitivity to flowing air. **Figure 37b-d** show the dependencies of the temperature difference utilization ratio φ_{th} (defined by the ratio of the maximum temperature difference across the TE legs to the available temperature difference), output voltage V_{oc}, and maximum output power P_{max} on the length of each TE leg L_{leg} under various air velocities v_{air}. Under an air flowing condition (v_{air} = 0.2 $m \cdot s^{-1}$, T_{air} = 6 °C), both φ_{th} and V_{oc} are significantly increased as the L_{leg} increases from 5 to 10 mm, and then show saturated tendencies with a L_{leg} of 20 mm. However, their dependencies on v_{air} are more complicated. Increasing the v_{air} may not lead to higher φ_{th} and V_{oc}, which must be taken into consideration when one designed similar TE devices using other materials. As for the P_{max}, when L_{leg} is increased to a certain value, P_{max} reaches a peak value, and when L_{leg} is kept going up, P_{max} then declines. This result indicates the existence of a trade-off effect between φ_{th} and the internal resistance R_{in} of the device. Specifically, leaf-TEG with shorter leaves has smaller φ_{th} and R_{in}, while the one with longer leaves has larger φ_{th} and

R_{in}. This trade-off effect occurs in many TE devices, which can be utilized to achieve output power optimization. **Figure 37f** presents the timing diagram of the response characteristic and sensitivity of leaf-TEG. Clearly, the leaf-TEG promptly (delay time <0.1 s) captures the temperature fluctuation (0.2 °C) and generates corresponding voltage fluctuation (70 μV) even under a short period of 0.2 s. This result demonstrates the ultra-high sensitivity of the response characteristic of the leaf-TEG, which further reinforces its benefit for the energy harvesting from the environment with limited temperature difference and air convention. **Figure 37g** shows the power output of the 100-leaf-TEG module on an arm while walking and standing situation. In a room environment with an ambient temperature of 20 °C, a stable V_{oc} of ~52 mV and output power of 7.2 μW are obtained when standing still. While walking at a speed of ~1 $m \cdot s^{-1}$ and swinging the arms, a larger stable V_{oc} of ~64 mV and higher output power of 11 μW are obtained, which are very competitive with flexible TEG with some bulk TE elements.

Another similar case is the recently reported vertically aligned F-TEG with self-healing, recycling, and Lego-like reconfiguring capabilities [21]. **Figure 37h** presents the design and fabrication of the TEG. The presented images also illustrate several key characteristics, including self-healability, recyclability, and Lego-like reconfigurability, of the as-fabricated FTEG. **Figure 37i** shows the output power density P_{out} as a function of output voltage V_{load} at various temperature differences ranging from 6 K to 95 K with the cold-side temperature kept at 20 °C. Clearly, the maximum P_{out} increases with ΔT and reaches 19 $\mu W \cdot cm^{-2}$ at a ΔT of 93 K. The open-circuit voltage per unit area V_{oc}, as shown in **Figure 37j**, increases linearly with ΔT and reaches 1 $V \cdot cm^{-2}$ at ΔT = 95 K. **Figure 37k** shows the optical and infrared (inset) images of the as-fabricated FTEG attached on a forearm at a room temperature of 25 °C. The infrared image gives the infrared measurement of temperature distribution across the device. This FTEG attached to the human arm can generate different output power when the wearer was under different movements. **Figure 37l** demonstrates average output power densities of 45 and 83 $nW \cdot cm^{-2}$ and average output voltages of 25 and 33 $mV \cdot cm^{-2}$ when the wearer was sitting and walking, which are sufficient to power on some portable electronics like sensors and watches [21].

Although this newly emerging topological structure shows the great potential to generate high power and voltage, one should be notified that this special structure requests more space in the height direction than other common two-dimensional structures. This characteristic impact engineering applications in some situations where usable space is limited. Moreover, no analytical relationship between the length of the TE films and other working conditions (including temperature difference, material properties, film thickness, and heat convection coefficient) was established. In fact, the output power density of these reported devices can be further optimized using the appropriate method to obtain optimal lengths of TE films by securing both sufficient temperature difference and minimum internal resistance [381].

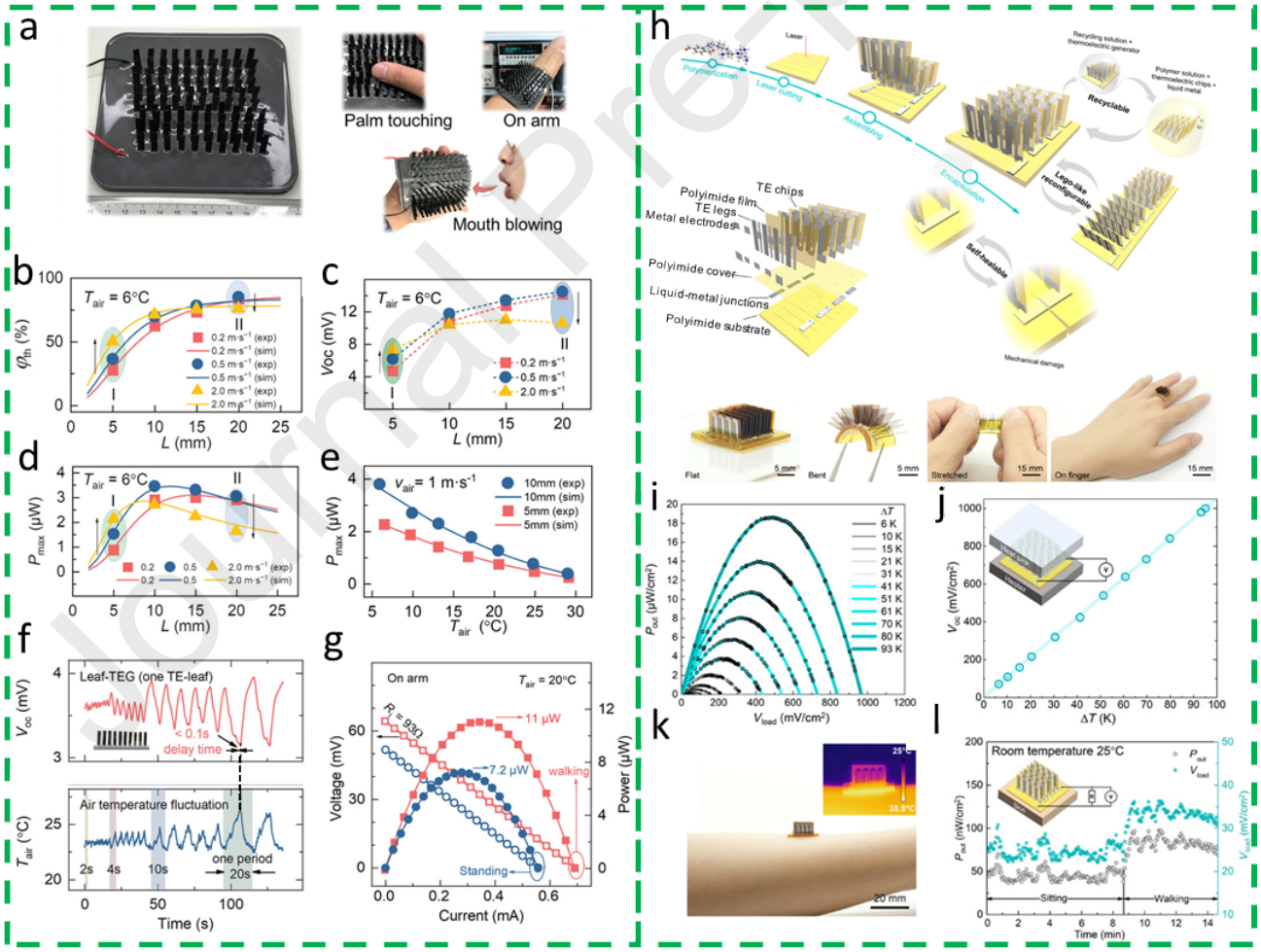

Figure 37. a) Optical images of a 100-leaf-TEG for energy harvesting from the human body heat at room temperature; b) temperature difference utilization ratio φ_{th}, c) Open-circuit voltage V_{oc}, and d) maximum output power P_{max} of leaf-TEG with different length under different air velocity conditions (0.2, 0.5, and 2.0 $m \cdot s^{-1}$); e) Maximum output power P_{max} varies with the air temperature; f) Timing diagram of the response characteristic and sensitivity of leaf-TEG for air temperature fluctuation; g) power output of the 100-leaf-TEG module on an arm while walking and standing situation. Reproduced under the terms of the Creative Commons CC BY license [373]. Copyright 2021, Wiley-VCH; h) schematic diagram of the design and fabrication of the FTEG; i) output power density P_{out} as a function of output voltage (V_{load}) at various temperature differences (ΔT), with the cold-side temperature kept at 20 °C. The black points are measurement data; j) Open-circuit voltage (V_{oc}) versus temperature difference; k) optical and infrared (inset) images of a TEG attached on an arm; l) Power generation (P_{out}) and output voltage (V_{load}) of the TEG with 112 TE legs on the human skin when the wearer was sitting and walking. Reproduced under the terms of the Creative Commons Attribution-NonCommercial license [21]. Copyright 2021, Wiley-VCH.

5.4 Mechanical Improvements

The mechanical properties of FTE materials and devices, such as flexibility and the tensile strength, are important because these devices will need to function under some mechanical constraints and conditions. This mechanical environment may significantly influence the stability of both structures and the TE performance [13,153]. In order to maintain acceptable mechanical properties for these FTE materials and devices, rational designs are needed during their fabrication. Generally, there are several factors that need to be considered, including strengthening the mechanical properties of CPs-based TE legs (units), reinforcement of the material interfaces between the legs and substrates (electrodes and interconnectors), and careful selection of appropriate flexible substrates that possess both high flexibility and high tensile strength.

For the improvement of mechanical properties of TE legs, due to the organic nature of polymers, the pure CPs-based TE legs always possess good flexibility and tensile strengths [154]; while for the organic-inorganic hybrid legs, the incorporation of inorganic materials may considerably reduce the flexibility of these hybrids [48], one suitable strategy is to reduce the dimensions of these inorganic materials, such as using finely ground powders obtained by some specific techniques such as mechanical alloying (ball-milling), and using solution-based synthesis routes such as conventional aqueous solution [188], hydrothermal [183], and solvothermal syntheses to fabricate nanoscale crystals as fillers, such as Te nanorods [188] and SnSe nanosheets [184,203]. Some novel techniques such as chemical exfoliation by Li ions have also been employed to achieve a few-layer thick nanosheet from a bulk ingot, such as SnSe nanosheets exfoliated from the ingots fabricated by solid-state solutions [183]. To evaluate the flexibility and tensile strength of CPs-based legs, there are mainly three factors that need to be considered, namely minimum bending radius, stress-strain relationships, and maximum bending cycles before cracking. For example, **Figure 38a** shows a stress-strain curve obtained *via* tensile measurements of the PPBH/CNT/PUBI films, and the inset shows a photograph taken during the measurement of the minimum bending radius [198]. The as-designed films possess strength of~6 MPa, as well as a small minimum bending radius of only 1 mm, indicating both high flexibility and high tensile strength. Similarly, **Figure 38b** shows stress-strain curves from tensile measurements for the PPy/SWCNT composite films with different treatments [161], from which the composites with a SWCNT: Py ratio of 40 wt% prepared in the medium of water or aqueous ethanol can result in the highest tensile stress of ~14.2 MPa. The as-designed films also possess a high tensile modulus of ~655 MPa and a high elongation at fracture of ~3.1 %, indicating good mechanical performance

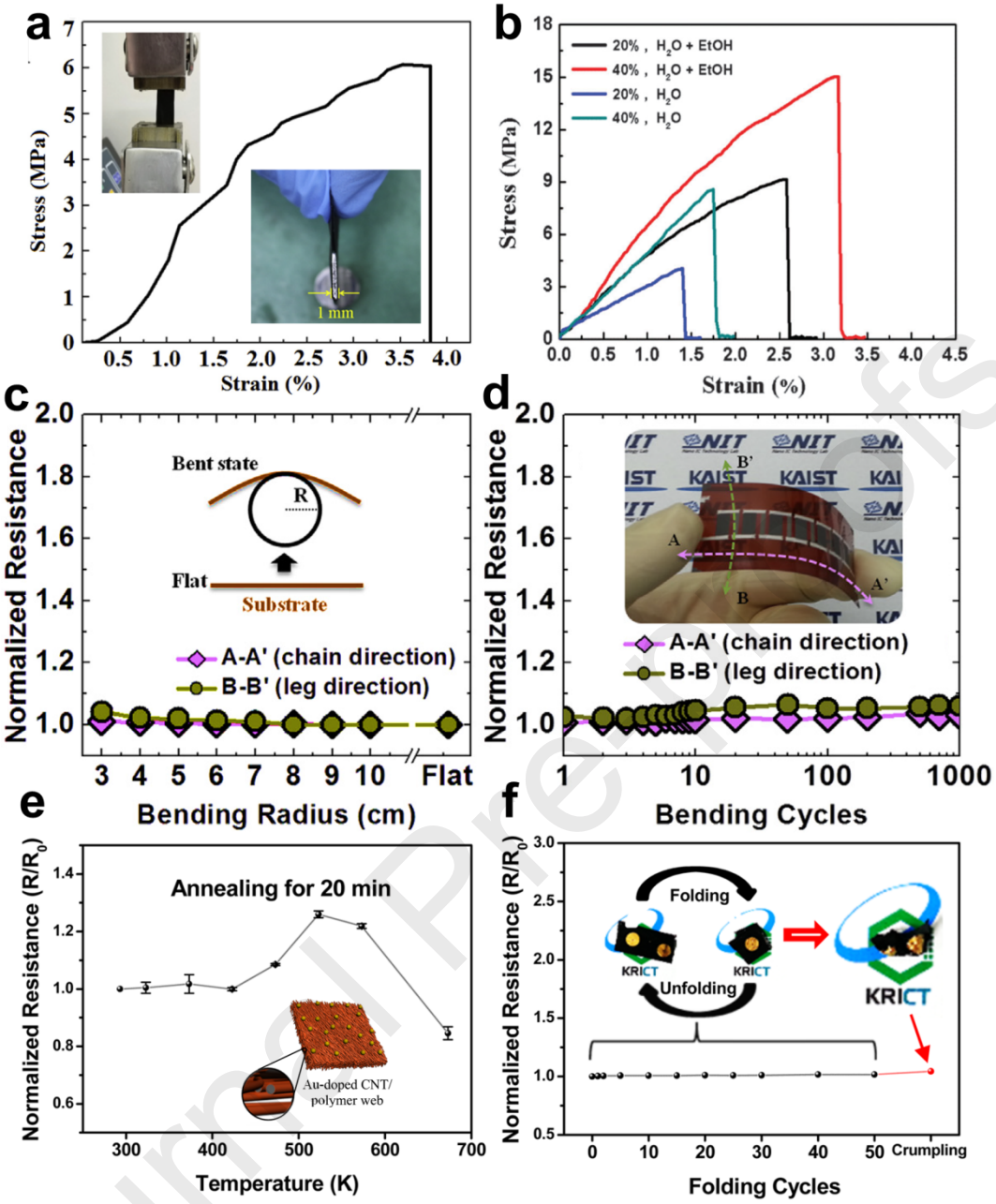

Figure 38. a) Stress-strain curves obtained *via* tensile measurements of the PPBH/CNT/PUBI films, the inset shows a photograph taken during the measurement of the minimum bending radius. Reproduced with permission [198]. Copyright 2018, Elsevier; b) stress-strain curves of tensile measurements for the PPy/SWCNT composite films. Reproduced with permission [161]. Copyright 2016, Royal Society of Chemistry; c) resistance changes of the FET module as a function of bending radius in chain direction and leg direction, d) resistance changes of the module as a function of the number of bending cycles with bending radius of 4 cm. Reproduced with permission [193]. Copyright

2014, Elsevier; e) resistance *R* as a function of temperature and f) number of folding cycles for Au-doped CNT/PANI webs, where R_0 is the corresponding resistance of the original state before annealing and folding. Reproduced with permission [171]. Copyright 2016, American Chemical Society.

For the strengthening of material interfaces between TE legs, interconnectors (such as electrodes and wires), and flexible substrates, a strong "adhesive force" between these components is needed, which can be achieved by carefully choosing appropriate materials for these components. Currently, the selection of these materials is still based on experience, and the studies of these interfaces, such as direct observation and theoretical models are still at a preliminary stage. For example, in many FTE devices, Ag acts as both electrodes and interconnectors (wires) because Ag possesses good adhesive force between TE legs and the substrates [188]. To ensure that the TE performance of the devices can be maintained during bending or stressing, an evaluation of resistance is needed. **Figure 38c** shows the resistance changes of a FTE module as a function of bending radius in chain direction and leg direction [193], and **Figure 38d** shows the resistance changes of the module as a function of the number of bending cycles with bending radius of 4 cm [193]. The as-designed FTE device is composed of PEDOT:PSS/Bi_2Te_3 as n-type legs, PEDOT:PSS/Sb_2Te_3 as p-type legs, and PI films as flexible substrates, fabricated by a typical screen-printing technique. The internal resistance of the unbent TEG module is 145.2 Ω. The results indicate that a stable internal resistance can be maintained by either increasing bending radius or increasing bending times, which is of significance for maintaining a high and stable TE performance for FTE devices during operation.

Furthermore, a careful selection of flexible substrate is also vital for maintaining good mechanical performance of a FTE device [195]. At the same time, how to strengthen the ability to bear external thermal shock is also a concern in current FTE designs since most of the components in FTE devices are organic materials, which are insufficient to resist external heat at high temperatures. Generally, to achieve high flexibility in FTE devices, some special substrates such as polyimide are commonly

chosen due to their high flexibility and acceptable tensile strengths [188]. At the same time, some treatments are needed for the substrates to increase the stability between TE units and substrates [387]. For example, for the roll-to-roll printing of thin-film organic FTE devices [360], the plastic substrate is originally hydrophobic (contact angle between water and substrate is more than 90°), and subjected to surface treatment *via* different chemical solutions, resulting in tuneable ink wettability. Besides, a novel design for the structure of a flexible substrate is also a good choice [182,196]. For example, **Figure 38e** and **38f** show the resistance R as a function of temperature and number of folding cycles for Au-doped CNT/PANI webs [171], respectively, where R_0 is the corresponding resistance of the original state before annealing and folding. The FTE device was achieved by embedding CPs into Au-doped CNT webs. The CNT bundles, which are interconnected by a direct spinning method to form 3D networks without interfacial contact resistance, provide both high σ of >1000 $S \cdot cm^{-1}$ and high ZT of >0.2 at room temperature [171]. From **Figure 38e-f**, it is can be clearly observed t no significant change was observed in the normalized resistance under condition of thermal shocking, folding, and subsequent crumpling tests, indicating good flexibility and high stability.

6. Conclusion and Perspective

Plenty of profound progress has been made since the discovery of CPs. Theoretically, the factors including oxidation level, morphological crystallinity, as well as the average energy carried by charges were shown to be significant in the determination of the TE properties of CPs. This review elucidated the independent influences and the synergetic effects of these factors upon charge and phonon transportation within CPs. Generally, increasing the oxidation level improves the σ but depresses S as numerous low energy charges make non-negligible contributions, which request further action to increase the average energy carried by the effective charges to optimize the TE performance of CPs. Furthermore, charge transport models, including the VRH model, NNH model, ME model, TE model, and series heterogeneous media model were proposed to account for the obtained experimental results. These models cover the charge transport mechanisms for most existing CPs. With regard to

experimental progress, much effort has been expended to advance performance by tuning the oxidation level and improving the structural crystallinity of CPs by strategies such as redox doping, secondary doping, post-treatments, polymerization, metal-based coordination polymer and Se substitution. It has been shown that a suitable combination of some of these strategies yielded better results for pure CPs. For inorganic-organic hybrid composites, current research work mainly focused on the resolution of three major problems, namely large particle size, inhomogeneity and oxidation resulting in ineffective loading. Simply by physical mixing, the composite films might suffer two or even all three of these problems. Instead, *in-situ* synthesis and the combination of physical vapor deposition (PVD) and vapor phase polymerization (VPP) are better alternatives. To date, the highest *ZT* of 0.42 achieved for pure CPs and 0.58 for Bi_2Te_3-PEDOT composite films convinced us that there is a bright future for high-performance CPs and their derivatives. Additionally, FTE devices with rational structure design method and promising power output performance have been reviewed and the current status has been summarized. The corresponding efficient fabrication techniques were also reviewed. It turned out that compact structure-designed devices composed of high performance TE elements presented excellent power output under large temperature gradients induced by in-plane heat transfer. Accordingly, a rationally designed FTE device could meet the requirements to power microwatt electronics. In addition to traditional TE devices, we also reviewed the newly emerging self-powered temperature-pressure sensor based on CPs. This idea provides new perspectives for CPs to be applied in e-skin and health monitor in the near future.

Despite the progress made in the rapidly-developing CPs, it should be noted that the performance optimization of CPs is still in its infancy and there is a need for further creative research effort to overcome the challenges ahead. The morphological complexity of CPs invalidates the verified knowledge for one CP in another. For inorganic semiconductors, the optimal *n* is in the range of 10^{19}~10^{21} cm^{-3}; however, the optimal oxidation level highly varies for different CPs, e.g. the optimal oxidation level is 22 % for PEDOT:Tos [52], but 76.9 % for $FeCl_3$-doped PCDTBT [36], although the

trade-off effect between σ and S exists in both types of materials. None of the current models is universal in the description of charge transport within all CPs due to the co-existing amorphous and crystalline microstructures. Additionally, these models are more suitable for verification of obtained experimental results instead of property prediction for unmeasured samples, as the charge transport behaviour varies even for the same type of CP synthesized under different conditions. These problems hinder the development of charge transport theory, and in turn slow down the progress to achieve higher TE performance CPs. For molecular structure, challenges are faced in many aspects such as the basic mechanism of charge transport and electro-acoustic coupling effect in molecular systems, the relationship between molecular structure and performance, the basic physical image of TE energy conversion in organic systems from a molecular scale, the doping mechanism of conjugated molecular systems, the key technology of material patterning, and the direction of functional applications. For microstructures, advanced characterization techniques are needed to disclose the relationship between microstructures and properties, and in turn find new ways to improve the TE performance of CPs from the aspect of microstructure, such as balancing the ordering level and κ_l, as well as further explain the mechanism of energy filtering effect at the interfaces between different components. For optimization strategies, it seems that ZT has reached the top limit for pure CPs as no other significant breakthroughs have been made within the past five years; while inorganic-organic hybrid composites are becoming promising in recent years [51,319,450]. For doping, it is an important problem to precisely control the doping level (compared to inorganic materials with doping level up to 10 %) [6], and there is a lack of efficient and universal dopant in organic thermoelectric research, and n-type dopants also face problems such as poor air stability. Besides, because the short-range accumulation of organic molecules is diverse, and the long-range arrangement has a huge difference in order, how to control the uniformity and crystallinity of CPs has always been an important topic of organic TE research, and this problem has a significant impact on the corresponding doping mechanism. For post-treatment, it is still a challenge to precisely control the level of post-treatment, and the interactions between different strategies should be

carefully concerned. Besides, finding new and effective post-treatment method is still a tricky work. For hybrid design, more effort should be directed toward the emerging problems in the hybridization of inorganic and organic materials, including the creation of a highly conductive interfacial layer between the polymer and fillers, the transition of energy band structure in the inorganic-organic interfaces and the impact of the intrinsic parameters such as E_F, n and E_g of the applied fillers upon the hybrid composites. For preparation methods, more advanced fabrication techniques are needed to be developed for achieving stable and high-performance CPs-based TE materials. Especially, many issues and unclear points are still existed between the TE properties and preparations, such as mechanisms of physical mixing, *in-situ* polymerization/reaction, and layer-by-layer assembly. By resolving these problems, we would be able to understand the charge transport mechanisms on a new level and to achieve highly concise control over the performance optimization strategies for CPs. In terms of FTE devices, one big challenge is the high cost and low efficiency of device fabrication for high performance CPs derivatives, especially for the excellent inorganic-organic hybrid composites whose preparation processes are complicated. An effective solution to this problem would lead to a dramatic leap in the power output of FTE devices.

In this respect, we summarize several prospects as below:

1) **Universal theoretical model.** To propose a universal theoretical model that can describe charge transport behaviour in all CPs would be unrealistic due to their variable sophisticated morphologies. Pragmatically, to give specific and accurate prerequisites for the proposed charge transport models would be a better alternative. Oxidation level and μ are two quantitative parameters determining the correct model to accurately predict the TE properties of a certain CP. Therefore, establishing accurate and one-to-one correspondence relationships between these two parameters and the charge transport behaviour such as variable range hopping and nearest neighbouring hopping is necessary to direct design of experiments.

2) **Advanced hybrid composites.** More effort should be concentrated upon addressing the aforementioned emerging problems of inorganic-organic hybrid composites. A complete understanding of the causes of the highly conductive interfacial layer between the polymer and fillers would enable us to achieve controllable enhancement in σ. In addition, microscopically, the energy band structure of the fillers is the key factor that distinguishes the σ of hybrid composites. The combination of two materials with high TE performance (PEDOT and Bi_2Te_3) actually leads to a compromised TE performance for the hybrid composite compared with their components; however, suitable materials (PEDOT:PSS and Te nanorods) hybridized together would present TE performance exceeding that of either component. The mechanism behind this phenomenon is still unclear. We believe that by figuring out how the aforementioned intrinsic parameters of fillers impact the TE properties of the hybrid composite, rational combinations of CPs and inorganic fillers can be found to achieve more significant breakthroughs in performance and further development of CPs based TE materials.

3) **Flexible device design**. FTE generators and refrigerators are particularly attracting significant attention because they possess the highest potential for personal use. These devices can be operated by directly collecting heat from the human body. Polymer-based flexible TEs are fascinating because of their intrinsic flexibility, economical cost, and none or low toxicity. For inorganic TE materials as fillers, multi-dimensional nanocrystals with high surface activities and nanometer effects are good candidates for developing composites with these organic polymers in order to improve the thermopower of the composite thin films. The research on flexible generators are still at a very preliminary stage, and more fundamental studies are needed to explore the strategies of improving the performance of flexible TE devices, such as understanding the delocalizing carriers in conductive polymers, theoretically establishing models that explain carrier transport properties, optimizing the effects of fillers through interfacial engineering, intensifying the connections

between inorganic particles for highly crystalline films, and overcoming the mechanical inflexibility of inorganic TE materials as legs.

4) **Commercialization of FTE devices.** Lowering the manufacturing cost and increasing the manufacturing efficiency are key factors in the commercialization of FTE devices. So far both two factors cannot meet the demands of the state-of-the art CPs based TE materials due to the unsuitable and outdated fabrication techniques for these emerging materials. Novel and creative fabrication techniques are an important and urgent research topic. Current prototypes might suffer from non-optimized geometrical parameters, especially the length. For FTE films, their micron-level thicknesses dramatically diminish the in-plane heat conduction, in case of which optimal lengths are far smaller than their current values to hold the same temperature gradients. Unfortunately, no study can be found on this field, and hence the relationships that exist between the TE performance and the geometrical parameters of the FTE device needs to be established.

5) **Interdisciplinary applications of CPs.** CPs are well-known for their excellent electrical conduction and outstanding flexibility, suggesting that TEG is only one of their possible applications. In fact, this versatile material can also be applied in sensor, organic light-emitting diode (OLED) and etc. Therefore, by reasonable design, self-powered sensors or OLED are highly achievable. We believe the CPs-based self-powered electronics would prevail in the near future because of both the non-toxicity and the easy-availability of this materials, and more effort should be paid on this meaningful research topic.

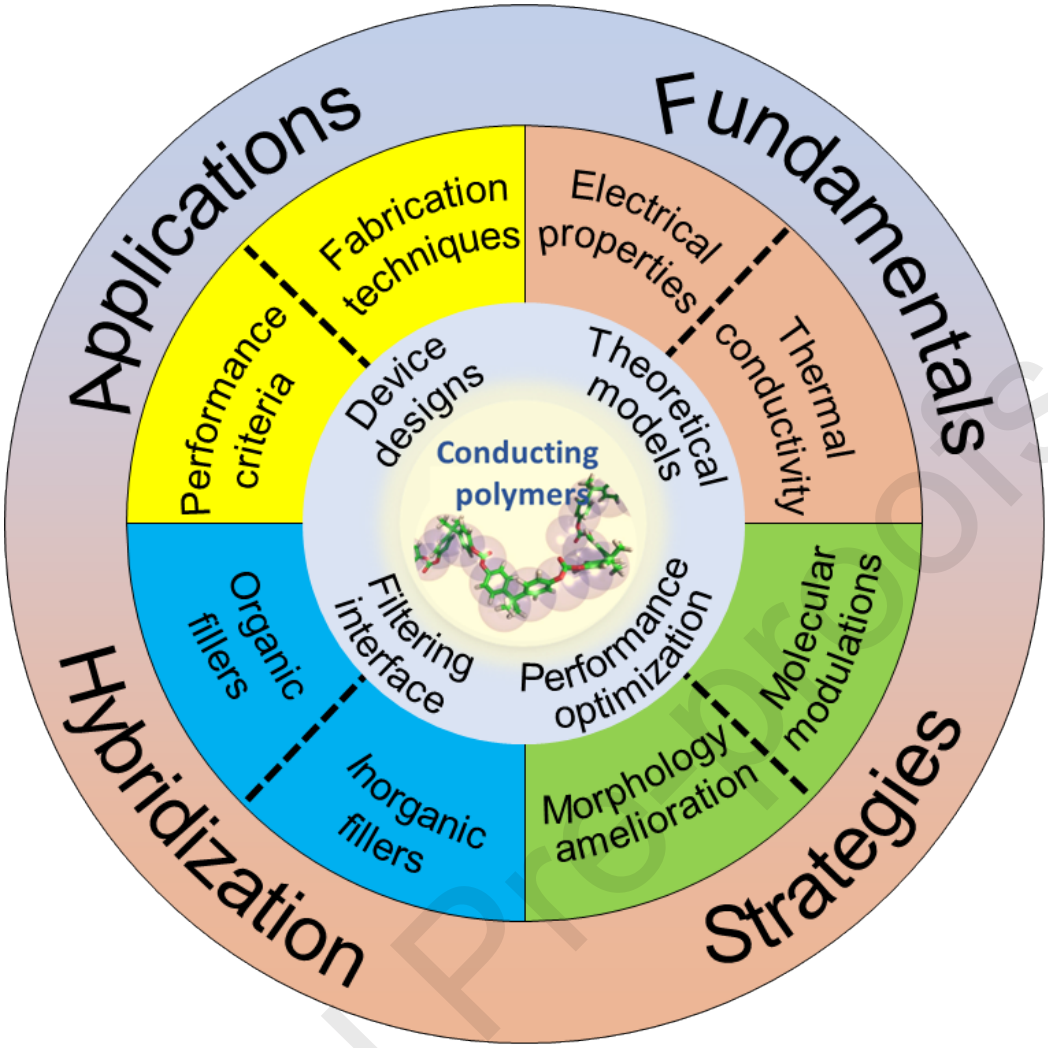

Figure 39. Strategy and prospects for high-performance conducting polymers and their FTEGs.

Author Contributions

The manuscript was written through contributions of all authors. All authors have given approval to the final version of the manuscript.

Acknowledgements

The authors acknowledge the financial support provided by the Australia Research Council. ZGC thanks the USQ Strategic re-search fund and USQ start-up grant. Shengduo Xu acknowledges the China Scholarship Council for providing the Ph.D. stipend. The Australian Microscopy and Microanalysis Research Facility is acknowledged for providing the characterization facilities.

REFERENCES

[1] Tan G, Zhao LD, Kanatzidis MG. Rationally Designing High-Performance Bulk Thermoelectric Materials. Chem Rev 2016;116:12123-49.

[2] Snyder GJ, Toberer ES. Complex Thermoelectric Materials. Nat Mater 2008;7:105-14.

[3] Zhao L-D, Dravid VP, Kanatzidis MG. The Panoscopic Approach to High Performance Thermoelectrics. Energy Environ Sci 2014;7:251-68.

[4] Chen R, Lee J, Lee W, Li D. Thermoelectrics of Nanowires. Chem Rev 2019;119:9260-302.

[5] Dresselhaus MS, Chen G, Tang MY, Yang RG, Lee H, Wang DZ, et al. New Directions for Low-Dimensional Thermoelectric Materials. Adv Mater 2007;19:1043-53.

[6] Shi X-L, Zou J, Chen Z-G. Advanced Thermoelectric Design: From Materials and Structures to Devices. Chem Rev 2020;120:7399-515.

[7] Liu W, Kim HS, Chen S, Jie Q, Lv B, Yao M, et al. n-type thermoelectric material $Mg_2Sn_{0.75}Ge_{0.25}$ for high power generation. Proc Natl Acad Sci 2015;112:3269-74.

[8] Siddique ARM, Mahmud S, Heyst BV. A Review of the State of the Science on Wearable Thermoelectric Power Generators (TEGs) and Their Existing Challenges. Renew Sust Energ Rev 2017;73:730-44.

[9] Shi X, Chen L. Thermoelectric Materials Step Up. Nat Mater 2016;15:691-2.

[10] Dai D, Zhou Y, Liu J. Liquid metal based thermoelectric generation system for waste heat recovery. Renew Energ 2011;36:3530-6.

[11] Li S, Li X, Ren Z, Zhang Q. Recent progress towards high performance of tin chalcogenide thermoelectric materials. J Mater Chem A 2018;6:2432-48.

[12] Zhao W, Ding J, Zou Y, Di C-a, Zhu D. Chemical doping of organic semiconductors for thermoelectric applications. Chem Soc Rev 2020;49:7210-28.

[13] Bharti M, Singh A, Samanta S, Aswal DK. Conductive Polymers for Thermoelectric Power Generation. Prog Mater Sci 2018;93:270-310.

[14] Hong M, Chasapis TC, Chen Z-G, Yang L, Kanatzidis MG, Snyder GJ, et al. n-Type $Bi_2Te_{3-x}Se_x$ Nanoplates with Enhanced Thermoelectric Efficiency Driven by Wide-Frequency Phonon Scatterings and Synergistic Carrier Scatterings. ACS Nano 2016;10:4719-27.

[15] Tan M, Liu WD, Shi XL, Gao H, Li H, Li C, et al. Anisotropy Control-Induced Unique Anisotropic Thermoelectric Performance in the n-Type $Bi_2Te_{2.7}Se_{0.3}$ Thin Films. Small Methods 2019;3:1900582.

[16] Wang Y, Liu W, Gao H, Wang L, Li M, Shi X-L, et al. High Porosity in Nanostructured n-Type Bi_2Te_3 Obtaining Ultralow Lattice Thermal Conductivity. ACS Appl Mater Interfaces 2019;11:31237-44.

[17] Zhao LD, Lo SH, Zhang Y, Sun H, Tan G, Uher C, et al. Ultralow Thermal Conductivity and High Thermoelectric Figure of Merit in SnSe Crystals. Nature 2014;508:373-7.

[18] Shirakawa H. The Discovery of Polyacetylene Film: The Dawning of an Era of Conducting Polymers (Nobel Lecture). Angew Chem Int Ed Engl 2001;40:2574-80.

[19] Kroon R, Mengistie DA, Kiefer D, Hynynen J, Ryan JD, Yu L, et al. Thermoelectric Plastics: From Design to Synthesis, Processing and Structure-Property Relationships. Chem Soc Rev 2016;45:6147-64.

[20] Wang Y, Yang L, Shi X, Shi X, Chen L, Dargusch M, et al. Flexible Thermoelectric Materials and Generators: Challenges and Innovations. Adv Mater 2019;31:1807916.

[21] Ren W, Sun Y, Zhao D, Aili A, Zhang S, Shi C, et al. High-performance wearable thermoelectric generator with self-healing, recycling, and Lego-like reconfiguring capabilities. Sci Adv 2021;7:eabe0586.

[22] Zhu T, Liu Y, Fu C, Heremans JP, Snyder JG, Zhao X. Compromise and Synergy in High-Efficiency Thermoelectric Materials. Adv Mater 2017;29:1605884.

[23] Yang L, Chen Z-G, Dargusch MS, Zou J. High Performance Thermoelectric Materials: Progress and Their Applications. Adv Energy Mater 2017;8:1701797.

[24] Pei Y, Wang H, Snyder GJ. Band engineering of thermoelectric materials. Adv Mater 2012;24:6125-35.

[25] Zhang Q, Sun Y, Xu W, Zhu D. Organic thermoelectric materials: emerging green energy materials converting heat to electricity directly and efficiently. Adv Mater 2014;26:6829-51.

[26] Yao H, Fan Z, Cheng H, Guan X, Wang C, Sun K, et al. Recent Development of Thermoelectric Polymers and Composites. Macromol Rapid Comm 2018;39:1700727.

[27] Sun Q, Chen Z-Y, Li M, Shi X-L, Xu S-D, Yin Y, et al. Structural Evolution of High-Performance Mn-Alloyed Thermoelectric Materials: A Case Study of SnTe. Small 2021;https://doi.org/10.1002/smll.202100525.

[28] Ji W, Shi X-L, Liu W-D, Yuan H, Zheng K, Wan B, et al. Boosting the Thermoelectric Performance of n-type Bi_2S_3 by Hierarchical Structure Manipulation and Carrier Density Optimization. Nano Energy 2021;87:106171.

[29] Sun Q, Li M, Shi X-L, Xu S-D, Liu W-D, Hong M, et al. Versatile Vanadium Doping Induces High Thermoelectric Performance in GeTe via Band Alignment and Structural Modulation. Adv Energy Mater 2021;11:2100544.

[30] Gu Y, Shi X-L, Pan L, Liu W-D, Sun Q, Tang X, et al. Rational Electronic and Structural Designs Advance BiCuSeO Thermoelectrics. Adv Funct Mater 2021;https://doi.org/10.1002/adfm.202101289.

[31] Zheng Z-H, Shi X-L, Ao D-W, Liu W-D, Chen Y-X, Li F, et al. Rational band engineering and structural manipulations inducing high thermoelectric performance in n-type $CoSb_3$ thin films. Nano Energy 2021;81:105683.

[32] Chen Y-X, Shi X-L, Zheng Z-H, Li F, Liu W-D, Chen W-Y, et al. Two-Dimensional WSe_2/SnSe p-n Junctions Secure Ultrahigh Thermoelectric Performance in n-type Pb/I Co-doped Polycrystalline SnSe. Mater Today Phys 2021;16:100306.

[33] Shi X-L, Wu H, Liu Q, Zhou W, Lu S, Shao Z, et al. $SrTiO_3$-Based Thermoelectrics: Progress and Challenges. Nano Energy 2020;78:105195.

[34] Wu H, Shi X-L, Liu W-D, Li M, Gao H, Zhou W, et al. Double perovskite Pr_2CoFeO_6 thermoelectric oxide: Roles of Sr-doping and Micro/nanostructuring. Chem Eng J 2021;425:130668.

[35] Cochran JE, Junk MJN, Glaudell AM, Miller P, Levi Cowart JS, Toney MF, et al. Molecular Interactions and Ordering in Electrically Doped Polymers: Blends of PBTTT and F4TCNQ. Macromolecules 2014;47:6836-46.

[36] Aïch RdB, Blouin N, Bouchard Al, Leclerc M. Electrical and Thermoelectric Properties of Poly(2,7-Carbazole) Derivatives. Chem Mater 2009:751-7.

[37] Culebras MG, C. M. Cantarero, A. Enhanced thermoelectric performance of PEDOT with different counter-ions optimized by chemical reduction. J Mater Chem A 2014;2:10109-15.

[38] Kang K, Watanabe S, Broch K, Sepe A, Brown A, Nasrallah I, et al. 2D coherent charge transport in highly ordered conducting polymers doped by solid state diffusion. Nat Mater 2016;15:896-902.

[39] Zhang S, Kumar P, Nouas AS, Fontaine L, Tang H, Cicoira F. Solvent-induced changes in PEDOT:PSS films for organic electrochemical transistors. APL Mater 2015;3:014911.

[40] Fadhil Muhammad Tarmidzi1 SBS. Highly Conductive PEDOT: PSS Flexible Film with Secondary Doping and Spray Pyrolysis Method. Int J Eng Sci 2018;13:10234-9.

[41] Liu C, Lu B, Yan J, Xu J, Yue R, Zhu Z, et al. Highly conducting free-standing poly(3,4-ethylenedioxythiophene)/poly(styrenesulfonate) films with improved thermoelectric performances. Synthetic Met 2010;160:2481-5.

[42] Xu K, Chen G, Qiu D. Convenient Construction of Poly(3,4-ethylenedioxythiophene)–Graphene Pie-Like Structure with Enhanced Thermoelectric Performance. J Mater Chem A 2013;1:12395-9.

[43] Yoo D, Kim J, Kim JH. Direct Synthesis of Highly Conductive Poly(3,4-ethylenedioxythiophene):Poly(4-styrenesulfonate) (PEDOT:PSS)/Graphene Composites and Their Applications in Energy Harvesting Systems. Nano Res 2014;7:717-30.

[44] Hiroshi Ito TH, Hisaaki Tanaka, Shin-ichi Kuroda. Critical regime for the insulator–metal transition in highly ordered conjugated polymers gated with ionic liquid. Jpn J Appl Phys 2016;55:03DC8.

[45] Massonnet N, Carella A, Jaudouin O, Rannou P, Laval G, Celle C, et al. Improvement of the Seebeck coefficient of PEDOT:PSS by chemical reduction combined with a novel method for its transfer using free-standing thin films. J Mater Chem C 2014;2:1278-83.

[46] Kim N, Kee S, Lee SH, Lee BH, Kahng YH, Jo YR, et al. Highly conductive PEDOT:PSS nanofibrils induced by solution-processed crystallization. Adv Mater 2014;26:2268-72.

[47] Yuji Hiroshige MO, Naoki Toshima. High Thermoelectric Performance of Poly(2,5-dimethoxyphenylenevinylene) and Its Derivatives. Synthetic Met 2006;156:1341-7.

[48] Wang L, Zhang Z, Liu Y, Wang B, Fang L, Qiu J, et al. Exceptional Thermoelectric Properties of Flexible Organic-Inorganic Hybrids with Monodispersed and Periodic Nanophase. Nat Commun 2018;9:3817.

[49] Qin Q, He F, Zhang W. One-Step Electrochemical Polymerization of Polyaniline Flexible Counter Electrode Doped by Graphene. J Nanomater 2016;2016:1-7.

[50] Kim G, Shao L, Zhang K, Pipe KP. Engineered doping of organic semiconductors for enhanced thermoelectric efficiency. Nat Mater 2013;12:719-23.

[51] Ju H, Kim J. Chemically Exfoliated SnSe Nanosheets and Their SnSe/Poly(3,4-ethylenedioxythiophene):Poly(styrenesulfonate) Composite Films for Polymer Based Thermoelectric Applications. ACS Nano 2016;10:5730-9.

[52] Bubnova O, Khan ZU, Malti A, Braun S, Fahlman M, Berggren M, et al. Optimization of the Thermoelectric Figure of Merit in the Conducting Polymer Poly(3,4-ethylenedioxythiophene). Nat Mater 2011;10:429-33.

[53] Chen X, Feng L, Yu P, Liu C, Lan J, Lin Y-H, et al. Flexible Thermoelectric Films Based on Bi_2Te_3 Nanosheets and Carbon Nanotube Network with High n-Type Performance. ACS Appl Mater Interfaces 2021;13:5451-9.

[54] Fan J, Huang X, Liu F, Deng L, Chen G. Feasibility of using chemically exfoliated SnSe nanobelts in constructing flexible SWCNTs-based composite films for high-performance thermoelectric applications. Compos Commun 2021;24:100612.

[55] Zhang L, Shi X-L, Yang Y-L, Chen Z-G. Flexible thermoelectric materials and devices: From materials to applications. Mater Today 2021;46:62-108.

[56] Kamarudin MA, Sahamir SR, Datta RS, Long BD, Mohd Sabri MF, Mohd Said S. A review on the fabrication of polymer-based thermoelectric materials and fabrication methods. Sci World J 2013;2013:713640.

[57] Culebras M, Gomez CM, Cantarero A. Review on Polymers for Thermoelectric Applications. Materials (Basel) 2014;7:6701-32.

[58] Peng S, Wang D, Lu J, He M, Xu C, Li Y, et al. A Review on Organic Polymer-Based Thermoelectric Materials. J Polym Environ 2016;25:1208-18.

[59] Petsagkourakis I, Tybrandt K, Crispin X, Ohkubo I, Satoh N, Mori T. Thermoelectric Materials and Applications for Energy Harvesting Power Generation. Sci Technol Adv Mat 2018;19:836-62.

[60] Dongmin Kang S, Jeffrey Snyder G. Charge-transport model for conducting polymers. Nat Mater 2017;16:252-7.

[61] Kaiser AB. Electronic transport properties of conducting polymers and carbon nanotubes. Rep Prog Phys 2001;64:1-49.

[62] Saxena N, Keilhofer J, Maurya AK, Fortunato G, Overbeck J, Müller-Buschbaum P. Facile Optimization of Thermoelectric Properties in PEDOT:PSS Thin Films through Acido-Base and Redox Dedoping Using Readily Available Salts. ACS Appl Energy Mater 2018;1:336-42.

[63] Shi W, Yao Q, Qu S, Chen H, Zhang T, Chen L. Micron-thick highly conductive PEDOT films synthesized *via* self-inhibited polymerization: roles of anions. NPG Asia Mater 2017;9:e405.

[64] Shi W, Qu S, Chen H, Chen Y, Yao Q, Chen L. One-Step Synthesis and Enhanced Thermoelectric Properties of Polymer-Quantum Dot Composite Films. Angew Chem Int Ed 2018;57:8037-42.

[65] Bubnova O, Crispin X. Towards polymer-based organic thermoelectric generators. Energy Environ Sci 2012;5:9345-62.

[66] Hideki Shirakawa EJL, Alan G. Macdiarmid, Chwan K. Chiang, and Alan J. Heeger. Synthesis of electrically conducting organic polymers-halogen derivatives of polyacetylene, $(CH)_x$. J Chem Soc Chem Commun 1977;16:578-80.

[67] Ashkenazi J, Pickett WE, Krakauer H, Wang CS, Klein BM, Chubb SR. Ground state of trans-polyacetylene and the Peierls mechanism. Phys Rev Lett 1989;62:2016-9.

[68] Tang F-C, Chang J, Wu F-C, Cheng H-L, Hsu SL-C, Chen J-S, et al. Alignment of Poly(3,4-ethylenedioxythiophene) Polymer Chains in Photovoltaic Cells by Ultraviolet Irradiation. J Mater Chem 2012;22:22409-17.

[69] Ouyang J, Xu Q, Chu C-W, Yang Y, Li G, Shinar J. On the mechanism of conductivity enhancement in poly(3,4-ethylenedioxythiophene):poly(styrene sulfonate) film through solvent treatment. Polymer 2004;45:8443-50.

[70] Yamamoto T, Fukuda T, Yoneda Y, Begum F, Ikeda T, Sasaki S, et al. pi-Conjugated Poly(pyridine-2,5-diyl), Poly(2,2'-bipyridine-5,5'-diyl), and Their Alkyl Derivatives, Preparation, Linear Structure, Function as a Ligand to Form Their Transition Metal Complexes, Catalytic Reactions, n-Type Electrically Conducting Properties, Optical Properties, and Alignment on Substrates. J Am Chem Soc 1994;116:4832-45.

[71] Khan ZU, Bubnova O, Jafari MJ, Brooke R, Liu X, Gabrielsson R, et al. Acido-basic control of the thermoelectric properties of poly(3,4-ethylenedioxythiophene)tosylate (PEDOT-Tos) thin films. J Mater Chem C 2015;3:10616-23.

[72] Hongkwan Park SHL, Felix Sunjoo Kim, Hyang Hee Choi, In Woo Cheong and Jung Hyun Kim. Enhanced thermoelectric properties of PEDOT:PSS nanofilms by a chemical dedoping process. J Mater Chem A 2014;2:6532-9.

[73] Bubnova O, Berggren M, Crispin X. Tuning the thermoelectric properties of conducting polymers in an electrochemical transistor. J Am Chem Soc 2012;134:16456-9.

[74] Street JLBaGB. Polarons, Bipolarons, and Solitons in Conducting Polymers. Accounts Chem Res 1985;18:309-15.

[75] Shi X-L, Chen W-Y, Zhang T, Zou J, Chen Z-G. Fiber-based thermoelectrics for solid, portable, and wearable electronics. Energy Environ Sci 2021;14:729-64.

[76] Luo C, Kyaw AKK, Perez LA, Patel S, Wang M, Grimm B, et al. General Strategy for Self-Assembly of Highly Oriented Nanocrystalline Semiconducting Polymers with High Mobility. Nano Lett 2014;14:2764-71.

[77] Tseng H-R, Phan H, Luo C, Wang M, Perez LA, Patel SN, et al. High-Mobility Field-Effect Transistors Fabricated with Macroscopic Aligned Semiconducting Polymers. Adv Mater 2014;26:2993-8.

[78] Bubnova O, Khan ZU, Wang H, Braun S, Evans DR, Fabretto M, et al. Semi-Metallic Polymers. Nat Mater 2014;13:190-4.

[79] Kim J-Y, Kwon M-H, Kim J-T, Kwon S, Ihm D-W, Min Y-K. Journal Of Solid State Electrochemistry. J Phys Chem C 2007;111:11252-8.

[80] Park T, Park C, Kim B, Shin H, Kim E. Flexible PEDOT electrodes with large thermoelectric power factors to generate electricity by the touch of fingertips. Energy Environ Sci 2013;6:788-92.

[81] Xiao D, Zhang S, Zhang D, Xie D, Zeng Q, Xiang Y, et al. Reversible transformation of self-assemblies and fluorescence by protonation–deprotonation in pyrimidinylene–phenylene macrocycles. Chem Commun 2016;52:4357-60.

[82] Gueye MN, Carella A, Massonnet N, Yvenou E, Brenet S, Faure-Vincent J, et al. Structure and Dopant Engineering in PEDOT Thin Films: Practical Tools for a Dramatic Conductivity Enhancement. Chem Mater 2016;28:3462-8.

[83] Scholes DT, Yee PY, Lindemuth JR, Kang H, Onorato J, Ghosh R, et al. The Effects of Crystallinity on Charge Transport and the Structure of Sequentially Processed F4TCNQ-Doped Conjugated Polymer Films. Adv Funct Mater 2017;27:1702654.

[84] Aasmundtveit KE, Samuelsen EJ, Pettersson LAA, Inganäs O, Johansson T, Feidenhans'l R. Structure of thin films of poly(3,4-ethylenedioxythiophene). Synthetic Met 1999;101:561-4.

[85] Chou T-R, Chen S-H, Chiang Y-T, Lin Y-T, Chao C-Y. Highly conductive PEDOT:PSS films by post-treatment with dimethyl sulfoxide for ITO-free liquid crystal display. J Mater Chem C 2015;3:3760-6.

[86] Wei Q, Mukaida M, Naitoh Y, Ishida T. Morphological Change and Mobility Enhancement in PEDOT: PSS by Adding Co-solvents. Adv Mater 2013;25:2831-6.

[87] Liang J, Wang T, Qiu P, Yang S, Ming C, Chen H, et al. Flexible Thermoelectrics: From Silver Chalcogenides to Full-Inorganic Devices. Energy Environ Sci 2019;12:2983-90.

[88] Wei T-R, Jin M, Wang Y, Chen H, Gao Z, Zhao K, et al. Exceptional Plasticity in the Bulk Single-Crystalline Van Der Waals Semiconductor InSe. Science 2020;369:542.

[89] Huang C, Barlow S, Marder SR. Perylene-3,4,9,10-tetracarboxylic Acid Diimides: Synthesis, Physical Properties, and Use in Organic Electronics. The Journal of Organic Chemistry 2011;76:2386-407.

[90] Mott NF, Davis EA. Electronic Processes in Non-Crystalline Materials: Oxford university press; 2012.

[91] Crispin X, Cornil Jrm, Friedlein R, Okudaira KK, Lemaur V, Crispin A, et al. Electronic Delocalization in Discotic Liquid Crystals: A Joint Experimental and Theoretical Study. J Am Chem Soc 2004;126:11889-99.

[92] Veaceslav Coropceanu JrmC, Demetrio A. da Silva Filho, Yoann Olivier, Robert Silbey, and Jean-Luc Bre´das. Charge Transport in Organic Semiconductors. Chem Rev 2007;107:926-52.

[93] Koller G, Berkebile S, Oehzelt M, Puschnig P, Ambrosch-Draxl C, Netzer FP, et al. Intra- and Intermolecular Band Dispersion in an Organic Crystal. Science 2007;317:351.

[94] Jerôme Cornil DB, Jean-Philippe Calbert, and Jean-Luc Bredas. Interchain Interactions in Organic π-Conjugated Materials Impact on Electronic Structure, Optical Response, and Charge Transport. Adv Mater 2001;13:1053.

[95] J. Cornil DAdS, X. Crispin, R. Silbey, and J. L. Bre´das. Influence of Interchain Interactions on the Absorption and Luminescence of Conjugated Oligomers and Polymers: A Quantum-Chemical Characterization. J Am Chem Soc 1998;120:1289-99.

[96] Cho B, Park KS, Baek J, Oh HS, Koo Lee YE, Sung MM. Single-Crystal Poly(3,4-ethylenedioxythiophene) Nanowires with Ultrahigh Conductivity. Nano Lett 2014;14:3321-7.

[97] Winther-Jensen BF, Maria West, Keld Andreasen, Jens Wenzel Wallace, Gordon MacFarlane, Douglas R. High Current Density and Drift Velocity in Templated Conducting Polymers. Org Electron 2007;8:796-800.

[98] Ashizawa SS, Y. Shindo, H. Watanabe, Y. Okuzaki, H. Polymer FET with a conducting channel. Synthetic Met 2005;153:41-4.

[99] Anderson PW. Absence of diffusion in certain random lattices. Phys Rev 1958;109:1492.

[100] Safa Kasap P. Handbook of Electronic and Photonic Materials. Springer 2017.

[101] Yoshio Nogami HKaTI. On the metallic states in highly conducting iodine-doped polyacetylene. Solid State Commun 1990;76:583-6.

[102] Coehoorn R, Pasveer WF, Bobbert PA, Michels MAJ. Charge-Carrier Concentration Dependence of the Hopping Mobility in Organic Materials with Gaussian Disorder. Phys Rev B 2005;72:155206.

[103] Lee K, Cho S, Park SH, Heeger AJ, Lee C-W, Lee S-H. Metallic transport in polyaniline. Nature 2006;441:65-8.

[104] Fishchuk II, Arkhipov VI, Kadashchuk A, Heremans P, Bässler H. Analytic Model of Hopping Mobility at Large Charge Carrier Concentrations in Disordered Organic Semiconductors: Polarons versus Bare Charge Carriers. Phys Rev B 2007;76:045210.

[105] Mott NF. Conduction in non-crystalline materials. Philos Mag 1969;19:835-52.

[106] Nardes AM, Kemerink M, Janssen RAJ. Anisotropic hopping conduction in spin-coated PEDOT:PSS thin films. Phys Rev B 2007;76:085208.

[107] Epstein AJ, Rommelmann H, Bigelow R, Gibson HW, Hoffmann DM, Tanner DB. Role of Solitons in Nearly Metallic Polyacetylene. Phys Rev Lett 1983;50:1866-9.

[108] Glaudell AM, Cochran JE, Patel SN, Chabinyc ML. Impact of the Doping Method on Conductivity and Thermopower in Semiconducting Polythiophenes. Adv Energy Mater 2015;5:1401072.

[109] Jones TE, Ogden TR, McGinnis WC, Butler WF, Gottfredson DM. Electronic Properties of Polyacetylene Doped with $FeCl_3$. J Chem Phys 1985;83:2532-7.

[110] Kaiser AB. Thermoelectric power and conductivity of heterogeneous conducting polymers. Phys Rev B 1989;40:2806-13.

[111] Mott NF. The minimum metallic conductivity. Int Rev Phys Chem 1985;4:1-18.

[112] Mateeva N, Niculescu H, Schlenoff J, Testardi L. Correlation of Seebeck Coefficient and Electric Conductivity in Polyaniline and Polypyrrole. J Appl Phys 1998;83:3111-7.

[113] Zhang Q, Sun Y, Xu W, Zhu D. What To Expect from Conducting Polymers on the Playground of Thermoelectricity: Lessons Learned from Four High-Mobility Polymeric Semiconductors. Macromolecules 2014;47:609-15.

[114] Xuan Y, Liu X, Desbief S, Leclère P, Fahlman M, Lazzaroni R, et al. Thermoelectric Properties of Conducting Polymers: The Case of Poly(3-hexylthiophene). Phys Rev B 2010;82:115454.

[115] Zhang Q, Sun Y, Qin Y, Xu W, Zhu D. Two soluble polymers with lower ionization potentials: doping and thermoelectric properties. J Mater Chem A 2016;4:1432-9.

[116] Stevens MP. Polymer Chemistry: An Introduction. 2nd ed: Oxford University Press; 1990.

[117] Heeger AJ, Kivelson S, Schrieffer JR, Su WP. Solitons in conducting polymers. Rev Mod Phys 1988;60:781-850.

[118] Sheng P, Klafter J. Hopping conductivity in granular disordered systems. Phys Rev B 1983;27:2583-6.

[119] Xu X, Zhou J, Chen J. Thermal Transport in Conductive Polymer-Based Materials. Adv Funct Mater 2020;30:1904704.

[120] Yan H, Sada N, Toshima N. Thermal Transporting Properties of Electrically Conductive Polyaniline Films as Organic Thermoelectric Materials. J Therm Anal Calorim 2002;69:881-7.

[121] Weathers A, Khan ZU, Brooke R, Evans D, Pettes MT, Andreasen JW, et al. Significant Electronic Thermal Transport in the Conducting Polymer Poly(3,4-ethylenedioxythiophene). Adv Mater 2015;27:2101-6.

[122] Piraux L, Kinany-Alaoui M, Issi JP, Begin D, Billaud D. Thermal conductivity of an oriented polyacetylene film. Solid State Commun 1989;70:427-9.

[123] Schweizer RJ, Menke K, Roth S. Thermal conductivity of polyacetylene. J Chem Phys 1984;81:6301-3.

[124] Chen H, Ginzburg VV, Yang J, Yang Y, Liu W, Huang Y, et al. Thermal conductivity of polymer-based composites: Fundamentals and applications. Prog Polym Sci 2016;59:41-85.

[125] Wu J, Sun Y, Pei W-B, Huang L, Xu W, Zhang Q. Polypyrrole Nanotube Film for Flexible Thermoelectric Application. Synthetic Met 2014;196:173-7.

[126] Bao-Yang L, Cong-Cong L, Shan L, Jing-Kun X, Feng-Xing J, Yu-Zhen L, et al. Thermoelectric Performances of Free-Standing Polythiophene and Poly(3-Methylthiophene) Nanofilms. Chinese Phys Lett 2010;27:057201.

[127] Rausch S, Rauh D, Deibel C, Vidi S, Ebert HP. Thin-film thermal-conductivity measurement on semi-conducting polymer material using the 3ω technique. Int J Thermophys 2013;34:820-30.

[128] Scholdt M, Do H, Lang J, Gall A, Colsmann A, Lemmer U, et al. Organic Semiconductors for Thermoelectric Applications. J Electron Mater 2010;39:1589-92.

[129] Sun Y, Sheng P, Di C, Jiao F, Xu W, Qiu D, et al. Organic Thermoelectric Materials and Devices Based on p-and n-Type Poly(metal 1,1,2,2-ethenetetrathiolate)s. Adv Mater 2012;24:932-7.

[130] Moses D, Denenstein A. Experimental determination of the thermal conductivity of a conducting polymer: Pure and heavily doped polyacetylene. Phys Rev B 1984;30:2090-7.

[131] Feng-Xing J, Jing-Kun X, Bao-Yang L, Yu X, Rong-Jin H, Lai-Feng L. Thermoelectric Performance of Poly(3,4-ethylenedioxythiophene): Poly(styrenesulfonate). Chinese Phys Lett 2008;25:2202-5.

[132] Culebras M, Uriol B, Gomez CM, Cantarero A. Controlling the thermoelectric properties of polymers: application to PEDOT and polypyrrole. Phys Chem Chem Phys 2015;17:15140-5.

[133] Xu L, Liu Y, Chen B, Zhao C, Lu K. Enhancement in thermoelectric properties using a p-type and n-type thin-film device structure. Polym Composite 2013;34:1728-34.

[134] Nath C, Kumar A, Kuo Y-K, Okram GS. High thermoelectric figure of merit in nanocrystalline polyaniline at low temperatures. Appl Phys Lett 2014;105:133108.

[135] Park YW. Structure and morphology: relation to thermopower properties of conductive polymers. Synthetic Met 1991;45:173-82.

[136] Henry A, Chen G. High thermal conductivity of single polyethylene chains using molecular dynamics simulations. Phys Rev Lett 2008;101:235502.

[137] Yorifuji D, Ando S. Molecular Structure Dependence of Out-of-Plane Thermal Diffusivities in Polyimide Films: A Key Parameter for Estimating Thermal Conductivity of Polymers. Macromolecules 2010;43:7583-93.

[138] Kumar HGCaS. Making Strong Fibers. Science 2008;43:7583-93.

[139] Yamanaka A, Takao T. Thermal Conductivity of High-Strength Polyethylene Fiber and Applications for Cryogenic Use. ISRN Mater Sci 2011;2011:1-10.

[140] Xu Y, Kraemer D, Song B, Jiang Z, Zhou J, Loomis J, et al. Nanostructured Polymer Films with Metal-like Thermal Conductivity. Nat Commun 2019;10:1771.

[141] Liu J, Yang R. Length-dependent thermal conductivity of single extended polymer chains. Phys Rev B 2012;86:104307.

[142] Zhang T, Luo T. Morphology-influenced thermal conductivity of polyethylene single chains and crystalline fibers. J Appl Phys 2012;112:094304.

[143] Zhang T, Wu X, Luo T. Polymer Nanofibers with Outstanding Thermal Conductivity and Thermal Stability: Fundamental Linkage between Molecular Characteristics and Macroscopic Thermal Properties. J Phys Chem C 2014;118:21148-59.

[144] Luo T, Esfarjani K, Shiomi J, Henry A, Chen G. Molecular Dynamics Simulation of Thermal Energy Transport in Polydimethylsiloxane. J Appl Phys 2011;109:074321.

[145] Yu J, Sundqvist B, Tonpheng B, Andersson O. Thermal conductivity of highly crystallized polyethylene. Polymer 2014;55:195-200.

[146] Aghelinejad M, Leung SN. Enhancement of Thermoelectric Conversion Efficiency of Polymer/Carbon Nanotube Nanocomposites through Foaming - Induced Microstructuring. J Appl Polym Sci 2017;134:45073.

[147] Choy CL. Thermal conductivity of polymers. Polymer 1977;18:984-1004.

[148] Kurabayashi K. Anisotropic thermal properties of solid polymers. Int J Thermophys 2001;22:277-88.

[149] Y.S. Ju KK, K.E. Goodson. Thermal characterization of anisotropic thin dielectric films using harmonic joule heating. Thin Solid Films 1999;339:160-4.

[150] Fan Z, Li P, Du D, Ouyang J. Significantly Enhanced Thermoelectric Properties of PEDOT:PSS Films through Sequential Post-Treatments with Common Acids and Bases. Adv Energy Mater 2017;7:1602116.

[151] Li Z, Sun H, Hsiao CL, Yao Y, Xiao Y, Shahi M, et al. A Free-Standing High-Output Power Density Thermoelectric Device Based on Structure-Ordered PEDOT:PSS. Adv Electron Mater 2018;4:1700496.

[152] A. G. Gibson DG, M. Sahota, I. M. Ward and C. L. Choy, J. Thermal conductivity of ultrahigh -modulus polyethylene. J Polym Sci Pol Lett Ed 1977;15:183-92.

[153] Wang L, Liu Y, Zhang Z, Wang B, Qiu J, Hui D, et al. Polymer Composites-Based Thermoelectric Materials and Devices. Compos Part B-eng 2017;122:145-55.

[154] Mengistie DA, Chen CH, Boopathi KM, Pranoto FW, Li LJ, Chu CW. Enhanced thermoelectric performance of PEDOT:PSS flexible bulky papers by treatment with secondary dopants. ACS Appl Mater Interfaces 2015;7:94-100.

[155] Wei Q, Mukaida M, Kirihara K, Naitoh Y, Ishida T. Polymer thermoelectric modules screen-printed on paper. RSC Adv 2014;4:28802-6.

[156] Fan Z, Du D, Yu Z, Li P, Xia Y, Ouyang J. Significant Enhancement in the Thermoelectric Properties of PEDOT:PSS Films through a Treatment with Organic Solutions of Inorganic Salts. ACS Appl Mater Interfaces 2016;8:23204-11.

[157] Fan Z, Du D, Guan X, Ouyang J. Polymer films with ultrahigh thermoelectric properties arising from significant seebeck coefficient enhancement by ion accumulation on surface. Nano Energy 2018;51:481-8.

[158] Lu G, Bu L, Li S, Yang X. Bulk Interpenetration Network of Thermoelectric Polymer in Insulating Supporting Matrix. Adv Mater 2014;26:2359-64.

[159] Lee HJ, Anoop G, Lee HJ, Kim C, Park J-W, Choi J, et al. Enhanced thermoelectric performance of PEDOT:PSS/PANI–CSA polymer multilayer structures. Energy Environ Sci 2016;9:2806-11.

[160] Zhang K, Qiu J, Wang S. Thermoelectric properties of PEDOT nanowire/PEDOT hybrids. Nanoscale 2016;8:8033-41.

[161] Liang L, Gao C, Chen G, Guo C-Y. Large-Area, Stretchable, Super Flexible and Mechanically Stable Thermoelectric Films of Polymer/Carbon Nanotube Composites. J Mater Chem C 2016;4:526-32.

[162] Wang L, Yao Q, Bi H, Huang F, Wang Q, Chen L. Large Thermoelectric Power Factor in Polyaniline/Graphene Nanocomposite Films Prepared by Solution-Assistant Dispersing Method. J Mater Chem A 2014;2:11107-13.

[163] Wang L, Yao Q, Bi H, Huang F, Wang Q, Chen L. PANI/Graphene Nanocomposite Films with High Thermoelectric Properties by Enhanced Molecular Ordering. J Mater Chem A 2015;3:7086-92.

[164] Cho C, Wallace KL, Tzeng P, Hsu JH, Yu C, Grunlan JC. Outstanding Low Temperature Thermoelectric Power Factor from Completely Organic Thin Films Enabled by Multidimensional Conjugated Nanomaterials. Adv Energy Mater 2016;6:1502168.

[165] Cho C, Stevens B, Hsu J-H, Bureau R, Hagen DA, Regev O, et al. Completely Organic Multilayer Thin Film with Thermoelectric Power Factor Rivaling Inorganic Tellurides. Adv Mater 2015;27:2996-3001.

[166] Meng C, Liu C, Fan S. A Promising Approach to Enhanced Thermoelectric Properties Using Carbon Nanotube Networks. Adv Mater 2010;22:535-9.

[167] Yao Q, Wang Q, Wang L, Chen L. Abnormally Enhanced Thermoelectric Transport Properties of SWNT/PANI Hybrid Films by the Strengthened PANI Molecular Ordering. Energy Environ Sci 2014;7:3801-7.

[168] Wang L, Yao Q, Xiao J, Zeng K, Qu S, Shi W, et al. Engineered Molecular Chain Ordering in Single-Walled Carbon Nanotubes/Polyaniline Composite Films for High-Performance Organic Thermoelectric Materials. Chem Asian J 2016;11:1804-10.

[169] Wang L, Yao Q, Shi W, Qu S, Chen L. Engineering Carrier Scattering at the Interfaces in Polyaniline Based Nanocomposites for High Thermoelectric Performances. Mater Chem Front 2017;1:741-8.

[170] Wang H, Yi S-i, Pu X, Yu C. Simultaneously Improving Electrical Conductivity and Thermopower of Polyaniline Composites by Utilizing Carbon Nanotubes as High Mobility Conduits. ACS Appl Mater Interfaces 2015;7:9589-97.

[171] An CJ, Kang YH, Lee AY, Jang K-S, Jeong Y, Cho SY. Foldable Thermoelectric Materials: Improvement of the Thermoelectric Performance of Directly Spun CNT Webs by Individual Control of Electrical and Thermal Conductivity. ACS Appl Mater Interfaces 2016;8:22142-50.

[172] Wang Y, Zhang SM, Deng Y. Flexible Low-Grade Energy Utilization Devices Based on High-Performance Thermoelectric Polyaniline/Tellurium Nanorod Hybrid Films. J Mater Chem A 2016;4:3554-9.

[173] Chatterjee K, Mitra M, Kargupta K, Ganguly S, Banerjee D. Synthesis, Characterization and Enhanced Thermoelectric Performance of Structurally Ordered Cable-Like Novel Polyaniline–Bismuth Telluride Nanocomposite. Nanotechnology 2013;24:215703.

[174] Bounioux C, Díaz-Chao P, Campoy-Quiles M, Martín-González MS, Goñi AR, Yerushalmi-Rozen R, et al. Thermoelectric Composites of Poly(3-hexylthiophene) and Carbon Nanotubes with a Large Power Factor. Energy Environ Sci 2013;6:918-25.

[175] Hong CT, Lee W, Kang YH, Yoo Y, Ryu J, Cho SY, et al. Effective Doping by Spin-Coating and Enhanced Thermoelectric Power Factors in SWCNT/P3HT Hybrid Films. J Mater Chem A 2015;3:12314-9.

[176] He M, Ge J, Lin Z, Feng X, Wang X, Lu H, et al. Thermopower Enhancement in Conducting Polymer Nanocomposites *via* Carrier Energy Scattering at the Organic–Inorganic Semiconductor Interface. Energy Environ Sci 2012;5:8351-8.

[177] Kim D, Kim Y, Choi K, Grunlan JC, Yu C. Improved Thermoelectric Behavior of Nanotube-Filled Polymer Composites with Poly(3,4-ethylenedioxythiophene) Poly(styrenesulfonate). ACS Nano 2010;4:513–23.

[178] Zhang K, Wang S, Zhang X, Zhang Y, Cui Y, Qiu J. Thermoelectric Performance of p-Type Nanohybrids Filled Polymer Composites. Nano Energy 2015;13:327-35.

[179] Choi J, Lee JY, Lee S-S, Park CR, Kim H. High-Performance Thermoelectric Paper Based on Double Carrier-Filtering Processes at Nanowire Heterojunctions. Adv Energy Mater 2016;6:1502181.

[180] Song H, Qiu Y, Wang Y, Cai K, Li D, Deng Y, et al. Polymer/Carbon Nanotube Composite Materials for Flexible Thermoelectric Power Generator. Compos Sci Technol 2017;153:71-83.

[181] Lee W, Kang YH, Lee JY, Jang K-S, Cho SY. Improving the Thermoelectric Power Factor of CNT/PEDOT:PSS Nanocomposite Films by Ethylene Glycol Treatment. RSC Adv 2016;6:53339-44.

[182] Yusupov K, Stumpf S, You S, Bogach A, Martinez PM, Zakhidov A, et al. Flexible Thermoelectric Polymer Composites Based on a Carbon Nanotubes Forest. Adv Funct Mater 2018;28:1801246.

[183] Ju H, Park D, Kim K, Kim J. Chemical Exfoliation of $SnSe_{1-x}Te_x$ Nanosheets with Conductive PEDOT:PSS for Flexible Thermoelectric Composite Films. J Alloys Compd 2019;792:638-43.

[184] Ju H, Park D, Kim J. Effect of Polymer Nanolayers on Tin-Chalcogenide Nanosheet/Conductive Polymer Flexible Composite Films and Their Enhanced Thermoelectric Performance. Nanoscale 2019;11:8502-9.

[185] Ju H, Park D, Kim J. Thermoelectric Enhancement in Multilayer Thin-Films of Tin Chalcogenide Nanosheets/Conductive Polymers. Nanoscale 2019;11:16114-21.

[186] Lee D, Sayed SY, Lee S, Kuryak CA, Zhou J, Chen G, et al. Quantitative Analyses of Enhanced Thermoelectric Properties of Modulation-Doped PEDOT:PSS/Undoped Si (001) Nanoscale Heterostructures. Nanoscale 2016;8:19754-60.

[187] See KC, Feser JP, Chen CE, Majumdar A, Urban JJ, Segalman RA. Water-Processable Polymer-Nanocrystal Hybrids for Thermoelectrics. Nano Lett 2010;10:4664-7.

[188] Song H, Cai K. Preparation and Properties of PEDOT:PSS/Te Nanorod Composite Films for Flexible Thermoelectric Power Generator. Energy 2017;125:519-25.

[189] Coates NE, Yee SK, McCulloch B, See KC, Majumdar A, Segalman RA, et al. Effect of Interfacial Properties on Polymer–Nanocrystal Thermoelectric Transport. Adv Mater 2013;25:1629-33.

[190] Ma S, Anderson K, Guo L, Yousuf A, Ellingsworth EC, Vajner C, et al. Temperature Dependent Thermopower and Electrical Conductivity of Te Nanowire/Poly(3,4-ethylenedioxythiophene):Poly(4-styrene sulfonate) Microribbons. Appl Phys Lett 2014;105:073905.

[191] Bae EJ, Kang YH, Jang K-S, Cho SY. Enhancement of Thermoelectric Properties of PEDOT:PSS and Tellurium-PEDOT:PSS Hybrid Composites by Simple Chemical Treatment. Sci Rep 2016;6:18805.

[192] Zaia EW, Sahu A, Zhou P, Gordon MP, Forster JD, Aloni S, et al. Carrier Scattering at Alloy Nanointerfaces Enhances Power Factor in PEDOT:PSS Hybrid Thermoelectrics. Nano Lett 2016;16:3352-9.

[193] We JH, Kim SJ, Cho BJ. Hybrid Composite of Screen-Printed Inorganic Thermoelectric Film and Organic Conducting Polymer for Flexible Thermoelectric Power Generator. Energy 2014;73:506-12.

[194] Jiang F, Xiong J, Zhou W, Liu C, Wang L, Zhao F, et al. Use of Organic Solvent-Assisted Exfoliated MoS_2 for Optimizing the Thermoelectric Performance of Flexible PEDOT:PSS Thin Films. J Mater Chem A 2016;4:5265-73.

[195] Zhou W, Fan Q, Zhang Q, Cai L, Li K, Gu X, et al. High-Performance and Compact-Designed Flexible Thermoelectric Modules Enabled by a Reticulate Carbon Nanotube Architecture. Nat Commun 2017;8:14886.

[196] Wan C, Gu X, Dang F, Itoh T, Wang Y, Sasaki H, et al. Flexible n-type thermoelectric materials by organic intercalation of layered transition metal dichalcogenide TiS_2. Nat Mater 2015;14:622-7.

[197] Xu Q, Qu S, Ming C, Qiu P, yao q, Zhu C, et al. Conformal Organic-Inorganic Semiconductor Composites for Flexible Thermoelectrics. Energy Environ Sci 2020;13:511-8.

[198] Xiao C, Xue Y, Liu M, Xu X, Wu X, Wang Z, et al. Polymer Composites with Lychee-Like Core Covered by Segregated Conducting and Flexible Networks: Unique Morphology, High Flexibility, Stretchability and Thermoelectric Performance. Compos Sci Technol 2018;161:16-21.

[199] Suemori K, Watanabe Y, Hoshino S. Carbon Nanotube Bundles/Polystyrene Composites as High-Performance Flexible Thermoelectric Materials. Appl Phys Lett 2015;106:113902.

[200] Li F, Cai K, Shen S, Chen S. Preparation and Thermoelectric Properties of Reduced Graphene Oxide/PEDOT:PSS Composite Films. Synthetic Met 2014;197:58-61.

[201] Xu S, Hong M, Shi X-L, Wang Y, Ge L, Bai Y, et al. High-Performance PEDOT:PSS Flexible Thermoelectric Materials and Their Devices by Triple Post-Treatments. Chem Mater 2019;31:5238-44.

[202] Yao Q, Chen L, Zhang W, Liufu S, Chen X. Enhanced Thermoelectric Performance of Single-Walled Carbon Nanotubes/Polyaniline Hybrid Nanocomposites. ACS Nano 2010;4:2445-51.

[203] Ju H, Park D, Kim J. Solution-Processable Flexible Thermoelectric Composite Films Based on Conductive Polymer/$SnSe_{0.8}S_{0.2}$ Nanosheets/Carbon Nanotubes for Wearable Electronic Applications. J Mater Chem A 2018;6:5627-34.

[204] Yu C, Choi K, Yin L, Grunlan JC. Light-Weight Flexible Carbon Nanotube Based Organic Composites with Large Thermoelectric Power Factors. ACS Nano 2011;5:7885-92.

[205] Ju H, Kim J. Fabrication of Conductive Polymer/Inorganic Nanoparticles Composite Films: PEDOT:PSS with Exfoliated Tin Selenide Nanosheets for Polymer-Based Thermoelectric Devices. Chem Eng J 2016;297:66-73.

[206] Lu B, Chen S, Xu J, Zhao G. Thermoelectric Performances of Different Types of Polyselenophene and its Copolymers with 3-Methylthiophene via Electropolymerization. Synthetic Met 2013;183:8-15.

[207] Lee WP, Park YW, Choi YS. Metallic electrical transport of pf6-doped polypyrrole : Dc conductivity and thermoelectric power. Synthetic Met 1997;84:841-2.

[208] Kemp NT, Kaiser AB, Liu CJ, Chapman B, Mercier O, Carr AM, et al. Thermoelectric power and conductivity of different types of polypyrrole. J Polym Sci Pol Phys 1999;37:953-60.

[209] Yue R, Chen S, Lu B, Liu C, Xu J. Facile electrosynthesis and thermoelectric performance of electroactive free-standing polythieno[3,2-*b*]thiophene films. J Solid State Electr 2011;15:539-48.

[210] Hiraishi KM, Akito Nakanishi, Hachiro Oikawa, Hidetoshi Shinohara, Yosikazu. Evaluation of Thermoelectric Properties of Polythiophene Films Synthesized by Electrolytic Polymerization. Jpn J Appl Phys 2009;48:071501.

[211] Qu S, Yao Q, Wang L, Chen Z, Xu K, Zeng H, et al. Highly Anisotropic P3HT Films with Enhanced Thermoelectric Performance *via* Organic Small Molecule Epitaxy. NPG Asia Mater 2016;8:e292-e.

[212] Kee S, Haque MA, Corzo D, Alshareef HN, Baran D. Self-Healing and Stretchable 3D-Printed Organic Thermoelectrics. Adv Funct Mater 2019;29:1905426.

[213] Imae I, Goto T, Ooyama Y, Harima Y. Thermoelectric properties of poly(3,4-ethylenedioxythiophene) with fluorine-containing polyanion as dopant. Polymer 2020;199:122538.

[214] Akbar ZA, Jeon J-W, Jang S-Y. Intrinsically self-healable, stretchable thermoelectric materials with a large ionic Seebeck effect. Energy Environ Sci 2020;13:2915-23.

[215] Kim N, Lienemann S, Petsagkourakis I, Alemu Mengistie D, Kee S, Ederth T, et al. Elastic conducting polymer composites in thermoelectric modules. Nat Commun 2020;11:1424.

[216] Wang X, Xu J, Liu G, Fu Y, Liu Z, Tan X, et al. Optimization of Thermoelectric Properties in n-Type SnSe Doped with $BiCl_3$. Appl Phys Lett 2016;108:083902.

[217] Sarkar K, Debnath A, Deb K, Bera A, Saha B. Effect of NiO incorporation in charge transport of polyaniline: Improved polymer based thermoelectric generator. Energy 2019;177:203-10.

[218] Wang S, Liu F, Gao C, Wan T, Wang L, Wang L, et al. Enhancement of the thermoelectric property of nanostructured polyaniline/carbon nanotube composites by introducing pyrrole unit onto polyaniline backbone *via* a sustainable method. Chem Eng J 2019;370:322-9.

[219] Kim S-i, Lee KY, Lim J-H. Fabrication of PEDOT: PSS-PVP Nanofiber-Embedded Sb_2Te_3 Thermoelectric Films by Multi-Step Coating and Their Improved Thermoelectric Properties. Materials 2020;13:2835.

[220] Meng Q, Jiang Q, Cai K, Chen L. Preparation and thermoelectric properties of PEDOT:PSS coated Te nanorod/PEDOT:PSS composite films. Org Electron 2019;64:79-85.

[221] Fan W, Liang L, Zhang B, Guo C-Y, Chen G. PEDOT thermoelectric composites with excellent power factors prepared by 3-phase interfacial electropolymerization and carbon nanotube chemical doping. J Mater Chem A 2019;7:13687-94.

[222] Wang Y, Hong M, Liu W-D, Shi X-L, Xu S-D, Sun Q, et al. $Bi_{0.5}Sb_{1.5}Te_3$/PEDOT:PSS-Based Flexible Thermoelectric Film and Device. Chem Eng J 2020;397:125360.

[223] Lu Y, Ding Y, Qiu Y, Cai K, Yao Q, Song H, et al. Good Performance and Flexible PEDOT:PSS/Cu_2Se Nanowire Thermoelectric Composite Films. ACS Appl Mater Interfaces 2019;11:12819-29.

[224] Ni D, Song H, Chen Y, Cai K. Significantly enhanced thermoelectric performance of flexible PEDOT nanowire film *via* coating Te nanostructures. J Materiomics 2020;6:364-70.

[225] Feng K, Guo H, Wang J, Shi Y, Wu Z, Su M, et al. Cyano-Functionalized Bithiophene Imide-Based n-Type Polymer Semiconductors: Synthesis, Structure–Property Correlations, and Thermoelectric Performance. J Am Chem Soc 2021;143:1539-52.

[226] Kluge RM, Saxena N, Chen W, Körstgens V, Schwartzkopf M, Zhong Q, et al. Doping Dependent In-Plane and Cross-Plane Thermoelectric Performance of Thin n-Type Polymer P(NDI2OD-T2) Films. Adv Funct Mater 2020;30:2003092.

[227] Kim B, Hwang JU, Kim E. Chloride transport in conductive polymer films for an n-type thermoelectric platform. Energy Environ Sci 2020;13:859-67.

[228] Guan X, Yildirim E, Fan Z, Lu W, Li B, Zeng K, et al. Thermoelectric polymer films with a significantly high Seebeck coefficient and thermoelectric power factor obtained through surface energy filtering. J Mater Chem A 2020;8:13600-9.

[229] Yang C-Y, Stoeckel M-A, Ruoko T-P, Wu H-Y, Liu X, Kolhe NB, et al. A high-conductivity n-type polymeric ink for printed electronics. Nat Commun 2021;12:2354.

[230] Hu S, Zeng S, Li X, Jiang J, Yang W, Chen Y, et al. Flexible and high performance of n-type thermoelectric PVDF composite film induced by nickel nanowires. Mater Design 2020;188:108496.

[231] Tang J, Chen R, Chen L, Bazan GC, Liang Z. Semiconducting polymer contributes favorably to the Seebeck coefficient in multi-component, high-performance n-type thermoelectric nanocomposites. J Mater Chem A 2020;8:9797-805.

[232] Wu J, Sun Y, Xu W, Zhang Q. Investigating thermoelectric properties of doped polyaniline nanowires. Synthetic Met 2014;189:177-82.

[233] Geethalakshmi D, Muthukumarasamy N, Balasundaraprabhu R. CSA-doped PANI semiconductor nanofilms: synthesis and characterization. J Mater Sci-Mater El 2015;26:7797-803.

[234] Lee J-H, Kim H-M, Kim K-B, Kabe R, Anzenbacher P, Kim J-J. Homogeneous dispersion of organic *p*-dopants in an organic semiconductor as an origin of high charge generation efficiency. Appl Phys Lett 2011;98:173303.

[235] Tietze ML, Burtone L, Riede M, Lüssem B, Leo K. Fermi Level Shift and Doping Efficiency in *p*-doped Small Molecule Organic Semiconductors: A Photoelectron Spectroscopy and Theoretical Study. Phys Rev B 2012;86:035320.

[236] Zhang Y, de Boer B, Blom PWM. Controllable Molecular Doping and Charge Transport in Solution-Processed Polymer Semiconducting Layers. Adv Funct Mater 2009;19:1901-5.

[237] Pingel P, Neher D. Comprehensive picture of p-type doping of P3HT with the molecular acceptor F4TCNQ. Phys Rev B 2013;87:115209.

[238] Zhu L, Kim E-G, Yi Y, Brédas J-L. Charge Transfer in Molecular Complexes with 2,3,5,6-Tetrafluoro-7,7,8,8-tetracyanoquinodimethane (F4-TCNQ): A Density Functional Theory Study. Chem Mater 2011;23:5149-59.

[239] Bender CJ. Theoretical Models of Charge-transfer Complexes. Chem Soc Rev 1986;15:475-502.

[240] Goetz KP, Vermeulen D, Payne ME, Kloc C, McNeil LE, Jurchescu OD. Charge-transfer complexes: new perspectives on an old class of compounds. J Mater Chem C 2014;2:3065-76.

[241] Yim K-H, Whiting GL, Murphy CE, Halls JJM, Burroughes JH, Friend RH, et al. Controlling Electrical Properties of Conjugated Polymers *via* a Solution-Based p-Type Doping. Adv Mater 2008;20:3319-24.

[242] Avilov I, Geskin V, Cornil J. Quantum-Chemical Characterization of the Origin of Dipole Formation at Molecular Organic/Organic Interfaces. Adv Funct Mater 2009;19:624-33.

[243] Crispin X, Marciniak S, Osikowicz W, Zotti G, Gon AWDVD, Fahlman M, et al. Conductivity, morphology, interfacial chemistry, and stability of poly(3,4-ethylene dioxythiophene)-poly(styrene sulfonate): A photoelectron spectroscopy study. J Polym Sci Pol Phys 2003;41:2561-83.

[244] Kim JY, Jung JH, D.E. Lee JJ. Enhancement of electrical conductivity of poly(3,4-ethylenedioxythiophene)poly(4-styrenesulfonate) by a change of solvents. Synthetic Met 2002;126:311-6.

[245] Kim WH, Mäkinen AJ, Nikolov N, Shashidhar R, Kim H, Kafafi ZH. Molecular organic light-emitting diodes using highly conducting polymers as anodes. Appl Phys Lett 2002;80:3844-6.

[246] Epstein AGMaAJ. Secondary doping in polyaniline. Synthetic Met 1995;69:85-92.

[247] Leif A.A. Pettersson SG, Olle Inganas. Optical anisotropy in thin films of poly(3,4-ethylenedioxythiophene)–poly(4-styrenesulfonate). Org Electron 2002;3:143-8.

[248] Luo J, Billep D, Waechtler T, Otto T, Toader M, Gordan O, et al. Enhancement of the Thermoelectric Properties of PEDOT:PSS Thin Films by Post-Treatment. J Mater Chem A 2013;1:7576-83.

[249] Wang Y, Zhu C, Pfattner R, Yan H, Jin L, Chen S, et al. A highly stretchable, transparent, and conductive polymer. Sci Adv 2017;3:e1602076.

[250] Nogami Y. Structure of highly conducting PF^{6-}-doped polypyrrole. Synthetic Met 1994;62:257-63.

[251] Skotheim TA, Reynolds J. Handbook of Conducting Polymers, 2 Volume Set: CRC press; 2007.

[252] Yang X, Loos J, Veenstra SC, Verhees WJ, Wienk MM, Kroon JM, et al. Nanoscale Morphology of High-Performance Polymer Solar Cells. Nano Lett 2005;5:579-83.

[253] Mihailetchi VD, Xie HX, de Boer B, Koster LJA, Blom PWM. Charge Transport and Photocurrent Generation in Poly(3-hexylthiophene): Methanofullerene Bulk-Heterojunction Solar Cells. Adv Funct Mater 2006;16:699-708.

[254] Erb T, Zhokhavets U, Gobsch G, Raleva S, Stühn B, Schilinsky P, et al. Correlation Between Structural and Optical Properties of Composite Polymer/Fullerene Films for Organic Solar Cells. Adv Funct Mater 2005;15:1193-6.

[255] Migliaccio L, Manini P, Altamura D, Giannini C, Tassini P, Maglione MG, et al. Evidence of Unprecedented High Electronic Conductivity in Mammalian Pigment Based Eumelanin Thin Films After Thermal Annealing in Vacuum. Front Chem 2019;7:162.

[256] Yano H, Kudo K, Marumo K, Okuzaki H. Fully soluble self-doped poly(3,4-ethylenedioxythiophene) with an electrical conductivity greater than 1000 S cm^{-1}. Sci Adv 2019;5:eaav9492.

[257] Xu Y, Jia Y, Liu P, Jiang Q, Hu D, Ma Y. Poly(3,4-ethylenedioxythiophene) (PEDOT) as promising thermoelectric materials and devices. Chem Eng J 2021;404:126552.

[258] Yemata TA, Zheng Y, Kyaw AKK, Wang X, Song J, Chin WS, et al. Binary treatment of PEDOT:PSS films with nitric acid and imidazolium-based ionic liquids to improve the thermoelectric properties. Mater Adv 2020;1:3233-42.

[259] Alemu D, Wei H-Y, Ho K-C, Chu C-W. Highly conductive PEDOT:PSS electrode by simple film treatment with methanol for ITO-free polymer solar cells. Energy Environ Sci 2012;5:9662-71.

[260] Yu Z, Xia Y, Du D, Ouyang J. PEDOT:PSS Films with Metallic Conductivity through a Treatment with Common Organic Solutions of Organic Salts and Their Application as a Transparent Electrode of Polymer Solar Cells. ACS Appl Mater Interfaces 2016;8:11629-38.

[261] Luo J, Billep D, Blaudeck T, Sheremet E, Rodriguez RD, Zahn DRT, et al. Chemical post-treatment and thermoelectric properties of poly(3,4-ethylenedioxylthiophene):poly(styrenesulfonate) thin films. J Appl Phys 2014;115:054908.

[262] Zhao J, Tan D, Chen G. A strategy to improve the thermoelectric performance of conducting polymer nanostructures. J Mater Chem C 2017;5:47-53.

[263] Wu X, Liu J, He G. A highly conductive PEDOT:PSS film with the dipping treatment by hydroiodic acid as anode for organic light emitting diode. Org Electron 2015;22:160-5.

[264] Meng W, Ge R, Li Z, Tong J, Liu T, Zhao Q, et al. Conductivity Enhancement of PEDOT:PSS Films *via* Phosphoric Acid Treatment for Flexible All-Plastic Solar Cells. ACS Appl Mater Interfaces 2015;7:14089-94.

[265] Li Z, Ma G, Ge R, Qin F, Dong X, Meng W, et al. Free-Standing Conducting Polymer Films for High-Performance Energy Devices. Angew Chem Int Ed 2016;55:979-82.

[266] Lee SH, Park H, Kim S, Son W, Cheong IW, Kim JH. Transparent and flexible organic semiconductor nanofilms with enhanced thermoelectric efficiency. J Mater Chem A 2014;2:7288-94.

[267] Tsai T-C, Chang H-C, Chen C-H, Huang Y-C, Whang W-T. A facile dedoping approach for effectively tuning thermoelectricity and acidity of PEDOT:PSS films. Org Electron 2014;15:641-5.

[268] Zhu Z, Liu C, Jiang F, Xu J, Liu E. Effective Treatment Methods on PEDOT:PSS to Enhance Its Thermoelectric Performance. Synthetic Met 2017;225:31-40.

[269] Yang E, Kim J, Jung BJ, Kwak J. Enhanced thermoelectric properties of sorbitol-mixed PEDOT:PSS thin films by chemical reduction. J Mater Sci-Mater El 2015;26:2838-43.

[270] Carothers WH. Polymerization. Chem Rev 1931;8:353-426.

[271] Jurgen Heinze BAF-U, and Sabine Ludwigs. Electrochemistry of conducting polymers-persistent models and new concepts. Chem Rev 2010;110:4724-71.

[272] Poverenov EL, Mao Bitler, Arkady Bitler, Bendikov Michael. Major Effect of Electropolymerization Solvent on Morphology and Electrochromic Properties of PEDOT Films. Chem Mater 2010;22:4019-25.

[273] L. Groenendaal GZ, Pierre-Henri Aubert, Shane M. Waybright, and John R. Reynolds. Electrochemistry of Poly(3,4-alkylenedioxythiophene) Derivatives. Adv Mater 2003;15:11.

[274] Li Niu CK, K. Fro¨berg, Ari Ivaska. Electrochemically controlled surface morphology and crystallinityin poly(3,4-ethylenedioxythiophene) films. Synthetic Met 2001;122:425-9.

[275] Xu K, Chen G, Qiu D. *In Situ* Chemical Oxidative Polymerization Preparation of Poly(3,4-ethylenedioxythiophene)/Graphene Nanocomposites with Enhanced Thermoelectric Performance. Chem-Asian J 2015;10:1225-31.

[276] Fabretto MV, Evans DR, Mueller M, Zuber K, Hojati-Talemi P, Short RD, et al. Polymeric Material with Metal-Like Conductivity for Next Generation Organic Electronic Devices. Chem Mater 2012;24:3998-4003.

[277] Yasuo Kudoh KA, Yasue Matsuya. Chemical polymerization of 3,4-ethylenedioxythiophene using an aqueous medium containing an anionic surfactant. Synthetic Met 1998;98:65–70.

[278] Evans D, Fabretto M, Mueller M, Zuber K, Short R, Murphy P. Structure-directed growth of high conductivity PEDOT from liquid-like oxidant layers during vacuum vapor phase polymerization. J Mater Chem 2012;22:14889.

[279] Kim JY, Kwon MH, Min YK, Kwon S, Ihm DW. Self-Assembly and Crystalline Growth of Poly(3,4-ethylenedioxythiophene) Nanofilms. Adv Mater 2007;19:3501-6.

[280] Alexis Laforgue LR. Production of Conductive PEDOT Nanofibers by the Combination of Electrospinning and Vapor-Phase Polymerization. Macromolecules 2010;43:4194-200.

[281] Kim B, Shin H, Park T, Lim H, Kim E. NIR-sensitive poly(3,4-ethylenedioxyselenophene) derivatives for transparent photo-thermo-electric converters. Adv Mater 2013;25:5483-9.

[282] Cheng N, Zhang L, Joon Kim J, Andrew TL. Vapor phase organic chemistry to deposit conjugated polymer films on arbitrary substrates. J Mater Chem C 2017;5:5787-96.

[283] Taggart DK, Yang Y, Kung S-C, McIntire TM, Penner RM. Enhanced Thermoelectric Metrics in Ultra-long Electrodeposited PEDOT Nanowires. Nano Lett 2011;11:125-31.

[284] L. Groenendaal FJ, Dieter Freitag, Harald Pielartzik, and John R. Reynolds. Poly(3,4 - ethylenedioxythiophene) and Its Derivatives Past, Present, and Future. Adv Mater 2000;12:481-94.

[285] Zuber K, Fabretto M, Hall C, Murphy P. Improved PEDOT Conductivity *via* Suppression of Crystallite Formation in Fe(III) Tosylate During Vapor Phase Polymerization. Macromol Rapid Comm 2008;29:1503-8.

[286] Masubuchi S, Kazama S, Mizoguchi K, Shimizu F, Kume K, Matsushita R, et al. The transport properties of metallic Shirakawa polyacetylenes with different dopant species. Synthetic Met 1995;69:71-2.

[287] Huang D, Zou Y, Jiao F, Zhang F, Zang Y, Di C-a, et al. Interface-Located Photothermoelectric Effect of Organic Thermoelectric Materials in Enabling NIR Detection. ACS Appl Mater Interfaces 2015;7:8968-73.

[288] Sun Y, Qiu L, Tang L, Geng H, Wang H, Zhang F, et al. Flexible n-Type High-Performance Thermoelectric Thin Films of Poly(nickel-ethylenetetrathiolate) Prepared by an Electrochemical Method. Adv Mater 2016;28:3351-8.

[289] Ding J, Liu Z, Zhao W, Jin W, Xiang L, Wang Z, et al. Selenium-Substituted Diketopyrrolopyrrole Polymer for High-Performance p-Type Organic Thermoelectric Materials. Angew Chem Int Ed 2019;58:18994-9.

[290] Moshwan R, Yang L, Zou J, Chen Z-G. Eco-friendly SnTe Thermoelectric Materials: Progress and Future Challenge. Adv Funct Mater 2017;27:1703278.

[291] Moshwan R, Liu W-D, Shi X-L, Wang Y-P, Zou J, Chen Z-G. Realizing High Thermoelectric Properties of SnTe *via* Synergistic Band Engineering and Structure Engineering. Nano Energy 2019;65:104056.

[292] Liu W-D, Shi X-L, Moshwan R, Yang L, Chen Z-G, Zou J. Solvothermal Synthesis of High-Purity Porous $Cu_{1.7}Se$ Approaching Low Lattice Thermal Conductivity. Chem Eng J 2019;375:121996.

[293] Liu W, Shi X-L, Moshwan R, Sun Q, Yang L, Chen Z-G, et al. Effectively restricting MnSi precipitates for simultaneously enhancing the Seebeck coefficient and electrical conductivity in higher manganese silicide. J Mater Chem C 2019;7:7212-8.

[294] Liu W, Shi X-L, Gao H, Moshwan R, Xu S, Wang Y, et al. Kinetic Condition Driven Phase and Vacancy Enhancing Thermoelectric Performance of Low-cost and Eco-friendly $Cu_{2-x}S$. J Mater Chem C 2019;7:5366-73.

[295] Moshwan R, Shi X-L, Liu W-D, Wang Y, Xu S, Zou J, et al. Enhancing Thermoelectric Properties of InTe Nanoprecipitate-Embedded $Sn_{1-x}In_xTe$ Microcrystals through Anharmonicity and Strain Engineering. ACS Appl Energy Mater 2019;2:2965-71.

[296] Liu W, Shi X, Hong M, Yang L, Moshwan R, Chen Z-G, et al. Ag Doping Induced Abnormal Lattice Thermal Conductivity in Cu_2Se. J Mater Chem C 2018;6:13225-31.

[297] Moshwan R, Shi X-L, Liu W-D, Yang L, Wang Y, Hong M, et al. High Thermoelectric Performance in Sintered Octahedron-Shaped $Sn(CdIn)_xTe_{1+2x}$ Microcrystals. ACS Appl Mater Interfaces 2018;10:38944-52.

[298] Liu W, Shi X, Moshwan R, Hong M, Yang L, Chen Z-G, et al. Enhancing Thermoelectric Performance of $(Cu_{1-x}Ag_x)_2Se$ *via* CuAgSe Secondary Phase and Porous Design. Sustain Mater Technol 2018;17:e00076.

[299] Shi X-L, Tao X, Zou J, Chen Z-G. High-performance Thermoelectric SnSe: Aqueous Synthesis, Innovations, and Challenges. Adv Sci 2020;7:1902923.

[300] Chen Z-G, Shi X, Zhao L-D, Zou J. High-Performance SnSe Thermoelectric Materials: Progress and Future Challenge. Prog Mater Sci 2018;97:283-346.

[301] Shi X-L, Chen W-Y, Tao X, Zou J, Chen Z-G. Rational Structure Design and Manipulation Advance SnSe Thermoelectrics. Mater Horiz 2020;7:3065-96.

[302] Dun C, Hewitt CA, Huang H, Xu J, Zhou C, Huang W, et al. Flexible n-type thermoelectric films based on Cu-doped Bi_2Se_3 nanoplate and Polyvinylidene Fluoride composite with decoupled Seebeck coefficient and electrical conductivity. Nano Energy 2015;18:306-14.

[303] Liu W-D, Yu Y, Dargusch M, Liu Q, Chen Z-G. Carbon allotrope hybrids advance thermoelectric development and applications. Renew Sust Energ Rev 2021;141:110800.

[304] Shao Y, Wang J, Wu H, Liu J, Aksay IA, Lin Y. Graphene Based Electrochemical Sensors and Biosensors: A Review. Electroanal 2010;22:1027-36.

[305] Li X, Zhang G, Bai X, Sun X, Wang X, Wang E, et al. Highly conducting graphene sheets and Langmuir-Blodgett films. Nat Nano 2008;3:538-42.

[306] Lee C, Wei X, Kysar JW, Hone J. Measurement of the Elastic Properties and Intrinsic Strength of Monolayer Graphene. Science 2008;321:385.

[307] Kim GH, Hwang DH, Woo SI. Thermoelectric Properties of Nanocomposite Thin Films Prepared with Poly(3,4-ethylenedioxythiophene) Poly(styrenesulfonate) and Graphene. Phys Chem Chem Phys 2012;14:3530-6.

[308] Du Y, Shen SZ, Yang W, Donelson R, Cai K, Casey PS. Simultaneous increase in conductivity and Seebeck coefficient in a polyaniline/graphene nanosheets thermoelectric nanocomposite. Synthetic Met 2012;161:2688-92.

[309] Erden F, Li H, Wang X, Wang F, He C. High-performance thermoelectric materials based on ternary TiO_2/CNT/PANI composites. Phys Chem Chem Phys 2018;20:9411-8.

[310] Abad B, Alda I, Díaz-Chao P, Kawakami H, Almarza A, Amantia D, et al. Improved power factor of polyaniline nanocomposites with exfoliated graphene nanoplatelets (GNPs). J Mater Chem A 2013;1:10450-7.

[311] Toshima N, Oshima K, Anno H, Nishinaka T, Ichikawa S, Iwata A, et al. Novel Hybrid Organic Thermoelectric Materials: Three-Component Hybrid Films Consisting of a Nanoparticle Polymer Complex, Carbon Nanotubes, and Vinyl Polymer. Adv Mater 2015;27:2246-51.

[312] Feng N, Gao C, Guo C-Y, Chen G. Copper-Phenylacetylide Nanobelt/Single-Walled Carbon Nanotube Composites: Mechanochromic Luminescence Phenomenon and Thermoelectric Performance. ACS Appl Mater Interfaces 2018;10:5603-8.

[313] Zhao Y, Tang G-S, Yu Z-Z, Qi J-S. The effect of graphite oxide on the thermoelectric properties of polyaniline. Carbon 2012;50:3064-73.

[314] Zhang K, Davis M, Qiu J, Hope-Weeks L, Wang S. Thermoelectric properties of porous multi-walled carbon nanotube/polyaniline core/shell nanocomposites. Nanotechnology 2012;23:385701.

[315] Wang Q, Yao Q, Chang J, Chen L. Enhanced Thermoelectric Properties of CNT/PANI Composite Nanofibers by Highly Orienting the Arrangement of Polymer Chains. J Mater Chem 2012;22:17612-8.

[316] Yu C, Kim YS, Kim D, Grunlan JC. Thermoelectric Behavior of Segregated-Network Polymer Nanocomposites. Nano Lett 2008;8:4428-32.

[317] Zhang B, Sun J, Katz HE, Fang F, Opila RL. Promising Thermoelectric Properties of Commercial PEDOT:PSS Materials and Their Bi_2Te_3 Powder Composites. ACS Appl Mater Interfaces 2010;2:3170-8.

[318] Oh JY, Lee JH, Han SW, Chae SS, Bae EJ, Kang YH, et al. Chemically Exfoliated Transition Metal Dichalcogenide Nanosheet-Based Wearable Thermoelectric Generators. Energy Environ Sci 2016;9:1696-705.

[319] Du Y, Cai KF, Chen S, Cizek P, Lin T. Facile Preparation and Thermoelectric Properties of Bi_2Te_3 Based Alloy Nanosheet/PEDOT:PSS Composite Films. ACS Appl Mater Interfaces 2014;6:5735-43.

[320] Teweldebrhan D, Goyal V, Balandin AA. Exfoliation and Characterization of Bismuth Telluride Atomic Quintuples and Quasi-Two-Dimensional Crystals. Nano Lett 2010;10:1209-18.

[321] Teweldebrhan D, Goyal V, Rahman M, Balandin AA. Atomically-thin crystalline films and ribbons of bismuth telluride. Appl Phys Lett 2010;96:053107.

[322] Ren L, Qi X, Liu Y, Hao G, Huang Z, Zou X, et al. Large-scale production of ultrathin topological insulator bismuth telluride nanosheets by a hydrothermal intercalation and exfoliation route. J Mater Chem 2012;22:4921-6.

[323] Jin M, Shi X-L, Feng T, Liu W, Feng H, Pantelides ST, et al. Super Large $Sn_{1-x}Se$ Single Crystals with Excellent Thermoelectric Performance. ACS Appl Mater Interfaces 2019;11:8051-9.

[324] Shi X, Chen Z-G, Liu W, Yang L, Hong M, Moshwan R, et al. Achieving High Figure of Merit in p-Type Polycrystalline $Sn_{0.98}Se$ *via* Self-Doping and Anisotropy-Strengthening. Energy Storage Mater 2018;10:130-8.

[325] Shi XL, Zheng K, Liu WD, Wang Y, Yang YZ, Chen ZG, et al. Realizing High Thermoelectric Performance in n-Type Highly Distorted Sb-Doped SnSe Microplates *via* Tuning High Electron Concentration and Inducing Intensive Crystal Defects. Adv Energy Mater 2018;8:1800775.

[326] Dargusch M, Shi X-L, Tran XQ, Feng T, Somidin F, Tan X, et al. *In-Situ* Observation of the Continuous Phase Transition in Determining the High Thermoelectric Performance of Polycrystalline $Sn_{0.98}Se$. J Phys Chem Lett 2019;10:6512-7.

[327] Shi XL, Zheng K, Hong M, Liu WD, Moshwan R, Wang Y, et al. Boosting the Thermoelectric Performance of p-Type Heavily Cu-Doped Polycrystalline SnSe *via* Inducing Intensive Crystal Imperfections and Defect Phonon Scattering. Chem Sci 2018;9:7376-89.

[328] Shi X, Wu A, Feng T, Zheng K, Liu W, Sun Q, et al. High Thermoelectric Performance in p-type Polycrystalline Cd-doped SnSe Achieved by a Combination of Cation Vacancies and Localized Lattice Engineering. Adv Energy Mater 2019;9:1803242.

[329] Shi X, Wu A, Liu W, Moshwan R, Wang Y, Chen Z-G, et al. Polycrystalline SnSe with Extraordinary Thermoelectric Property *via* Nanoporous Design. ACS Nano 2018;12:11417-25.

[330] Shi X-L, Liu W-D, Wu A-Y, Nguyen VT, Gao H, Sun Q, et al. Optimization of Sodium Hydroxide for Securing High Thermoelectric Performance in Polycrystalline $Sn_{1-x}Se$ *via* Anisotropy and Vacancy Synergy. InfoMat 2020;2:1201-15.

[331] Zheng Y, Shi X-L, Yuan H, Lu S, Qu X, Liu W, et al. A Synergy of Strain Loading and Laser Radiation in Determining the High-Performing Electrical Transports in the Single Cu-Doped SnSe Microbelt. Mater Today Phys 2020;13:100198.

[332] Zeng Z, Yin Z, Huang X, Li H, He Q, Lu G, et al. Single-Layer Semiconducting Nanosheets: High-Yield Preparation and Device Fabrication. Angew Chem Int Ed 2011;50:11093-7.

[333] Bos JWG, Zandbergen HW, Lee MH, Ong NP, Cava RJ. Structures and Thermoelectric Properties of the Infinitely Adaptive Series $(Bi_2)_m(Bi_2Te_3)_n$. Phys Rev B 2007;75:195203.

[334] X. B. Zhao XHJ, Y. H. Zhang, T. J. Zhu, J. P. Tu, and X. B. Zhang. Bismuth telluride nanotubes and the effects on the thermoelectric properties of nanotube-containing nanocomposites. Appl Phys Lett 2005;86:062111.

[335] Wang Y, Liu W-D, Shi X-L, Hong M, Wang L-J, Li M, et al. Enhanced Thermoelectric Properties of Nanostructured *n*-Type Bi_2Te_3 by Suppressing Te Vacancy through Non-Equilibrium Fast Reaction. Chem Eng J 2019;391:123513.

[336] Gao T, Wang B, Ding B, Lee JK, Leu PW. Uniform and ordered copper nanomeshes by microsphere lithography for transparent electrodes. Nano Lett 2014;14:2105-10.

[337] Chen CY, Lee WK, Chen YJ, Lu CY, Lin HY, Wu CC. Enhancing Optical Out-Coupling of Organic Light-Emitting Devices with Nanostructured Composite Electrodes Consisting of Indium Tin Oxide Nanomesh and Conducting Polymer. Adv Mater 2015;27:4883-8.

[338] Gao P, He J, Zhou S, Yang X, Li S, Sheng J, et al. Large-Area Nanosphere Self-Assembly by a Micro-Propulsive Injection Method for High Throughput Periodic Surface Nanotexturing. Nano Lett 2015;15:4591-8.

[339] Zhang L, Zhong X, Pavlica E, Li S, Klekachev A, Bratina G, et al. A nanomesh scaffold for supramolecular nanowire optoelectronic devices. Nat Nano 2016;11:900-6.

[340] Liu J, Wang Z, Zhao Y, Cheng H, Hu C, Jiang L, et al. Three-Dimensional Graphene–Polypyrrole Hybrid Electrochemical Actuator. Nanoscale 2014;4:7563.

[341] Zhou J, Lubineau G. Improving Electrical Conductivity in Polycarbonate Nanocomposites Using Highly Conductive PEDOT/PSS Coated MWCNTs. ACS Appl Mater Interfaces 2013;5:6189-200.

[342] Shi H, Liu C, Xu J, Song H, Lu B, Jiang F, et al. Facile Fabrication of PEDOT:PSS/Polythiophenes Bilayered Nanofilms on Pure Organic Electrodes and Their Thermoelectric Performance. ACS Appl Mater Interfaces 2013;5:12811-9.

[343] Toshima N. Conductive polymers as a new type of thermoelectric material. Macromol Symp 2002;186:81–6.

[344] Han G, Shi G. Conducting Polymer Electrochemical Actuator Made of High-Strength Three-Layered Composite Films of Polythiophene and Polypyrrole. Sensor Actuat B-Chem 2004;99:525-31.

[345] Zhang J, Gao L, Sun J, Liu Y, Wang Y, Wang J. Incorporation of Single-Walled Carbon Nanotubes with PEDOT/PSS in DMSO for the Production of Transparent Conducting Films. Diam Relat Mater 2012;22:82-7.

[346] Hewitt CA, Kaiser AB, Roth S, Craps M, Czerw R, Carroll DL. Multilayered Carbon Nanotube/Polymer Composite Based Thermoelectric Fabrics. Nano Lett 2012;12:1307-10.

[347] Zebarjadi M, Joshi G, Zhu G, Yu B, Minnich A, Lan Y, et al. Power Factor Enhancement by Modulation Doping in Bulk Nanocomposites. Nano Lett 2011;11:2225-30.

[348] Yu B, Zebarjadi M, Wang H, Lukas K, Wang H, Wang D, et al. Enhancement of Thermoelectric Properties by Modulation-Doping in Silicon Germanium Alloy Nanocomposites. Nano Lett 2012;12:2077-82.

[349] Zhao D, Wang H, Khan ZU, Chen JC, Gabrielsson R, Jonsson MP, et al. Ionic thermoelectric supercapacitors. Energy Environ Sci 2016;9:1450-7.

[350] Guan X, Cheng H, Ouyang J. Significant enhancement in the Seebeck coefficient and power factor of thermoelectric polymers by the Soret effect of polyelectrolytes. J Mater Chem A 2018;6:19347-52.

[351] Jiao F, Naderi A, Zhao D, Schlueter J, Shahi M, Sundström J, et al. Ionic thermoelectric paper. J Mater Chem A 2017;5:16883-8.

[352] Aranguren P, Roch A, Stepien L, Abt M, Von Lukowicz M, Dani I, et al. Optimized Design for Flexible Polymer Thermoelectric Generators. Appl Therm Eng 2016;102:402-11.

[353] Liu J, Jia Y, Jiang Q, Jiang F, Li C, Wang X, et al. Highly Conductive Hydrogel Polymer Fibers toward Promising Wearable Thermoelectric Energy Harvesting. ACS Appl Mater Interfaces 2018;10:44033-40.

[354] Jia Y, Shen L, Liu J, Zhou W, Du Y, Xu J, et al. An Efficient PEDOT-Coated Textile for Wearable Thermoelectric Generators and Strain Sensors. J Mater Chem C 2019;7:3496-502.

[355] Zhang J, Xuan Y. An integrated design of the photovoltaic-thermoelectric hybrid system. Sol Energy 2019;177:293-8.

[356] Lee JJ, Yoo D, Park C, Choi HH, Kim JH. All organic-based solar cell and thermoelectric generator hybrid device system using highly conductive PEDOT:PSS film as organic thermoelectric generator. Sol Energy 2016;134:479-83.

[357] Glatz W, Muntwyler S, Hierold C. Optimization and Fabrication of Thick Flexible Polymer Based Micro Thermoelectric Generator. Sensor Actuat A-phys 2006;132:337-45.

[358] Aswal DK, Basu R, Singh A. Key issues in development of thermoelectric power generators: High figure-of-merit materials and their highly conducting interfaces with metallic interconnects. Energ Convers Manage 2016;114:50-67.

[359] Pires AL, Cruz IF, Silva J, Oliveira GNP, Ferreira-Teixeira S, Lopes AML, et al. Printed Flexible μ-Thermoelectric Device Based on Hybrid Bi_2Te_3/PVA Composites. ACS Appl Mater Interfaces 2019;11:8969-81.

[360] Zhang Z, Qiu J, Wang S. Roll-to-Roll Printing of Flexible Thin-Film Organic Thermoelectric Devices. Manuf Lett 2016;8:6-10.

[361] Chen A, Madan D, Wright PK, Evans JW. Dispenser-Printed Planar Thick-Film Thermoelectric Energy Generators. J Micromech Microeng 2011;21:104006.

[362] Park T, Lim H, Hwang JU, Na J, Lee H, Kim E. Roll Type Conducting Polymer Legs for Rigid-Flexible Thermoelectric Generator. APL Mater 2017;5:074106.

[363] Madan D, Wang Z, Chen A, Juang R-c, Keist J, Wright PK, et al. Enhanced Performance of Dispenser Printed MA n-Type Bi_2Te_3 Composite Thermoelectric Generators. ACS Appl Mater Interfaces 2012;4:6117-24.

[364] Fang H, Popere BC, Thomas EM, Mai CK, Chang WB, Bazan GC, et al. Large-Scale Integration of Flexible Materials into Rolled and Corrugated Thermoelectric Modules. J Appl Polym Sci 2017;134:44208.

[365] Im H, Moon HG, Lee JS, Chung IY, Kang TJ, Kim YH. Flexible Thermocells for Utilization of Body Heat. Nano Res 2014;7:443-52.

[366] Li M, Hong M, Dargusch M, Zou J, Chen Z-G. High-Efficiency Thermocells Driven by Thermo-Electrochemical Processes. Trends Chem 2020;10.1016/j.trechm.2020.11.001.

[367] Chen G, Li Y, Bick M, Chen J. Smart Textiles for Electricity Generation. Chem Rev 2020;120:3668-720.

[368] McGrail BT, Sehirlioglu A, Pentzer E. Polymer Composites for Thermoelectric Applications. Angew Chem Int Ed 2015;54:1710-23.

[369] Petsagkourakis I, Kim N, Tybrandt K, Zozoulenko I, Crispin X. Poly(3,4-ethylenedioxythiophene): Chemical Synthesis, Transport Properties, and Thermoelectric Devices. Adv Electron Mater 2019;5:1800918.

[370] Ding J, Zhao W, Jin W, Di C-a, Zhu D. Advanced Thermoelectric Materials for Flexible Cooling Application. Adv Funct Mater 2021;31:2010695.

[371] Liu Y, Liu P, Jiang Q, Jiang F, Liu J, Liu G, et al. Organic/inorganic hybrid for flexible thermoelectric fibers. Chem Eng J 2021;405:126510.

[372] Deng L, Chen G. Recent progress in tuning polymer oriented microstructures for enhanced thermoelectric performance. Nano Energy 2021;80:105448.

[373] Zhou Q, Zhu K, Li J, Li Q, Deng B, Zhang P, et al. Leaf-Inspired Flexible Thermoelectric Generators with High Temperature Difference Utilization Ratio and Output Power in Ambient Air. Adv Sci 2021;https://doi.org/10.1002/advs.202004947.

[374] Lund A, Tian Y, Darabi S, Müller C. A polymer-based textile thermoelectric generator for wearable energy harvesting. J Power Sources 2020;480:228836.

[375] Zhang C, Zhang Q, Zhang D, Wang M, Bo Y, Fan X, et al. Highly Stretchable Carbon Nanotubes/Polymer Thermoelectric Fibers. Nano Lett 2021;21:1047-55.

[376] Kang YH, Ko S-J, Lee M-H, Lee YK, Kim BJ, Cho SY. Highly efficient and air stable thermoelectric devices of poly(3-hexylthiophene) by dual doping of Au metal precursors. Nano Energy 2021;82:105681.

[377] Xu J, Wang H, Du X, Cheng X, Du Z, Wang H. Highly Stretchable PU Ionogels with Self-Healing Capability for a Flexible Thermoelectric Generator. ACS Appl Mater Interfaces 2021;13:20427-34.

[378] Jung S-J, Shin J, Lim S-S, Kwon B, Baek S-H, Kim SK, et al. Porous organic filler for high efficiency of flexible thermoelectric generator. Nano Energy 2021;81:105604.

[379] Jiang C, Wei P, Ding Y, Cai K, Tong L, Gao Q, et al. Ultrahigh performance polyvinylpyrrolidone/Ag_2Se composite thermoelectric film for flexible energy harvesting. Nano Energy 2021;80:105488.

[380] Wang H, Yu C. Organic Thermoelectrics: Materials Preparation, Performance Optimization, and Device Integration. Joule 2019;3:53-80.

[381] Xu S, Hong M, Shi X-L, Li M, Sun Q, Chen Q, et al. Computation-Guided Design of High-Performance Flexible Thermoelectric Modules for Sunlight-to-electricity Conversion. Energy Environ Sci 2020;13:3480-8.

[382] Cai B, Li J, Sun H, Zhao P, Yu F, Zhang L, et al. Sodium doped polycrystalline SnSe: High pressure synthesis and thermoelectric properties. J Alloys Compd 2017;727:1014-9.

[383] Wan C, Tian R, Azizi AB, Huang Y, Wei Q, Sasai R, et al. Flexible thermoelectric foil for wearable energy harvesting. Nano Energy 2016;30:840-5.

[384] Kim CS, Lee GS, Choi H, Kim YJ, Yang HM, Lim SH, et al. Structural design of a flexible thermoelectric power generator for wearable applications. Appl Energ 2018;214:131-8.

[385] Qu D, Huang X, Li X, Wang H, Chen G. Annular flexible thermoelectric devices with integrated-module architecture. npj Flexible Electronics 2020;4:1.

[386] Jo SE, Kim MK, Kim MS, Kim Y-J. Flexible Thermoelectric Generator for Human Body Heat Energy Harvesting. Electron Lett 2012;48:1015-7.

[387] Søndergaard RR, Hösel M, Espinosa N, Jørgensen M, Krebs FC. Practical Evaluation of Organic Polymer Thermoelectrics by Large-Area R2R Processing on Flexible Substrates. Energ Sci Eng 2013;1:81-8.

[388] Liang J, Tong K, Pei Q. A Water-Based Silver-Nanowire Screen-Print Ink for the Fabrication of Stretchable Conductors and Wearable Thin-Film Transistors. Adv Mater 2016;28:5986-96.

[389] Faddoul R, Reverdy-Bruas N, Blayo A. Formulation and Screen Printing of Water Based Conductive Flake Silver Pastes onto Green Ceramic Tapes for Electronic Applications. Mat Sci Eng B 2012;177:1053-66.

[390] Le HP. Progress and Trends in Ink-Jet Printing Technology. J Imaging Sci Techn 1998;42:49-62.

[391] Truby RL, Lewis JA. Printing soft matter in three dimensions. Nature 2016;540:371-8.

[392] Yuk H, Zhao X. A New 3D Printing Strategy by Harnessing Deformation, Instability, and Fracture of Viscoelastic Inks. Adv Mater 2018;30:1704028.

[393] Yuk H, Lu B, Lin S, Qu K, Xu J, Luo J, et al. 3D printing of conducting polymers. Nat Commun 2020;11:1604.

[394] Hwang JK, Cho S, Dang JM, Kwak EB, Song K, Moon J, et al. Direct nanoprinting by liquid-bridge-mediated nanotransfer moulding. Nat Nano 2010;5:742-8.

[395] Suh KY, Lee HH. Capillary Force Lithography: Large-Area Patterning, Self-Organization, and Anisotropic Dewetting. Adv Funct Mater 2002;12:405-13.

[396] Abargues R, Rodríguez-Cantó PJ, García-Calzada R, Martínez-Pastor J. Patterning of Conducting Polymers Using UV Lithography: The *in-Situ* Polymerization Approach. J Phys Chem C 2012;116:17547-53.

[397] Mahmoodian M, Hajihoseini H, Mohajerzadeh S, Fathipour M. Nano patterning and fabrication of single polypyrrole nanowires by electron beam lithography. Synthetic Met 2019;249:14-24.

[398] Fan X, Nie W, Tsai H, Wang N, Huang H, Cheng Y, et al. PEDOT:PSS for Flexible and Stretchable Electronics: Modifications, Strategies, and Applications. Adv Sci 2019;6:1900813.

[399] Zhang Q, Wang W, Li J, Zhu J, Wang L, Zhu M, et al. Preparation and Thermoelectric Properties of Multi-Walled Carbon Nanotube/Polyaniline Hybrid Nanocomposites. J Mater Chem A 2013;1:12109-14.

[400] Wang J, Cai K, Shen S, Yin J. Preparation and Thermoelectric Properties of Multi-Walled Carbon Nanotubes/Polypyrrole Composites. Synthetic Met 2014;195:132-6.

[401] Yue R, Xu J. Poly(3,4-ethylenedioxythiophene) as promising organic thermoelectric materials: A mini-review. Synthetic Met 2012;162:912-7.

[402] Li P, Zhao Y, Li H, Liu S, Liang Y, Cheng X, et al. Facile Green Strategy for Improving Thermoelectric Performance of Carbon Nanotube/Polyaniline Composites by Ethanol Treatment. Compos Sci Technol 2020;189:108023.

[403] Cho C, Qin S, Choi K, Grunlan JC. Improved Thermoelectric Power Factor in Completely Organic Nanocomposite Enabled by l-Ascorbic Acid. ACS Appl Polym Mater 2019;1:1942-7.

[404] Wang H, Hsu JH, Yi SI, Kim SL, Choi K, Yang G, et al. Thermally Driven Large n-Type Voltage Responses from Hybrids of Carbon Nanotubes and Poly(3,4-ethylenedioxythiophene) with Tetrakis(dimethylamino)ethylene. Adv Mater 2015;27:6855-61.

[405] Zheng Y, Zhang Q, Jin W, Jing Y, Chen X, Han X, et al. Carbon Nanotube Yarn Based Thermoelectric Textiles for Harvesting Thermal Energy and Powering Electronics. J Mater Chem A 2020;8:2984-94.

[406] Liang L, Fan J, Wang M, Chen G, Sun G. Ternary Thermoelectric Composites of Polypyrrole/PEDOT:PSS/Carbon Nanotube with Unique Layered Structure Prepared by One-Dimensional Polymer Nanostructure as Template. Compos Sci Technol 2020;187:107948.

[407] Prabhakar R, Hossain MS, Zheng W, Athikam PK, Zhang Y, Hsieh Y-Y, et al. Tunneling-Limited Thermoelectric Transport in Carbon Nanotube Networks Embedded in Poly(dimethylsiloxane) Elastomer. ACS Appl Energy Mater 2019;2:2419-26.

[408] An CJ, Lee YC, Kang YH, Cho SY. Improved Interaction between Semiconducting Polymer and Carbon Nanotubes in Thermoelectric Composites through Covalent Grafting. Carbon 2017;124:662-8.

[409] Li C, Jiang F, Liu C, Wang W, Li X, Wang T, et al. A Simple Thermoelectric Device Based on Inorganic/Organic Composite Thin Film for Energy Harvesting. Chem Eng J 2017;320:201-10.

[410] Hu X, Zhang K, Zhang J, Wang S, Qiu Y. Thermoelectric Properties of Conducting Polymer Nanowire–Tellurium Nanowire Composites. ACS Appl Energy Mater 2018;1:4883-90.

[411] Lu Y, Qiu Y, Jiang Q, Cai K, Du Y, Song H, et al. Preparation and Characterization of Te/Poly(3,4-ethylenedioxythiophene):Poly(styrenesulfonate)/Cu_7Te_4 Ternary Composite Films for Flexible Thermoelectric Power Generator. ACS Appl Mater Interfaces 2018;10:42310-9.

[412] Novak TG, Shin H, Kim J, Kim K, Azam A, Nguyen CV, et al. Low-Cost Black Phosphorus Nanofillers for Improved Thermoelectric Performance in PEDOT:PSS Composite Films. ACS Appl Mater Interfaces 2018;10:17957-62.

[413] Thongkham W, Lertsatitthanakorn C, Jiramitmongkon K, Tantisantisom K, Boonkoom T, Jitpukdee M, et al. Self-Assembled Three-Dimensional Bi_2Te_3 Nanowire–PEDOT:PSS Hybrid Nanofilm Network for Ubiquitous Thermoelectrics. ACS Appl Mater Interfaces 2019;11:6624-33.

[414] Kim WS, Anoop G, Jeong I-S, Lee HJ, Kim HB, Kim SH, et al. Feasible Tuning of Barrier Energy in PEDOT:PSS/Bi_2Te_3 Nanowires-Based Thermoelectric Nanocomposite Thin Films through Polar Solvent Vapor Annealing. Nano Energy 2020;67:104207.

[415] Goo G, Anoop G, Unithrattil S, Kim WS, Lee HJ, Kim HB, et al. Proton-Irradiation Effects on the Thermoelectric Properties of Flexible Bi_2Te_3/PEDOT:PSS Composite Films. Adv Electron Mater 2019;5:1800786.

[416] Bharti M, Singh A, Saini G, Saha S, Bohra A, Kaneko Y, et al. Boosting Thermoelectric Power Factor of Free-Standing Poly(3,4ethylenedioxythiophene):Polystyrenesulphonate Films by Incorporation of Bismuth Antimony Telluride Nanostructures. J Power Sources 2019;435:226758.

[417] Cheng X, Wang L, Wang X, Chen G. Flexible Films of Poly(3,4-ethylenedioxythiophene):Poly (styrenesulfonate)/SnS Nanobelt Thermoelectric Composites. Compos Sci Technol 2018;155:247-51.

[418] Ju H, Park D, Kim K, Kim J. Exfoliated Sn–Se–Te Based Nanosheets and Their Flexible Thermoelectric Composites with Poly(3,4-ethylenedioxythiophene):Poly(styrenesulfonate) Fabricated by Solution Processing. Org Electron 2019;71:131-5.

[419] Pammi SVN, Jella V, Choi J-S, Yoon S-G. Enhanced Thermoelectric Properties of Flexible $Cu_{2-x}Se$ ($x \geq 0.25$) NW/Polyvinylidene Fluoride Composite Films Fabricated *via* Simple Mechanical Pressing. J Mater Chem C 2017;5:763-9.

[420] Wang X, Meng F, Jiang Q, Zhou W, Jiang F, Wang T, et al. Simple Layer-by-Layer Assembly Method for Simultaneously Enhanced Electrical Conductivity and Thermopower of PEDOT:PSS/ce-MoS_2 Heterostructure Films. ACS Appl Energy Mater 2018;1:3123-33.

[421] Guan X, Feng W, Wang X, Venkatesh R, Ouyang J. Significant Enhancement in the Seebeck Coefficient and Power Factor of p-Type Poly(3,4-ethylenedioxythiophene):Poly(styrenesulfonate) through the Incorporation of n-Type MXene. ACS Appl Mater Interfaces 2020;12:13013-20.

[422] Kim S, Yeol Hyeon D, Su Ham S, Youn J, Seong Lee H, Yi S, et al. Synergetic enhancement of the energy harvesting performance in flexible hybrid generator driven by human body using thermoelectric and piezoelectric combine effects. Appl Surf Sci 2021;558:149784.

[423] Tian R, Wan C, Wang Y, Wei Q, Ishida T, Yamamoto A, et al. A solution-processed TiS_2/organic hybrid superlattice film towards flexible thermoelectric devices. J Mater Chem A 2017;5:564-70.

[424] Meng Q, Qiu Y, Cai K, Ding Y, Wang M, Pu H, et al. High Performance and Flexible Polyvinylpyrrolidone/Ag/Ag_2Te Ternary Composite Film for Thermoelectric Power Generator. ACS Appl Mater Interfaces 2019;11:33254-62.

[425] Deng L, Zhang Y, Wei S, Lv H, Chen G. Highly foldable and flexible films of PEDOT:PSS/Xuan paper composites for thermoelectric application. J Mater Chem A 2021;9:8317-24.

[426] Wei S, Huang X, Deng L, Yan Z-C, Chen G. Facile preparations of layer-like and honeycomb-like films of poly(3,4-ethylenedioxythiophene)/carbon nanotube composites for thermoelectric application. Compos Sci Technol 2021;208:108759.

[427] Chen Y, Zhao Y, Liang Z. Solution processed organic thermoelectrics: towards flexible thermoelectric modules. Energy Environ Sci 2015;8:401-22.

[428] Bahk J-H, Fang H, Yazawa K, Shakouri A. Flexible thermoelectric materials and device optimization for wearable energy harvesting. J Mater Chem C 2015;3:10362-74.

[429] Liu E, Negm A, Howlader MMR. Thermoelectric generation *via* tellurene for wearable applications: recent advances, research challenges, and future perspectives. Mater Today Energy 2021;20:100625.

[430] Varghese T, Dun C, Kempf N, Saeidi-Javash M, Karthik C, Richardson J, et al. Flexible Thermoelectric Devices of Ultrahigh Power Factor by Scalable Printing and Interface Engineering. Adv Funct Mater 2020;30:1905796.

[431] Byun S-H, Kim CS, Agno K-C, Lee S, Li Z, Cho BJ, et al. Design Strategy for Transformative Electronic System toward Rapid, Bidirectional Stiffness Tuning using Graphene and Flexible Thermoelectric Device Interfaces. Adv Mater 2021;33:2007239.

[432] Niu H, Liu Y, Song H, Meng Q, Du Y, Shen SZ. Facile preparation of flexible all organic PEDOT:PSS/methyl cellulose thermoelectric composite film by a screen printing process. Synthetic Met 2021;276:116752.

[433] Liu C, Yin X, Chen Z, Gao C, Wang L. Improving the thermoelectric performance of solution-processed polymer nanocomposites by introducing platinum acetylides with tailored intermolecular interactions. Chem Eng J 2021;419:129624.

[434] Park D, Ju H, Kim J. Enhanced thermoelectric properties of flexible N-type Ag_2Se nanowire/polyvinylidene fluoride composite films synthesized via solution mixing. J Ind Eng Chem 2021;93:333-8.

[435] El-Shamy AG. Acido-treatment of PEDOT:PSS/Carbon Dots (C_{Dots}) nano-composite films for high thermoelectric power factor performance and generator. Mater Chem Phys 2021;257:123762.

[436] Meng Q, Song H, Du Y, Ding Y, Cai K. Facile preparation of poly(3,4-ethylenedioxythiophene): poly(styrenesulfonate)/Ag_2Te nanorod composite films for flexible thermoelectric generator. J Materiomics 2021;7:302-9.

[437] Zhang J, Seyedin S, Qin S, Lynch PA, Wang Z, Yang W, et al. Fast and scalable wet-spinning of highly conductive PEDOT:PSS fibers enables versatile applications. J Mater Chem A 2019;7:6401-10.

[438] Liang L, Wang X, Wang M, Liu Z, Chen G, Sun G. Flexible poly(3,4-ethylenedioxythiophene)-tosylate/SWCNT composite films with ultrahigh electrical conductivity for thermoelectric energy harvesting. Compos Commun 2021;25:100701.

[439] Song H, Yao Y, Tang C, Zhang L, Lu Y, Sun Q, et al. Tunable thermoelectric properties of free-standing PEDOT nanofiber film through adjusting its nanostructure. Synthetic Met 2021;275:116742.

[440] Klochko NP, Klepikova KS, Khrypunova IV, Zhadan DO, Petrushenko SI, Kopach VR, et al. Flexible thermoelectric module based on zinc oxide thin film grown *via* SILAR. Curr Appl Phys 2021;21:121-33.

[441] Cao Y, Abu-Hamdeh NH, Moria H, Asaadi S, Alsulami R, Sadighi Dizaji H. A novel proposed flexible thin-film solar annular thermoelectric generator. Appl Therm Eng 2021;183:116245.

[442] Lu Y, Li X, Cai K, Gao M, Zhao W, He J, et al. Enhanced-Performance PEDOT:PSS/Cu_2Se-Based Composite Films for Wearable Thermoelectric Power Generators. ACS Appl Mater Interfaces 2021;13:631-8.

[443] Zhang L, Lin S, Hua T, Huang B, Liu S, Tao X. Fiber-Based Thermoelectric Generators: Materials, Device Structures, Fabrication, Characterization, and Applications. Adv Energy Mater 2018;8:1700524.

[444] Huang L, Lin S, Xu Z, Zhou H, Duan J, Hu B, et al. Fiber-Based Energy Conversion Devices for Human-Body Energy Harvesting. Adv Mater 2020;32:1902034.

[445] Chen W-Y, Shi X-L, Zou J, Chen Z-G. Wearable Fiber-Based Thermoelectrics from Materials to Applications. Nano Energy 2020;81:105684.

[446] Hwang B, Lund A, Tian Y, Darabi S, Müller C. Machine-Washable Conductive Silk Yarns with a Composite Coating of Ag Nanowires and PEDOT:PSS. ACS Appl Mater Interfaces 2020;12:27537-44.

[447] Kim Y, Lund A, Noh H, Hofmann AI, Craighero M, Darabi S, et al. Robust PEDOT:PSS Wet-Spun Fibers for Thermoelectric Textiles. Macromol Mater Eng 2020;305:1900749.

[448] Liu J, Zhu Z, Zhou W, Liu P, Liu P, Liu G, et al. Flexible metal-free hybrid hydrogel thermoelectric fibers. J Mater Sci 2020;55:8376-87.

[449] Zhang F, Zang Y, Huang D, Di C-a, Zhu D. Flexible and self-powered temperature–pressure dual-parameter sensors using microstructure-frame-supported organic thermoelectric materials. Nat Commun 2015;6:8356.

[450] Zhang Q, Ai X, Wang L, Chang Y, Luo W, Jiang W, et al. Improved Thermoelectric Performance of Silver Nanoparticles-Dispersed Bi_2Te_3 Composites Deriving from Hierarchical Two-Phased Heterostructure. Adv Funct Mater 2015;25:966-76.

Graphical abstract

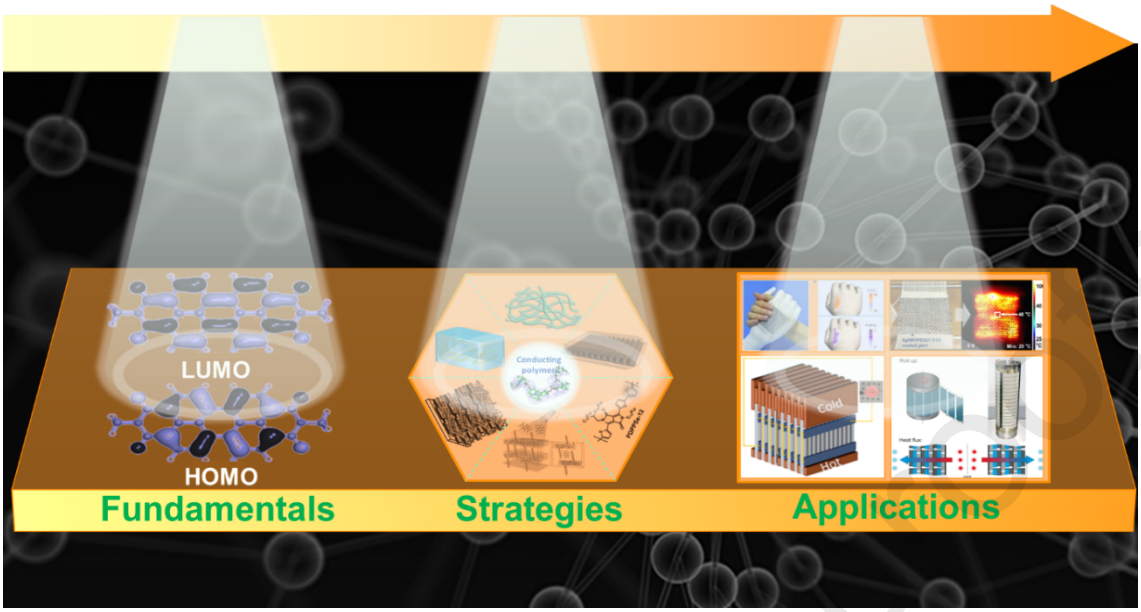

Declaration of interests

☒ The authors declare that they have no known competing financial interests or personal relationships that could have appeared to influence the work reported in this paper.

☐The authors declare the following financial interests/personal relationships which may be considered as potential competing interests: